論文 / 著書情報
Article / Book Information

題目(和文)	
Title(English)	Mechanical Behavior of Cantilever-type Large Diameter Steel Tubular Pile Wall Embedded in Stiff Ground
著者(和文)	KunasegaramVijayakanthan
Author(English)	Kunasegaram Vijayakanthan
出典(和文)	学位:博士(学術), 学位授与機関:東京工業大学, 報告番号:甲第11659号, 授与年月日:2020年9月25日, 学位の種別:課程博士, 審査員:竹村 次朗,北詰 昌樹,髙橋 章浩,笠間 清伸,田村 修次
Citation(English)	Degree:Doctor (Academic), Conferring organization: Tokyo Institute of Technology, Report number:甲第11659号, Conferred date:2020/9/25, Degree Type:Course doctor, Examiner:,,,,
学位種別(和文)	博士論文
Type(English)	Doctoral Thesis

Mechanical Behavior of Cantilever-type Large Diameter Steel Tubular Pile Wall Embedded in Stiff Ground

by

Kunasegaram Vijayakanthan

A dissertation submitted in partial fulfilment of the requirements for the degree of Doctor of Philosophy

Academic advisor

Dr.Jiro Takemura

Department of Civil and Environmental Engineering

Tokyo Institute of Technology

Tokyo, Japan

July 2019

Abstract

This thesis describes the hypothesis behind the mechanical behavior of cantilever type large diameter steel tubular pipe (CSTP) retaining walls embedded in soft rock. Cantilever type retaining wall has several advantages, it can be constructed in very simple process in a limited space, which is a common condition in highly populated urban area. However, the applications of cantilever type retaining walls are limited to a moderate retained height of earth in relatively soft foundation conditions. Limitations arises from large displacements caused by the flexural bending and wall deflection as well as less redundancy of the structure without additional reinforcing mechanisms, such as tie-back plates or ground anchors in soft grounds. On the other hand, the wall deflection can be significantly reduced in relatively hard mediums such as soft to hard rocks. Hence the excessive deformation of large height cantilever wall could be untangled by large diameter cantilever steel tubular pipe (CSTP) walls embedded in hard mediums, even with relatively small embedment depths. For the application of these CSTP walls in to relatively hard mediums no specific design guidelines are available up to date.

Current design practices adopted from the concept of beams on elastic foundation requires minimum embedment depth (d_e) of '$3/\beta$' for the application of CSTP walls, where 'β' is a characteristic value related to the subgrade reaction of the embedded medium and flexural stiffness (EI) of the wall. Attributing to the assumptions made in this design method, required minimum embedment depth increases with increasing EI value, regardless of the retained height. This phenomenon yields unrealistically large embedment depths even for relatively short cantilevered walls even in hard mediums, this is the major drawback of this design method. Which cause difficulties in the pile installation, especially for the large diameter piles into the ground with considerable strength and stiffness, such as soft rock. Therefore, if this type of retaining wall can be constructed with a rational embedment depth in the soft rock type ground with an additional safety margin over the ultimate loads, its applicability can be increased, which could contribute in the reduction of construction time and cost. For the reduction of the embedment depth smaller than the one determined by the current design practice, both the survivability limit and ultimate limit should be reasonably examined in the design. In other words, the design condition should secure allowable displacement by a reasonable evaluation method and the extra margin of safety over the ultimate condition must be confirmed to prevent the catastrophic failure. The process from the design conditions to the failure should be well studied by physical means, such as a physical modelling.

To understand the mechanical behavior of CSTP walls embedded in soft rock and to investigate the influence of '$d_e\beta$' values on the deformation and failure behavior of the walls, a series of model tests were conducted using TIT-Mark-III geotechnical centrifuge under static loading conditions. Dynamic stability of a specific prototype also investigated using a centrifuge model. Observed outcomes under ultimate loading conditions reveals the possibility of a rational design method. Which could provide an economical solution in the construction of CSTP walls in stiff ground conditions.

Deformation and failure behavior of CSTP walls were investigated by using a simplified rectangular wall model with the simulation of excavation and additional loading inflight. A centrifuge modelling system has been developed, in which the loading process from design condition to the ultimate failure conditions can be simulated on a simplified rectangular wall embedded in soft rock at a constant centrifugal (50g) acceleration. For the stiff model grounds, two different artificial soft rock models namely sand rock and mud rock were developed using sand-cement-clay mixture. In-flight excavation and additional lateral loading processes were simulated by means of draining water from the wall front and feeding water to the retained soil side respectively. Outcomes reveal that, wall can stand in the design condition

with relatively small embedment depth (1/β), and poses reasonable safety margin against ultimate loading conditions. Also a small increment in the embedment depth e.g., 0.5 m, can significantly increase the stability of the wall in rock type grounds.

As the observation of simplified wall models reveal the possibility of optimization, further investigations are necessary to observe the behavior of real tubular pile walls and the influential factors regarding to the embedment and loading conditions. Which could provide useful information for the development of a rational design concept. Therefore, the influential factors were investigated through a series of lateral load tests on large diameter steel tubular piles and steel tubular pile walls embedded in different soil profiles such as soft rock and soft rock overlain by sand. Similar to the observation in simplified models, a small increment of embedment depth (1m) significantly increase the lateral resistance and highly control the deformation and failure modes of laterally loaded large diameter steel tubular piles embedded in stiff ground. Unlike soft mediums, a load bearing mechanism of shallow rock layers, provides large lateral resistance at relatively small pile top displacements (1%Φ), which diminish the influence of embedment depths. Observed deformation and failure modes reveals that, there is an optimum embedment depth from which the ultimate failure changes from ground failure to structural failure.

Different failure modes were observed for the single pile and tubular pile wall with the identical embedment (d_e=2Φ) and loading conditions in single soft rock layer. The former exhibited structural buckling and the latter was a clear wedge type ground failure. It reveals that the optimum embedment depth is deeper for the tubular pile wall than single pile, which indicates that the rational embedment for cantilever tubular pile wall is larger than single pile with same cross section. Both, wall model and single pile with the embedment depth of 1.5Φ in single rock layer showed the ground failure as an ultimate failure condition, however the normalized ultimate resistance for single pile is about 1.6times that of wall model and the wall model exhibited a clear wedge type ground failure, while the single pile showed more confined deformations. The difference in the observed ground failures as an ultimate condition for the single pile and wall model embedded in single rock layer is highly influenced by the wall or pile width and thereby the mobilized subgrade reaction. Attributing to the 2-dimensional condition, the influence zone, which contribute to the lateral resistance for a unit width of the wall is much narrower compare to an isolated single pile. This phenomenon causes an increased stress level or strain in the shallow layer of the rock and resulting significant reduction in subgrade reaction. This mechanism causing large deflection of the wall compare to the condition of an isolated single pile. Due to the large deflection of the wall, eventual accumulation of wall deflection in the embedded zone, causing the deterioration of subgrade reaction along the wall embedded zone and eventually causing a wedge type ground failure at the ultimate resistance of the embedded medium.

As the retaining walls are mostly associated to the lifelines and the residential areas, dynamic stability of CSTP wall is a major concern especially when we call for a short embedment depth than the current design practice. Stability of a specific prototype, CSTP wall with a retained height of 12m was investigated under dry and submerged backfill conditions with an embedment depth of 1.2/β. Based on the deformations under dynamic loads, and the creep deformation characteristics of the CSTP wall it can be confirmed that the wall exhibits reasonable safety margin against the ultimate collapse even in a dynamic loading event. The imposed maximum load in the dynamic loading was about 1.2 times the ultimate load applied by static loading in the simplified wall model.

Acknowledgements

I would like to express my sincere gratitude to my thesis supervisor, Associate Professor Jiro Takemura for his continuous support and guidance during this thesis work. His moral and expert advice has played a key role in the successful completion of this work. I am also grateful for the critical insights he has put into my work.

I am also grateful to the rest of my thesis committee: Prof. Masaki Kitazume, Prof. Akihiro Takahashi, Associate Prof. Kiyonobu kasama and Associate Prof.Shuji Tamura for their kind advice, and helpful comments.

I am indebted to the Ministry of Education, Culture, Sports, Science and Technology (MEXT), Japan for granting me a Monbukagakusho scholarship. Without the financial aid from MEXT, this research would not have been possible.

I gratefully acknowledge the invaluable advice and guidance provided by the members and advisers of the IPA TC1 (Committee on Application of Cantilever-type Steel Tubular Pile Wall Embedded in Stiff Ground) in connection with this research.

I would like to acknowledge Mr. Shouhei Akazawa, Miss. Hsiao Wei Hsuan and Mr.Sakae Seki for their continuous support and guidance during my research activities. I also thankful to my colleagues in the Takemura Lab who supported me extensively throughout my studies.

I would like to show my sincere gratitude to Mr. K. Fujiwara and Mr. Y. Ishihama for their insight and expertise that greatly assisted in this research.

I am grateful to my family members Kunasegaram, Kanthimalar, Vijayaluxmi, Vijitharan, Sajanthan, and Thanusiya for their continuous support.

My deepest gratitude goes to my wife, Keerthana, for her understanding, continuous support and encouragement throughout my stay in Japan, this thesis is dedicated to her.

Table of Contents

Table of Figures

List of Table

1 Introduction

1.1 General background

Cantilever type retaining walls has several advantages. It can be constructed in very simple process in very narrow space, which is a common condition in highly populated urban area. However, the applications of cantilever type sheet pile walls are limited to moderate retained height of earth (Madabhushi and Chandrasekaran, 2005) in relatively soft foundation conditions, owing to several limitations raised from the soil, structure and the soil-structure interaction. Rapid urbanization and infrastructure development nearby mountain sites often require relatively large height cantilever type retaining walls due to the space limitation or the complications in the anchoring. In case of a taller retaining wall with large retained height, the active pressures and corresponding moment loads are much higher under static or dynamic excitations.

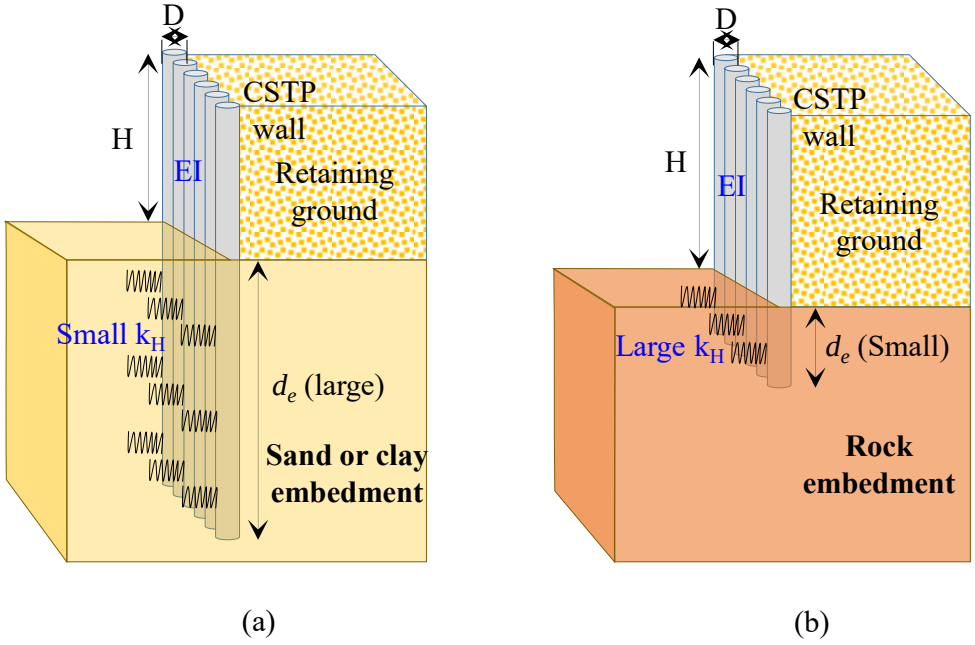

Figure 1.1 Cantilever steel tubular pile (CSTP) wall embedded in (a) soft ground and (b) rock

There are two main concerns in the application of this type of walls with large retain height as permanent structures. One is large displacements caused by the wall bending and the wall deflection (translation and rotation) in the embedded soil, which exponentially increase with the retaining height. The other is less redundancy of the structure without structural supports, such as tie-back plates or ground anchors. Although the bending deformation can be reduced by high stiffness walls, such as large-diameter steel tubular pile walls or reinforced concrete walls, very large embedment depth is required to control the wall deflection within the allowable limits in soft ground (Figure 1.1(a)). This requirement is economically non-feasible (Powrie, 1996). On the other hand, the wall deflection can be significantly reduced in relatively hard mediums such as soft to hard rocks. Hence the excessive deformation of large height cantilever wall could be untangled by high stiffness (EI) large diameter cantilever steel tubular pipe (CSTP) walls embedded in hard mediums, even with relatively small embedment depths as illustrated in Figure 1(b). However, as for the application of these CSTP walls into relatively hard mediums, no specific design guidelines are available up to date.

As for the pile installation into hard media, thanks to the technology advancement in 21st century (ArcelorMittal, 2008; Miyanohara et al., 2018), large diameter steel tubular pile can be installed into very hard ground, like, rock and gravel, and even concrete as shown in Figure 1.2. Although the innovative technology is available to construct relatively taller (12-15 m) CSTP walls with high flexural rigidities even in hard rocks, owing to the absence of specific guidelines for the design of large diameter CSTP walls in relatively hard mediums, the designs of abovementioned walls have been carried out based on the theory of beams on elastic foundation (Suzuki and Kajino, 2018; ASP, 2009). In this design method, the required minimum embedment depth (d_e) increases with the flexural rigidity of the wall (EI) regardless of the applied lateral loads or independent to the retained height of earth. This might yield relatively large embedment depth requirement and overestimation of steel pipe length. This is a major limitation of this design method for the application of large diameter CSTP walls.

(a) **(b)** **(c)**

Figure 1.2 (a) Pile installation in rock embedment (b & c) Rotary drilled sample with 130MPa strength

1.2 Problem statement

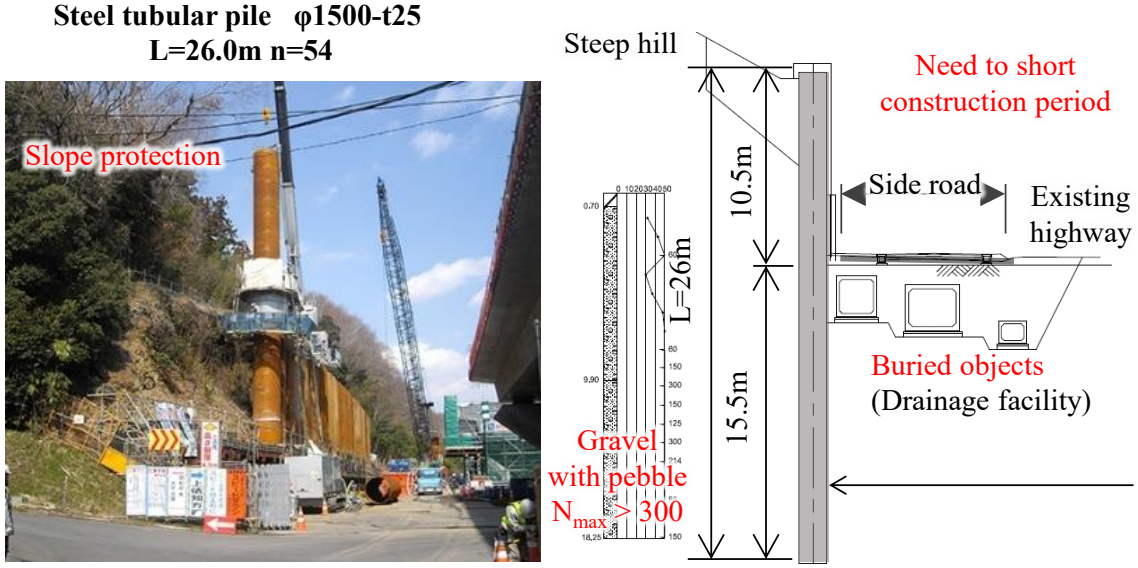

Figure 1.3 One of the constructed cantilever type steel tubular pile (CSTP) walls in Tokyo (Miyanohara et al., 2018)

Utilizing the advanced technologies, relatively taller cantilever type retaining walls can be constructed with different type of wall elements. Depending on the ground conditions the required construction techniques (press-in or rotary cutting press-in) and the wall element (I-sections, conventional steel sheet pile sections, steel tubular sheet pile) could be decided (IPA, 2016). Among these various type of elements and construction techniques, considering the highest flexural rigidity (EI) achievable, this research focuses on the "application of cantilever type large diameter steel tubular pile (CSTP) walls in to relatively hard mediums". This type of pile can be constructed in rock only by Gyro Piler (press-in with rotary cutting). As a real field application of this pioneering technology, relatively taller and cantilever type retaining walls have been constructed in Japan (Miyanohara et al., 2018) with the use of large diameter steel tubular piles in to hard mediums as described in Figure 1.3.

Although the innovative technology is available to construct above mentioned (12-15 m) CSTP walls with high flexural rigidities even in hard rocks, owing to the absence of specific guidelines for the design of large diameter CSTP walls in relatively hard mediums, the designs of constructed walls in Tokyo have been carried out (Suzuki et al., 2018) based on the theory of beams on elastic foundation (ASP, 2009) as mentioned in 1.1. Attributing to the major drawbacks of this design method for the application of large diameter CSTP walls, the required minimum embedment depth (d_e) increases with the flexural rigidity of the wall (EI) regardless of the applied lateral loads or independent to the retained height of earth. This phenomenon might yield relatively large embedment depth requirements even in relatively hard mediums (soft to hard rocks), which might be an overestimation of the embedment depth.

Owing to the requirement of relatively large embedment depth even in hard mediums, the application of large diameter piles are often eliminated from the alternatives, attributing to not only the material cost but also the additional works, such as onsite butt welding to extend the length. Therefore, to enhance the CSTP wall by reducing the construction cost and time, a new design method is needed, by which an optimized embedment depth of walls can be determined.

For the development of a new design method to optimize the embedment depth, both the serviceability limit and ultimate limit states should be reasonably examined in the design. In other words, the design condition should secure allowable displacement by a reasonable evaluation method and the extra margin of safety over the ultimate loading condition must be confirmed to prevent the catastrophic failure. These examinations in a rational manner are critical to address the concerns for the application of cantilever type wall as a permanent structure as pointed in 1.1. Therefore, the process from the design conditions to the failure should be well studied by physical means, such as physical modelling.

1.3 Objectives

1.3.1 Main objective

The main objective of this research is to investigate the hypothesis behind the static and dynamic stability of cantilever type large diameter steel tubular pile (CSTP) walls embedded in soft rock in order to develop a design method with the rationalized embedment depth.

1.3.2 Detail objectives

To accomplish the main objective, various detailed objectives are defined as follows:

a) To modelling of artificial soft rock by using sand-cement-clay mixtures with different combinations and the selection of proper mix for the soft rock

b) To investigate the deformation and failure mechanism of a simplified cantilever type retaining walls embedded in soft rocks

c) To explore the influential factors on the stability and deformation of laterally loaded steel tubular piles embedded in soft rock

d) To study the behavior of laterally loaded steel tubular pile walls embedded in soft rock and layered profile

e) To investigate the dynamic stability of steel tubular pile wall embedded in soft rock under dry and submerged backfill conditions

f) To validate the experimental observations by numerical models in Plaxis-2D and create a chart for the design of cantilever type steel tubular pile walls.

1.4 Scope and limitations

Cantilever type retaining walls can be constructed in numerous ways with different wall elements and soil profiles. Therefore, the investigations in this study are bounded with the application of cantilever type large diameter steel tubular pile (CSTP) walls in soft rock. The behavior of CSTP wall could be investigated in different alternative ways, however each alternative has certain limitations as follows;

1.4.1 Real field testing

In real field condition the soft rock profiles are more diverse and complex as its existence. Deformation characteristics of soft rocks could be altered by several factors such as discontinuities, fissures, cavities and associated high mass permeability, slaking and swelling by wetting and drying cycles, shrinkage etc. Therefore, a general definition could not be given for these widely varying nature of geo-materials. Also the application of loads in order to study the behavior of CSTP walls from elastic to plastic deformations in the real field testing is not feasible. Also the cost associated with the testing process in the real field test is relatively large. Attributing to the uncertainties existing in the real filed testing, the characterization of mechanical properties of embedded medium for a generalized design method also another challenge since it varies from place to place. Therefore, this option is not be suitable for the development of design guideline and generalized design method.

1.4.2 Numerical simulation

Numerical simulation has certain advantages over the experiments, where wide range of analysis could be conducted by varying the strength and stiffness of the embedded medium, such as a strength or stiffness reduction measure to incorporate the discontinuities, fissures and degradation of soft rock materials. However, from the numerical models the actual behavior of rock- wall interactions, nonlinear deformations of embedded mediums, local deformations and failure modes of both structure (tubular pile walls) and rock, time dependent characteristics (creep) could not be effectively captured. Attributing to these deficiencies the numerical models could be used as to predict the behavior upon validating the experimental outcomes up to certain extent, rather than entire dependency.

1.4.3 Undisturbed sampling of actual soft rock for a model study

Although physical models using actual rock with required dimensions is somewhat feasible (Choo and Kim., 2016), similar to the real field testing the variations in the mechanical properties between the different models could not be avoided. Also the cost associated with the

undisturbed sampling would be much higher and the repeatability of experiment with the same ground condition is almost impossible.

1.4.4 Artificial modelling of soft rocks for centrifuge study

The modelling of synthetic soft rock for experimental investigations has a long history (Johnston and Choi., 1986; Indraratna, 1990; Choo and Kim., 2016). Previous researchers proved that the artificial modelling of soft rocks with similar stress-strain behavior of naturally existing soft rocks is feasible. It could also be modelled in any dimensions inside the containers for experimental study with the acceptable range of variations in the mechanical properties and good repeatability in each models. Having a good repeatability of embedded medium, the parametric studies can be conducted to investigate the influential factors, such as embedment depth, loading height, loading mechanisms and stiffness of the wall.

Uniform conditions of artificial soft rocks helps to conduct more sophisticated experimental investigations and the characterization of embedded medium for a generalized design method based on strength and stiffness of the medium. However, the major disadvantage in this modelling compare to the real field is that, this method could not capture the non-uniformities and the discontinuities existing in the real field. Hence, for the construction of these massive retaining structures it is highly recommended to conduct an intensive field investigations and numerical or theoretical analysis, while decision making about the ground parameters for design. A design engineer must work with caution regarding to the adverse weathering characteristics (strength and stiffness reduction) of soft rock materials as well as the possibility of failures as a rock mass or along the discontinuities (BS8002, 1994).

Advantages of centrifuge modelling regarding to this study could be listed as follows:

- Stress similarity between the model and the prototype could be achieved by centrifuge modelling, which enables to model the rock–wall interaction under same confining pressures similar to the prototype up to certain extent.
- Excavation in the wall front and very large water pressures behind the retaining walls, similar to a cofferdam could be simulated by means of inflight drainage and water feeding systems. Which can be used to study the behavior of structures in hard mediums from elastic to plastic deformations.
- Time dependent deformation characteristics (creep (model to prototype (1:1))) could be studied under similar confining stresses. Also the long term consolidation (model to prototype ($1:N^2$)) characteristics can be simulated in a short period depending on the centrifugal acceleration.
- The geotechnical centrifuge is often utilized as an alternative to the real field experiments, also it provides more reliable outcomes in an economic way for complicated real world problems.

Considering different alternatives and associated limitations, the cost effective, good repeatability and well define mechanical properties with the uniform conditions of embedded medium could be achieved by the physical modelling. Geotechnical centrifuge modelling technique with the key principle of stress similarity (Schofield 1980) between model and prototype has facilitated the study the behavior of large structures in a small scale model with Ng environment. Stress similarity can be achieved at Ng, which helps to study the local deformations of the structures and the embedded medium and the possible failure modes which cannot be achieved in the numerical modelling or 1g models. Besides the centrifuge modelling the numerical modelling also was considered as an option to extend the parametric study and the construction of a design chart for the application of CSTP walls in soft rocks.

1.5 Organization of the dissertation

The thesis organization including the number of each chapter is presented as a schematic diagram in Figure 1.4, where Chapter 1 describes the introductory part including the background of the research, objectives, scope of the study and the limitations. The literature reviews related to the soft rocks, cantilever type retaining walls, current design methods some failure histories around the world and centrifuge modelling principles are presented in Chapter 2. Subsequently the Chapter 3 illustrates the artificial soft rock modelling and the behavior of simplified cantilever high stiffness retaining walls embedded in soft rock by means of 50g centrifuge models. Chapter 4 mainly focused on the behavior laterally loaded large diameter steel tubular piles in firm ground by 50g centrifuge models and one 1g model.

The deformation and failure of cantilever large diameter steel tubular pile walls embedded in soft rock are described in Chapter 5 by experimental and numerical analysis. Successive Chapter describes the dynamic stability of cantilever steel tubular pile wall embedded in soft rock by centrifuge modelling under dry and submerged back fill conditions. Finally, the conclusions and recommendations for the design of cantilever type steel tubular retaining walls in firm ground are given in Chapter 7. Although few numerical and analytical solutions are included, the centrifuge modelling is the heart of this thesis. The Authors included the key findings of each objective as much as possible in this thesis. We do hope the reader could clearly understand the explanations and the key findings of this dissertation.

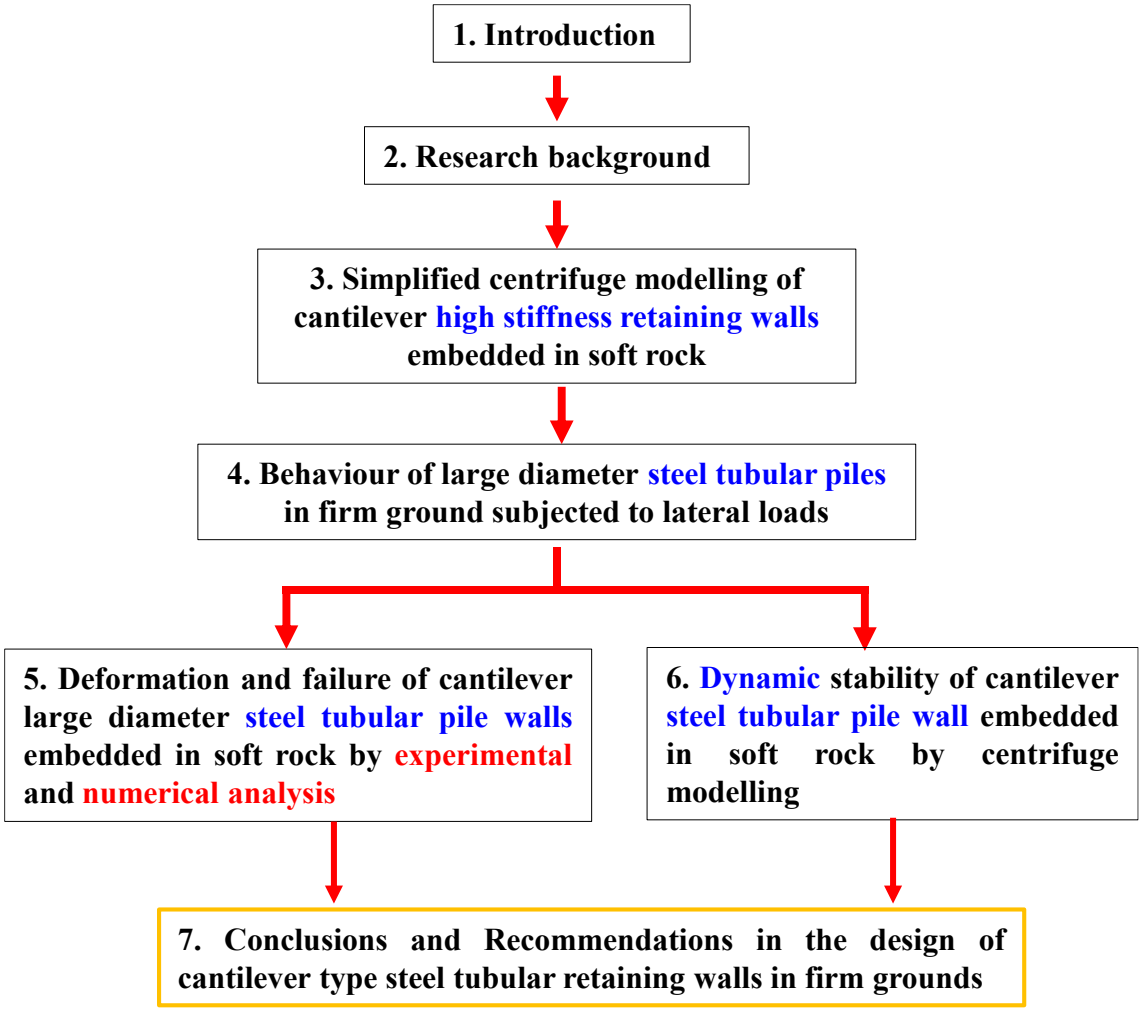

Figure 1.4 Organization of the Thesis

1.6 References

ArcelorMittal, 2008. Piling Handbook, 8th ed, ArcelorMittal, Esch-sur-Alzette, Luxembourg, Installation of sheet piles. Ch-11, pp.284-337.

Association of Steel Pile (ASP), 2009, Design manual of self-standing steel sheet pile wall. (In Madabhushi, S.P.G. and Chandrasekaran, V.S., 2005. Rotation of cantilever sheet pile walls. Journal of Geotechnical and Geoenvironmental Engineering, 131(2), pp.202-212. (Japanese)

BS8002, B.S., 1994. British Standards Institution, Code of practice for earth retaining structures.

Choo, Y.W. and Kim, D., 2016. Experimental Development of the p-y Relationship for Large-Diameter Offshore Monopiles in Sands: Centrifuge Tests. Journal of Geotechnical and Geoenvironmental Engineering, 142(1), p.04015058.

Indraratna, B., 1990. Development and applications of a synthetic material to simulate soft sedimentary rocks. Geotechnique, 40(2), pp.189-200.

International Press-in Association (IPA), 2016. Press-in Retaining Structures: a handbook, 1st ed.

Johnston, I.W. and Choi, S.K., 1986. A synthetic soft rock for laboratory model studies. Geotechnique, 36(2), pp.251-263.

Madabhushi, S.P.G. and Chandrasekaran, V.S., 2005. Rotation of cantilever sheet pile walls. Journal of Geotechnical and Geoenvironmental Engineering, 131(2), pp.202-212.

Miyanohara,T., Kurosawa,T., Harata,N., Kitamura,K., Suzuki,N. and Kajino,K., 2018. Overview of the Self-standing and High Stiffness Tubular Pile Walls in Japan, Proceedings of the 1st International Conference on Press-in Engineering 2018, Kochi, Japan,pp.167-174.

Powrie, W., 1996. Limit equilibrium analysis of embedded retaining walls. Géotechnique, 46(4), pp.709-723.

Schofield, A.N., 1980. Cambridge geotechnical centrifuge operations. Geotechnique, 30(3), pp.227-268.

Suzuki, N. and Kajino,K.,2018. Issues for the Reduction of the Embedded Length of Cantilevered Steel Tubular Retaining Wall Pressed into Stiff Ground, Proceedings of the 1st International Conference on Press-in Engineering 2018, Kochi, Japan,pp.159-166.

2 Literature Reviews and Geotechnical Centrifuge Modelling

2.1 Introduction

Retaining structures are often used in civil engineering construction sites to stabilize the earth. Based on the stabilizing mechanism it can be sub-divided in to two major categories, such as externally stabilizing and internally stabilizing structures. Detail breakdown of retaining structures are described in **Figure 2.1**, which describes the major type of structures used in current engineering practice in different soil profiles and the environment. Among these structures, only retaining walls are mainly focused in this thesis.

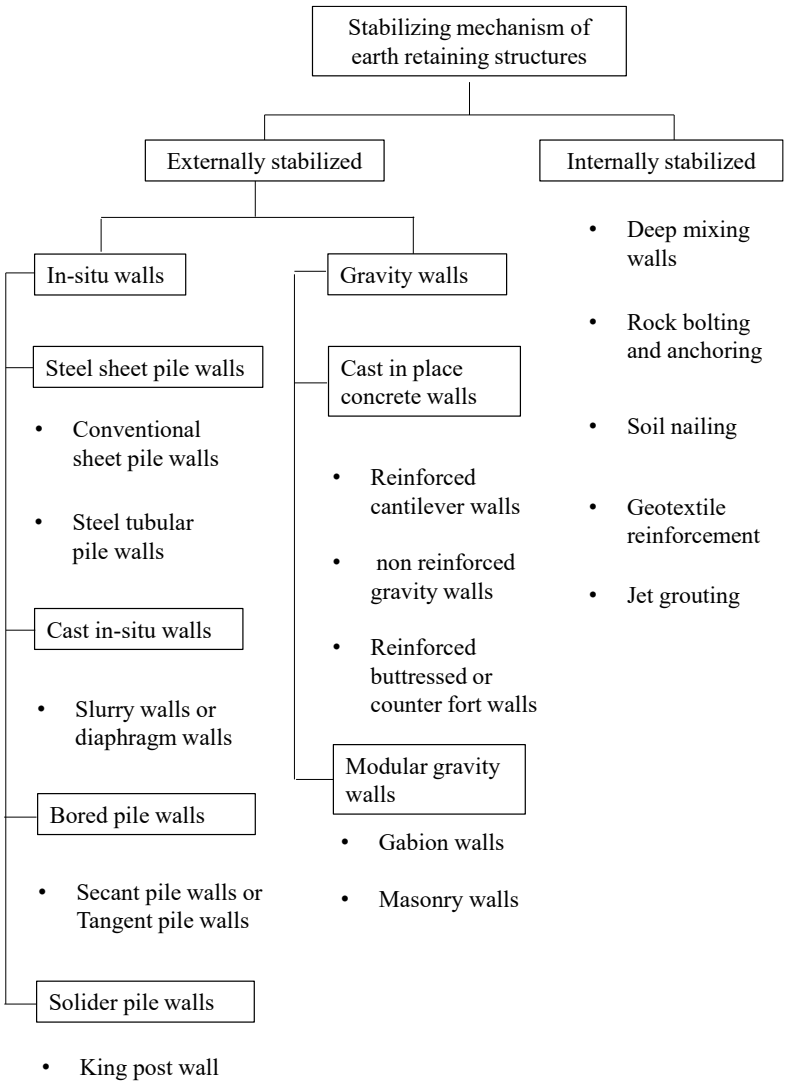

Figure 2.1 Earth retaining structures

2.1.1 Types of retaining walls, applications and retaining mechanism

As described in **Figure 2.1**, the retaining walls are generally fall in the group of externally stabilizing structures, where based on the retaining mechanism and the mass it can further divided in to in-situ walls and gravity retaining walls. Different types of gravity retaining walls are illustrated in **Figure 2.2** and **Figure 2.3**. Subsequently the common construction types of in-situ walls also describe by images given in **Figure 2.4**, **Figure 2.5**, **Figure 2.6** and **Figure 2.7**. In-situ

walls are relatively lighter in mass compare to the gravity walls, where the sliding resistance is mainly given by the embedded portion of the wall or additional lateral bracings depending on the type of wall. Meanwhile in the case of gravity walls, the sliding resistance is mainly govern by the weight and base are of the structure as described in Equation (2.1).

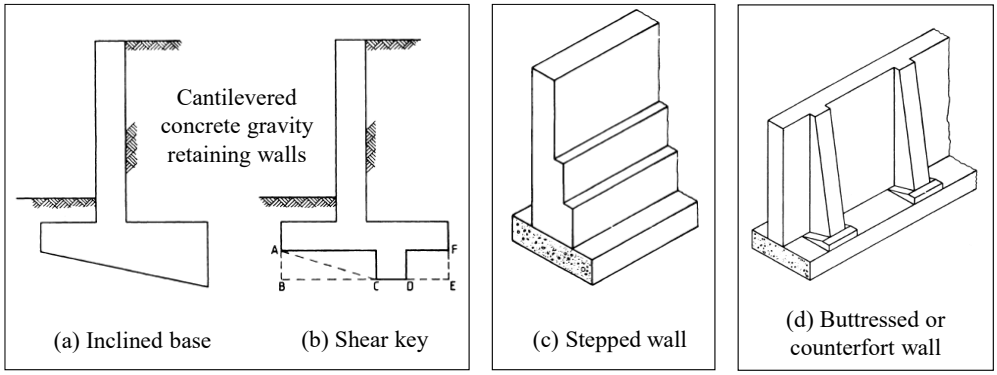

Figure 2.2 Cast in place concrete gravity walls (BS8002:1994)

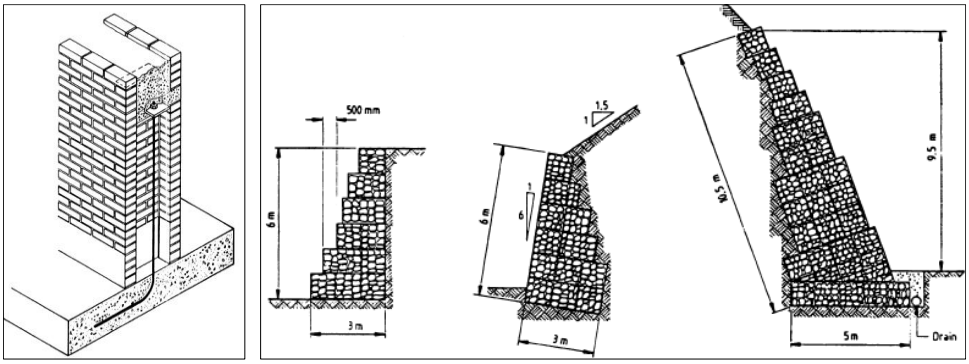

(a) Masonry diaphragm wall

(b) Gabion walls

Figure 2.3 Modular gravity walls (BS8002:1994)

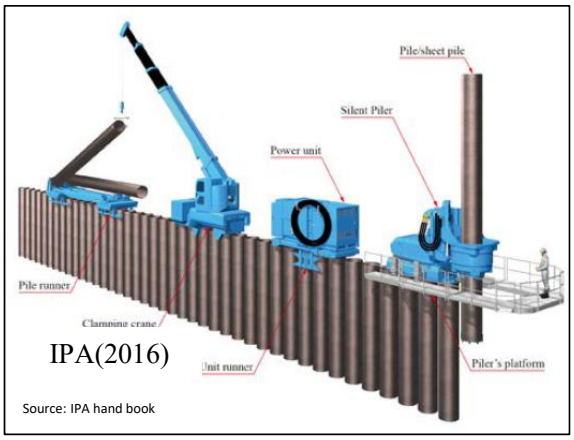

(a) Conventional steel sheet pile wall

(b) Steel tubular pile wall

Figure 2.4 Steel sheet pile walls (IPA), 2016

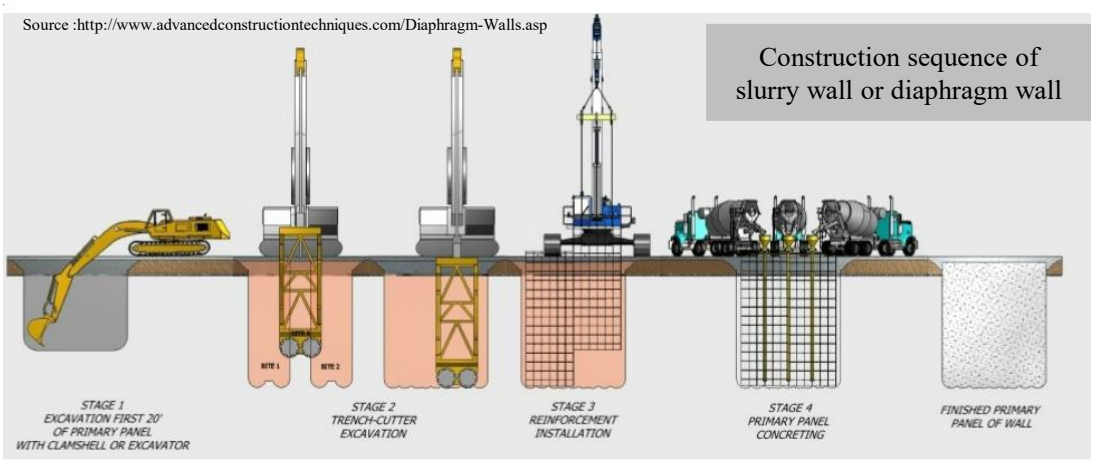

Figure 2.5 Cast in-situ walls (Diaphragm wall)

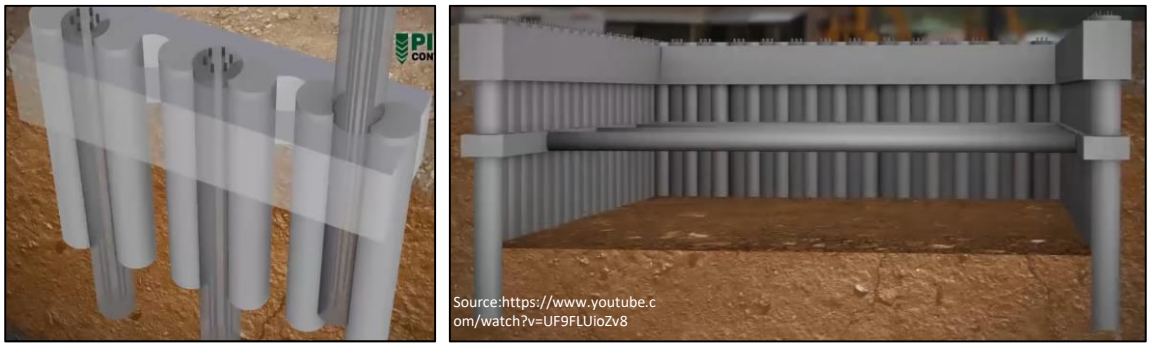

(a) Installation of male and female piles (b) Deep excavation and lateral support bracing

Figure 2.6 Bored pile walls (Secant pile wall)

Figure 2.7 King post walls

$$S = \sigma_v \tan \delta + c_a \quad \text{Equation (2.1)}$$

S – Base share resistance

σ_v – Net vertical stress acting at the base of structure

δ – Friction angle between soil and retaining wall base

c_a – Adhesion between the retaining wall base and soil

In some situations, to overcome the sliding failure, an inclined base or shear key could be utilized in the design and construction of concrete gravity retaining walls as described in **Figure 2.2**(a) and **Figure 2.2** (b) respectively. The counter moments against the overturning failure of massive gravity walls are mainly gained from the weight (gabion walls) of the structure, however for an L-shaped concrete gravity wall or stepped walls in addition to the weight component certain contribution from the backfill surcharge also presents. The applications and desirable features of in-situ and gravity retaining walls are described in **Table 2-1**. In the basic design practice, the stability of a retaining wall must be confirmed with additional factor of safety (FOS) against rotational, sliding and flexural bending. Apart from that, excessive vertical settlements, seepage, creep deformations, deep-seated failures, failure of anchors and bracings are major concern in the long term stability. The mobilization of active and passive earth pressures nearby an embedded retaining wall during an excavation process and corresponding change of stress in the active and passive soil wedges are illustrated in **Figure 2.8** and **Figure 2.9** respectively.

Table 2-1 Applications and desirable features of in-situ and gravity retaining walls

Wall type	Applications and desirable features
Gabion walls	Mostly desirable when the backfill soil is likely to be saturated and the soils where the bearing resistance is very poor. High permeability and flexibility of these walls are desirable features for the dissipation of excess water pressures behind the wall during low tide and to maintain the stability under large deformations nearby water bodies.
Non reinforced concrete gravity or masonry walls	Suitable and cost effective solution to retain relatively small height of earth about 1.5 m.
Reinforced cantilever retaining walls (stem walls)	Generally economical up to 8 m retained height of earth, beyond which the required section of the vertical stem would be much higher. In those situations counter fort walls could be adopted with relatively large retain heights and as an economic solution.
Diaphragm walls	Could be used as dual purpose structure while retaining the ground it could also be used as high capacity vertical foundation. It can be used as an earth retaining structure for deep excavations, basement constructions, and tunneling. Mostly used as a permanent water retaining wall.
Slurry walls (Diaphragm walls)	Desirable option to construct a diaphragm wall where the ground water flow and seepage exist. Could be used to prevent the contaminated water flow into the trench by means of bentonite-soil slurry. It can be used as a gas barrier or in the land fill sites to prevent leachate in flow. Mostly used in deep excavations.
Secant pile walls or tangent pile walls	Mostly applied in the basement construction with additional lateral bracing systems for deep excavations. It also provides large retained heights with water tide conditions and prevent seepage of water or contaminated liquids from retained soil to the excavation side. Depending on the purpose of structure either permanent or temporary it can be constructed in three different types, such as; hard/soft secant, hard/firm secant and hard /hard secant.

	Generally hard/soft secant is used for temporary retaining wall. Secant pile walls often have certain overlapping between male and female piles however the tangent files are connected face to face.
Conventional Sheet pile walls	Can be used to retain relatively large height of earth by means of sheet piles with different section modulus and could be utilized even in hard mediums. More durable, and reusable, faster construction, could be used as temporary or permanent.
Steel tubular pile walls	High flexural rigidities could be achieved by means of large diameter piles and applicable even in hard rocks. Mostly used to retain large height of earth around 12-15 m. Act as a permanent sheet pile foundation as well as a cofferdam in water related construction activities. Faster in construction and could be constructed in a limited construction yard.

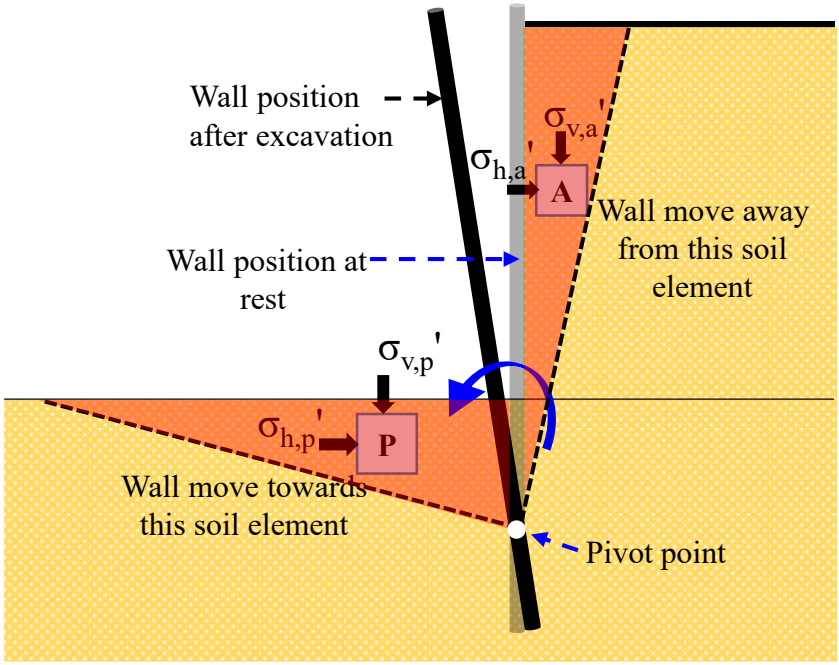

Figure 2.8 Mobilization of earth pressures

From **Figure 2.9** the one can simply understand the failure mechanism of soil wedges at the verge of active and passive limits. Retaining mechanism or the stability of embedded retaining walls in loose mediums (loose sand or clays) highly depends on the mobilization of passive pressures above and below the pivot point in the embedded zone as described in **Figure 2.10**(a). The illustration given in **Figure 2.10**(b) indicates the further simplified distribution as described in CIRIA 104. In order to mobilize large passive pressure in loose mediums, certain amount of wall movement is an essential requirement, however it also increase the possibility of overturning failure of walls where the penetration depth is inadequate. Therefore the design embedment depths of these structures must be remote from rotational failure. The simplified earth pressure distribution given in **Figure 2.10**(b) is widely used as a fixed earth support design, also it provides more conservative results according to CIRIA 104. For further details of idealization and the design guidance please refer CIRIA 104

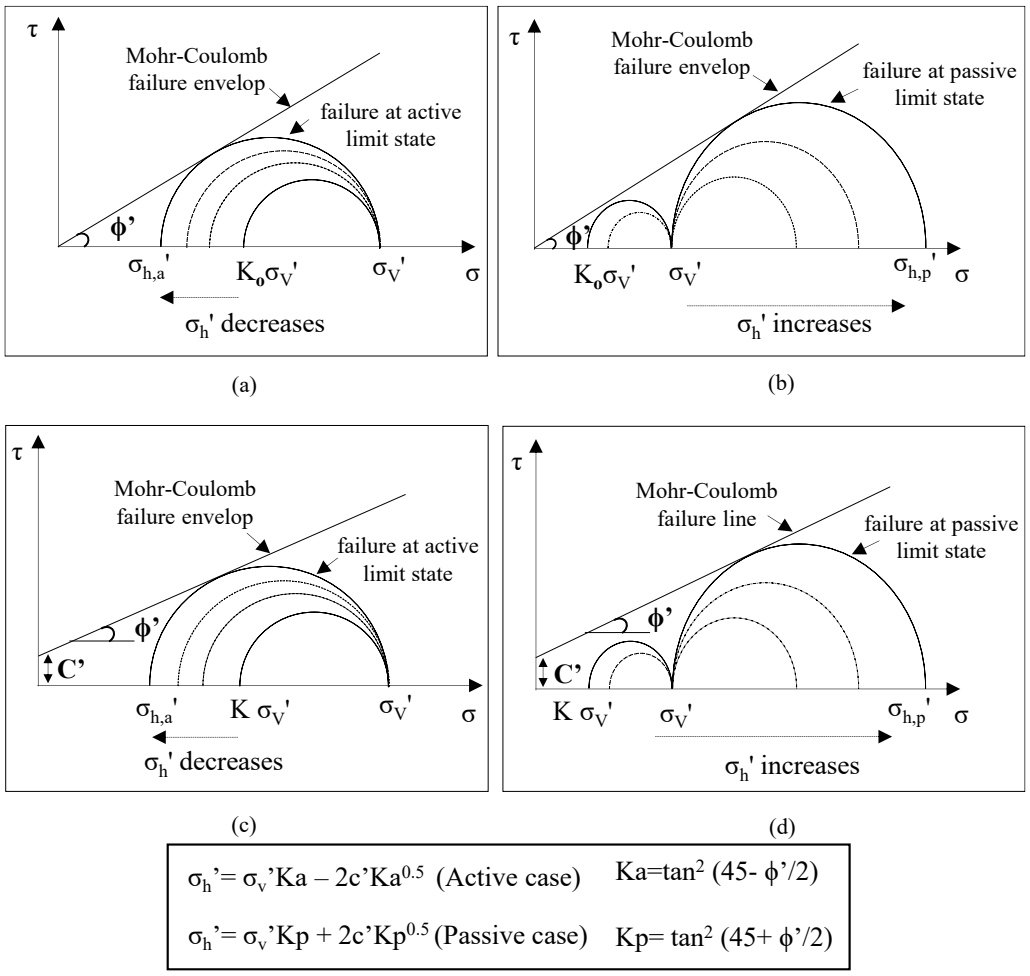

Figure 2.9 Change of stress in (a) soil element 'A' and (b) soil element 'P' as described in Figure 2.7 during unloading in the wall front

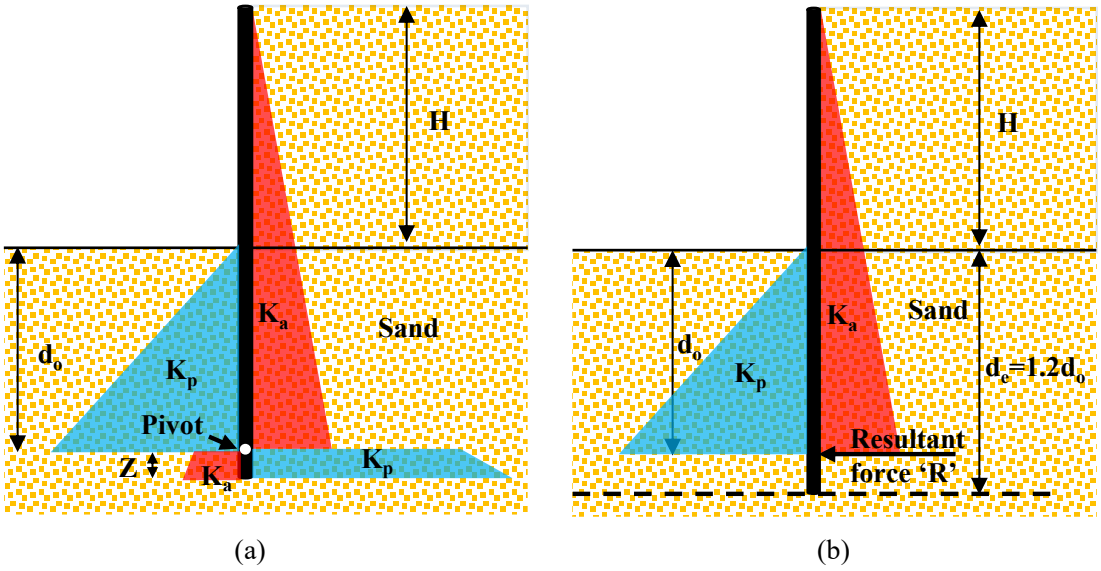

Figure 2.10 (a) Idealised and (b) simplified earth pressure distributions at limit equilibrium conditions (CIRIA 104)

2.2 Cantilever type retaining walls in the past and present design methods

Classical methods of analysis on the equilibrium of cantilever type retaining structures from 18th and 19th century provides the upper (Coloumb 1776) and lower (Rankine 1857) bound solutions for the stability analysis. Coulomb's method of analysis provides the limiting active force on the retaining wall as a function of the height soil below the retained surface, his method was failed to predict the stress state at a specific depth of retained soil. Although Rankine's assumptions are most appropriate in ideal conditions (smooth wall and soil behind the wall is in uniform state of plastic equilibrium), he derived the stress state behind wall as linearly increasing with the depth in uniform materials. Rankine's method of analysis yields the lateral earth pressure coefficient at any depth as a fraction of lateral to vertical earth pressure at considered depth. Eventually his method of analysis became popular and basis of the limit equilibrium analysis for embedded retaining walls. Cantilever sheet pile walls often used in civil engineering applications from the beginning of 20th century due to its simplicity and time and cost saving in construction. Although it has a long journey in the revisions, new findings and developments in the design of cantilever sheet pile walls continues up to date.

Researchers have been proposing different design procedures based on the observed experimental data and analytical methods. Both numerical and experimental methods have pro and cons, throughout sever arguments and new findings the classical design methods are still being revised by researchers. Different oldest design methods and corresponding earth pressure distributions are illustrated in **Figure 2.11**. Engle has proposed one of the oldest methods to design self-standing retaining structures in 1903 form his experimental observations. A parabolic net earth pressure distribution along the embedded portion of the wall was suggested and the required embedment depth was calculated from the horizontal force and moment equilibrium analysis. Krey (1936) considered a rectilinear net earth pressure distribution based on fully mobilized active and passive earth pressure distributions. The embedment depth was calculated from the evaluation

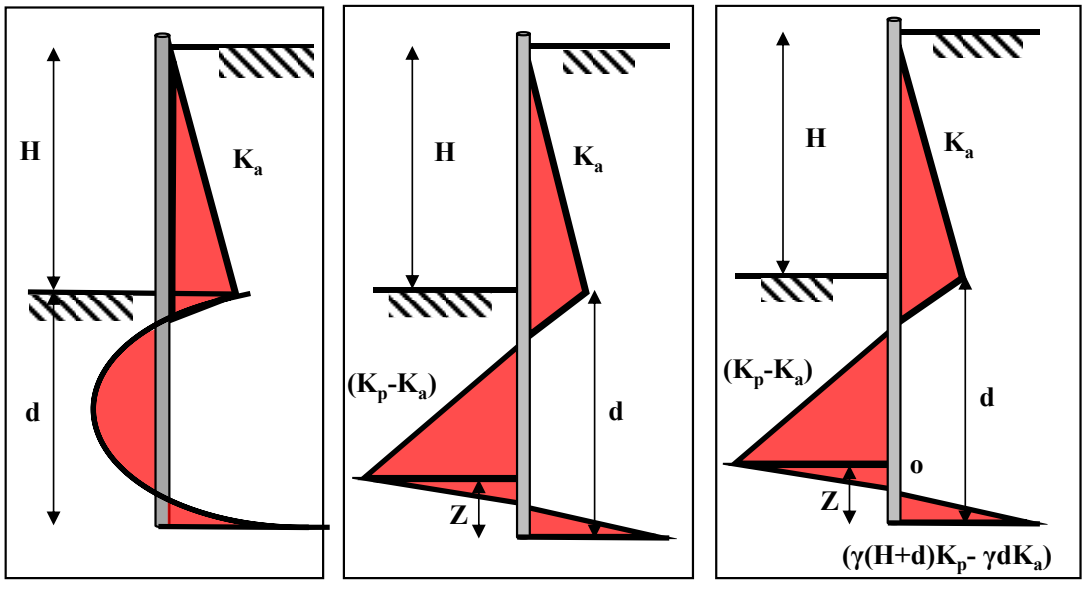

(a) Engle (1903) (b) Krey (1936) (c) USA/ Gradual method

Figure 2.11 Earth pressure distributions proposed by different researchers

of the height ‘z’ based on the maximum passive pressure mobilization in front of the retaining structure, and considering the force and moment equilibriums about the toe of the retaining wall. The gradual method is almost similar method as Krey (1936), the assumption made in this method is that the net earth pressure changes gradually from the front side to the backside of the retaining wall. The changing of the net earth pressure region located around the point of rotation and a linear variation is assumed as shown in **Figure 2.11**(c). In this method the earth pressure at the bottom of the wall is given as the function of wall and soil parameters. Therefore, the height from the bottom to the point of rotation ‘z’ is the unknown parameter to be obtained in order to estimate the embedment depth.

Most popular method in the present design practice is the Full or UK method. The method is clearly described in CIRIA 104, in this method of analysis the stress distribution at the limiting equilibrium was considered as shown in **Figure 2.10**. The contribution against the rotation of sheet pile wall was received from the mobilized passive earth pressures in the front and back of the retaining structure. Earth pressure distributions with sudden jump and requiring an iteration process to estimate the point of rotation are the complexities in this method of analysis. In order to reduce the complexity in the design process, this method was revised by Padfield and Mair (1984), the sudden jump in the earth pressure distribution below the point of rotation was represented as an equivalent concentrated force at the point of rotations shown in **Figure 2.10**(b). Estimated depth of embedment in the simplified method was comparatively smaller than that of full method. The most common design practice is to increase the embedment depth by 20%, therefore the final embedment depth achieved from this method is equal to 1.2 times (1.2d) of the one calculated form simplified method. Since the resultant force is a favourable action on the stability of retaining structure, the verification must be done in order to confirm that the additional 0.2d can be able to generate the force equivalent to the one observed from full method.

Available literatures or specific design guidance for the embedded retaining walls in soft to hard rocks are extremely rare. Perhaps it might be attributed to the limited applications in the past or difficulties in the construction of retaining walls in relatively hard mediums. Recently the applications of stiff sheet pile walls in soft to hard rocks have increased (Miyanohara et al.2018, Suzuki et al.2018) with the development of novel penetration techniques (ArcelorMittal, 2008), which reveal the emergence of specific design guidelines for the application of embedded retaining walls in rocks. Although documented guidance for the design of embedded retaining walls in rock are not available, the design guide for the rock socketed piles or walls can be found from Geoguide 1 (a guide to retaining wall design in Hong Kong). Where three different scenarios of rock socketing and the overlying stratum are considered and the design equation to estimate the point of rotation in the rock socket and the earth pressure distributions are given as described in **Figure 2.12**, **Figure 2.13** and **Figure 2.14**. In the rectangular shape of earth pressure distributions described in above-mentioned figures the contribution of surcharge is simply neglected. This assumption could be reasonable for relatively hard rocks, where the surcharge or self-weights components are very minor compare to the strength of rock.

However the concept of soft rocks in geo-mechanics and the properties are lies in between hard soils and hard rocks as described in **Figure 2.15** based on Johnston, 1991. From **Figure 2.16**, in the lower boundary of soft rocks the behavior can be expected to match hard soils and the limiting earth pressure distributions could be assumed as described in **Figure 2.16**. Also this limiting earth pressure distributions could be simplified by using rectangular shape for hard rocks as described in **Figure 2.12** for the socketed piles or walls. Unlike the behavior of walls in compliant mediums (sand or clays) a large resistance against the sliding and overturning could

be expected at the intact condition of rocks. As the deformation of embedded medium took place, the deterioration of the rock stiffness highly influences the behavior of embedded walls. Depending on the type of rocks (brittle or ductile) the allowable deformations of the embedded medium could vary to prevent the abrupt failure of rock and the catastrophic failure of entire system.

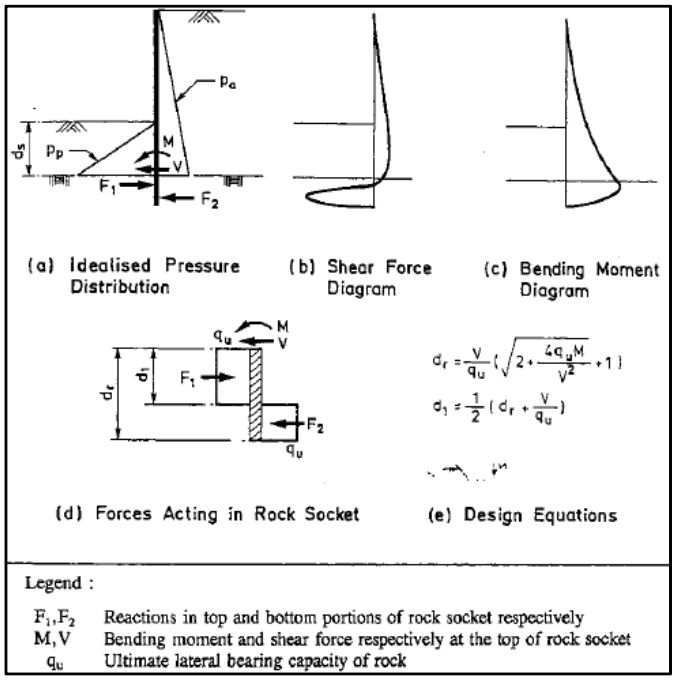

Figure 2.12 Design of rock socket against bearing failure for the case where the top of the socket is above the point of zero shear (GEOCEDHG, 1993)

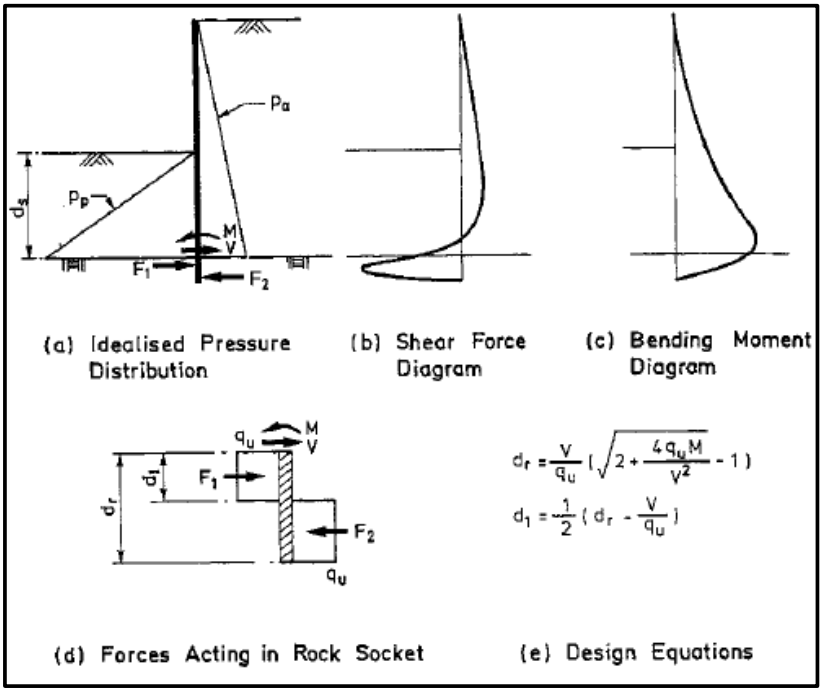

Figure 2.13 Design of rock socket against bearing failure for the case where the top of the socket is below the point of zero shear (GEOCEDHG, ,1993)

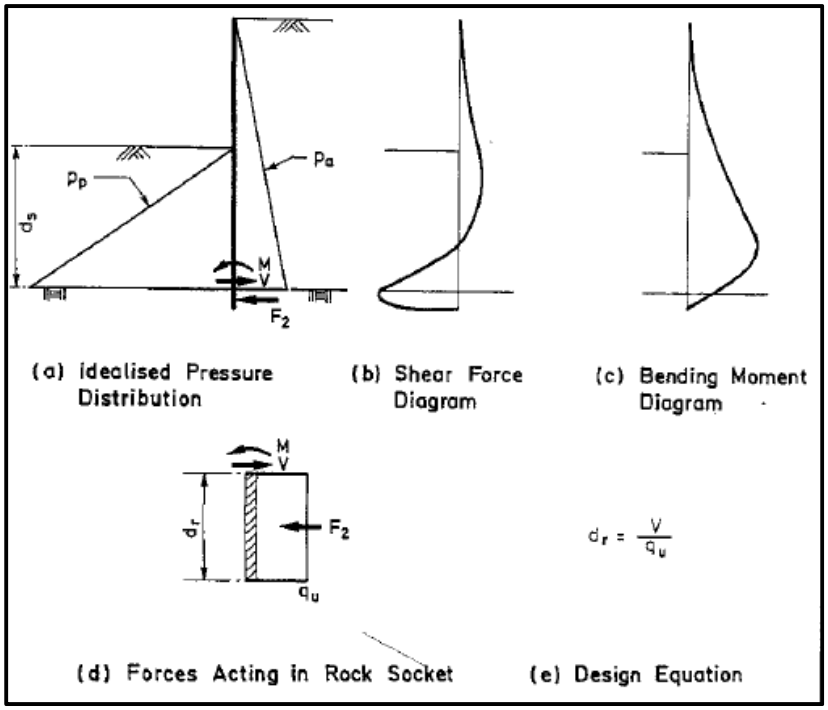

Figure 2.14 Design of rock socket against bearing failure for the case where d1 < 0 (GEOCEDHG, 1993)

Therefore, the design of embedded wall in rock is more critical compare to the compliant mediums, where the attention must be given in terms of allowable displacements in the embedded zone or the deformation of embedded medium rather than the mobilized strength.

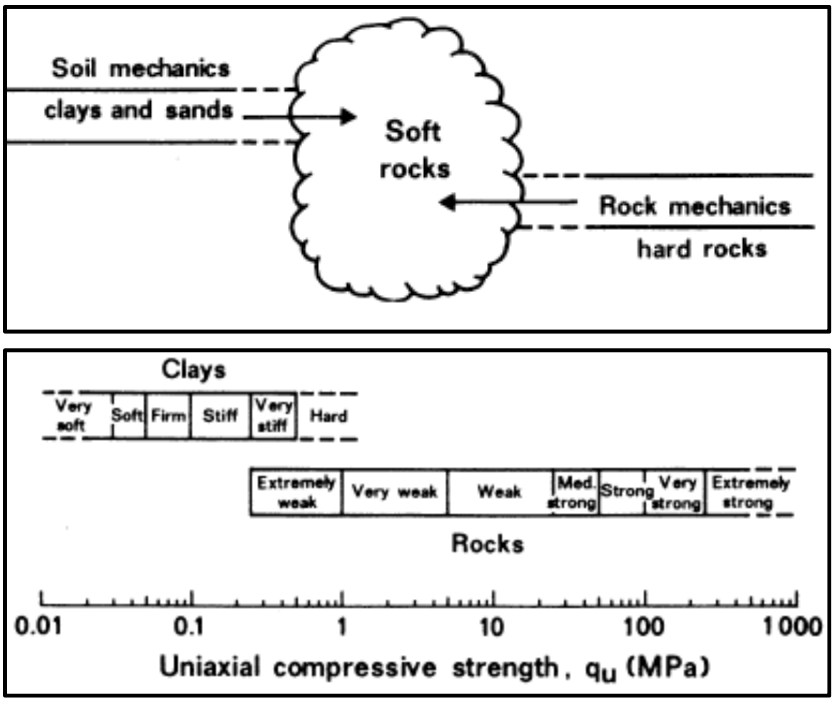

Figure 2.15 Current view of soft rocks in geo-mechanics and the ISRM classification after Brown 1981 (From Johnston, 1991)

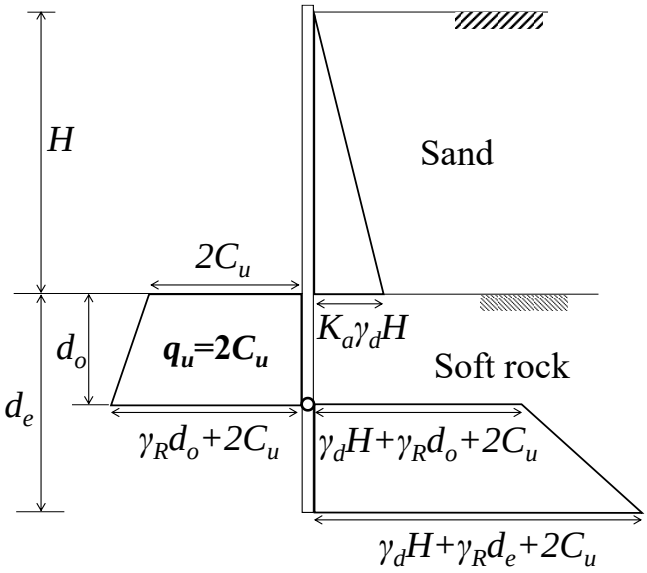

Figure 2.16 Possible limiting earth pressure distribution in soft rocks at their lower boundary (Assuming a behavior similar to hard soils)

2.2.1 Physical modelling of excavations

Table 2-2 Objectives and utilized simulation techniques in the previous physical modelling of excavations

Authors	Experiment type	Objective	Simulation Technique
Lyndon and Schofield, (1970)	Centrifuge models tests on cut slopes in clay	To simulate a 10 m excavation and short term failure of cut slopes in London clay	Two unequal slopes were made at 1 g and Gravity Turn On (GTO) was used to reach the prototype at 66 g
Bransby and Milligan,(1975)	Laboratory based 1 g model tests on a flexible and stiff cantilever sheet pile walls in loose and dense sand	To study the soil deformations near the cantilever walls embedded in loose and dense sand	Excavations were made at 1 g by means of vertical tubes connected to the domestic vacuum cleaner.
Bolton and Powrie, (1987) & (1988)	Centrifuge model tests on stiff cantilever walls embedded in over consolidated clay	To study the Collapse behavior of diaphragm walls retaining clay To investigate the influence of mobilized shear strength on the deformation of cantilever walls	Draining a heavy fluid to simulate the excavation at 125 g. Modelling of 18.75 m wall retaining 10 m of over consolidated clay
Kimura et al., (1993) Takemura et al., (1999)	Centrifuge model tests on propped and non-propped sheet pile walls embedded in normally consolidated clay and double layers	To study the mechanical behavior of soft clay during excavation and the influence of propping. And to study the influence stiff bottom layer on the on the behavior wall and ground deformations	Inflight excavation simulator Simulating 3 m – 5.6 m excavation at 50 g with different embedment depths and propping at different levels of excavation.

Bica and Clayton, (1998)	Laboratory based 1 g model tests	To investigate the behavior of wall below the excavation level (Mobilization of earth pressures and wall friction) and to optimize the use of instrumentation	A simplified cantilever wall model Only embedment portion was modelled and the retained height of earth was simulated by means of vertical loads.
Leung et al., (2006) Ong et al., (2006)	Centrifuge model test on stable and collapsed cantilever walls embedded in soft clay and dense sand	To investigate the behavior of singles piles located behind a stable and collapsed wall and subjected to excavation induced soil movements	Draining a heavy fluid to simulate the excavation at 50 g. Simulating 1.2 m – 2.8 m excavation with different factor of safety against failure
Lam et al., (2012)	Centrifuge model tests on a rigid and flexible walls embedded in clay	To enhance the understanding of the mechanisms involved in soil excavation and simulate the construction sequence of multi propped retaining walls	In flight excavation simulator was used to simulate 5.5 m depth of excavation at 60 g. Props were installed at 0.8 m and 3 m excavation depths inflight.

Over the past decades, extensive investigations based on the physical modelling of excavations on a cantilever and propped walls (Padfield and Mair.1984 ;Richards and Poweri.1998) embedded in clays and sandy soils have been contributed to the development of design codes and the calibration of numerical models as summarized in **Table 2-2**. Also the observations from numerous case histories (Long.2001; Ou et al.1993) related to the real field applications in a vast range of soil conditions and the failure of earth retaining structures (D'Andrea and Day.1998; Whittle and Davies.2006) oftentimes revised the codes for the safe and economic design of retaining structures in sand and clays. However, the available literatures (Richards et al.2004) based on physical models or the real field experiments to illustrate the behavior of self-standing walls embedded in soft rocks are extremely rear. Perhaps it might be attributed to the difficulties in the installation and creating the failure of such large retaining structures in the real field or the undisturbed sampling of soft rock grounds with required dimensions for the centrifuge models.

2.2.2 Failure histories of retaining walls and possible causes

Retaining structures are the heart of any civil engineering construction or mining activities which are relate to the earth work. Although several incidents happened in the past century, only few documented records related to the catastrophic failure of retaining walls during the construction activities and possible causes are available, perhaps it might be attributed to the security concern of the designers and contractors. However, the failure of retaining walls under extreme loading conditions by nature or manmade activities are freely available. Based on authors intensive literature review, the failure histories during the construction activities are often caused by the poor construction activities (lack of pre-stressing in strut or anchor, improper way of prop connections, ignorance of real time observations, accidental over excavations etc..) even in developed countries or the lack of knowledge (Improper use of commercial software and higher dependency on those results for the design , over estimation of the strength and stiffness of retaining soil or embedded medium, assumption of highly idealized boundary conditions etc..). This sub chapter discusses some of the failure histories related to the retaining wall or knowledge shared by engineers and researchers.

2.2.2.1 Edinburgh tower basement construction Hong Kong (1981)

The failure history was associated with the inadequate lateral support or bracing at the end of construction. During the construction of two level basement for the Edinburgh tower in Hong Kong, the underlain rock layer was at a higher elevation then the expected level. Therefore, the toe of sheet pile was penetrated in to the rock strata and the excavation adjacent to the Queens road was completed with two level propping at the top and the bottom. However, for the construction of base slab the construction team was decided to remove the bottom level propping and relying on the rock socket resistance from the toe of sheet pile. Unfortunately, lateral sliding occurred in the socketed portion due to the inadequate lateral resistance and eventually the sheet pile was rotate about the top level propping and the half span of the Queens road was collapsed in the construction site as shown in **Figure 2.17**.

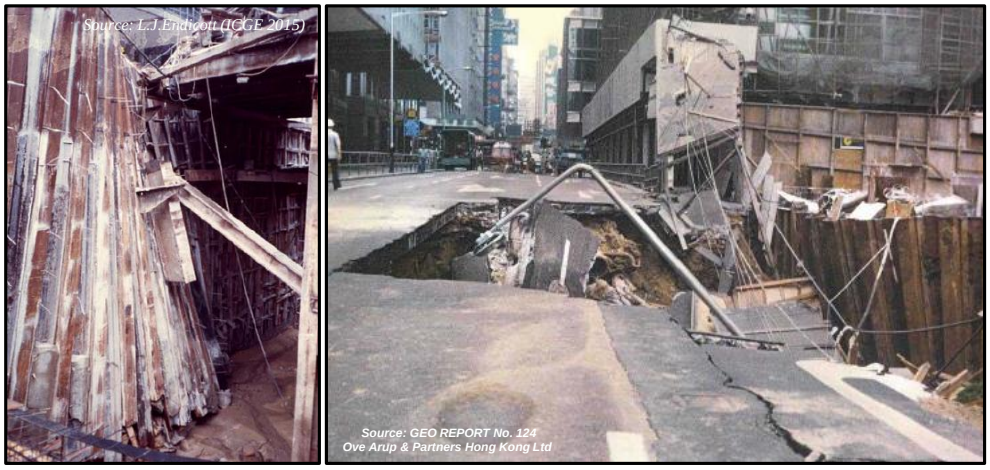

Figure 2.17 Sheet pile failure and Queen's road collapse during Edinburgh tower basement construction

2.2.2.2 Sao Paolo metro Pinheiros station shaft collapse in Brazil (2007)

This failure was explained by the shear bands develop along the discontinuities and the existence of highly fractured rocks on the roof level of Pinheros station which was located in the underground at an elevation of about 35m deep. The 3 dimensional view of the shaft and the cavern construction and the observed failures are shown in **Figure 2.18**, the height of overburden above the cavern was about 20m. The top heading of the cavern and the retreating of excavation from the shaft location towards the end of one side platform (about 46 m length, 14.2 m height) are shown in **Figure 2.19**. According to Saratsis and Stavropoulou (2013) the failure is explained as a trap-door mechanism. As the cavern excavation progresses with the help of shotcrete lining, lattice girders, and fore poling at the length of about 30m cavern excavation the collapse was occurred with a huge mass flow. The cause of failure was attributed to two different share bands, former one was a cylindrical upwards shear band initiated from the bottom of the shaft and the second one was propagated from the edges of the cavern and the collapse was observed during the intersection of both shear bands according to the numerical studies of Saratsis and Stavropoulou (2013). These shear bands could have initiated from the top-heading edges of the cavern, where the high stress concentrations can be expected and the localization of plastic strains from that point could be directed along the discontinuities existed in the collapse site.

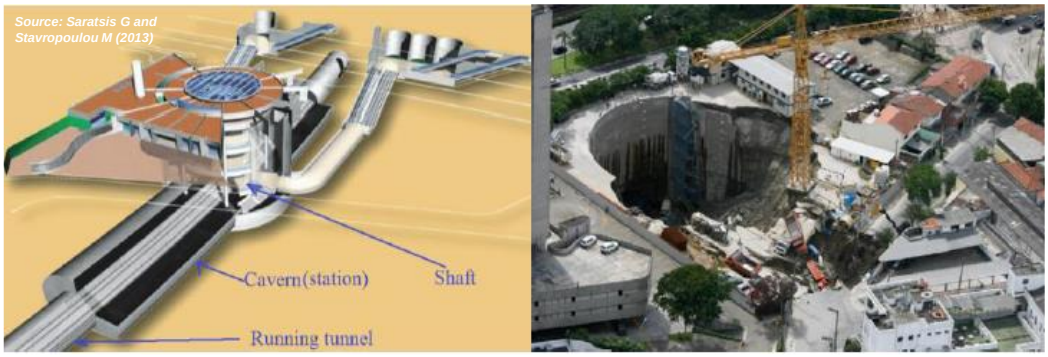

Figure 2.18 Sao Paolo metro Pinheiros station shaft collapse in Brazil (2007), (Saratsis and Stavropoulou ,2013)

Figure 2.19 Aerial view of the Pinheiros Station shaft. The black curved arch at 20m depth down the shaft wall is the top heading of the station platform cavern. The shaft wall chainage at 7080 m and the rear discontinuity (FF) at chainage 7120 m, mark the approximate limits of the 40 m long station cavern collapse (Barton, 2009) (from Saratsis and Stavropoulou ,2013)

2.2.2.3 Nicoll highway collapse Singapore (2004) (Whittle and Davies, 2006)

Figure 2.20 Nicoll highway collapse during the tunnel construction of an MRT line

Figure 2.21 Strut and Waler buckling observed in Nicoll highway collapse incident

The cause of this failure could be attributed to several reasons as an overall view as described in the end of this sub chapter. This construction was a cut and cover type tunnel in soft clay with the help of diaphragm walls constructed at 20 m apart and the steel struts were utilized to support the wall panels. Depth of the tunnel was 30 m and it was the first deepest cut and cover tunnel in Singapore, also the excavation was planned in 10 stage propping with two horizontal layers of jet grout piling as a buried strutting at 9th, 10th stages of excavation and below the final excavation level. It is important to emphasize that the site was a reclaimed land around 40 years back, about 3-5 m of dredged sand was placed on top of the shallow sea bed where it had about 30 m of marine clay underneath of the sand. During the construction of this tunnel, the consolidation of the clay deposit was not completed and the residual pore pressures were reported up to 3m.

The collapse of the walls were observed at the end of 30 m excavation and prior to the installation of 10th level strutting. The collapse was the severe one in Singapore, subsidence of land with about 100 m diameter crater was observed including a part of Nicoll highway adjacent to the excavation site. Possible cause of the failure was investigated by an independent committee and several reasons were found as described below.

The initial oversight came from the design Engineer, the overestimation of the undrained strength of clay and the wrong use of PLAXIS software by simply following the recommendations in the manual without having the knowledge of the undrained properties of soft marine clay. The designer used the 'Method A' described in PLAXIS with the setting of undrained setting, where the c' and ϕ' will be automatically calculated by using a Mohr-Coulomb model. The major problem in the use of 'Method A' undrained setting is that, the program considers as no volumetric change thereby it estimates the shear strength of a normally consolidated clay under the condition of a constant isotropic stress p'. However, the actual behavior of normally consolidated and lightly over consolidated clays follows the Roscoe surface as described in Atkinson and Bransby (1977) regardless of the drainage condition. Compare to the Roscoe surface, corresponding shear strength on the Mohr-Coulomb failure criterion under the same isotropic stress p' is relatively larger. Unfortunately, the shear strength of normally consolidated marine clay deposits behind the wall was relatively smaller than the design condition, which yields relatively large bending moments on the diaphragm walls and the yielding of struts. Please refer the discussion by J.H.Atkinson on the paper of Simpson (2011) for more deep understanding about the undrained stress paths and the critical state lines.

Two months prior to the collapse, the buckling of the Waler was noticed at the point of Waler-Strut connection as shown in **Figure 2.21**. An expert from Singapore Land Transport Authority (LTA) indicate the possible cause as the wrong use of compute program with the underestimation of bending moments in the wall and which caused bending and deformation of supporting system. However, the contractor disagreed with the comment, later in the morning of 20th April 2004 also similar buckling was observed at 8th and 9th levels of strutting. Finally the entire collapse happened in the evening (3.30 p.m.) of 20th April 2004 as shown in **Figure 2.20**. From this it can be said that the contractor also one of the cause since he or she ignored the valuable suggestion from the expert from LTA.

Besides the above mentioned reasons the field monitoring and the back analysis also were conducted, although the site engineers noticed totally different behavior or deformations compare to the design the careless or the ignorance and erroneous back analysis also one of the cause for the incident.

2.2.2.4 Common cause for the failure of cantilever type retaining walls

The most common cause for the failure of cantilever type retaining walls are attributed to the development of water table behind the wall as reported by Robert D'Andrea (1998) on the discussion of Day RW (1997) as shown in **Figure 2.22**. According to the discussion by Robert D'Andrea (1998), the contractors would like to use the on-site soil as a backfill material. Which could permit certain percentage of fines passing number 200 sieve, it strikes the permeability of the backfill as well as clog the drainage layers and eventually build-up the water table behind the retaining walls. The nature of this loading condition is similar to the case of a retaining walls embedded in an impermeable medium and the excavations under the undrained conditions of retain clay or silt zones as described in **Figure 2.23** (CIRIA C580). Attributing to these facts, the failure of cantilever type retaining structure was attributed to the large lateral and moment loads caused by the combined water and soil pressures in the past.

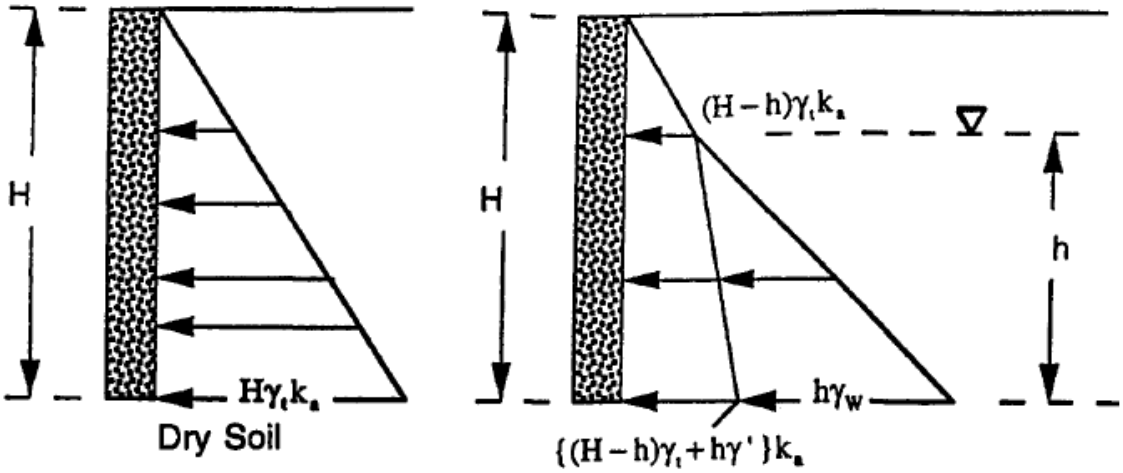

Figure 2.22 Soil with water table above the wall base (D'andrea, 1998)

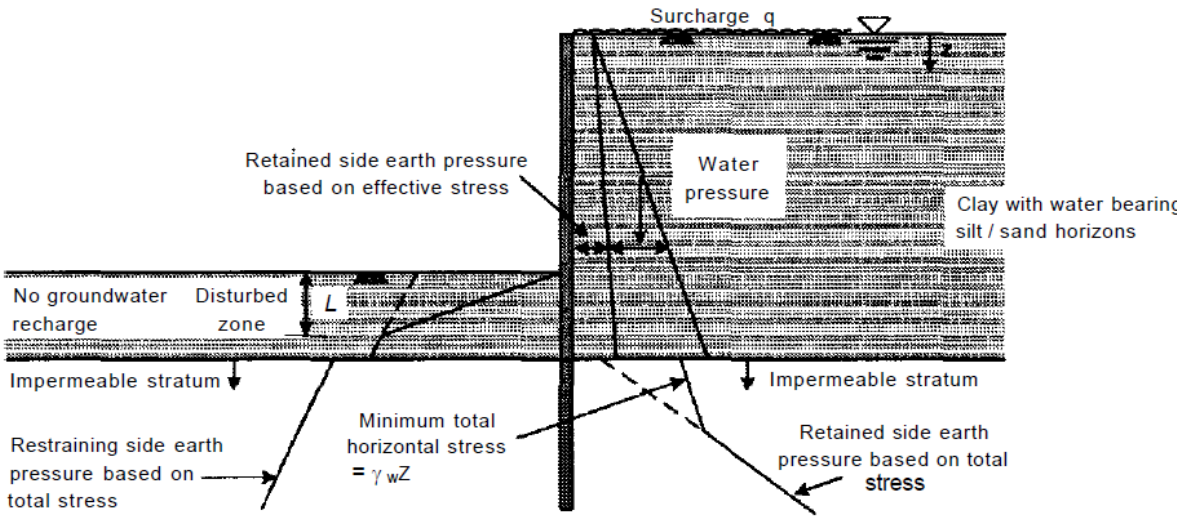

Figure 2.23 Temporary work assumptions in case of impermeable embedded zone (CIRIA C580)

2.2.3 Applicability of steel tubular pile walls by Press-in method and lack of research

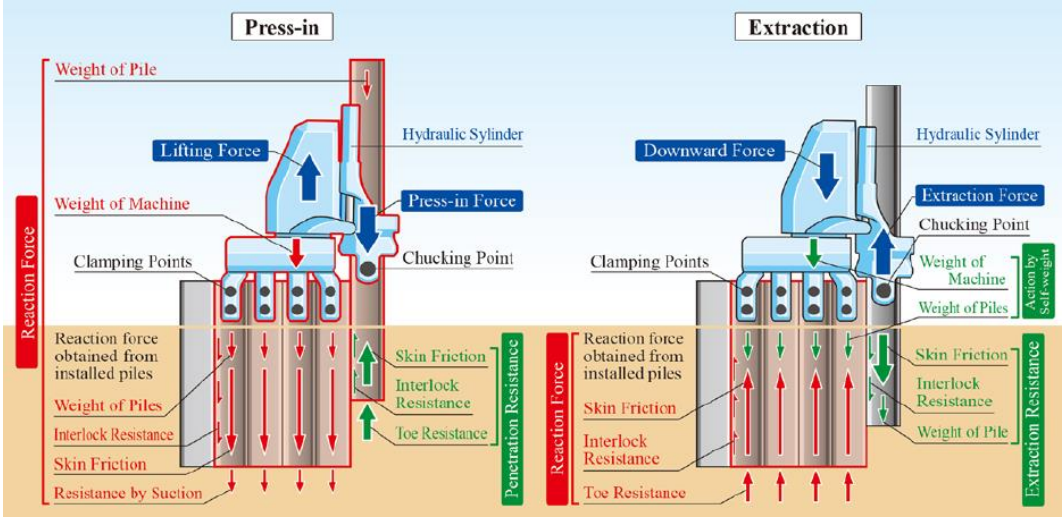

Figure 2.24 Press-in or extraction mechanism and associated forces (IPA, 2016)

Some of the steel tubular pile wall applications in Japan and overseas are described in **Figure 2.25** and **Figure 2.26** respectively. As we could observe, vast range of applications are available based on the construction requirements. Such as Coffer dam (**Figure 2.25** (a), **Figure 2.26** (a)), Cantilevered retaining wall (**Figure 2.25** (b), **Figure 2.26** (b)), basement walls (**Figure 2.25** (c)) etc… Based on extensive literature review the available records on the behavior of steel tubular pile walls embedded in relatively hard mediums such as soft to hard rocks are extremely rare. Technology is well advanced and the demand for the steel tubular piles also increased due to the requirement of high stiffness walls to secure the bending deformations caused by large retained heights, applicability in hard mediums, constructability in limited space and short

Thanks to the advanced penetration techniques (Gyro-press or rotary drilling and press-in), recently the applications of cantilever type retaining structures have been increased in Japan and some other countries (IPA,2016). Especially the walls which are being constructed by Press-in method are desirable in several construction sites where the limitations are encountered in terms of space, time and technology or constructability due to hard grounds. The novelty behind the press-in technique with vibration free installation (Silent Pilers) is the utilization of extraction resistance (due to the shaft friction, suction and interlocking effect of adjacent pile, which is much higher than the force required to penetrate the piles) provided by the former piles which were installed adjacent to the current pile. The working mechanism of the silent piler during press-in and the extraction of the pile is shown in **Figure 2.24**. The silent piler could install the pile with the help of hydraulic pressure meanwhile the counter balance of the piler is received form the extraction resistance. This implies that the piler cannot achieve the jacking or press-in force higher than the extraction resistance, therefore the efficiency of the piler is decided by the hardness of embedment medium. Harder the medium is smaller the efficiency. However, in hard mediums the piling efficiency is often improved by means of driving assistance (Rotary cutting, Gyro-press), which helps to reduce the driving resistance and the deformation of tubular piles while driving in to hard mediums. period of time etc. However, the detail mechanical behavior of large diameter steel tubular pile walls in hard medium is not well understood by any researchers. Besides the design of these walls are still being designed based on the conventional methods, which requires relatively large embedment depths and high construction costs as described in the chapter -1.

River revetment and highway protection wall (Singapore) Conservation of surrounding environment with no noise or vibration

Cofferdam for revetment with 1200 mm diameter tubular piles installed in soft and hard marine clay (Singapore)

(a)

Construction of cantilever type embedded retaining wall in a narrow space adjacent to the highway with operation (Yokohama ,Japan)

Pressing of steel tubular piles with 900 mm diameter in to mudstone (N-value of 166) to widen the existing highway (Yokohama ,Japan)

(b)

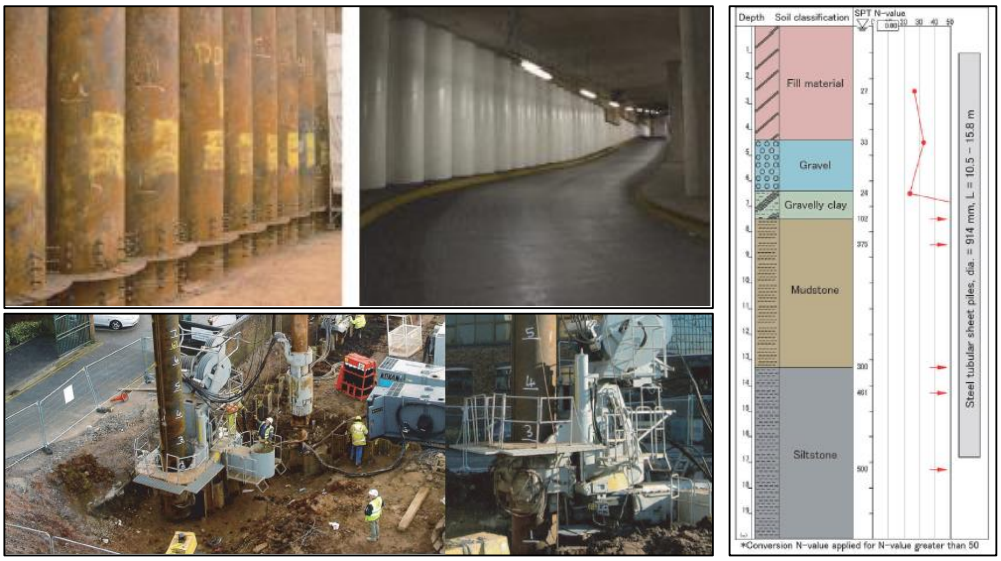

Construction of dual purpose underground wall and a retaining structure for a new shopping mall in Cardiff, UK using steel tubular piles with diameter of 914 mm

(c)

Figure 2.25 Some applications of steel tubular pile walls constructed by press-in method (IPA, 2016)

Construction of a subway station box in a canal (London, UK) Building of a cofferdam with high water cut-off performance using 1219 mm diameter tubular piles, Press-in application in to hard mudstone

(a)

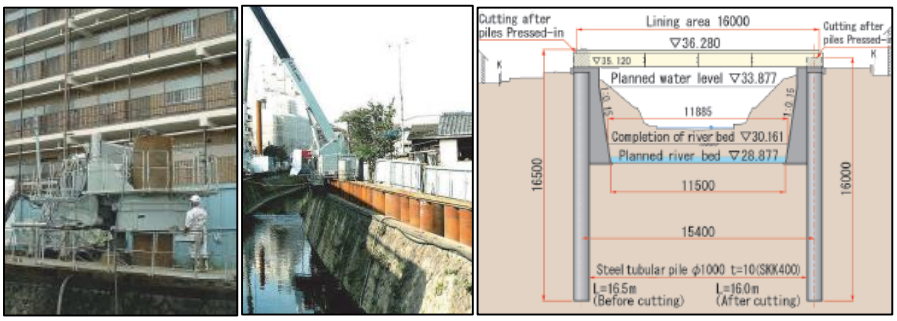

River renovation and the enlargement of cross section by river bed excavation with the assistance of cantilever steel tubular pile walls running nearby residential are in Suginami, Tokyo, Japan.

(b)

Steel tubular retaining walls for grade separation work related to a semi-underground railway in Toronto, Ontario, Canada. Press in tubular piles in to hard ground N-value greater than 160.

(c)

Figure 2.26 Some selected applications of steel tubular pile walls among several construction histories (IPA, 2016)

Therefore, the development of a specific design method with the detail understanding about the local and global behavior of tubular pile walls is an essential requirement to ensure the safety and economical constructions. The specific design method should consider two major aspects as follows; (1) the stability of the walls must be confirmed with additional safety margin against the ground failure or structural yielding under ultimate loading conditions and (2) displacement of the wall under ultimate loading conditions must be secured with in the allowable limits. Prior to the development of a design method, the detail mechanical behavior of tubular piles, tubular pile walls and their interaction mechanism with the embedment mediums and the local deformation characteristics must be well studied by physical mean.

Physical model study to simulate the prototype behavior of tubular pile walls from serviceability limits to the ultimate loading conditions could provide valuable information to understand the deformation and failure mechanism of such large geotechnical structures. However, for the development of design method, all the influential factors must be well addressed in the development process. In order to investigate the entire influential factors and to conclude as a generalized design method, required number of centrifuge model studies are extremely large, high cost and time consuming. Therefore, this limitation could be untangled with few critical experimental investigations and the validation by numerical modelling (such as PLAXIS 2D models). Further extensive parametric study could lead towards the generalized design method.

2.3 Single piles subjected to moment and lateral loads

Single piles or the pile groups are often subjected to lateral and moment loads induced by lateral earth pressures, wind, wave, earthquakes etc… Pile foundations are utilized in vast range of civil engineering applications either as a single pile or pile groups with one or more rows. Majority of the single pile foundations are utilized in offshore wind farms (so called mono-pile) to support the wind turbines. Main loading conditions of mono-pile foundation are the large lateral load induced by wind at the level of rotating blades, wave loads acting at the sea water level and the axial force cause by the weight of wind turbine, transition piece and the tower. Relative locations of these resultant lateral forces and the location of monopole foundation head where transition piece connect with the mono-pile foundation are described in **Figure 2.27**.

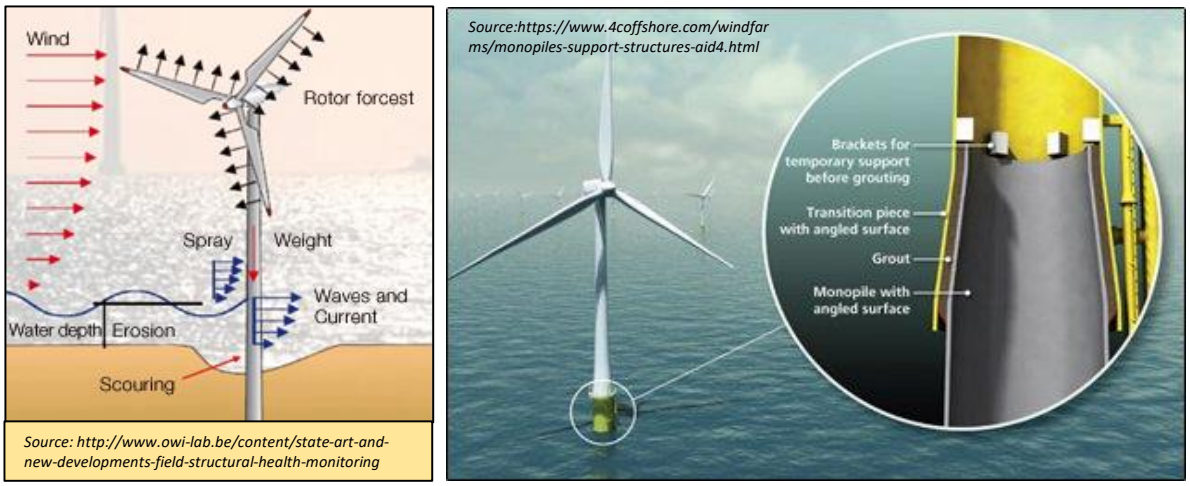

Figure 2.27 Mono pile foundation and wind turbine

Attributing to vertical eccentricities between the point of action of load and the head of the mono-pile foundation, relatively large moment loads also one of the major loadings. Mono-pile foundations are giant piles compare to the conventional pile foundation of a typical multi story building. Pile foundations supporting a building are mainly utilized to resist the axial loads, however large lateral accelerations could be expected during an earthquake excitation. Therefore, these piles should be design to resist lateral loads of at least 10% of the axial load generated from the super structure (Broms, 1964 a). Pile foundations which are supporting the retaining walls (**Figure 2.28** (a)), abutments (**Figure 2.28** (b)) also experience large lateral and moment loads due to the earth or hydrostatic pressure and from the bridge guiders respectively. Recently the applications of embedded tubular pile retaining walls also increased in the engineering practice, which can be considered as a group pile with single row. However major different between these type of walls and the group pile foundations for a building or the pile supported retaining walls and abutments is the fixity at the pile head and the confinement provided by the surrounding soil. While considering the above mentioned pile foundations it can be categorize in to two different types based on the fixity of piles. Where mono-piles and tubular pile retaining walls are lies in the group of free headed piles, meanwhile the piles supporting the super structures fall under the fix headed piles.

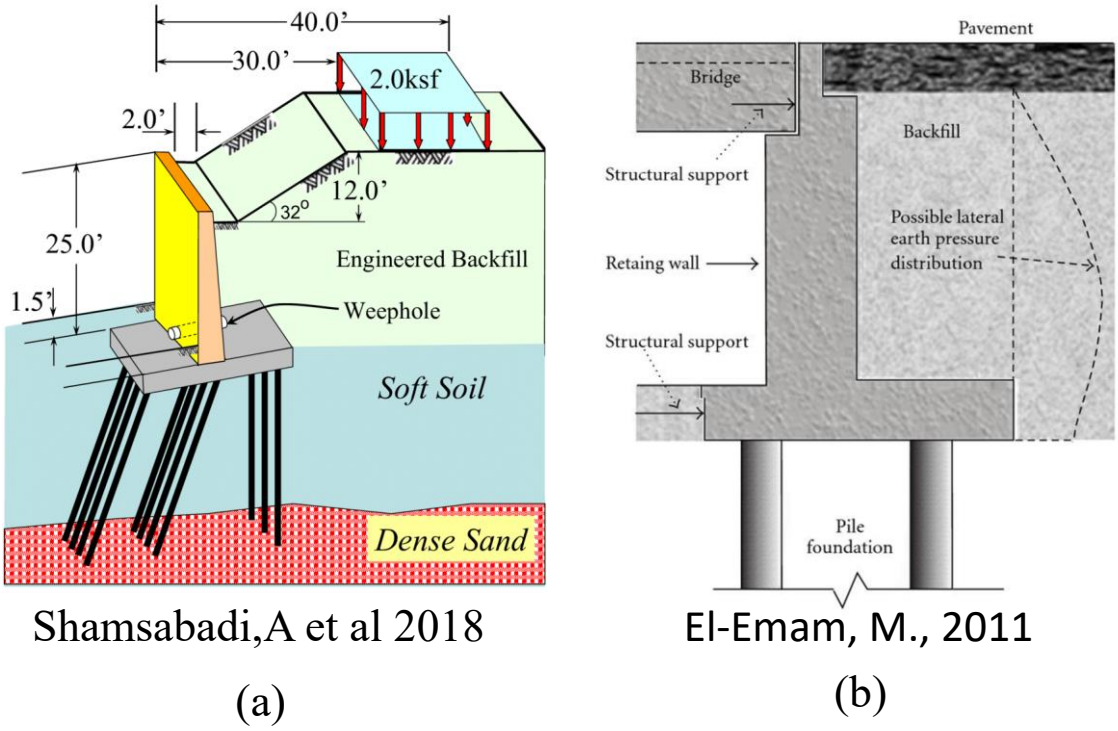

Shamsabadi,A et al 2018

(a)

El-Emam, M., 2011

(b)

Figure 2.28 Pile supported (a) retaining wall and (b) abutment

2.3.1 Behavior of single piles in sand

Classical records on the behavior and failure mechanism of piles in cohesive and cohesion less are described in Broms (1964a) and Broms (1964b) respectively. In the second paper (Broms (1964b)) the deformation mechanism of free and fix headed, both short and long laterally loaded piles embedded in cohesion less soil are described as shown in **Figure 2.29** and **Figure 2.30**. According to Broms (1964(b)), the failure of laterally loaded piles take place under two different scenarios, (1) when the pile reaches its yield resistance or (2) the lateral earth pressure in the soil reaches its ultimate lateral resistance in the entire portion of the pile. Referring to

Figure 2.29, the free headed short pile shows the mode of soil failure meanwhile the fix headed piles have the possibility of both soil yielding and structural failure closer to the fixed point. Furthermore, the free headed short piles could experience extremely large shear forces near the bottom tip of the piles which could increase possibility of pile local deformation at the tip, but in the case of fix headed piles the shear force at the bottom tip could be closer to zero. From **Figure 2.30**, the mobilization of soil resistance along the pile is quiet similar in case of long both free and fix headed piles. However, the fix headed pile could fail by yielding at the fixed pint or by buckling in the embedded zone.

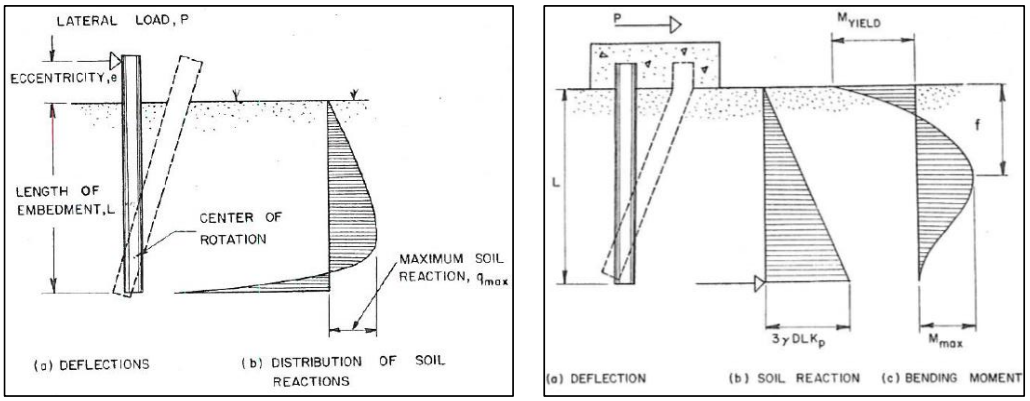

Figure 2.29 Failure mechanism of (a) short free headed piles and (b) Intermediate fix headed piles in cohesion less soil (Broms,1964b)

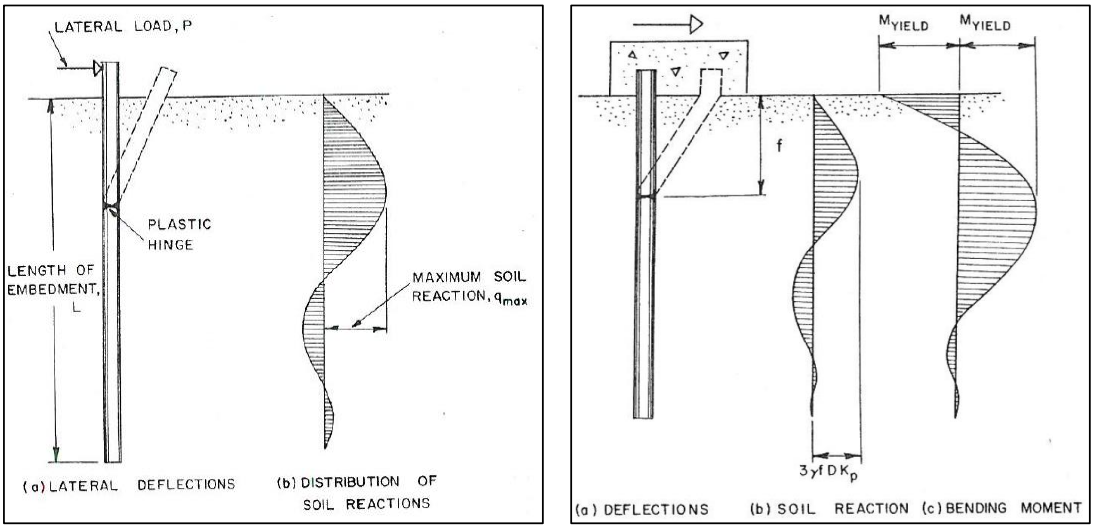

Figure 2.30 Failure mechanism of (a) long free headed piles and (b) long fix headed piles in cohesion less soil (Broms,1964b))

In the actual design practice the failure of the piles defined correspond to the allowable displacement rather than the complete yielding of the pile or soil, generally allowable displacement depends on the type of the structure and the expected performance. Majority of

the pile foundations are designed to satisfy the serviceability requirement with high margin of safety which is far remote from the failure or ultimate loads in order to avoid the structural failure. Broms (1964(b)) also illustrates the deflections at working loads (**Figure 2.31**) and the ultimate lateral resistance of short (**Figure 2.32**(a)) and long (**Figure 2.32** (b)) piles under different loading conditions with the assumption of linear increase of lateral subgrade reaction with the depth as proposed in Terzaghi (1955). Ultimate lateral resistance (Q) suggested by Broms (1964(b)) for unit length of the pile at a depth below the ground surface is defined in equation 2.2.

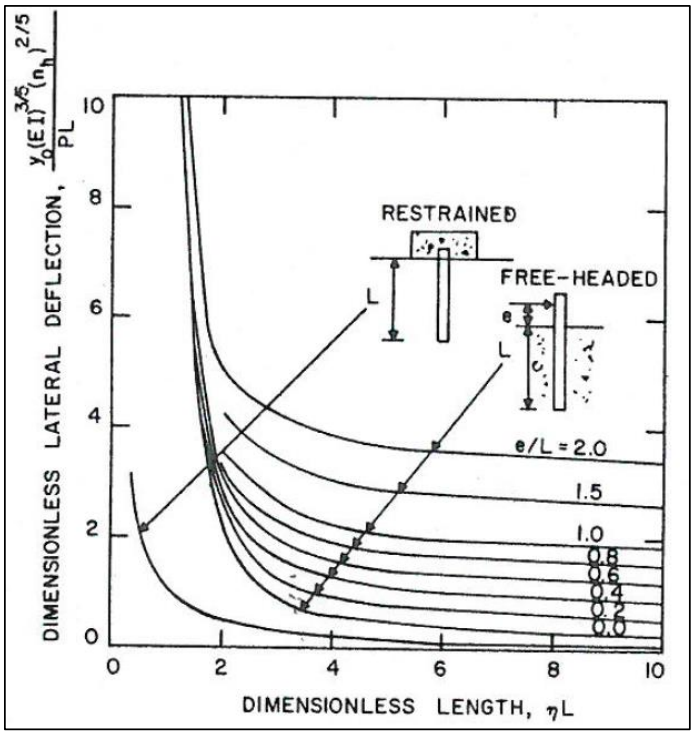

y_o= Deflection at ground surface

EI = Stiffness of the pile section

L = Embedment depth

e = Eccentricity

P = Lateral load

n_h= Coefficient of horizontal subgrade reaction

n_h= Coefficient of horizontal subgrade reaction

$\eta = (n_h/EI)^{0.2}$

Figure 2.31 Lateral deflections at ground surface for free headed and fix headed piles in cohesion less soil (Broms,1964(b))

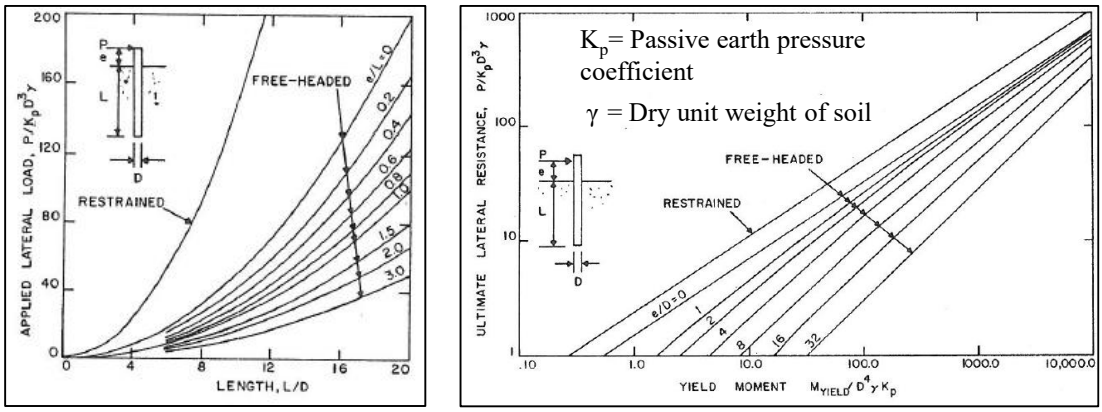

(a) (b)

Figure 2.32 Ultimate lateral resistance of free headed and fix headed (a) short piles and (b) long piles in cohesion less soil (Broms,1964(b))

$Q = 3D\gamma Z\mathrm{K}_P$…….....equation 2.2

$K_P = \frac{1+sin\phi'}{1-sin\phi'}$…….....equation 2.3

$K_h = \eta_h \frac{Z}{D}$…….....equation 2.4

Z – Depth at which the ultimate lateral resistance is considered

Q – Ultimate lateral resistance per unit length of the pile at a depth Z

D – Pile diameter

γ – Effective unit weight of sand

K_P – Passive earth pressure coefficient defined in equation 2.3

ϕ' – Effective friction angle

K_h – Horizontal subgrade reaction (Terzaghi (1955))

η_h – Coefficient of horizontal subgrade reaction per unit width

The simplified assumption of linearly increasing subgrade reaction with the depth (Terzaghi (1955)) is described in equation 2.4. For a preliminary design and quick forward calculations the charts given in **Figure 2.31** and **Figure 2.32** are much useful. However, for the detailed design and the application of massive geotechnical structures the underlying assumptions and the influences on these design charts must be verified. Especially the "dependency of stress and strain amplitude on the mobilized horizontal subgrade reaction" and "the influence of deformed shape of pile or the elastic properties of subgrade and associated pile flexure (or flexural rigidity (Biot,1937)) on the subgrade reaction" along the pile must be taken in to consideration since the fundamental assumptions in Terzaghi (1955) deals with these two phenomena.

2.3.2 Stress and strain dependency on the stiffness of sand

Figure 2.33 indicates the typical strain ranges of different geotechnical structures and their allowable strain levels from elastic to failure conditions along with the reduction of shear moduli with the increasing strain. The stiffness degradation could be divided under three different zones as elastic, elastic-plastic and the failure. Where in the former zone the shear moduli is independent of the strain level and in the intermediate zone shear moduli is highly influenced by shear strain meanwhile the latter one dictates the shear flow. Therefore, for an economical and safer design, strain dependent stiffness is a crucial factor at different displacement and loading conditions. Stress and strain dependency on the stiffness of Toyoura sand is well described by different researchers (Iwasaki et al, 1978; Jamiolkowski et al, 1994; Lo Presti et al, 1995). Consideration of stress or strain level dependency on the stiffness is highly important in the numerical modelling of soil structure interaction. Although the elastic behavior or the initial modulus at relatively small strains (10^{-6}) are independent of strain amplitude (**Figure 2.33**), at relatively large strains (10^{-4} to 10^{-2}), non-linear behavior of granular materials and associated shear modulus are highly depend on the strain level and the confining stress.

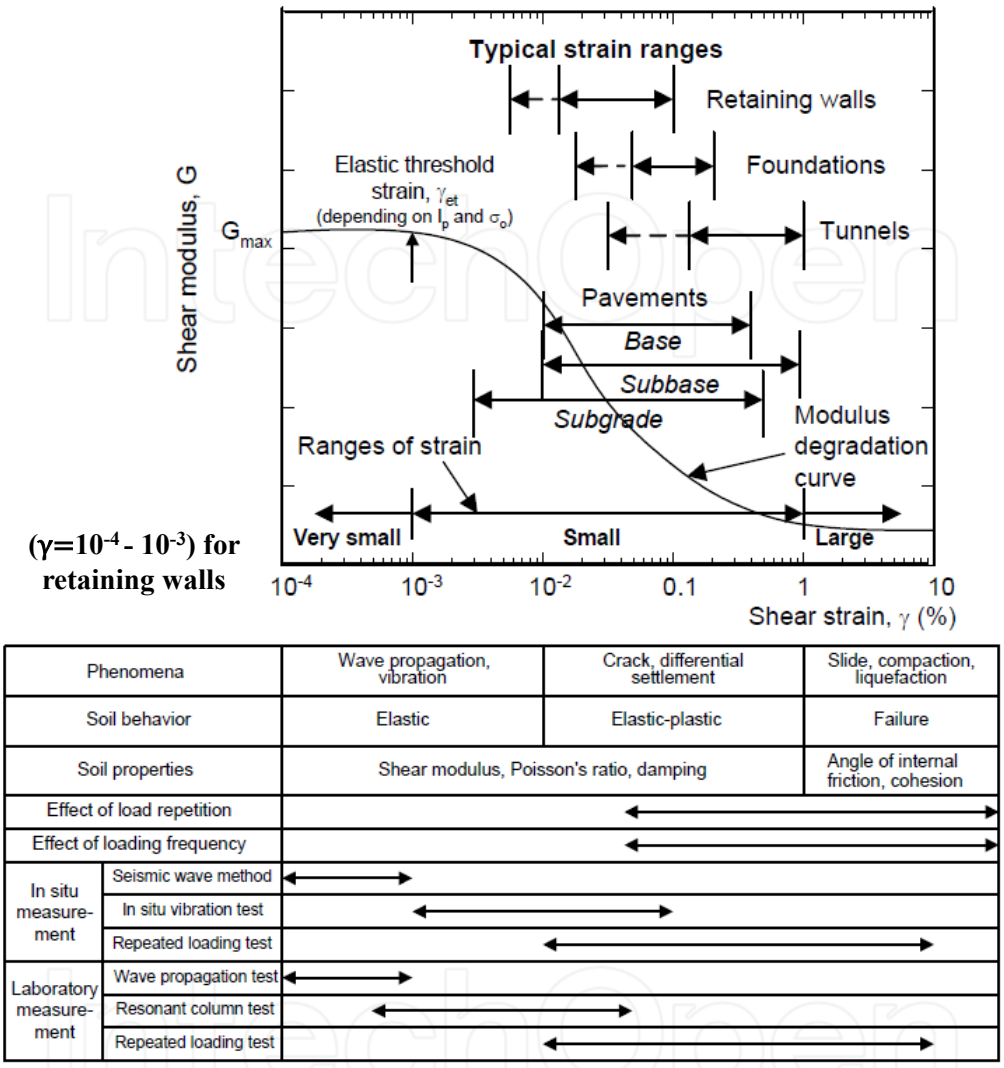

Figure 2.33 Stiffness - strain behavior of soil and design strain levels for various structures and laboratory tests (after Atkinson and Sallfors 1991, Mair 1993, Ishihara, 1996, Sawangsuriya et al. 2005) (Sawangsuriya ,2012)

Therefore, the consideration of strain or stress dependent stiffness of sand is very important in practical applications, where a design engineer could closely predict the possible subgrade reactions at working strain levels of structures. Which could provide more realistic unloading reloading stiffness and corresponding subgrade reactions for sand compare to the assumption of linear increase with depth. Iwasaki and and Tatsuoka (1977) proposed approximate functions to estimate the shear strain moduli for a clean sand based on the resonant- column test. The functions were proposed from the strain level of 10^{-6} to 10^{-4}, attributing to the non-linear response and large damping of soil beyond the strain level of 10^{-4} the resonant- column method could not be accurate. Proposed functions at different strain amplitudes are given in equation 2.5 to equation 2.7. Where the exponent of the mean effective stress increases with the increasing strain level and the constant in the decreases. Both the exponent and the constant are the function of shear strain. According to Iwasaki et al. (1978) the equation 2.7 was originally established by Hardin and Richart (1963). An extended strain measurement by Iwasaki et al. (1978) could measure up to the level of 10^{-2}, where they used resonant- column apparatus for $\gamma=10^{-6}$ to 10^{-4} and torsional shear device for the strain measurement of $\gamma=10^{-4}$ to 10^{-2}. Also a generalized form of equations to dictate the shear strain and the confining stress

dependent share moduli is given in Iwasaki et al. (1978) along with the design charts to estimate the exponents and the constants.

$G = \frac{900(2.17-e)^2 p^{0.40}}{1+e}$ $at\ \gamma = 10^{-6}$ ……equation 2.5

$G = \frac{850(2.17-e)^2 p^{0.44}}{1+e}$ $at\ \gamma = 10^{-5}$……equation 2.6

$G = \frac{700(2.17-e)^2 p^{0.50}}{1+e}$ $at\ \gamma = 10^{-4}$……equation 2.7

e – Void ratio

γ – Shear strain

p– Mean effective stress or confining pressure

G– Shear modulus

2.3.2.1 Influence of void ratio on the shear modulus of sand

Void ratio of a granular medium is simply defined as the ratio between the volume of voids and the volume of solids in a unit volume as described in equation 2.8.

$Void\ Ratio\ (e) = \frac{Volume\ of\ voids}{Volume\ of\ solids}$……equation 2.8

$D_r = \frac{e_{max}-e}{e_{max}-e_{min}}$……equation 2.9

This simple faction governs the mechanical behavior of a granular medium and their interactions between the structures. The influence of void ratio on the relative density of a granular medium is described in the equation 2.9, where;

e – Void ratio of the sand to be modelled (vary between min-max void ratio)

e_{max}– Maximum void ratio (corresponds to the minimum density)

e_{min}– Minimum void ratio (corresponds to the maximum attainable density)

D_r – Relative density (Maximum of 1)

Equation 2.9 indicates the dependency of void ratio on the density of a granular medium. Where e_{max} and e_{min} are corresponding to the minimum and maximum attainable densities. From the relation between void ratio and the density it can be said that, the density of a granular medium is inversely proportional to the void ratio. Iwasaki et al. (1978) illustrates the influence of void ratio on the shear modulus of Toyoura sand in a wide range of strain amplitudes (10^{-6} to $3x10^{-}$

[3]) under a constant confining pressure of 100kPa as shown in **Figure 2.34**. From large number of experimental outcomes, they found the empirical formula for the slope of *G-e* relation as described in equation 2.10. From **Figure 2.34** it can be confirmed that the slope of *G-e* relation is independent to the strain amplitude.

$$slope\ of\ G-e\ relation\ (S_{Ge}) = \frac{(2.17-e)^2}{1+e} \quad \text{.....equation 2.10}$$

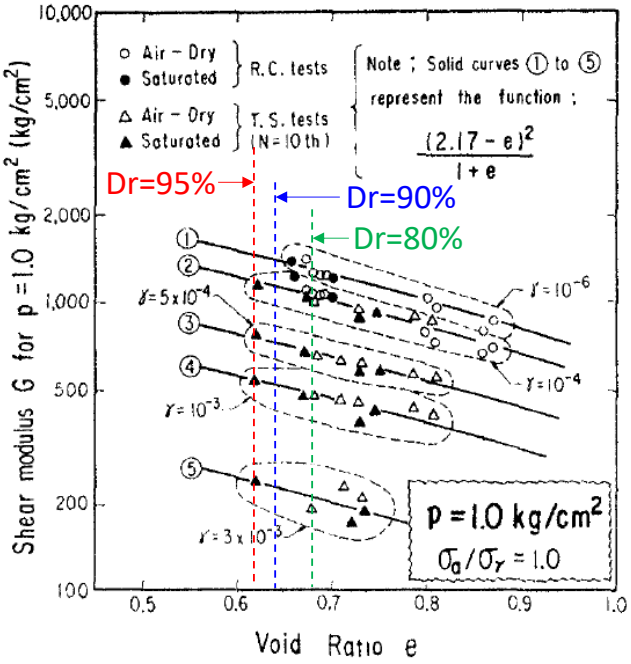

Figure 2.34 Dependency of stiffness on the void ratio of Toyoura sand at 98kPa confining pressure for different strain amplitudes (Iwasaki et al. , 1978)

2.3.2.2 Stress dependency on shear modulus of sand

Iwasaki and Tatsuoka (1978) described the influence of confining pressure on shear modulus of Toyoura sand based on their experimental outcomes. Where the influence of void ratio was eliminated by dividing the shear modulus by the slope of G-e relation described in equation 2.10. The relationship between the G/S_{Ge} and the confining pressure for air dried Toyoura sand and saturated Toyoura sand described in Iwasaki et al. (1978) are given **Figure 2.35**, where S_{Ge} is the slope of G-e relation described in equation 2.10. Based on the observations of **Figure 2.35** linear relation between shear moduli and confining pressure in logarithmic scale could be found. The relation was presented in a generalized form for Toyoura sand by Iwasaki et al. (1978) as shown in equation 2.11, where one can estimate the shear moduli at required strain level and interested confining pressure. According to Iwasaki et al. (1978), similar form of equation was presented as pioneering study by Silver and Seed (1971). Estimated stiffness profiles under different strain levels of Toyoura sand at a relative density of 80% are given in **Figure 2.37**. From **Figure 2.37** it can be confirmed that the assumption of linear increase in stiffness with the depth or confining pressure highly overestimate the stiffness. The assumption could yield non-conservative design and the expected performance of the structures under design and the real field will be entirely different. As most of the researchers followed based on their experience and observed agreement with the real field observations the exponent of m_γ=0.5 could provide more

realistic and conservative stress and strain dependent stiffness values. Considering the working strain levels of a retaining wall (10^{-4} to10^{-3}) the profile corresponding to the strain level of 10^{-3} as a conservative measure or averaged profile between 10^{-4} and 10^{-3} could be used for the numerical modelling.

Attributing to the limitations of Iwasaki and Tatsuoka (1978) and other researchers on the stiffness of Toyoura sand at high relative densities or small void ratios, the stress dependency on the stiffness of Toyoura sand could be predicted in the e- value range of 0.81-0.67. Which is correspond to the relative stiffness of 45%-82%. The stress- strain dependency on the stiffness of Toyoura sand at relatively high densities could be estimated based on shear modulus and void ratio relation described in **Figure 2.34**. **Figure 2.34** describes the shear modulus against the void ratio at 1kg/cm^2 confining pressure. Which enables us to estimate the K_γ values by based on the shear modulus and the correction factor for void ratio, which is the slope of G-e relation (S_{Ge}) described in equation 2.10.

Klinkvort et al. (2013) investigated the stress dependency on the stiffness of relatively high density using the sample with the height equals to the diameter (70mm). Stress dependency on the unloading reloading stiffness of Fontainebleau sand with a relative density of approximately 90% is described in Klinkvort et al. (2013) based on the triaxial tests on dry and saturated soil samples as described in **Figure 2.38**(c). The comparison between the physical properties of Fontainebleau sand and Toyoura sand are described in Table 2.1. From Table 2.1 the mean particle size of the Fontainebleau sand is about 10% higher compare to the Toyoura sand. Based on Table 2.1 and the equation 2.6 the void ratio of Fontainebleau sand at 90% relative density (e_{90}=0.579) can be calculated. This void ratio is much smaller than the minimum void ratio of Toyoura sand reported by Fukushima and Tatsuoka (1984). Attributing to the high density and relatively small void ratio of the Fontainebleau sand at 90% relative density the stiffness of the sand described in **Figure 2.38** (c) is one order higher than the variation of Toyoura sand with 80% and 90% relative density given in **Figure 2.38** (a) and **Figure 2.38** (b). Stress dependency on the stiffness of Fontainebleau sand at 90% is described in equation 2.12 (Klinkvort et al. (2013)) in terms of confining pressure.

$$(G)_{\gamma,p} = K_\gamma \frac{(2.17-e)^2 p^{m_\gamma}}{1+e} \quad \text{.....equation 2.11}$$

Where K_γ can be derived from **Figure 2.35** corresponding to the confining pressure of unity.

Meanwhile the m_γ values could be traced from the m_γ-γ relation given in **Figure 2.36**.

K_γ– Function of shear strain (But dimensionless constant for a specific strain)

m_γ– Exponent of "p" which is also a function of shear strain

$G_{\gamma,p}$– Shear moduli of sand unit will be represented by the unit of "p"

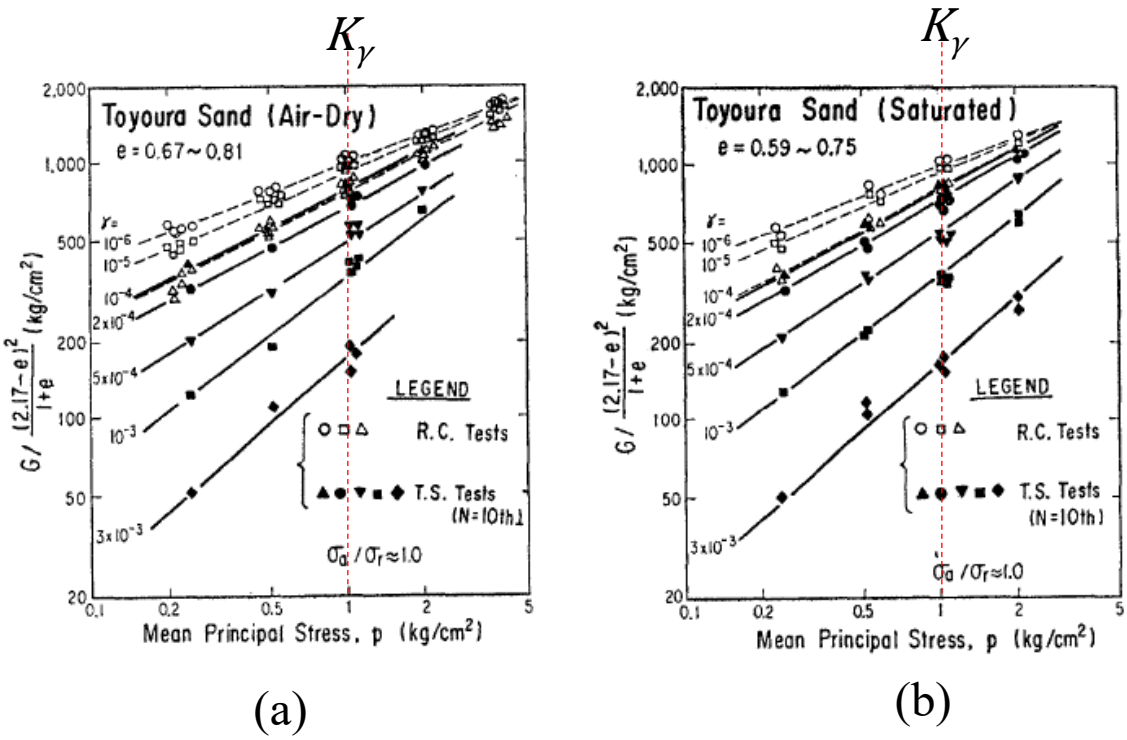

Figure 2.35 Relation between G / (((2.17−*e*)^2)/(1+*e*)) and confining pressure (p) for (a) air dried and (b) saturated Toyoura sand at different strain amplitudes (Iwasaki et al., 1978))

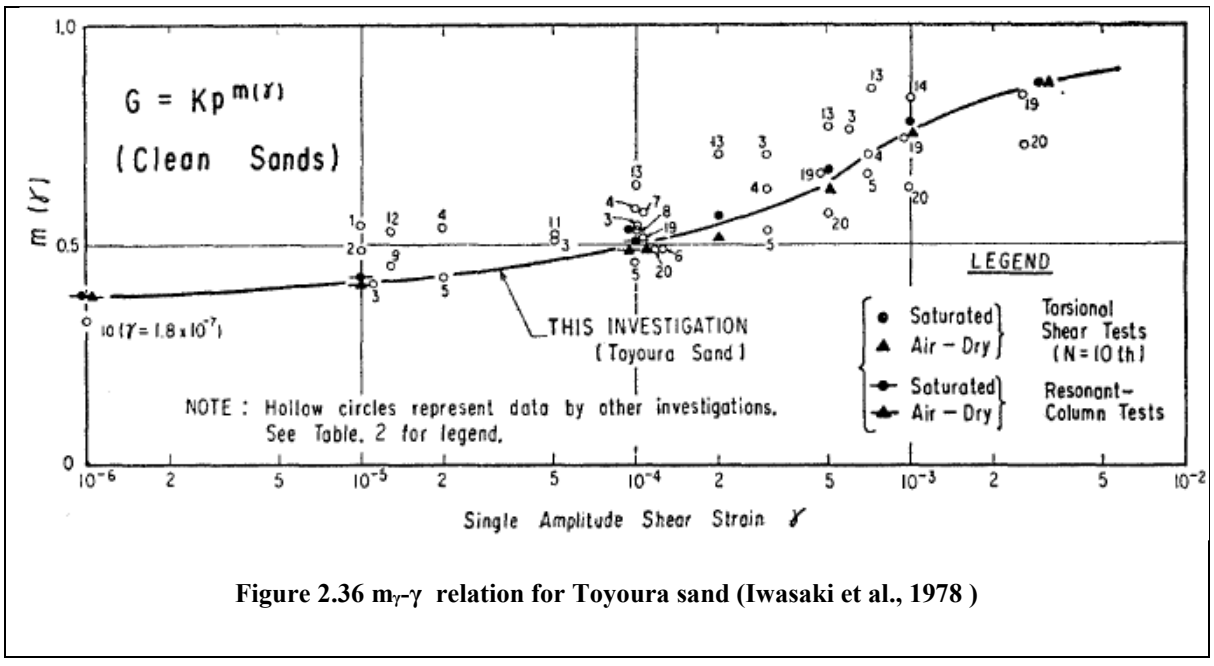

Figure 2.36 m_γ-γ relation for Toyoura sand (Iwasaki et al., 1978)

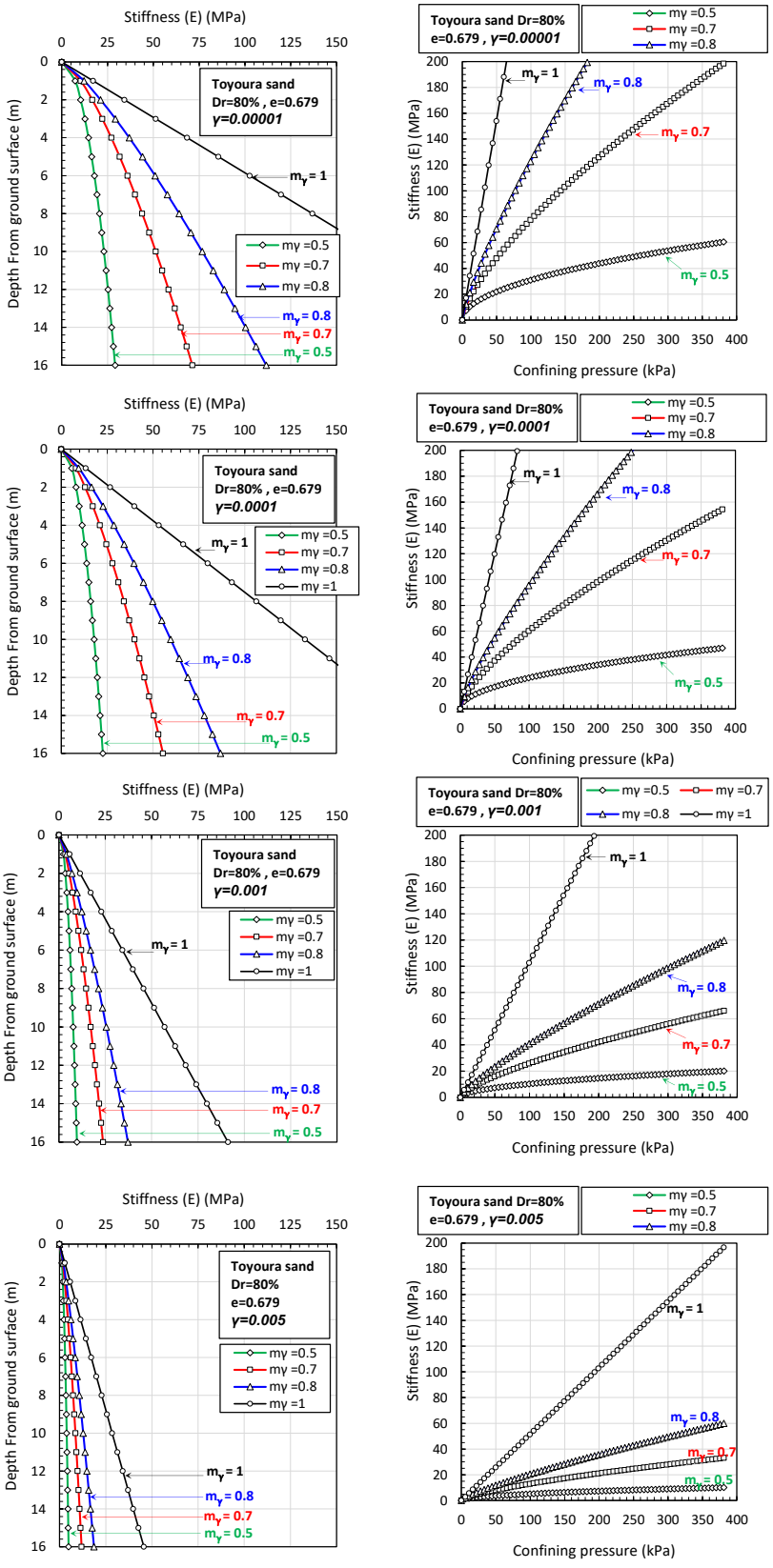

Figure 2.37 Estimated variation of stiffness profiles against the confining pressure or depth for Toyoura sand (Dr=80%) at different strain levels based on Iwasaki and Tatsuoka (1978)

$$E_{ur} = E_o \left(\frac{p\prime}{100kPa}\right)^{0.6226}$$ .....equation 2.12

$E_o = 138070\ kPa$ (Klinkvort et al. (2013))

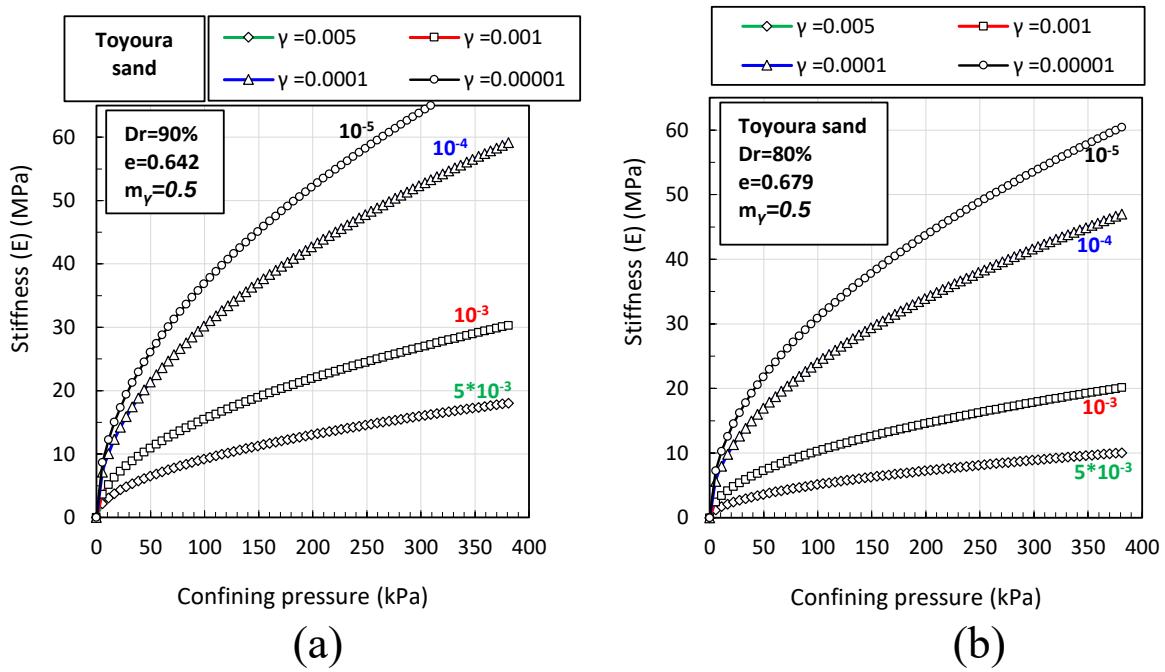

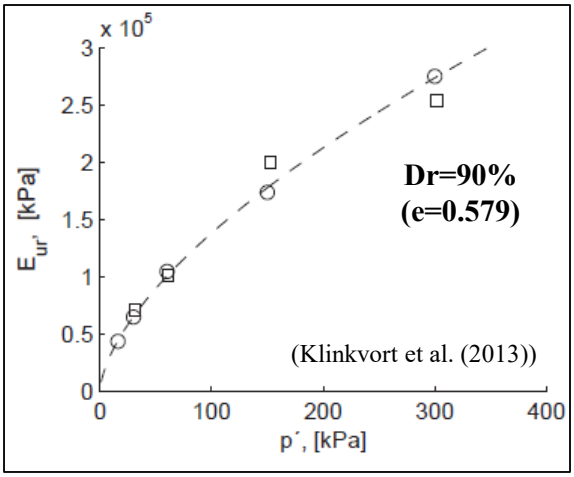

Figure 2.38 Stress dependency on the stiffness of (a) Toyoura sand Dr=80% ,(b) Toyoura sand Dr=90% (b) Fontainebleau sand

Table 2-3 Physical properties of Fontainbleau sand and Toyoura sand

Sand	Fontainebleau sand (Klinkvort et al.2013)	Toyoura sand (Fukushima and Tatsuoka1984)
Specific gravity of particles (G_s)	2.646	2.64
Minimum void ratio (e_{min})	0.548	0.605
Maximum void ratio (e_{max})	0.859	0.977
Average grain size (d_{50})	0.18	0.16
Coefficient of uniformity (C_u)	1.6	1.46

2.3.3 Piles embedded and socketed in to rocks

Applications of embedded piles in rock under lateral loading and relevant documented investigations are barely encountered (Guo and Lehane, 2016) in the past compare to the rock socketed shafts (Carter and Kulhawy, 1988; Chen et al., 2017), where substantial thickness of overburden soil govern the deformation characteristics of piles which yields negligible displacements at the underlying rock surface. However, recent infrastructure development nearby mountain sites (Xing et al., 2014; Miyanohara et al., 2018) or the application of onshore (Guo, 2015) and offshore (Kallehave et al., 2015) mono-pile foundations often encounter the rock surface near or at the ground level. In such situations the lateral resistance is mainly controlled by the rock embedment. To the best of authors' knowledge, the lateral response of large diameter steel tubular piles embedded in rock (Fragio et al., 1985) has not well studied by physical models or real field tests to observe the critical behavior, which is controlled by several influential factors such as pile properties (diameter, stiffness, embedment depth), ground factors (strength and stiffness), and loading conditions (loading height, monotonic and cyclic) (Arany et al., 2017). On the other hand, few field tests using concrete shafts (Digioia and Rojas-Gonzalez, 1994; Kahle and Brown, 2002; Guo and lehane, 2016) and numerical solutions are available based on continuum approach (Randolph 1981; Carter and Kulhawy, 1992; Zhang et al., 2000; Chen et al., 2016) and non-linear p-y curves (Reese, 1997; Gabr et al., 2002; Erbrich, 2004) for laterally loaded shafts in rock.

2.3.4 Available literatures and current design methods

Current design methods of embedded and rock socketed piles are lies in two different method of analysis. One type of design method based on continuum approach (Randolph 1981; Carter and Kulhawy, 1992; Zhang et al., 2000; Chen et al., 2016), meanwhile the other one (Reese, 1997; Gabr et al., 2002; Erbrich, 2004) model the behavior of rock mass as a set of non-linear springs based on the extension of p-y curves derived for sand. The current design method in Japan follows the theory of semi-infinite beams on elastic foundation (so-called Chang's method), where the design is based on the allowable deformations thereby the subgrade rations

are limited in the elastic range. Which could more or less similar approach to the linear elastic portion of the p-y curves extrapolated from the results of soil to analysis the behavior of rock. However, the design method and the required embedment depth to control the deformation with in allowable limits varies based on the assumptions and the estimated spring moduli or subgrade reactions of these methods.

2.3.4.1 Soil as an elastic continuum (Randolph, 1977)

Randolph (1977) conducted a 2D finite element analysis by treating the soil as an elastic continuum with the assumption of linearly varying soil moduli with the depth. However, in reality this assumption is not valid for the strain levels in the working loads. The assumption by Randolph (1977) could be valid in the range of shear strains from 10^{-6} to $10^{-5.}$ Beyond which the soil behavior is non-linear and shear moduli is the function of stress, strain and void ratio or density as discussed in chapter 2.3.2. Randolph (1977) further idealized the problem of a laterally loaded pile as an elastic beam resting on a series of uniform linear springs (elastic foundation) along the embedded length of the beam. Hetenyi (1964) provides the closed form solutions for the idealization of Randolph (1977) under different loading and restraint conditions. Hetenyi (1964) also describes the critical embedment of the pile as a function of bending rigidity of the pile and the subgrade reaction of soil, also the solutions for the deflection (u) and rotation (θ) of the long elastic piles at their loaded end as described from equations 2.13 to 2.15. It is important to emphasize that the critical embedment is defined as the depth beyond which the behavior of pile will not be influenced by the depth of embedment (pile behave as infinitely long).

$$Critical\ lengh\ (l_c) \simeq 4\left(\frac{EI_p}{k}\right)^{0.25} \quad \text{.....equation 2.13}$$

$$deflection\ (u) = \sqrt{\frac{2H}{k}\left(\frac{l_c}{4}\right)^{-1}} + \frac{M}{k}\left(\frac{l_c}{4}\right)^{-2} \quad \text{.....equation 2.14}$$

$$Rotation\ (\theta) = \sqrt{\frac{2M}{k}\left(\frac{l_c}{4}\right)^{-3}} + \frac{H}{k}\left(\frac{l_c}{4}\right)^{-3} \quad \text{.....equation 2.15}$$

H – Horizontal load at the pile head

M– Moment load at the pile head

EI_p – Flexural stiffness of the pile

Based on the dimensionless analysis, Randolph (1977) found that the behavior of the pile is simply govern by the $\boldsymbol{E_p/G}$ ratio and the **length** of the pile. Where the E_p is the effective Young's modulus of the pile when the pile is transformed from its original shape to a solid cylindrical inclusion with the radius r_o as described in equation 2.16.

$$Effective\ Young's\ modulus\ E_p = \left(EI_p\right) \Big/ \left(\pi {r_o}^4 / 4\right) \quad \text{.....equation 2.16}$$

In Randolph (1977), the influence of Poisson's ratio of a homogeneous embedded medium (constant shear modulus along the depth) is treated by a parameter G^* described in the equation 2.17. Where, G is the shear modulus of a homogeneous soil which is constant along the depth

and v is Poisson's ratio of the soil. It is important to emphasize that, in the design practice generally the stiffness of clay type materials assumed as constant with the value of $9C_u$, Where C_u is the undrained shear strength of clay.

$G^* = G(1 + {}^{3\nu}/_{4})$…….....equation 2.17

In case of shear modulus linearly varying with the depth the shear modulus was represented by m^* as describe in the equation 2.18. Where, m is the parameter which represents the rate of increase of shear modulus with the depth.

$m^* = m(1 + {}^{3\nu}/_{4})$…….....equation 2.18

Based on 2D finite element analysis and above mentioned assumptions Randolph (1977), proposed a set of equations to estimate the deflection and rotation at the ground level as given in equations 2.19 to 2.22. The proposed equations by Randolph (1977) are more useful for the predictions of the pile deformations under the strain levels of embedded medium under the elastic range (10^{-6}-10^{-5}), where the shear moduli is independent of the strain amplitude.

- In the case of **constant stiffness** and a Poisson's ratio of the soil along the depth

$$deflection\ (u) = 0.25\frac{H}{G^* r_o}\left(\frac{E_p}{G^*}\right)^{-1/7} + 0.27\frac{M}{G^* r_o^2}\left(\frac{E_p}{G^*}\right)^{-3/7}$$ ……..equation 2.19

$$rotation\ (\theta) = 0.27\frac{H}{G^* r_o^2}\left(\frac{E_p}{G^*}\right)^{-3/7} + 0.8\frac{M}{G^* r_o^3}\left(\frac{E_p}{G^*}\right)^{-5/7}$$ ……..equation 2.20

- In the case of **stiffness proportional to the depth** and a Poisson's ratio of the soil along the depth

$$deflection\ (u) = 0.54\frac{H}{G^* r_o^2}\left(\frac{E_p}{m^* r_o}\right)^{-3/9} + 0.60\frac{M}{m^* r_o^3}\left(\frac{E_p}{m^* r_o}\right)^{-5/9}$$ ……...equation 2.21

$$rotation\ (\theta) = 0.60\frac{H}{G^* r_o^3}\left(\frac{E_p}{m^* r_o}\right)^{-5/9} + 1.13\frac{M}{m^* r_o^4}\left(\frac{E_p}{m^* r_o}\right)^{-7/9}$$ ……..equation 2.22

From the parametric study conducted by Randolph (1977) the critical slenderness ratio for the abovementioned two cases were reported as described in equation 2.23 and 2.24.

$$For\ constant\ stiffness\ \left({}^{l}/_{r_o}\right)_c = 2\left(E_p/G^*\right)^{2/7}$$ …….....equation 2.23

$$For\ linearly\ increasing\ stiffness\ \left({}^{l}/_{r_o}\right)_c = 2\left(E_p/m^* r_o\right)^{2/9}$$…….....equation 2.24

2.3.4.2 Rock as an elastic continuum (Carter and Kulhawy, 1992)

Carter and Kulhawy (1992) express the closed form equations to assess the response of a rock socketed shafts with or without the overlying medium as shown in **Figure 2.39**, based on the concepts of Randolph (1977 & 1981). The assumption of homogeneous (Constant stiffness along the depth), isotropic elastic rock mass with the stiffness E_r and Poisson's ratio of v_r is incorporated in their proposed closed form solutions. Similar to Randolph (1977 & 1981) the effective Young's modulus is defined as describe in equation 2.25.

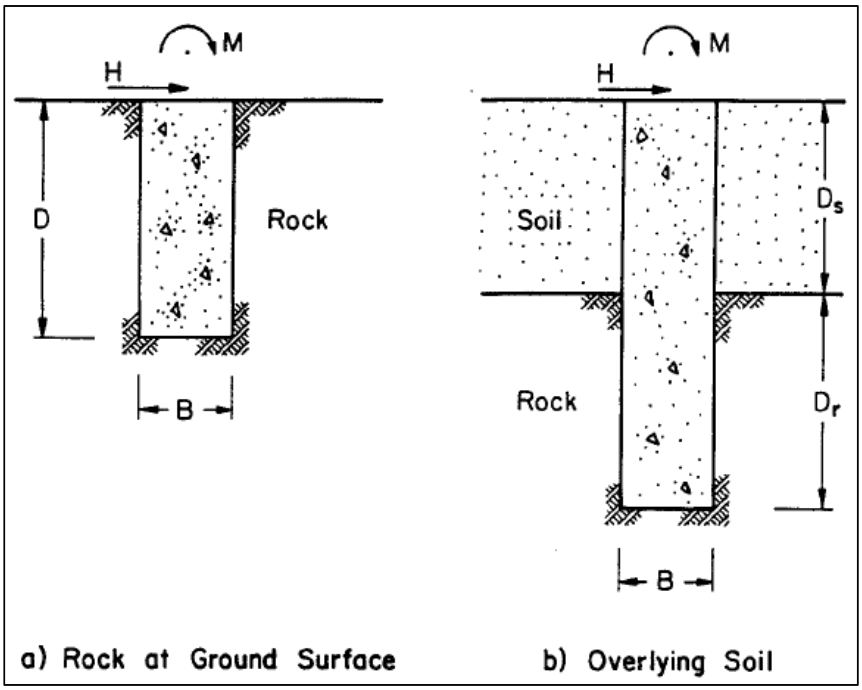

Figure 2.39 Rock socketed shafts (Carter,1988)

$$Effective\ Young's\ modulus\ E_e = {(EI)_c}\Big/{\left(\pi B^4/_{64}\right)} \quad \text{.....equation 2.25}$$

$(EI)_c$ – Actual bending rigidity of the pile

B – Diameter of the pile

D_r – Socketed depth in rock

D_s – Depth of overlying medium

The effects of variations in the Poisson's ratio was drawn as equation 2.26. Where G_r is the shear modulus of rock, it can be expressed in terms of Young's modulus as described in equation 2.27.

$$G^* = G_r\left(1 + {3\nu_r}/{4}\right) \quad \text{.....equation 2.26}$$

$$G_r = \frac{E_r}{2(1+\nu_r)} \quad \text{.....equation 2.27}$$

E_r – Young's modulus of rock

G_r – Shear modulus of rock

ν_r – Poisson's ratio of rock

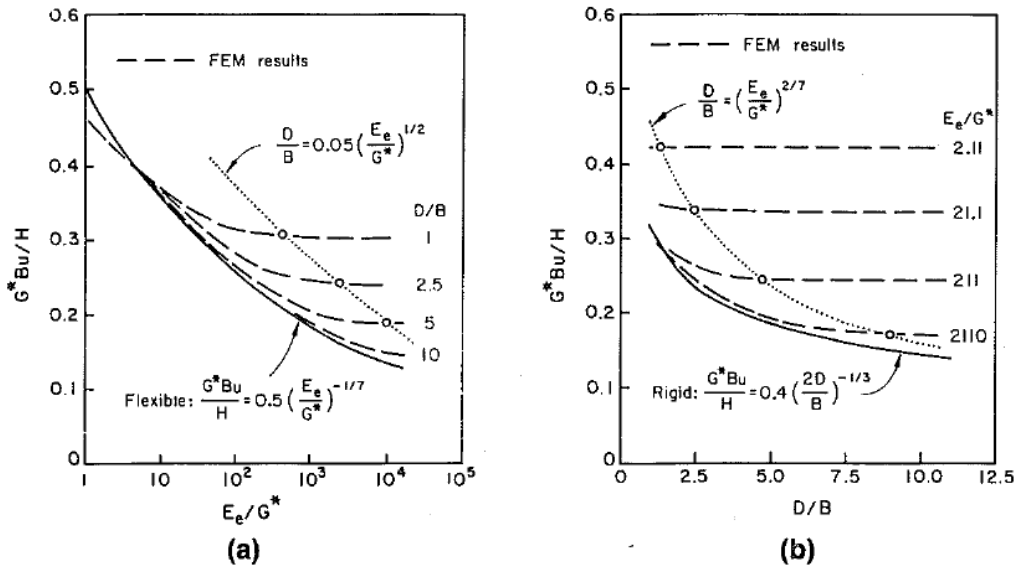

Figure 2.40 Lateral load –displacement relations for shafts embedded in rock (Carter and kulhawy,1992)

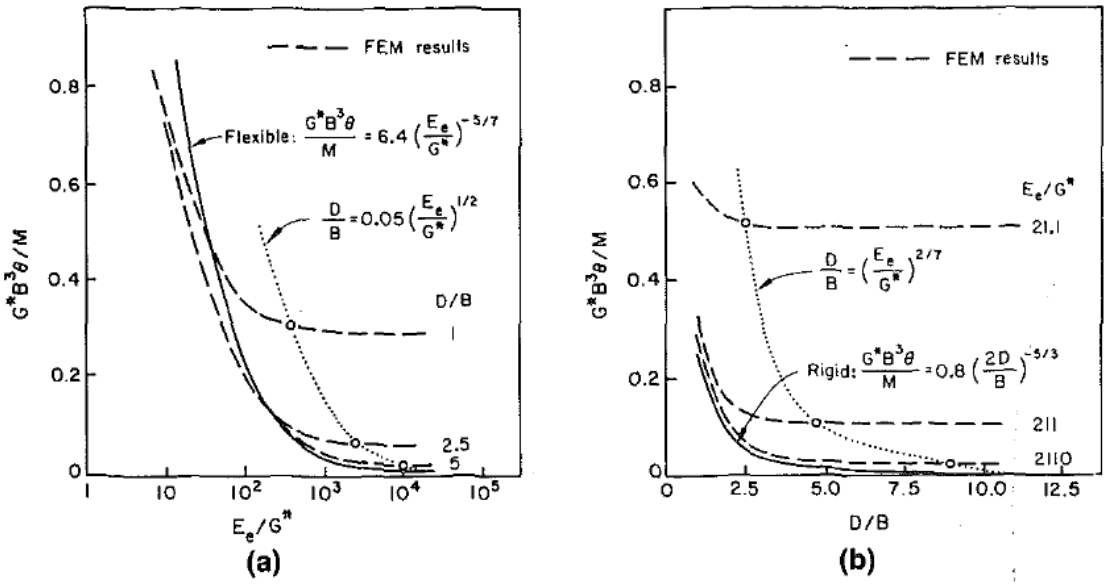

Figure 2.41 Moment –rotation relations for shafts embedded in rock (Carter and kulhawy,1992)

From the results of 2D finite element analysis Carter and Kulhawy (1992) found that, the displacement (u) and rotation (θ) at the surface of a homogeneous rock is governed by the modulus ratio (E_e/G^*) and the geometry of the shaft (D/B). Results of laterally loaded shafts obtain by Carter and Kulhawy (1992) under different (E_e/G^*) modulus ratios are provided in **Figure 2.40** and **Figure 2.41**. Where the **Figure 2.40** illustrates the lateral load – displacement

relation and **Figure 2.41** describes the moment – rotation relationship. From the FEM analysis results described in **Figure 2.40** and **Figure 2.41**by Carter and Kulhawy (1992), no significant influence on the displacement and rotation can be seen beyond certain *D/B* ratios for a specific modulus ratio. Randolph (1977 & 1981) defined this *D/B* ratio as the boundary of flexible shaft. As described in equation 2.28, beyond which the shaft behaves as infinitely long. The closed form equations proposed by Randolph (1977 & 1981) for flexible piles described in equations 2.19 and 2.20 are represented in different forms in equations 2.29 and 2.30 as Carter and Kulhawy (1992) presented. The applicability of the closed form equations 2.29 and 2.30 was verified by Carter and Kulhawy (1992) in the ranges of $1 \leq E_e/E_r \leq 10^6$ and for $D/B \geq 1$.

$$\frac{D}{B} \geq \left(\frac{E_e}{G^*}\right)^{2/7} \quad \text{.....equation 2.28}$$

- Closed form solutions for a flexible shaft embedded in homogeneous rock mass

$$deflection\ (u) = 0.50\frac{H}{G^*B}\left(\frac{E_e}{G^*}\right)^{-1/7} + 1.08\frac{M}{G^*B^2}\left(\frac{E_e}{G^*}\right)^{-3/7} \quad \text{.....equation 2.29}$$

$$rotation\ (\theta) = 1.08\frac{H}{G^*B^2}\left(\frac{E_e}{G^*}\right)^{-3/7} + 6.40\frac{M}{G^*B^3}\left(\frac{E_e}{G^*}\right)^{-5/7} \quad \text{.....equation 2.30}$$

The boundary of *D/B* ratio for the rigid shaft was defined by Carter and Kulhawy (1992) as described in equation 2.31. Where they considered that, the short shaft embedded in rock will behave as a rigid structural member, in such situations the displacements of the shaft will be independent of the modulus ratio (E_e/G^*) and only govern by the slenderness ratio *D/B* and Poisson's ratio (ν) of the rock. Also from their FEM analysis results, closed form solutions are given as given in equations 2.32 and 2.33, for the estimation of displacement and rotation at the rock surface level of a rigid shaft.

$$\frac{D}{B} \geq 0.05\left(\frac{E_e}{G^*}\right)^{1/2} \quad \text{.....equation 2.31}$$

- Closed form solutions for a rigid shaft embedded in homogeneous rock mass

$$deflection\ (u) = 0.4\left(\frac{H}{G^*B}\right)\left(\frac{2D}{B}\right)^{-1/3} + 0.3\frac{M}{G^*B^2}\left(\frac{2D}{B}\right)^{-7/8} \quad \text{.....equation 2.32}$$

$$rotation\ (\theta) = 0.3\left(\frac{H}{G^*B^2}\right)\left(\frac{2D}{B}\right)^{-7/8} + 0.8\frac{M}{G^*B^3}\left(\frac{2D}{B}\right)^{-5/3} \quad \text{.....equation 2.33}$$

2.4 Some literature review on soft rocks and its characteristics

Generally, the definition of soft rocks defined by the unconfined compressive strength and the hardness of the material evaluated based on geological classification. Geological description or lithological name alone may mislead understanding about the strength and stiffness of the soft rocks. For example, the mechanical properties of sandstone may differ in a vast range based on the degree of cementation, being very soft if poorly cemented and extremely hard if well cemented (Kanji, 2014). Several authors categorized the upper and lower limits of the soft rocks based on the unconfined compressive strength since it behaves in between soils and hard rocks.

Table 2-4 Usual types of soft rocks (After Kanji, 2014)

Basic Class	Sub classes
Sedimentary rocks	Soluble: limestone, dolomite, and gypsum; and Coal Clastic: mudstones, shales, siltsones, sandstones,conglomerates and beccias, and marl; Evaporites: salt rock, carnallite, etc
Igneous rocks	Volcanic conglomerates, breccias, and lahar, Basaltic breccia, Pyroclastic deposits, volcanic ash, tuff and ignimbrite and Weathering products of crystalline rocks
Metamorphic rocks	Slate, phyllite, schists, quartzite little cemented, Metavolcanic

2.4.1 Types of rocks and its formation

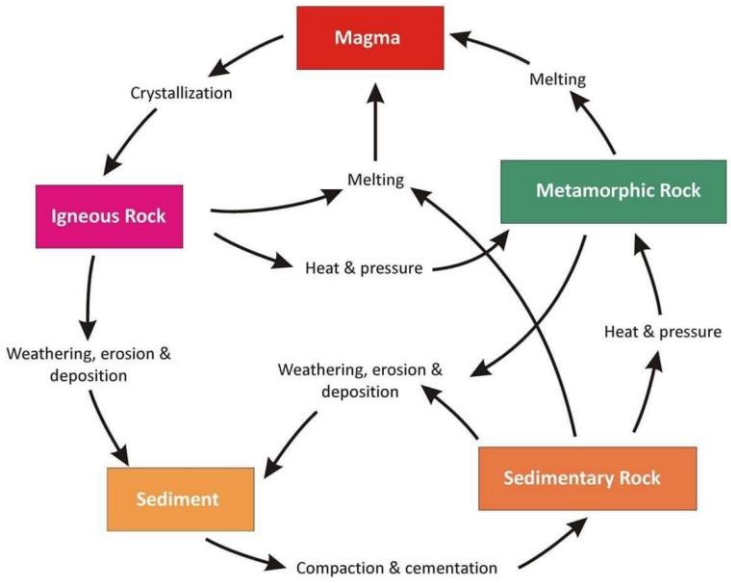

Figure 2.42 Rock formation and transformation

According to the engineering classification 0.6MPa -1.25MPa defined as very soft rock material and 1.25MPa-5.0MPa given as soft rock. In addition, it provides the upper limit of the soft rock as 12.5MPa but there is a practical coincident where the upper limit considered 25MPa as unconfined compressive strength (Kanji, 2014). Establishing the lower limit for the strength

of soft rock is more complicated since some hard soils also exhibits higher unconfined compressive strength. However, Terzaghi and peck (1967) defined based on an SPT value above 50 and UCS greater than 0.4 MPa as the lower limit of soft rocks. Usual types of soft rock s can be categorized under three basic classes as described in the **Table 2-4**.

Formation of parent rock (Igneous rocks) from Magma and subsequent transformation of different types of rocks by geological processes are described in **Figure 2.42**. Where rock forming mechanisms could be identified as follows;

- Crystallization by cooling from magma
- Weathering, erosion and deposition
- Compaction and cementation and consolidation
- Transformation by heat and pressure

Based on the processes in **Figure 2.42** the igneous rocks can be converted in to sediment by weathering, erosion and decomposition. As a continuous cycle these sediments could be transformed in to sedimentary rocks by compaction cementation and consolidation. In the civil engineering practice these sedimentary soft rocks are often encountered in numerous construction projects all over the world. Which could be categorized as described in **Table 2-4**. According to the geological survey of Japan (1995), sedimentary rocks occupy the major fraction in all around Japan followed by volcanic rocks as shown in **Figure 2.43**.

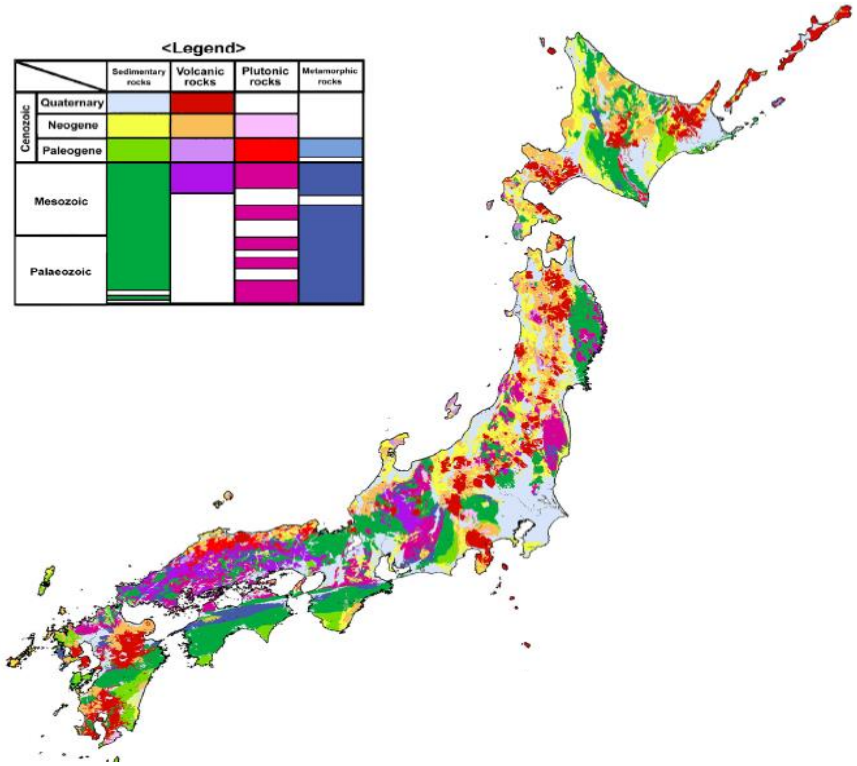

Figure 2.43 Distribution of subsurface rock types in Japan (Geological Survey of Japan, 1995)

2.4.2 Mechanical properties of soft rocks

In civil engineering, prior to the design and construction activities the mechanical properties of the sand or clay layers are evaluated in laboratory by utilizing the borehole samples, which were sampled during the site investigation. Evaluation of mechanical properties and site investigation activities in rock engineering is much deeper compare to the loose grounds. Although the investigation of a rock profile consists some laboratory tests on core samples, the variation of the mechanical properties is much more significant between core and intact conditions. Therefore prior to the engineering applications on the rock ground, certain properties of rock mass and intact rock should be assessed to predict the performance of the rock ground in the as build condition.

Unlike the loose grounds, the properties of the rock can be categorized into two classes (a) material properties of the rock (b) properties of the intact rock including the discontinuities. Rock material properties plays an important role in the assessment of degradability of intact rock mass such as rock type, texture, strength, hardness, cavities, particle size. Although the material properties govern some fraction on the strength and mechanical behavior of rock mass, the overall behavior is highly controlled by geological nature of the intact rock mass. Discontinuities are the main cause for the strength reduction and instability of intact rock, also it highly contributes for the weathering or degradation. Spacing between subsequent discontinuities or the number of discontinuities in a given volume of rock mass mainly controls the strength and stability.

Material properties take a major role in controlling the strength and stability of rock mass where the existence of the discontinuities less. On the other hand, the strongest intact rock material can lose the strength and stability due to closely spaced discontinuities, even though the core samples exhibit good mechanical properties in the laboratory testing, in these situations the material properties cannot control the behavior of the intact rock. There for the evaluation of the geological conditions and proper engineering judgment are essential requirements in case of the constructions on rock grounds. Always the strength and stiffness of the intact rock mass expected to be smaller than that of core samples due to the existence of unforeseen discontinuities and cavities, therefore the application of appropriate safety factors also another mandatory requirement in the design process.

Engineering classification of rock materials can be discussed under two main classes

(1) Rock material properties

- Principal rock type
- Mineralogy
- Primary porosity
- Hardness and unconfined compressive strength
- Dry unit weight
- Color
- Particle size

(2) Rock mass properties

- Permeability
- Consolidation
- Rock texture
- Shearing resistance
- Rock structure
- Attitude
- Discontinuities

2.4.2.1 Hardness and Unconfined compressive strength of rock material

Hardness and unconfined compressive strengths are the qualitative description of the rock material, hardness or the strength of rock material simply defined by the ability to resist the induced deformation by external forces. Unconfined compressive strength is the standard strength parameter for the intact rock material. ASTM D653 definition of uniaxial compressive strength of a material is given as the amount of applied stress at failure. There are several factors influencing the strength of intact rock such as mineral compositions, grain size and shape, lamination and stratification. Apart from these factors, secondary process of weathering and cementation highly influence the strength of intact rock mass.

Cementation of rock mass mainly caused by the primary bonding components such as silica, calcium carbonate, clay minerals and iron oxides. Durability of the bonds caused by clay minerals are very weak especially in case of saturated condition but the ones caused by silica is the most durable among these bonding components. Therefore, the mineral composition and the nature of cementing materials also should be taken in to account for the engineering classification of rock mass. Engineering classification of rock type is similar to the geological

Table 2-5 Hardness and unconfined compressive strength of rock materials in engineering classification (USDA-NRCS, 2012)

Hardness category	Typical range in unconfined compressive strength (MPa)	Field test on sample
Soil	< 0.60	
Very soft rock or hard soil	0.60–1.25	Scratched with fingernail. Slight indentation by light blow of point of geologic pick. Requires power tools for excavation. Peels with pocketknife.
Soft rock	1.25–5.0	Permits denting by moderate pressure of the fingers. Handheld specimen crumbles under firm blows with point of geologic pick.

Moderately soft rock	5.0–12.5	Shallow indentations (1–3 mm) by firm blows with point of geologic pick. Peels with difficulty with pocketknife. Resists denting by the fingers, but can be abraded and pierced to a shallow depth by a pencil point. Crumbles by rubbing with fingers.
Moderately hard rock	12.5–50	Cannot be scraped or peeled with pocketknife. Intact handheld specimen breaks with single blow of geologic hammer. Can be distinctly scratched with 20d common steel nail. Resists a pencil point, but can be scratched and cut with a knife blade.
Hard rock	50–100	Handheld specimen requires more than one hammer blow to break it. Can be faintly scratched with 20d common steel nail. Resistant to abrasion or cutting by a knife blade, but can be easily dented or broken by light blows of a hammer.
Very hard rock	100–250	Specimen breaks only by repeated, heavy blows with geologic hammer. Cannot be scratched with 20d common steel nail.
Extremely hard rock	> 250	Specimen can only be chipped, not broken by repeated, heavy blows of geologic hammer.

Classification based on the structure, composition, grain size and the genetic category. Although the geological classification and geologic names are not related with the engineering properties it can be utilized to predict the unforeseeable structural discontinuities and for some correlation purposes. Not only the rock material properties, but rock mass properties also governs major role in the design of civil engineering structures. Permeability, consolidation, shearing resistance and the discontinuities of the rock mass should be widely investigated in a construction site prior to the design and construction activities.

2.4.2.2 Permeability of rock mass

Figure 2.44 described in USDA NRCS illustrates the permeability of different type of rocks and soils in a wide range from 10^{-9} to 10^{5}. Permeability of rock mass may vary based on material properties and the existence of discontinuities. Which implies that a low porosity rock mass can have high permeability based on the fractures and joints, discontinuities are not specific features of rock types which can exist in any type of rock, it can be classified as “stratigraphic” and “structural discontinuities”. Stratigraphic discontinuities are mostly occurred by deposition or erosion of the sediment layers this kind of discontinuities are common in stratified sedimentary rocks, low grade metamorphic rocks and most of the volcanic flows. Structural discontinuities are caused by the mechanical deformation of the rock mass due to naturally occurring stress change and energy dissipation with in the earth’s crust.

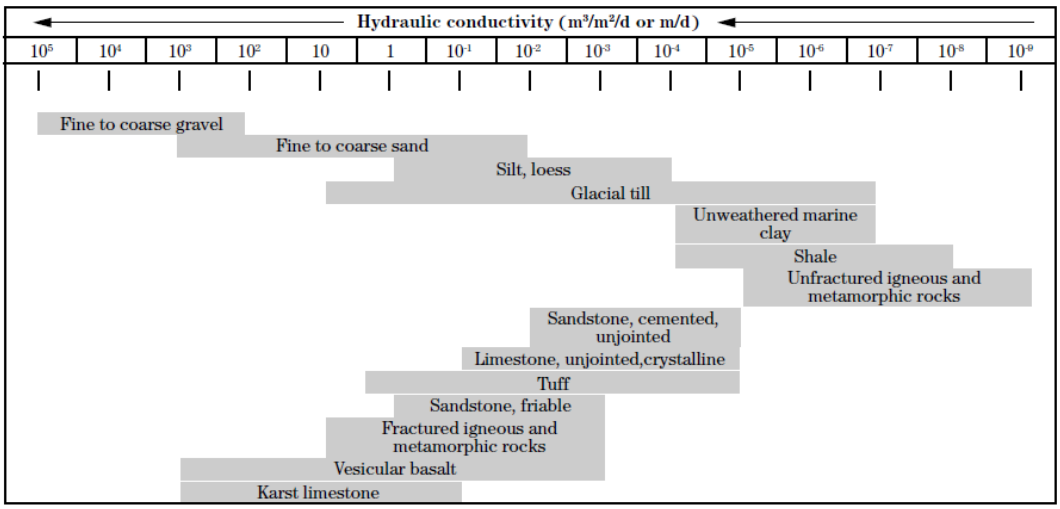

Figure 2.44 Permeability of different soils and rocks (USDA NRCS.,2012)

2.4.2.3 Weathering and consolidation of rock mass

Consolidation of rock mass is a long-term problem generally caused by the combination of physical and chemical weathering of rock masses. Initiating from the surface deterioration until the decomposition of the rock mass, rate and type of rock weathering controlled by several factors such as time ,climate change, physical and chemical composition of the rock mass, topography, etc. Weathering of rock mass with time is a long-term critical problem in civil engineering associated with most of the sedimentary rocks. Especially in weakly cemented sandstone, siltstone and shale type of rocks can be easily altered in to clay minerals and subsequently it may cause the problems associated with consolidation and bearing capacity. Therefore, in these kind of situations proper site investigation and sampling for laboratory studies should be done to implement remedial measures.

2.4.2.4 Rock structure

Rock structure is an important rock mass property in rock engineering, which highly influence on the geological conditions of a considered site for the construction, safety and the stability of the engineered structure. The rock structure can consist different unfavourable features such as joints, holes, bedding planes, cavities, fractures etc. These features can cause high permeability or problems related to leakage, sliding of rock mass, differential settlements and shear failure along the weak planes as described in the case of formation of shear bands subchapter 2.2.2.2. Shear resistance of rock mass is highly desirable property of rock mass, which has been utilized in several civil engineering projects all over the world. Poorly cemented rock materials often exhibits low shear strength and capacity can further reduced by saturation. Not only the material properties but "**adverse dipping"** of the rock mass also highly influence on the shear capacity of the rock mass. Therefore, the application of appropriate safety factors in the design and proper site investigation about the rock structure are essential requirements in order to overcome the shear failure of engineered structures in rock ground.

2.5 Significance and advantage of centrifuge modelling

Confining stresses similar to the real field and corresponding stiffness of interested medium or ground and be modelled in a small container at higher centrifugal accelerations. Thereby the

identical shear strain mobilization compare to the real field could be modelled in a sophisticated manner.

- Geotechnical problems associated with long durations; such as consolidation or diffusion could be studied in a short duration at high “g” environment.
- Possible deformation mechanism of geotechnical structures and the real failure mode and the investigations associated to the soil-structure interactions can be studied.
- Cost effective solution compare to the real field investigations of more complicated phenomena.
- 3 dimensional behavior of complicated soil structure interaction problems could be untangled with reasonable cost compare to the real field investigations.
- Dynamic behavior of an interested structure can be studied under desired ground excitation. Which is impossible to model in real field except some of the large shake tables in the world.

2.6 Principles of geotechnical centrifuge modelling

2.6.1 Stress similarity concept between model and prototype

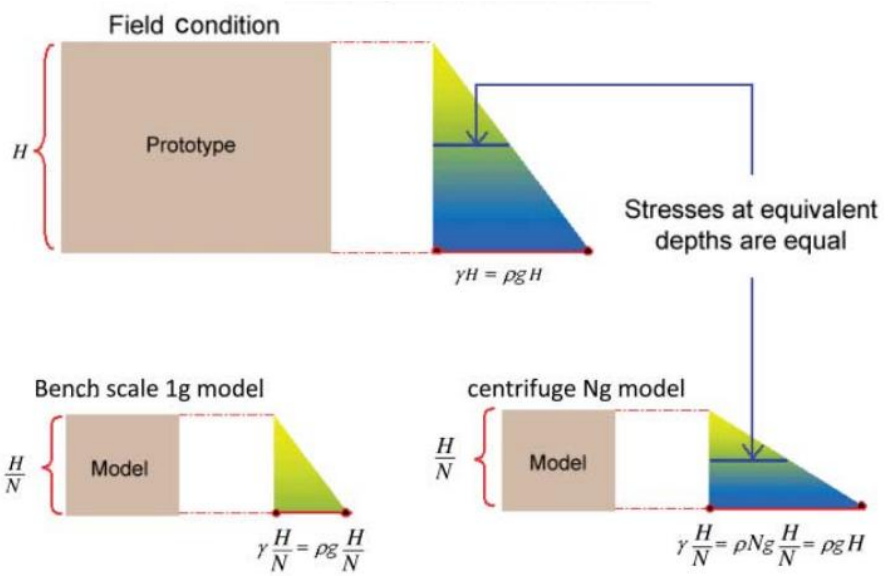

Figure 2.45 Stress similarity between model and prototype (Shamy_et_al, 2013)

2.6.2 Scaling law

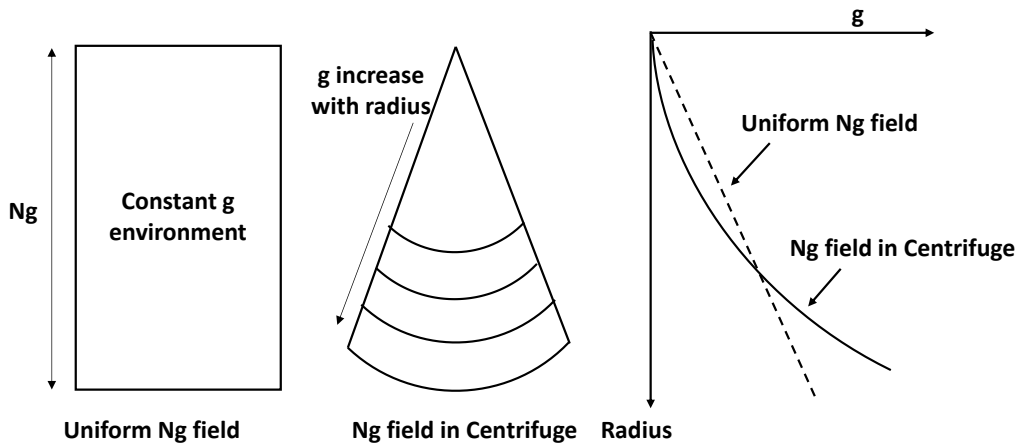

Figure 2.46 Variation of centrifugal acceleration with radius (Schofield, 1980)

Table 2-6 Centrifuge scaling laws

Parameter	Units	Ratio of model to prototype
Length	m	1/N
Area	m^2	$1/N^2$
Density	kg/m^3	1
Velocity	m/s	1
Acceleration	m/s^2	N
Stress	N/m^2	1
Strain	-	1
Force	N	$1/N^2$
Bending moment	Nm	$1/N^3$
Time(dynamic)	s	1/N
Time(consolidation)	s	$1/N^2$

The scaling laws described by (Schofield, 1980) for dynamic centrifuge modelling is summarized in **Table 2-6**. The main principle in centrifuge modelling is that a 1/N scale model placed at the end of a centrifuge arm subjected to a centrifugal acceleration of N g will feel the same stresses as the prototype. For instance, if a ground surface of 50 m depth has to be modelled the 1 m deep model container is filled with soil, placed on the end of a centrifuge and subject to a centrifugal acceleration of 50 g. The pressures and stresses are increased by a factor of 50. Therefore, the vertical stress at the base of the model container is equivalent to the vertical stress at a depth of 50 m below the ground surface on earth. Thus, the 1 m deep model represents 50 m of prototype soil. The reason for the centrifuge is to enable small-scale models to feel the same stresses as a full scale prototype. Even though the model studies are more beneficial to study the behavior of prototype, the accuracy of the model study depends on the size of the model and the spinning radius of the centrifuge. Unlike the earth's gravity field, in centrifuge the centrifugal acceleration increases with the increase of the radius therefore maintaining the same centrifugal acceleration throughout the model is impossible. The differences between the constant g environment and the parabolic distribution of the centrifugal acceleration are shown in **Figure 2.46** by maintaining the centre of gravity of the model at the intersection radius of both distributions the effects on the models studies could be minimized.

2.6.3 TIT MARK-III centrifuge

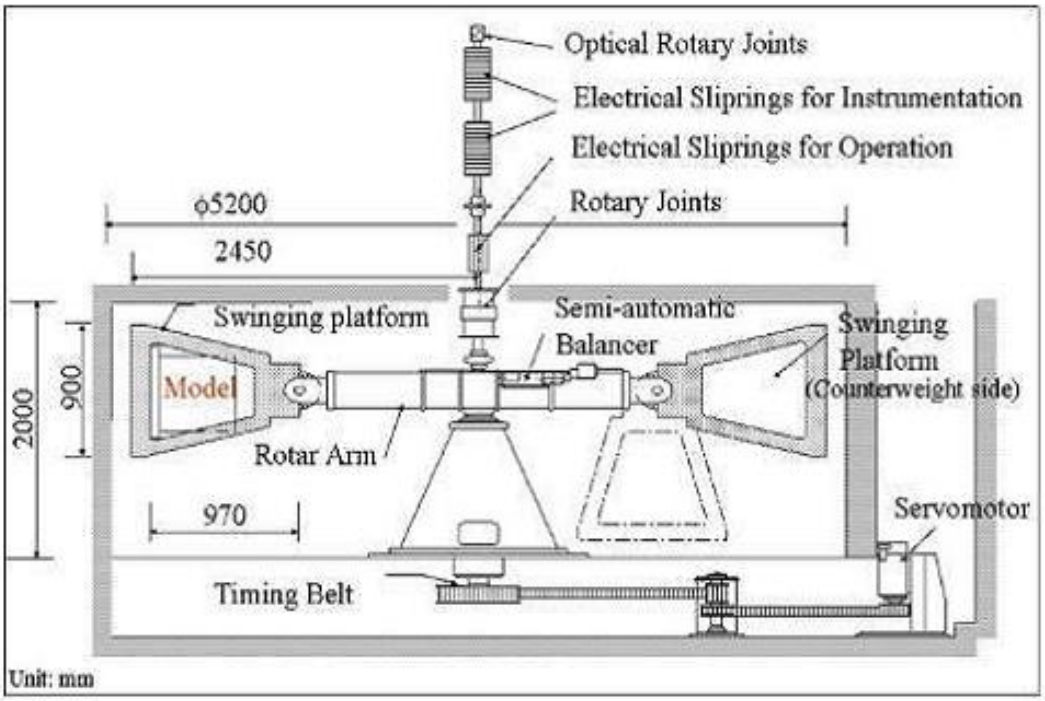

Figure 2.47 TIT-MARK-III Centrifuge

The Tokyo Tech Mark III centrifuge is a beam type centrifuge having a pair of parallel arms which hold platforms, one platform contains the model container and the opposite platform used to carry the weight for counterbalance as shown in **Figure 2.47**. According to Takemura et al.(1999), TIT Mark III Centrifuge was installed at soil mechanics laboratory of Tokyo Institute of Technology in 1995.The radius of rotation is 2.45 m, which is the distance from the rotating shaft to the platform base. The surface of the swinging platform is always normal to the resultant of the centrifugal acceleration. Specifications of the centrifuge are summarized in **Table 2-7**. For data acquisition, two types of signal transmission methods are used. One is

classical electrical slip rings. Transducers are connected to the slip rings through a junction box and signals are transferred to amplifiers on the laboratory floor. The other type is an optical rotary joint. Transducers are connected to signal conditioners on the centrifuge. Analog signals from the transducers are amplified there and then are converted to digital signals by A/D converters. Gains and the other conditions of the signal conditioners can be controlled by a PC on the lab floor. The digital signals are transferred to the PC on the lab floor through the optical rotary joint. A hydraulic rotary joint with maximum pressure of 20.5MPa mounted on the centrifuge is used for charging and discharging oil to the centrifuge during spinning of the centrifuge. A big hydraulic accumulator is mounted on the centrifuge to satisfy the required flow rate of the pressurized oil for the high performance 1D shaker

Table 2-7 Specifications of TIT-MARK-III Centrifuge

Radius	Platform radius	2.45m
	Effective radius	2.0-2.2m
Platform dimensions	Width	0.9m
	Depth	0.9m
	Maximum height	0.97m
Capacity	Maximum payload	50g.ton
	Maximum number of rotation	300rpm
	Maximum pay load at 80g	600kg
Electrical slip rings	For instrumentation	72 channels
	For operation	20 channels
Rotary joint	Working pressure for water and air	1MPa
	Working pressure for oil	21MPa
	Wireless LAN	64 channels

2.7 Summary

In this chapter intensive literature review has been made on the related topics of the research. Also the basic of centrifuge modelling is summarised.

2.8 References

R ArcelorMittal, 2008. Piling Handbook, 8th ed, ArcelorMittal, Esch-sur-Alzette, Luxembourg, Installation of sheet piles. Ch-11, pp.284-337.

Atkinson, J.H. and Bransby, P.L., 1977. The mechanics of soils, an introduction to critical state soil mechanics (No. Monograph)

Bica, A.V.D. and Clayton, C.R.I., 1998. An experimental study of the behavior of embedded lengths of cantilever walls. Geotechnique, 48(6), pp.731-745.

Bolton, M.D. and Powrie, W., 1987. The collapse of diaphragm walls retaining clay. Geotechnique, 37(3), pp.335-353.

Bolton, M.D. and Powrie, W., 1988. Behavior of diaphragm walls in clay prior to collapse. Géotechnique, 38(2), pp.167-189.

Bransby, P.L. and Milligan, G.W.E., 1975. Soil deformations near cantilever sheet pile walls. Geotechnique, 25(2), pp.175-195.

Broms, B. B. ,1964a. Lateral Resistance of Piles in Cohesive Soils, Journal of SMFED, Proc. ASCE, No. SM2, pp. 27-63.

Broms, B. B., 1964b. Lateral Resistance of Piles in Cohesionless Soils, Journal of SMFED, Proc. ASCE, No. SM3, pp. 123-156

BS8002, B.S., 1994. British Standards Institution, Code of practice for earth retaining structures.

Carter, J.P. and Kulhawy, F.H., 1992. Analysis of laterally loaded shafts in rock. Journal of Geotechnical Engineering, 118(6), pp.839-855.

Chen, J.J., Zeng, F.Y., Wang, J.H. and Zhang, L., 2017. Analysis of laterally loaded rock-socketed shafts considering the nonlinear behavior of both the soil/rock mass and the shaft. Journal of Geotechnical and Geoenvironmental Engineering, 143(3), p.06016025.

CIRIA 104 (1984) Embedded retaining walls in stiff clay

CIRIA C580 (2003) Embeded retaining walls- guidance for economic design

D'Andrea, R. and Day, R.W., 1998. Discussion and Closure: Design and Construction of Cantilevered Retaining Walls. Practice Periodical on Structural Design and Construction, 3(2), pp.87-88.

Day, R.W., 1997. Design and Construction of Cantilevered Retaining Walls. Practice Periodical on Structural Design and Construction, 2(1), pp.16-21

El Shamy, U., Abdoun, T., McMartin, F. and Pando, M.A., 2013. Integration of centrifuge testing in undergraduate geotechnical engineering education at remote campuses. European Journal of Engineering Education, 38(3), pp.268-280.

Fukushima, S. and Tatsuoka, F., 1984. Strength and deformation characteristics of saturated sand at extremely low pressures. Soils and Foundations, 24(4), pp.30-48.

GEOCEDHG(Geotechical Engineering Office, Civil Engineering Department, Hong Kong, 1993. Geoguide1 " Guide to Retaining Wall Design".

Hardin, B.O. and Richart, F.E, 1963. Elastic wave velocities in granular soils. Jounal of SMFD, ASCE, 89 (1), pp. 33-65.

International Press-in Association (IPA), 2016. Press-in retaining structure: a handbook, 1st ed.

Iwasaki, T. and Tatsuoka, F., 1977. Effects of grain size and grading on dynamic shear moduli of sand, Soils and Foundations, 18(1), pp.19-35.

Iwasaki, T. and Tatsuoka, F. Takagi, Y., 1978. Shear moduli of sands under cyclic torsional shear loading, Soils and Foundations, 17(3), pp.19-35.

Kanji, M.A., 2014. Critical issues in soft rocks. Journal of Rock Mechanics and Geotechnical Engineering, 6(3), pp.186-195.

Kimura,T., Takemura,J., Hiro-oka,A., Suemasa,N.and Kouda,N., (1993) Stability of unsupported and supported vertical cuts in soft clay. Proceedings of the 11th SEAGC, Singapore, pp. 61–70.

Lam, S.Y., Elshafie, M.Z., Haigh, S.K. and Bolton, M.D., 2012. A new apparatus for modelling excavations. International Journal of Physical Modelling in Geotechnics, 12(1), pp. 24-38.

Leung, C.F., Ong, D.E. and Chow, Y.K., 2006. Pile behavior due to excavation-induced soil movement in clay. II: Collapsed wall. Journal of Geotechnical and Geoenvironmental Engineering, 132(1), pp.45-53.

Long, M., 2001. Database for retaining wall and ground movements due to deep excavations. Journal of Geotechnical and Geoenvironmental Engineering, 127(3), pp.203-224.

Lyndon, A. and Schofield, A.N., 1970. Centrifugal model test of a short-term failure in London clay. Geotechnique, 20(4), pp.440-442.

Miyanohara,T., Kurosawa,T., Harata,N., Kitamura,K., Suzuki,N. and Kajino,K., 2018. Overview of the Self-standing and High Stiffness Tubular Pile Walls in Japan, Proceedings of the 1st International Conference on Press-in Engineering 2018, Kochi, Japan,pp.167-174.

Ong, D.E., Leung, C.E. and Chow, Y.K., 2006. Pile behavior due to excavation-induced soil movement in clay. I: Stable wall. Journal of Geotechnical and Geoenvironmental Engineering, 132(1), pp.36-44.

Ou, C.Y., Hsieh, P.G. and Chiou, D.C., 1993. Characteristics of ground surface settlement during excavation. Canadian Geotechnical Journal, 30(5), pp.758-767.

Padfield, C.J. and Mair, R.J., 1984. The design of propped cantilever walls embedded in stiff clays. CIRIA Rep, 104.

Randolph, M.F., 1981. The response of flexible piles to lateral loading. Geotechnique, 31(2), pp.247-259.

Reese, L.C., 1997. Analysis of laterally loaded piles in weak rock. Journal of Geotechnical and Geoenvironmental Engineering, 123(11), pp.1010-1017.

Richards, D.J., Clayton, C.R.I., Powrie, W. and Hayward, T., 2004. Geotechnical analysis of a retaining wall in weak rock. Proceedings of the Institution of Civil Engineers-Geotechnical Engineering, 157(1), pp.13-26.

Saratsis, G. and Stavropoulou, M. 2013. São Paulo cavern-shaft collapse viewed as a trap-door problem. Bulletin of the Geological Society of Greece, 47(3), 1864-1871.

Schofield, A.N., 1980. Cambridge geotechnical centrifuge operations. Geotechnique, 30(3), pp.227-268.

Silver, M. L. and Seed, H.B., 1971. Deformation characteristics of sand under cyclic loading. Journal of SMFD, ASCE, 97 (()), pp. 1081-1098.

Suzuki,N. and Kajino,K.,2018. Issues for the Reduction of the Embedded Length of Cantilevered Steel Tubular Retaining Wall Pressed into Stiff Ground, Proceedings of the 1st International Conference on Press-in Engineering 2018, Kochi, Japan,pp.159-166.

Takemura, J., Kondoh, M., Esaki, T., Kouda, M. and Kusakabe, O., 1999. Centrifuge model tests on double propped wall excavation in soft clay. Soils and Foundations, 39(3), pp.75-87.

USDA-NRCS, United State Department of Agriculture, Natural Resource Conservation Service, 2012. National Engineering Handbook. Engineering Classification of Rock Materials. Part 631.Ch- 4. (210–VI–NEH, Amend. 55, January 2012).

Whittle, A.J. and Davies, R.V., 2006, June. Nicoll Highway Collapse: Evaluation of Geotechnical Factors Affecting Design of Excavation Support System. International Conference on Deep Excavations, Singapore, 16p.

3 Simplified Centrifuge Modelling of Cantilever High Stiffness Retaining Walls Embedded in Soft Rock

3.1 Introduction

Over the past decades, extensive investigations based on physical modelling of excavation on a cantilever and propped walls (Padfield and Mair,1984 ;Richards and Poweri,1998) embedded in clays and sandy soils have been contributed to the development of design codes and the calibration of numerical models as summarized in Table 2.2. Also the observations from numerous case histories (Long, 2001; Ou et al., 1993) related to the real field applications in a vast range of soil conditions and the failure of earth retaining structures (Day and Andrea, 1998; Whittle and Davies, 2006) oftentimes revised the codes for the safe and economic design of retaining structures in sand and clays.

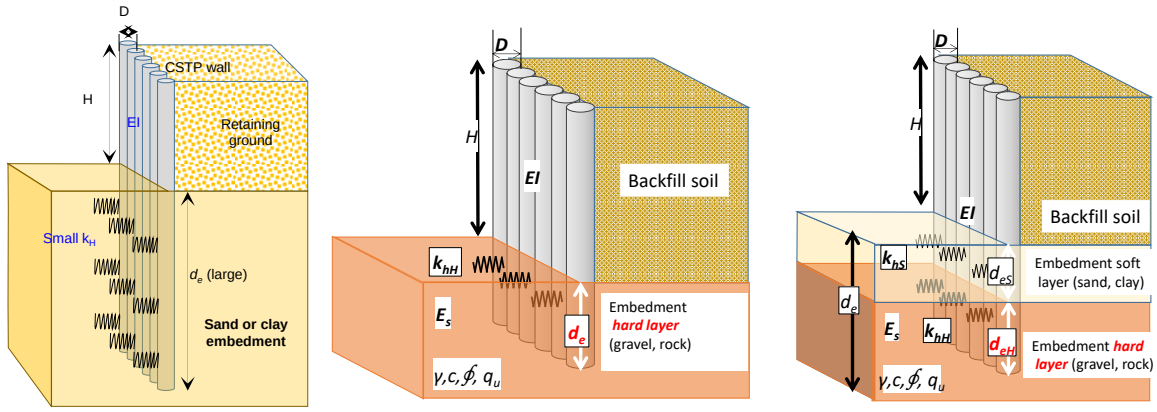

(a) (b) (c)

Figure 3.1 Self standing retaining walls embedded in (a) soft and (b,c) hard mediums

However the available literatures (Richards et al., 2004) based on physical models or the real field experiments to illustrate the behavior of self-standing walls embedded in soft rocks are extremely rear. Perhaps it might be attributed to the difficulties in the installation and creating the failure of such large retaining structures in the real field or the difficulties in the undisturbed sampling of soft rock grounds with required dimensions for the centrifuge models. Instead of retaining walls, few studies on the behavior of rock socketed single shafts (Carter et al.,1992; Reese,1997; Chen et al.,2017) and laterally loaded single piles (Kunasegaram et al.,2018) illustrates the individual behavior of shafts or piles.

Applications of cantilever type sheet pile walls are limited to medium to moderate retained height of earth (Madabhushi and Chandrasekaran, 2005) in relatively soft mediums. The limitations in the application of walls with large retain height are twofold, firstly the deformations induced by the flexibility of the wall, which increases with the retained height of earth. Secondly the compliant nature of soft medium requires large deformation to mobilize the passive resistance. Although the former deformation mechanism can be conquered with the use of high stiffness walls; such as self-standing steel tubular pile (SSTP) walls or reinforced concrete walls, the latter requires relatively large embedment depths as shown on Figure 3.1 Self standing retaining walls embedded in (a) soft and (b,c) hard mediums(a) to control the wall deformations within the allowable limits in soft ground. This requirement is economically non-feasible (Powrie, 1996). Thanks to the high strength and stiffness of relatively hard mediums such as soft to hard rocks, the both deformation mechanisms can be untangled by the use of SSTP walls with relatively small embedment depths as illustrated in Figure 3.1(b). For

the application of these SSTP walls in to relatively hard mediums no specific design guidelines are available up to date. Perhaps it might not be a concern of engineers due to the difficulties in the installation of high stiff steel tubular piles in to relatively hard mediums and the lack of technology advancement in the past.

However, currently available Japanese technology could penetrate the large diameter steel tubular piles even in to hard rocks by using combined auguring and silent pressing technique and the length of tubular piles can be extended by means of onsite butt welding (ArcelorMittal, 2008). Thanks to the high flexural rigidities of large diameter piles and sound lateral confinement of relatively hard embedment mediums, number of taller SSTP walls have been constructed in Japan. Where certain traffic, residential and cultural restrictions have been encountered (Miyanohara et al.,2018).

Although the innovative technology is available to construct relatively taller (12-15m) SSTP walls with high flexural rigidities even in hard rocks, owing to the absence of specific guidelines for the design of large diameter SSTP walls in relatively hard mediums, the design of abovementioned walls have been carried out (Suzuki et al.,2018) based on the theory of beams on elastic foundation (ASP,2009). Attributing to the major drawbacks of this design method for the application of large diameter SSTP walls, the required minimum embedment depth (de) increases with the flexural stiffness of the wall (EI) regardless of the applied lateral loads or independent to the retained height of earth. This phenomenon might yield relatively large embedment depth requirements even in relatively hard mediums (soft to hard rocks), which might be an overestimation of embedment depth since it based on the allowable deformation of the wall regardless of the stability.

Owing to the requirement of relatively large embedment depth even in hard mediums, the application of large diameter piles are often eliminated from the industry attributing to the additional construction costs induced by onsite butt welding to extend the length and installation of larger embedment depths. Therefore, if a specific design method can be proposed for the application of large diameter SSTP walls in relatively hard mediums and the embedment depth can be optimized, which could enhance the applicability and reduce the construction time and cost.

For the development of a new design method and an optimized embedment depth smaller than the one determined by the current design practice, both the survivability and ultimate limits should be reasonably examined in the design. In other words, the design condition should secure allowable displacement by a reasonable evaluation method and the extra margin of safety over the ultimate loading condition must be confirmed to prevent the catastrophic failure. Therefore, the process from the design conditions to the failure should be well studied by physical means, such as a physical modelling. In this research, a centrifuge modelling technique on a simplified SSTP wall embedded in soft rock has been developed, by which a design loading condition and the failure of the wall can be simulated in a sequential manner under a constant centrifugal acceleration.

3.2 Modelling of soft rocks for experimental investigations

Mechanical properties of soft rocks can vary based on the composition of primary bonding components (silica, calcium carbonate, clay minerals etc...), which enhance the performance of cementation. Since the strength and stiffness of the rock materials highly influenced by the degree of cementation and the mineral composition, therefore it is important to study the effects of mineral composition and the degree of cementation on the mechanical properties of artificial soft rocks in order to model the soft rocks with required strength and stiffness for centrifuge studies.

Strength of natural soft rocks vary in a wide range from 0.6 MPa to 5 MPa according to engineering classification (USDA, NRCS., 2012). Synthetic soft rocks modelled by researchers in the past also lies either in this range or closer to the upper or lower limits of soft rocks. Johnston and Choi (1986) modelled a synthetic soft rock using the powder of natural mudstone. The natural mudstone powder was prepared throughout several controlled processes and crushing. In the modelling of soft rock, they adopted a cement content of 2.5% by weight based

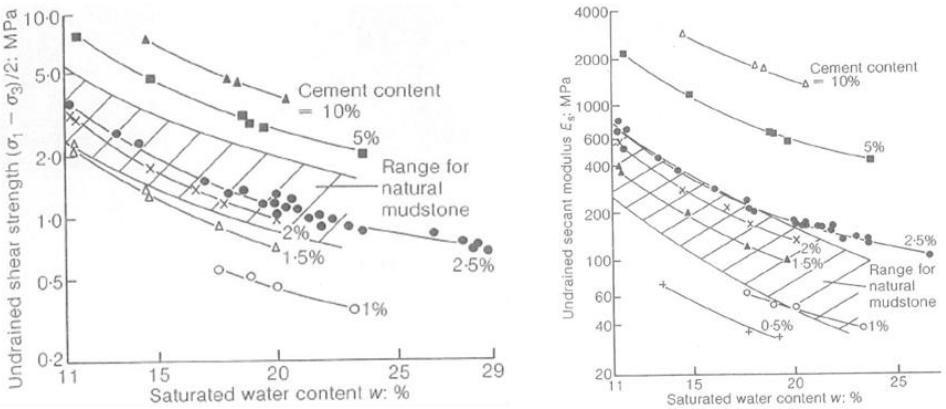

Figure 3.2 Relation between mechanical properties and water content for synthetic and natural rocks Johnston and Choi (1986)

on trial and error procedure with different cement contents above and below this limit. From the experience of Johnston and Choi (1986), model soft rocks prepared at a cement content of 2% or lesser was collapsed during vacuum saturation in a desiccator. Variation of undrained shear strength and undrained secant stiffness at different water contents and cement contents are given in Johnston and Choi (1986) as shown in Figure 3.2. From the observations the undrained shear strength of their model soft rock lies in the range of natural mudstone and the undrained secant stiffness is closer to the upper limit of natural mudstone.

Indraratna (1990) developed a synthetic soft rock to simulate the behavior of soft sedimentary rocks. The rock was modelled by Hydrocal white gypsum cement (10% by weight), fine uniform sand (75.8% by weight), anhydrous sodium phosphate (0.05% by weight), and water (14.15% by weight). Observed uniaxial compressive strength (3 - 4 MPa) and elastic modulus (1350 - 1550 MPa) of model soft rocks in Indraratna (1990) are closer to the upper boundary of soft rocks according engineering classification (USDA, NRCS., 2012).

3.2.1 Materials

In this research, two different soft rocks namely sand rock and mud rock were modelled by changing the material composition and the water cement ratio. Soft sand rock was modelled by using Toyoura sand, semi clay and early hardening Portland cement at different water cement ratios and clay-sand contents under a constant moisture content. Similarly, the soft mud rock also was modelled by using semi clay and early hardening Portland cement by changing the water cement ratios and two different moisture contents. Required moisture contents for sand and mud rocks were roughly estimated by considering the liquid limit of clay and the clay sand fraction of the mixture to achieve fully saturated mix. Altogether 168 cylindrical specimens were prepared from 14 different batches of sand-clay-cement and clay-cement mixes to study the mechanical properties of artificially made sand and mud rocks. Similar mixing procedures were maintained throughout the all batch mixes and the details of the mixing ratios are presented in Table 3-1 and Table 3-2. Here Table 3-1 and Table 3-2 are based on dry weights of sand, clay and cement.

Table 3-1 Mixing conditions of artificial sand rock

Mix number	Water-Cement ratio (%)	Clay-Sand content	Water content (%)	Bulk density (g/cm^3)
1	300	20:80	20	2.10-2.11
2	330	20:80	20	2.06-2.09
3	250	30:70	17	2.11-2.15
4	330	30:70	20	2.03-2.10
5	370	30:70	20	2.09-2.10
6	440	30:70	20	2.08-2.10
7	330	40:60	20	2.06-2.09

Table 3-2Mixing conditions of artificial mud rock

Mix number	Water-Cement ratio (%)	Clay-Sand content	Water content (%)	Bulk density (g/cm^3)
1	270	100:0	45	1.79-1.80
2	330	100:0	45	1.80-1.81
3	390	100:0	45	1.79-1.80
4	330	100:0	39	1.86-1.87
5	390	100:0	39	1.85-1.86
6	450	100:0	39	1.84-1.86
7	510	100:0	39	1.85-1.86

3.2.1.1 Toyoura sand

In the abovementioned type of artificial soft rocks, the main component of the soft sand rock is Toyoura sand which is about 55% by weight. Figure 3.3 describes the components of the soft sand rock, from which the reader can understand the appearance or texture of the Toyoura sand and used Semi clay. Besides the appearance the grain sixe distribution and physical properties of Toyoura sand is shown in Figure 3.4, which is a uniformly graded material with zero fine content which can be confirmed by referring the Figure 3.4.

3.2.1.2 Sumi clay

Figure 3.3 Material used for the modelling of artificial soft rock

Sumi clay used in this study was a factory processed one in Japan, having the specific gravity (G_s) of 2.67, liquid limit (LL) of =34% and plastic limit (PL) of 19%. Plasticity index of the semi clay was estimated as 15% based on the difference of liquid limit and plastic limit. From which it can be confirmed that the swelling potential of this clay is low and it can be considered as a normal clay.

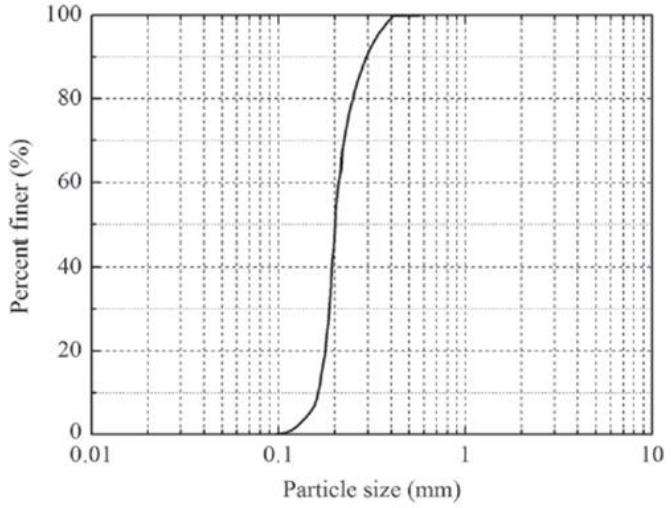

(Dong et al. 2015)

Sand	Toyoura sand (Fukushima and Tatsuoka1984)
Specific gravity of particles (G_s)	2.64
Minimum void ratio (e_{min})	0.605
Maximum void ratio (e_{max})	0.977
Average grain size (d_{50})	0.16
Coefficient of uniformity (C_u)	1.46

Figure 3.4 Grain size distribution and physical properties of Toyoura sand

The above mentioned liquid limit of the clay was estimated through cone penetration test conducted at different moisture contents of Sumi-clay. The results are illustrated in Figure 3.5.From Figure 3.5 the liquid limit of the Sumi-clay can be estimated corresponding to 20 mm penetration of the cone.

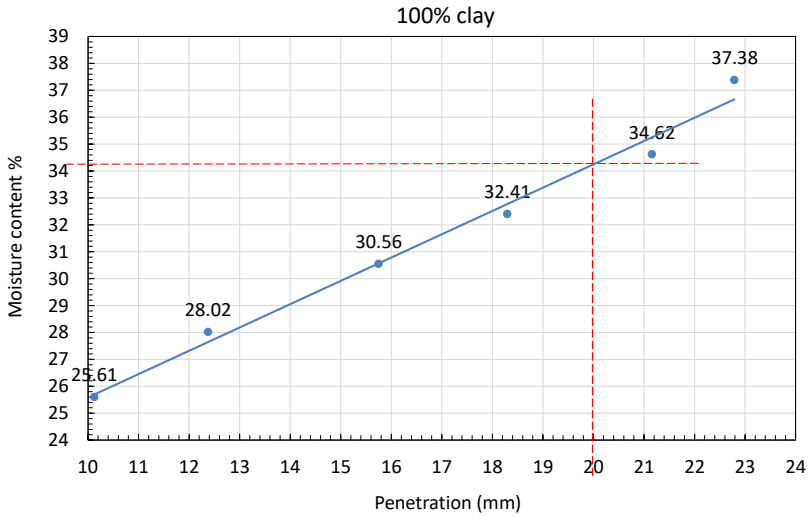

Figure 3.5 Results of cone-penetration test conducted by using Sumi-clay used in this study

Sumi clay is an artificial clay made by Sumitomo Osaka Cement Co., Ltd., the particle size distribution of Sumi clay and the inorganic components in the clay are given in Figure 3.6. From Figure 3.6 it can be observed that the mean particle size of the clay is 6.3μm and the major components of the clay is SiO_2, meanwhile the combination of Al_2O_3 and Fe_2O_3 deserves about 20% of the volume fraction.

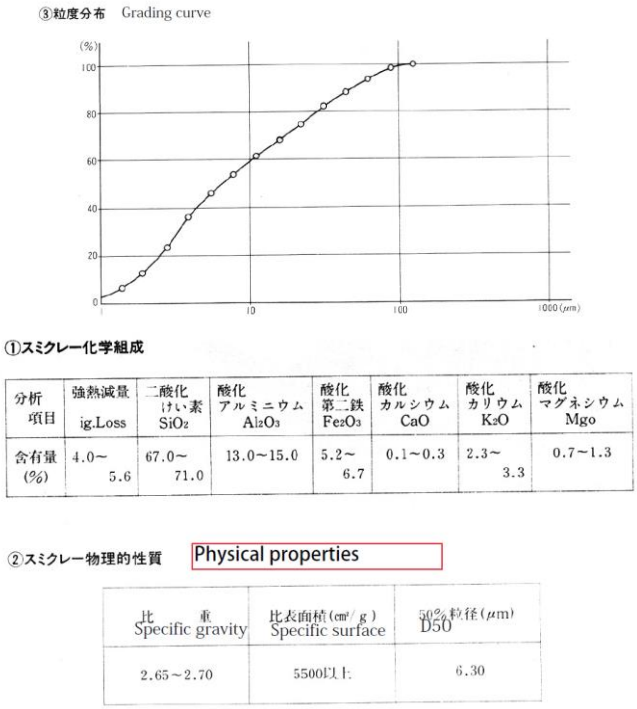

③粒度分布 Grading curve

①スミクレー化学組成

分析項目	強熱減量 ig.Loss	二酸化けい素 SiO_2	酸化アルミニウム Al_2O_3	酸化第二鉄 Fe_2O_3	酸化カルシウム CaO	酸化カリウム K_2O	酸化マグネシウム Mgo
含有量 (%)	4.0～5.6	67.0～71.0	13.0～15.0	5.2～6.7	0.1～0.3	2.3～3.3	0.7～1.3

②スミクレー物理的性質 Physical properties

比重 Specific gravity	比表面積 (cm²/g) Specific surface	50%粒径 (μm) D50
2.65～2.70	5500以上	6.30

Figure 3.6 Grading curve and % fraction components of Sumi clay

3.2.1.3 Portland cement

In this study early-strength Portland cement (G_s=3.14) was used to prepare the specimens which was manufactured by Taiheiyo Cement. The photo of used cement and the Sumi-clay are given in Figure 3.7.

Figure 3.7 Photo of used Taiheiyo cement and Sumi-clay

3.2.2 Calculation of required materials and modifications for the existing moisture

In order to explain the calculation process of each material in a specific mixing combination in this sub chapter the following mixing condition is described. Which is the combination of soft sand rock modelled for the centrifuge study. It is important to emphasize that the densities of water, cement, clay and sand are 1000kg/m^3, 3140kg/m^3, 2670kg/m^3 and 2600kg/m^3 respectively.

- Mixing conditions

$$\frac{water}{cement} = 395\%\ by\ weight$$

$$\frac{Clay}{Sand} = 30:70\ \ by\ weight$$

$$Moisture\ content\ = 21.5\%$$

$Required\ volume\ of\ mix\ = 28\ Litre$ (Including 20% extra volume to avoid the lack of material in case of any accident or scarcity of the mix due to unexpected causes. Required Volume includes the mix for centrifuge model and the test specimens)

- Equations to estimate the dry weights of each component

$$Water = 3.95\ Cement$$ .....equation 3.1

$$Clay = \frac{3}{7}Sand$$.....equation 3.2

$$\frac{Water}{Clay+Sand+Cement} = 0.215$$.....equation 3.3

$$\frac{28}{1000} = \frac{Water}{1000} + \frac{Cement}{3140} + \frac{Clay}{2670} + \frac{Sand}{2600}$$.....equation 3.4

Using the above mentioned four equations unknown weights of clay, cement, sand and water can be estimated. Calculated dry weights are given below.

$Cement \ = 2.569 \ kg$

$Sand \ = 31.245 \ kg$

$Clay \ = 13.391 \ kg$

$Water \ = 10.149 \ kg$

In reality it is impossible to get the dry condition of these materials since these absorb certain amount of moisture from the environment. Therefore prior to the mixing it is important to estimate the existing moisture content of clay, sand. From the experience of writer, the measured moisture content of Toyoura sand used in this study is negligible as its purchased state. However, Semi clay poses about 1.4% - 2% moisture content depending on the weather and preserved conditions. In order to model the mix with exact or closer to the target water cement ratio it is important to do the correction for existing moisture as follows.

- Correction for existing moisture in clay

Assume that the existing moisture content of clay is 1.7% then,

$$\frac{100}{101.7} * Bulk\ weight\ of\ caly = 13.391 \ kg$$

$$Bulk\ weight\ of\ caly = 13.618 \ kg$$

$$Moisture\ contribution\ from\ clay \ = \frac{1.7}{101.7} * 13.618 \ kg$$

$$Moisture\ contribution\ from\ clay \ = 0.227 \ kg$$

$$Corrected\ amount\ of\ water\ to\ be\ added\ in\ the\ mix \ = (10.149 - 0.227) = 9.922 \ kg$$

3.2.3 Specimen preparation and details of UC tests

During the preparation of soft sand rock mixes for batch study, required dry weights of clay sand and cement were estimated in order to make 4.5-litre volume of mixture at 20% moisture content for each batch. Prior to the addition of water in to the mixture the dry sand –clay – cement were mixed well for 15 minutes to achieve uniformly distributed dry mix. Upon completion of the dry state mixing, required amount of water to maintain the moisture content was added to the mixing mould and the slurry state mixing was continued. Initial mixing under wet condition was conducted for about 10 minutes, after that the machine (Figure 3.8 (a)) was stopped and the wet slurry layer attached in the periphery of the mixing mould was detached by a spatula and mixed with the main mix. Subsequently the mixing was continued for further 30 minutes to achieve well-saturated and uniform mix.

Moisture content of each batches were measured soon after the mixing to estimate the moisture loss during the mixing process and to confirm the initial condition of each mix before preparation of the cylindrical specimens. Prepared soil cement mixture was moulded into cylindrical specimens having the dimensions of Ø=50mm, H=100mm to conduct unconfined compression tests at 3, 7, 14, 28 days curing times. Mechanical vibrator was used to compact the mix in to the cylindrical moulds as shown in Figure 3.9 and each specimen was compacted by three subsequent layers having a layer thickness of 33mm.To remove the

air voids deep inside the mould and between layers to form a single cylindrical specimen, a metal stick was used as shown in Figure 3.9. One batch mix consists of 12 cylindrical specimens (Figure 3.8 (b)), and the variations of the bulk density of each specimen was maintained within a small rage by measuring the bulk weight of the specimens during the compaction. Upon completion of the cylindrical specimens the top surface of each specimen was covered to control the evaporation and cured under moisture controlled boxes as shown in Figure 3.8(b). Similar procedures were followed during the mixing of mud rock mixtures as well but the different between mud and sand rock was the moisture content and the absence of Toyoura sand in mud rocks.

(a) (b)

Figure 3.8 (a) Mixing apparatus and (b) Curing arrangement with top face covered specimens

Figure 3.9 Preparation of moulded specimens

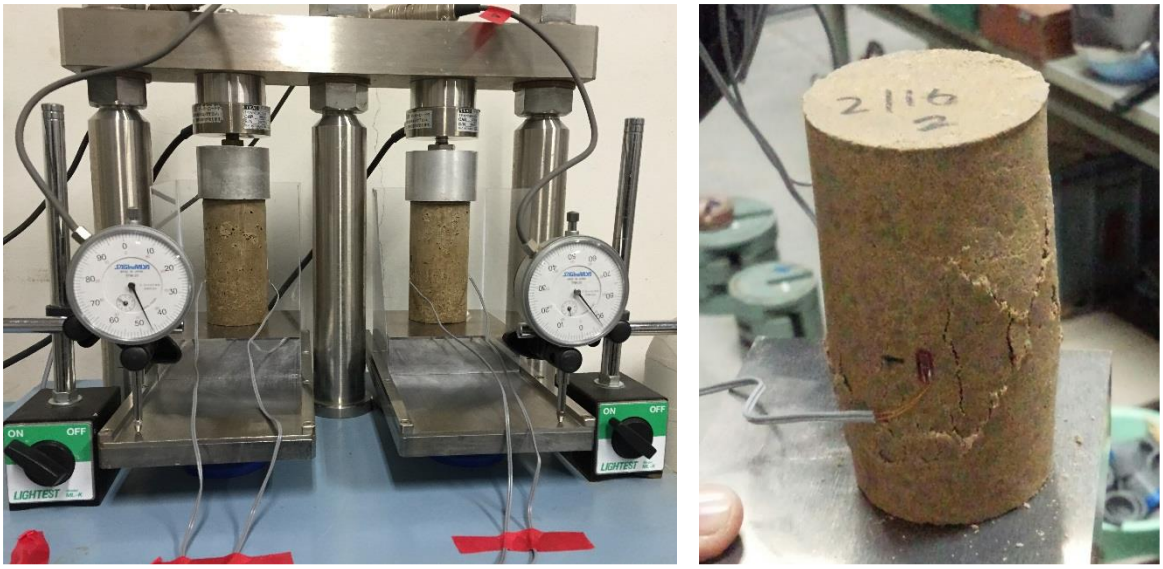

Figure 3.10 Unconfined compression test setup with local (strain gauge) and global (external averaged) strain measurement

Furthermore, to achieve high degree of saturation, mud rocks required high amount of moisture compare to the sand rocks there for the mud rock specimens were prepared at 39% and 45% moisture contents for the batch study.

By definition, the unconfined compression strength is defined as the amount of applied stress at which failure of the specimen occurs. Uniaxial compressive strength was estimated as the peak stress from the stress strain relationship obtained during the unconfined compression test. Setup for the unconfined compression test and the test specimen with the strain gauge is shown in Figure 3.10. Stiffness of the specimen can be defined in different ways based on the stages of loading or the level of deformation or strain. In this study, the secant stiffness was evaluated based on 50% of mobilized peak stress and corresponding averaged external strain and the averaged local strains separately. For the evaluation of the secant stiffness initially the observed

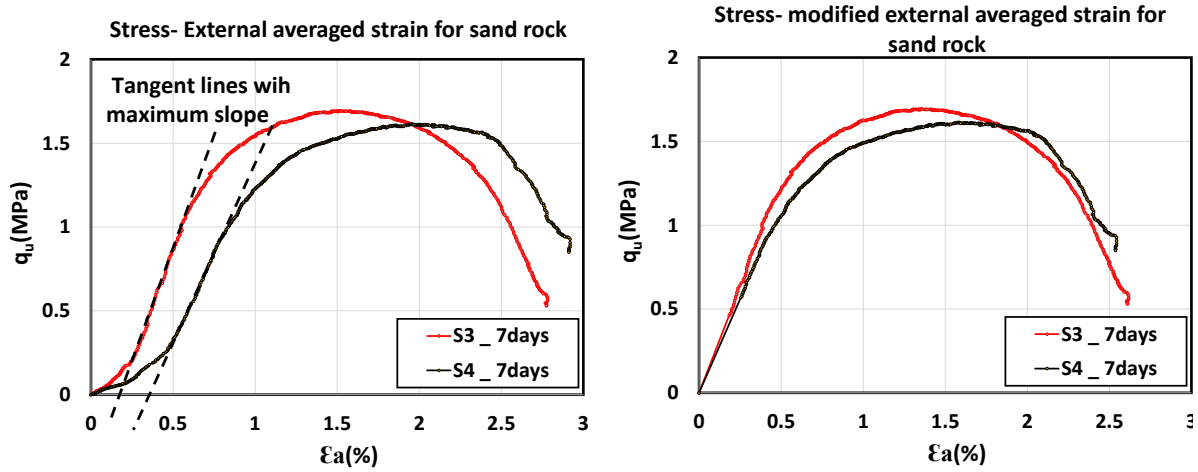

Figure 3.11 Modification of external average strain to eliminate the bedding error

external averaged strain was modified by considering the tangent line with maximum slope of the stress-external averaged strain relation as shown in Figure 3.11.

From this correction, the effect of the bedding error at the early stages of the loading was eliminated as much as possible and the secant stiffness based on averaged external strain was

estimated. Even though the remedial measures taken in to account to eliminate the bedding error, the secant stiffness measured from the external averaged strain is an under estimation of the actual stiffness of the specimen. For example, it was shown by Jardine et al. (1984) that the stiffness of various stiff specimens measured outside the triaxial cell underestimate the actual stiffness up to a great extant for the local axial strains less than 10^{-4}.

Measurement of the actual soil stiffness at small strain levels has been one of the most challenging topics in geotechnical engineering. Accurate measurement of the small strains and predicting the behavior of ground at small train levels are most important in several geotechnical engineering practices such as the problems related to settlements, stress distributions and the grounds subjected to loading unloading.

Therefore, the understanding of the soil stiffness in a vast range of strain levels (10^{-6} -10^{-2}) plays great importance in geotechnical practice. Small strain-stiffness can be studied up to some extent of accuracy by using the local strain measurements; the term local strain also implies that the averaged strain along a certain length of the specimen by utilizing different strain measurement technics and the influence of the bedding error can be eliminated for this measurement.

Generally, in rock engineering, strain gauges are being used to measure the local strains but the applicability and the accuracy of the measurements highly depends on the stiffness of the specimen, stiffness of the strain gauge plate and connection between the specimen and the gauge plate. In this research local strain measurements also were conducted by utilizing commercially available strain gauges. Two strain gauges were installed in the mid depth of each specimen at the opposite sides as shown in Figure 3.10. Measured average strain from both gauges were considered for the evaluation of the stiffness of the specimen. Although the obtained nonlinear stress strain measurements yield a high secant stiffness compare to the external average strain measurements, the actual stiffness of the specimen should be taken in-between the two stiffness measurements since the local strains partially influenced by the stiffness of glue and the stiffness of strain gauge plates.

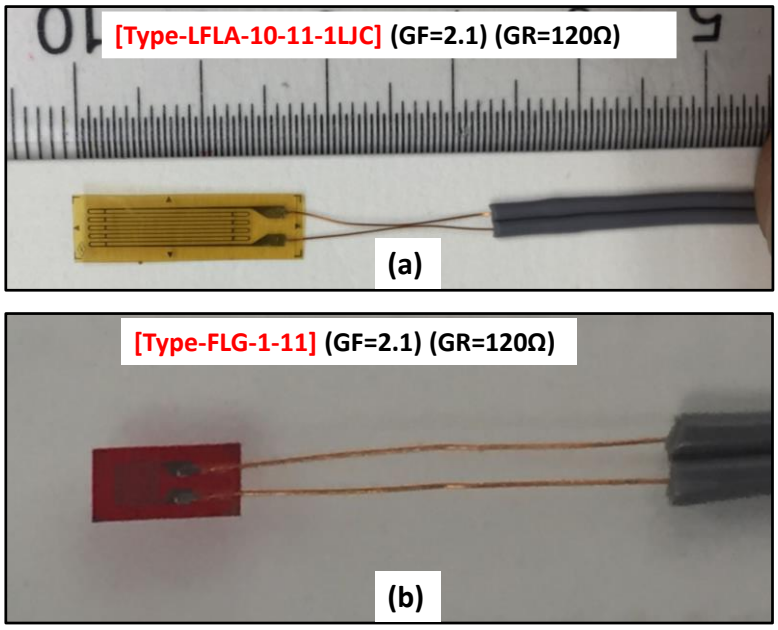

Figure 3.12 Utilized strain gauge types for local strain measurement

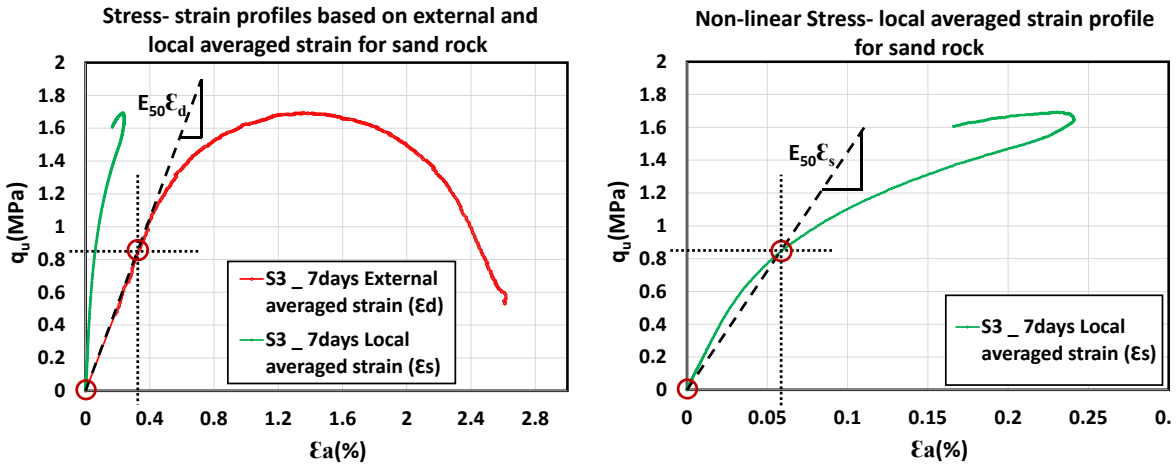

Figure 3.13 Evaluation method of secant stiffness and small strain measurements

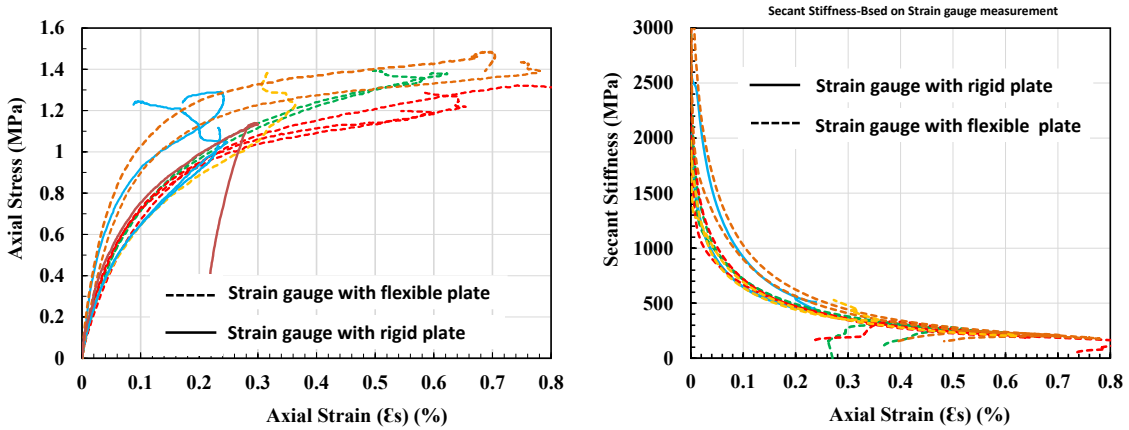

Figure 3.14 Evaluation method of secant stiffness and small strain measurements by flexible and rigid plate strain gauges

Two different types of strain gauges were utilized to measure the local strain of moulded specimens as shown in Figure 3.12. During the batch tests described in

Table 3-1 and

Table 3-2 only **FLG-1-11** type (Figure 3.12(b)) strain gauge was used. The stiffness of gauge plate is relatively higher for this type of strain gauges compare to the **LFLA-10-11-1LJC** type gauges describe in Figure 3.12(a). Attributing to higher gauge plate stiffness and smaller dimensions of plate the measurable range of **FLG-1-11** type gauges lies between 0 - 0.2 %, beyond which the gauge get detached from the specimen and exhibiting a reduction in strain as shown in Figure 3.13(b). However the gauge **LFLA-10-11-1LJC** could follow the strains up to 0 - 0.5% as shown in Figure 3.14, this type of gauges are known as flexible strain gauges and the price also much higher compare to the former ones. The large measurable range enables to study the variation of stiffness from elastic strains (10^{-6}) to elastoplastic deformations. Figure 3.13 shows the examples of stress strain curves obtained from the dial gauge and the strain gauge measurements. The strain measured by the strain gauges (ε_s) is the average of two gauges, which were installed opposite sides of the specimen. Although the modification of the initial portion of the curves obtained from the dial gauge measurement (ε_d) was done using the highest tangent stiffness, the large difference between the curves from the two measurement can be seen, which can be attributed to the bedding error of the loading cap and the specimen. This

implies that the non-linear relation shown in Figure 3.13(b) cannot be measured by the external displacement measurement, resulting in underestimation of stiffness at relatively small strain levels.

3.2.4 Mechanical properties of artificial soft rocks

For the design and stability evaluation of engineered structure, mechanical properties of the rock must be evaluated in a reliable manner. The mechanical properties rock materials can be evaluated base on time or creep behavior, tensile strength, compressive strength and shear strength, strain or deformation characteristics. Although the mechanical properties of rock like materials can be studied under broad testing methods, the required properties for the design entirely depends on the extent of the project. For example; in underground mining, the compressive strength of the rock material is the key parameter since the pillars and columns are penetrating to the rock and providing supports to the retained soil or rock. Therefore, the appropriate testing method to derive the properties for the design is the preliminary requirement of a construction project. However, in rock engineering, the unconfined compression strength is the most common mechanical property; it was widely been used as a basic property to design engineering structures in any type of rock ground.

The prime purpose of this study is to simulate the excavation process on self-standing sheet pile walls embedded in soft rocks. Considering the engineered structure in this research, the stability of the self-standing walls entirely depends of the passive pressure generated by artificial soft rock, therefore the main parameter for the stability analysis is the shear strength soft rock. Not only the strength of the artificial soft rock but the stiffness also another mechanical property which control the lateral movement or the deflection of the sheet pile walls there for the stiffness of the embedded medium also should be investigated in a reliable manner. In this study, investigation on the mechanical properties of artificial soft rocks were estimated by means of confined and unconfined compression tests of rock specimens. Unlike soil or intact rock specimens, the strength and stiffness of the artificially made soft rocks varies with the curing time especially at the early stages of the curing due to the hydration of the soil-cement mix. To predict the mechanical properties of specific mix the strength and stiffness must be evaluated with curing time of the moulded specimens.

3.2.4.1 Influential factors on measured strength and stiffness of test specimens

Even though the water cement ratio, moisture content and porosity of the artificial soft rocks are the main strength governing parameters of the soil-cement mix, this sub clause is dedicated to discuss the effect of some other factors on the measured strength and stiffness of compacted specimens. The unconfined compressive strength and the stress strain behavior of compacted specimens can be influenced by several other factors as follows,

- Bedding error due to loading system and Contact surfaces of the test specimen.
- Compaction method
- Strain non- uniformity of the specimen due to end restrains
- Shear banding or strain localization of the specimen.
- Sample disturbance
- Mixing method, volume of the mix and mixing time
- Rate of strain or loading

3.2.4.2 Bedding error due to the loading system and contact surfaces of the test specimen

In uniaxial compression test, to maintain the high quality of testing the surfaces loading cap and the bottom plate should be parallel to each other as well as perpendicular to the axis of the test specimen. In most of the standardized uniaxial compression test machines, the surface of

the bottom plate is already installed perpendicular to the axis of the specimen. The top cap and the loading frame can be adjusted by the user therefore additional care should be taken in to account to maintain the quality of loading system this is entirely depends on the user unless the physical deformations exist in the loading cap or frame. Because of the availability of high-quality equipment and the atomized systems, the possibility of causing the bedding error due to the loading system or the equipment is very rare in this century. The most common problems in rock testing is the surface quality of the test specimens. Even though specialized equipment are utilized in rock engineering to cut surfaces and smoothen, in fact the probability of achieving 100% smooth surfaces which are exactly parallel to each other is very rare in practical situations.

From the experience, that I gained throughout this study it is almost impossible to achieve exactly parallel surfaces of the specimen by manual operations. But I could be able to make the bottom surface of the specimens exactly flat and parallel to the bottom plate of the equipment since standard mould was utilized to prepare the cylindrical specimens. However, the top surface of the specimen was smoothened upon completion of the compaction of unsolidified mix by manually and slightly trimmed before the uniaxial compression test. The effect of bedding error on cylindrical specimens can be clearly seen by considering the stress-external averaged strain relationship obtained from unconfined compression tests as shown in Figure 3.11. Even though the strength and stiffness of the cylindrical specimens can be effected by bedding error, comparing to the influence on strength it has saver effect on the measured stiffness of the cylindrical specimens. Showing high strains at early stages of the loading due to the stress concentrations in contact area and poor contact between load cap and the specimen. Not only in unconfined compression but in the triaxial compression equipment also existence of bedding error is inevitable. Bedding error cannot be perfectly avoided in the current configuration of the triaxial specimen and the effect of disturbed zones formed at both ends of the specimens during the sample preparation may be serious for stiff materials, which could greatly under estimate the measured stiffness (Goto, 1991; Tatsuoka et al, 1991). Bedding error can be eliminated from the stiffness measurement by measuring the local averaged strains in triaxial tests (Goto, 1991; Tatsuoka et al, 1991). In this research, the sample strain was measured by external averaged measurement (dial gauge measurements) and the local strain by using the strain gauges, which were installed in the mid depth of the specimens.

3.2.4.3 Compaction method

Method of compaction and the compaction energy are highly influence on the material properties of artificial soft rocks. Mainly the dry density, porosity and the degree of saturation of the compacted specimens could vary based on the compaction method. Mechanical vibrator was used in this research to prepare the molded specimens and the density of the specimens were controlled by measuring the bulk weight. Kenai et al, (2006) were studied the effect of three different compaction methods on the mechanical properties of cement stabilized soil.

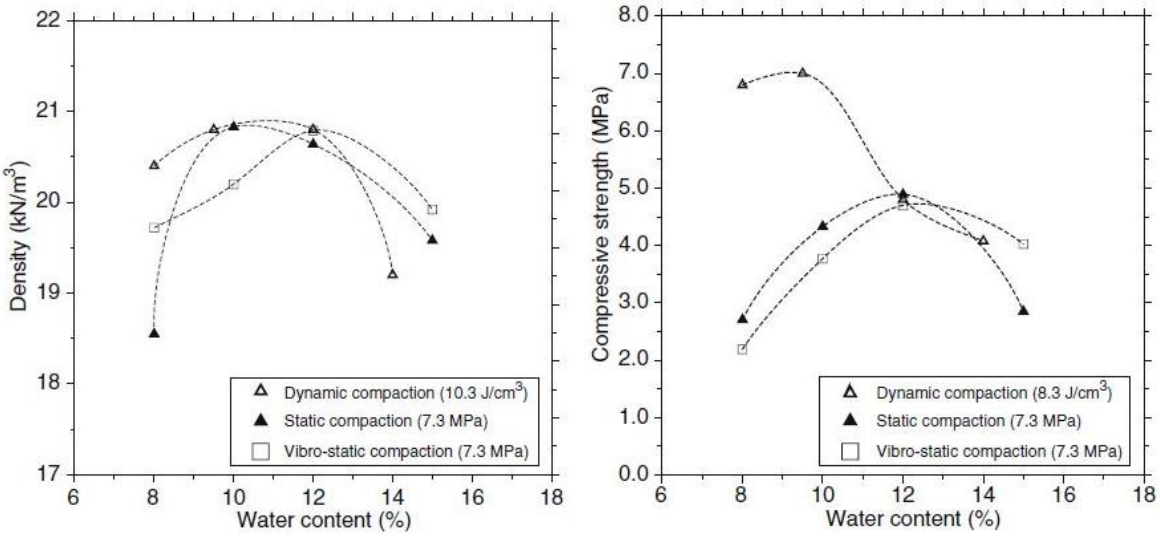

Figure 3.15 Effect of compaction method on mechanical properties of cement-stabilized soil (Kenai et al, (2006))

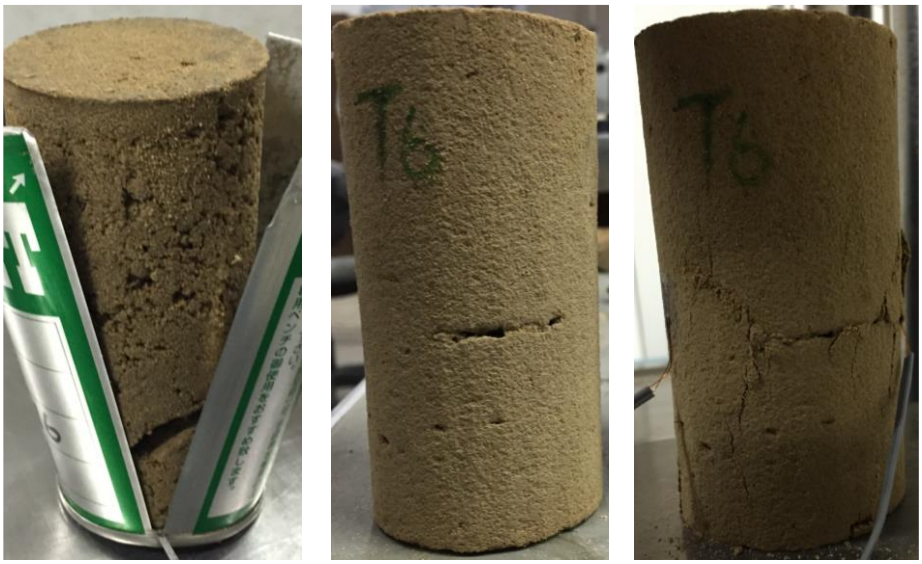

(a) **(b)** **(c)**

Figure 3.16 Examples for poor quality specimens (a) moulded, (b) trimmed from block sample (c) trimmed sample after testing

Figure 3.15 shows the variation of compressive strength and the bulk density obtained from different method of compaction. From this, it can be concluded that the dynamic compaction highly advanced the compression capacity of the cement stabilized soil compare to the static and vibro- static compaction methods. In addition, there is no significant variation in achieved maximum bulk density of the compacted specimens but comparing to the vibro-static compaction method the dynamic and static compaction produce higher values of maximum dry

density. Strength and stiffness of the artificial soft rock specimens not only depends on achieving the required bulk or dry density but it also depends on the quality of compacted specimen. Achieving the high quality compacted specimens entirely depends on the workability of the mix, effort and the experience of the person in that field. Specimens with cavities and separation between the compacted layers could alternate the failure mode of the

cylindrical specimens from shear failure to crushing of the specimen along the stress concentrated areas. Figure 3.16(a) is a good example for the poor compaction effort and for a poor quality specimen having large amount of pores with cavities and the layer separations. Figure 3.16(b) and Figure 3.16(c) are the state of same specimen trimmed from centrifuge model ground before and after the unconfined compression test. From this, it can be seen that the failure of the specimen initiated due to the stress concentration and the crushing of the specimen around the cavity therefore the quality of the cylindrical specimen also an important factor, which effects the strength of the specimen.

3.2.4.4 Strain non- uniformity of the specimen due to end restrains

Friction between the loading plates and contact surfaces of the specimen is the main cause of strain non-uniformity and it influence on the failure mode and the measured external strains of the specimens. In fact, the measured external strain is an averaged strain along the mid portion of the cylindrical specimens. If the friction at both end of the specimens could be removed by means of any additional measures, the bulging failure could be avoided (Figure 3.17) and the accuracy of the external average strain measurement could be enhanced.

Figure 3.17 Observed failure of (a) Sand rock in UC test and (b) Mud rock in triaxial compression

3.2.4.5 Shear banding or strain localization of the specimen

Shear banding is a phenomenon associated with strain localization and plastic deformations, which could be observable in vast range of ductile materials. Formation of shear band is an indirect indication of the extreme level of failure ductile materials, which can be formed not only in finite body, but possible in infinite body also when a ductile body undergoing sever deformation. Shear banding is an inevitable source of error in triaxial compression tests even cannot be excluded the effect when the ideal boundary conditions are applied to the soil element (Goto, 1991; Tatsuoka et al, 1991). The phenomenon shear banding, indirectly influence on measured stiffness of the artificial soft rocks and Figure 3.17(b) shows the observed failure patterns of mud rocks during triaxial compression tests. Ductile behavior of stress-averaged external strain observed for mud rocks can be explained from this failure mode.

3.2.4.6 Stress strain behavior between natural and artificial soft rocks

Typical Stress strain behavior of mud rocks under unconfined compression tests from Melbourne and Calgary are presented in Figure 3.18. From the stress strain behavior observed in Melbourne mudstone it can be noted that, with the decrease of moisture content the brittleness of the rock specimen increases and the failure strain level decreases which can be observed in the artificial soft rock as well as shown in Figure 3.19(b). Comparing to the stress strain behavior of typical natural soft rocks (Figure 3.18) with the artificial sand and mud rocks (Figure 3.19) there are some similarities and differences in the behavior. Failure strains observed for artificial mud rocks are almost similar to that of Melbourne mudstone at 14.4% and 19.8% moisture contents but the post peak behavior of natural soft rocks showing more brittle behavior compare to the artificial mud ad sand rocks.

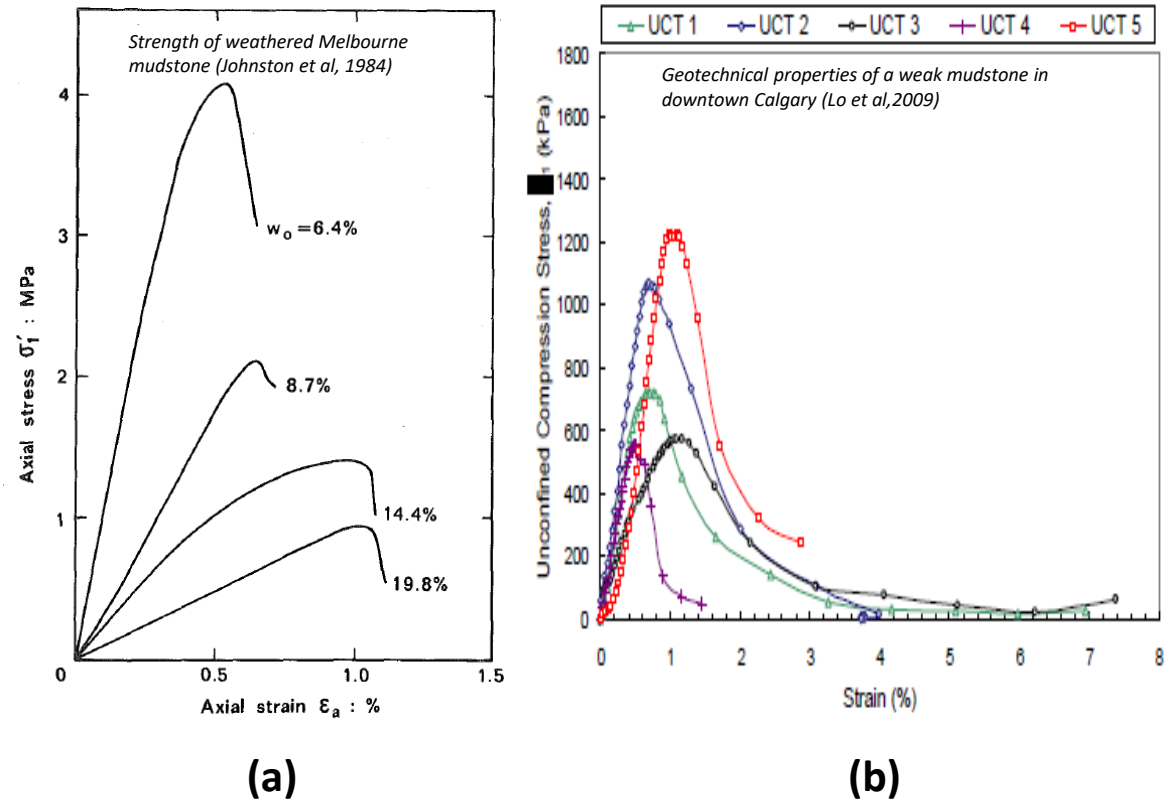

Figure 3.18 Typical stress strain behavior for soft rocks under unconfined compression tests

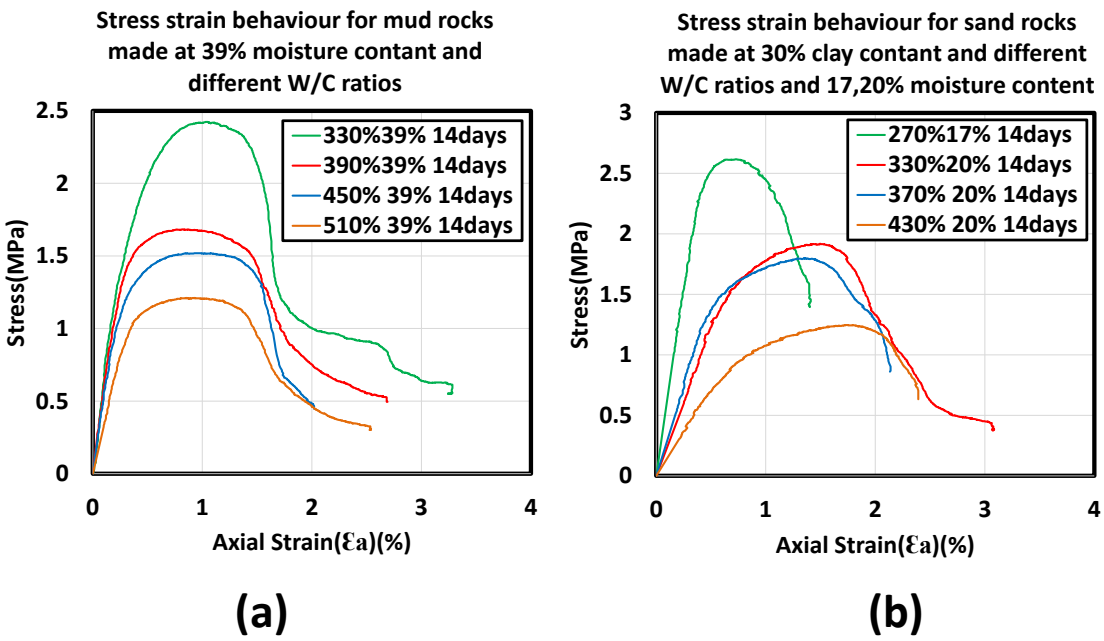

Figure 3.19 Stress strain behavior of artificial sand and mud rocks at 14 days curing time

The stress strain behavior obtained from Calgary mudstone and artificial sand rocks have some similarities in the failure strain as well as the post peak behavior. However, some of the specimens obtained from Calgary mudstone also exhibits more brittle behavior in post peak failure. Generally, in natural deposits the strength and stiffness of soft rocks or hard soils vary in a vast range. Therefore prior to the construction activities in rock ground it is important to conduct a detail investigation about the site, unforeseeable condition and consideration of different hazard scenarios are essential requirement in the design process.

3.2.5 Results of artificially modelled soft rocks and discussions

3.2.5.1 Unconfined compression results of artificially made soft sand rocks

Results of sand rock specimens with different clay contents are indicated with curing time in Figure 3.20.From Figure 3.20, it can be seen that the unconfined compressive strength (UCS) and secant modulus (E_{50}) of sand rock specimens influenced by the water-cement ratio and clay content of the mix. UCS and E_{50} are showing the increasing trend with curing time but the rate of increment decreases with time especially for UCS. In the early stages of the curing time, generally all specimens exhibit high rate of increment in strength and the stiffness, usage of early strength Portland cement may be one of the possible reason for this behavior.

Effect of clay content on the mechanical properties of artificial sand rock specimens can be described by referring to the identical water-cement ratio mixes. Figure 3.21 and Figure 3.22 describes the variation of q_u and E_{50} for mixes prepared at 330% water-cement ratio, 20% moisture content and different clay contents. From this variation, it can be concluded that q_u and E_{50} of artificial sand rock increases with the increase of clay content of the mix.

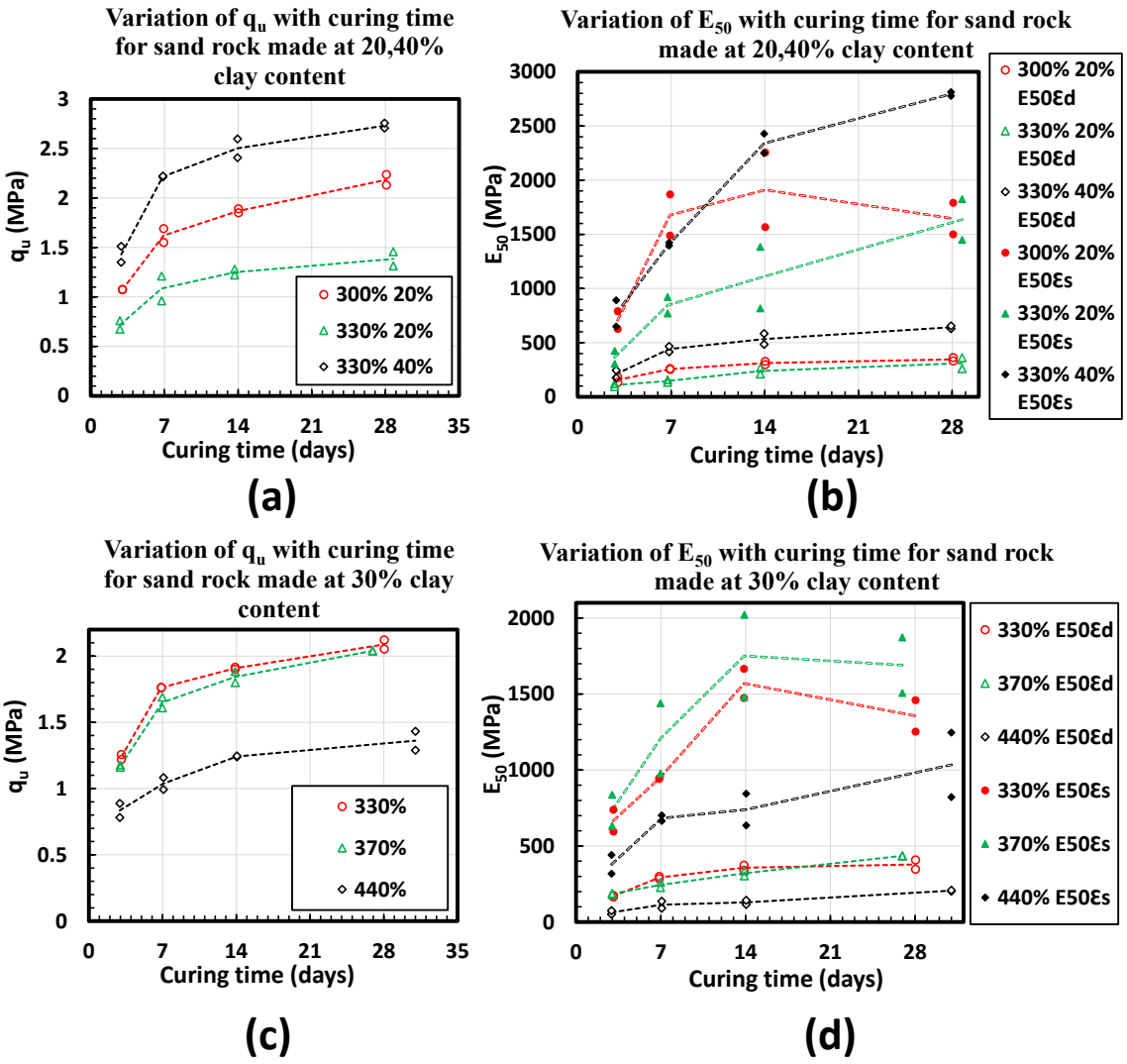

Figure 3.20 Variation of q_u and E_{50} with curing time for soft sand rocks made at different Water-cement ratios

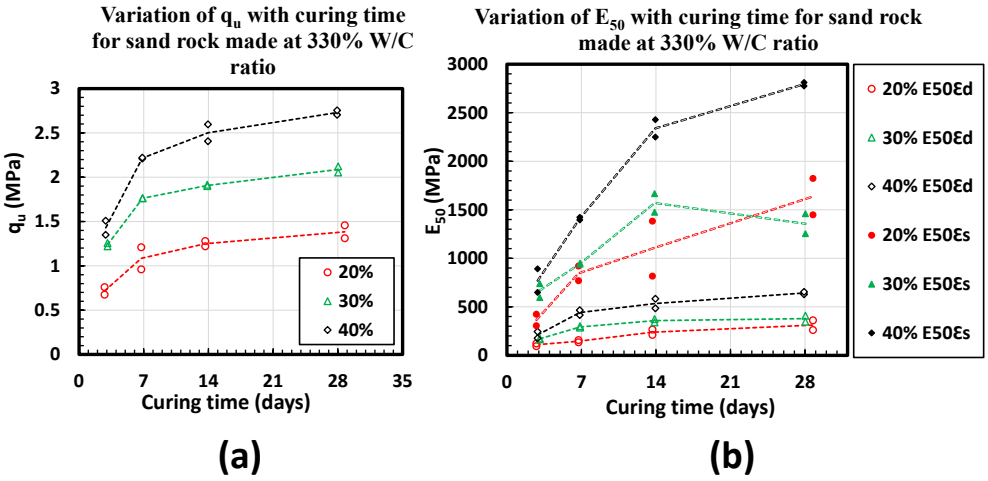

Figure 3.21 Variation of q_u and E_{50} with curing time under same W/C ratio and different clay contents

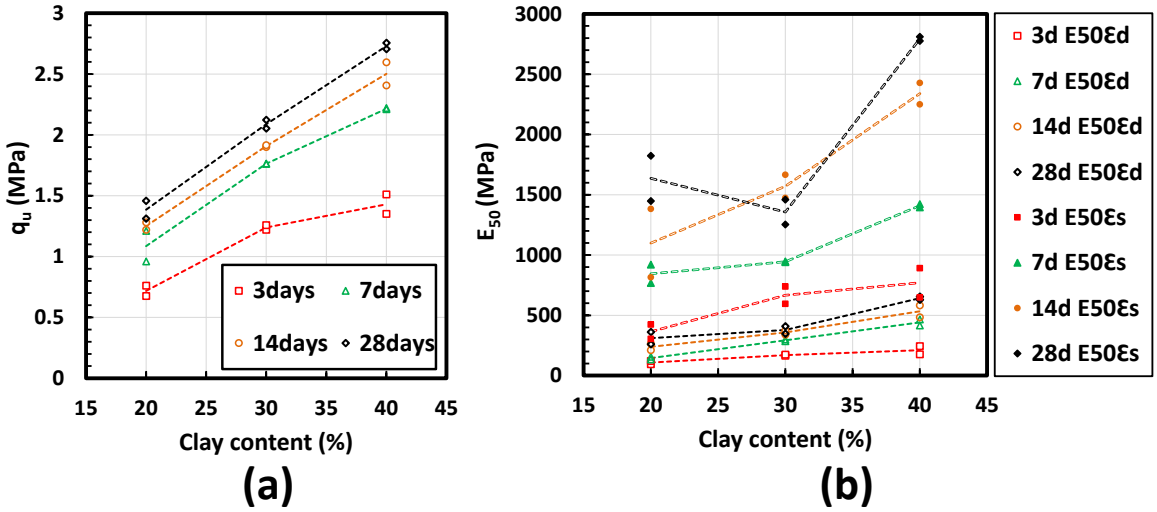

Figure 3.22 Effect of clay content on the mechanical properties of sand rock

However, E_{50} values show the significant variation compare to q_u values under same curing time. Water-cement ratio is one of the critical parameter, which governs the strength and stiffness of the artificially made soft rock specimens. Variation of q_u and E_{50} with water-cement ratio were investigated at different curing time intervals for 30% clay content mixes. Graphical representation of the results are illustrated in Figure 3.23.From Figure 3.23 (a) it can be

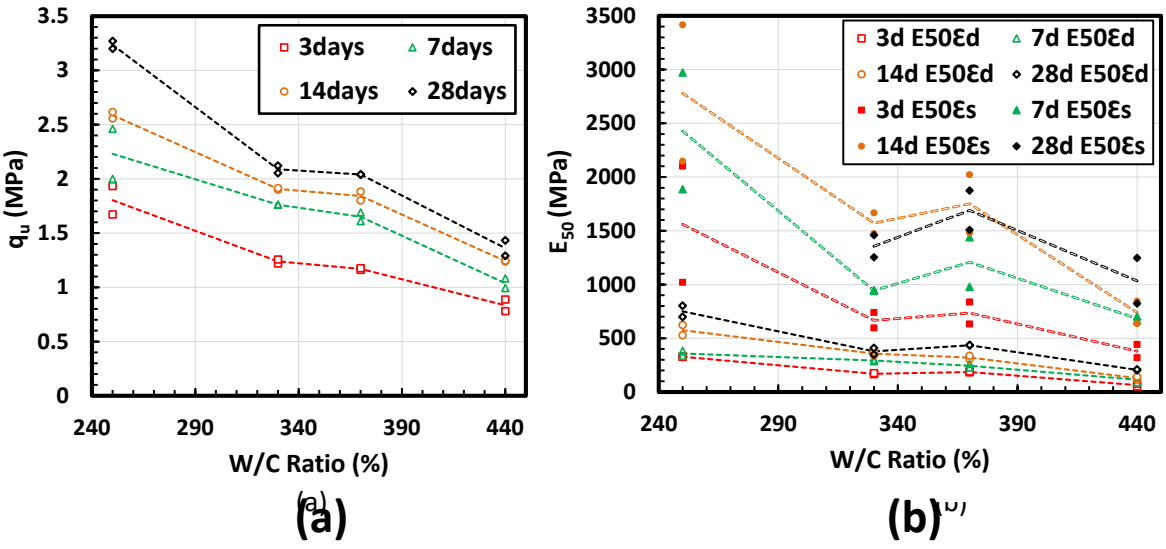

Figure 3.23 Effect of water -cement ratio on the mechanical properties of sand rock

observed that the unconfined compressive strength of artificially made sand rock samples show almost linearly decreasing trend with the increment of water-cement ratio. Secant modulus (E_{50}) of the artificially made sand rock specimens were estimated based on averaged external strain ($E_{50}\_\varepsilon_d$) and averaged strain gauge ($E_{50}\_\varepsilon_s$) measurements. E_{50} also shows generally decreasing trend with the increase of water-cement ratio as shown in Figure 3.23 (b) but the variation of E_{50} is much more significant compare to the q_u values under same water cement ratios. From the comparison of the results obtained by $E_{50}\_\varepsilon_d$ and $E_{50}\_\varepsilon_s$ at the same curing time, it can be observed that the stiffness measured by strain gauges always more than 3 times larger than that of dial gauge measurements. From this analysis it can be concluded that the results observed from unconfined compression test always under predict the stiffness of the

artificially made soft rocks. Application of the unconfined compressive results in design practice will produce very much conservative design but it will not be an economical solution.

3.2.5.2 Unconfined compression results of artificially made soft mud rocks

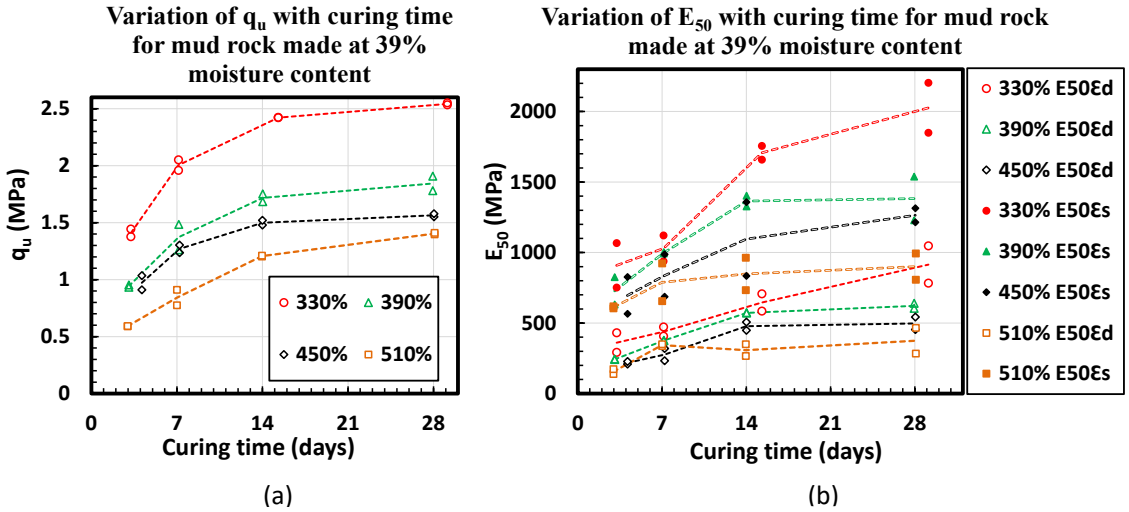

Figure 3.24 Variation of q_u and E_{50} with curing time for artificial mud rocks made at different water-cement ratios

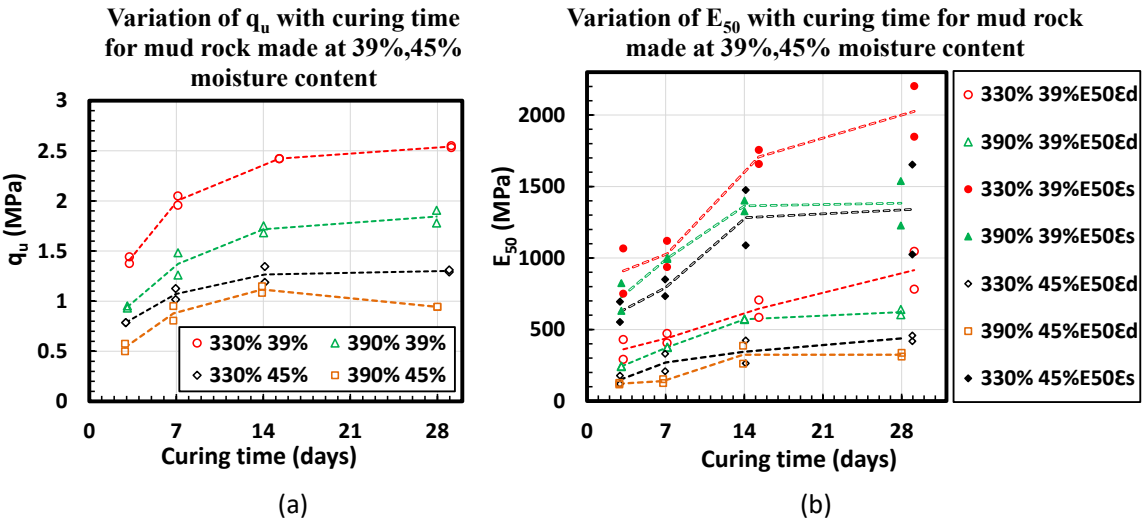

Figure 3.25 Effect of moisture content on the mechanical properties of mud rocks

Variation in the mechanical properties of mud rock specimens made under different water-cement ratios with curing time are indicated in Figure 3.24. Which illustrates the variation of q_u and E_{50} with curing time for artificial mud rocks made at different water-cement ratios. From Figure 3.24 it can be seen that the unconfined compressive strength (UCS) and secant modulus (E_{50}) of mud rock specimens highly influenced by the water-cement ratio of the mix. UCS and E_{50} are showing the increasing trend with curing time but the rate of increment decreases with time. In the early stages of the curing time, generally all specimens exhibit high rate of increment in strength and the stiffness, usage of early strength Portland cement may be one of the possible reason for this behavior. Comparing to the results observed for sand rocks, variation of q_u and E_{50} are not much significant and the results are showing good repeatability.

Effect of moisture content on the mechanical properties of artificial mud rock specimens can be described by referring to the identical water-cement ratio mixes made at two different moisture contents as shown in Figure 3.25. From this variation, it can be concluded that q_u and E_{50} of artificial sand rock decreases with the increase of moisture content of the mix. However, E_{50} and q_u obtained at 39% and 45% moisture content mixes are showing good repeatability comparing to the results observed from sand rock specimens.

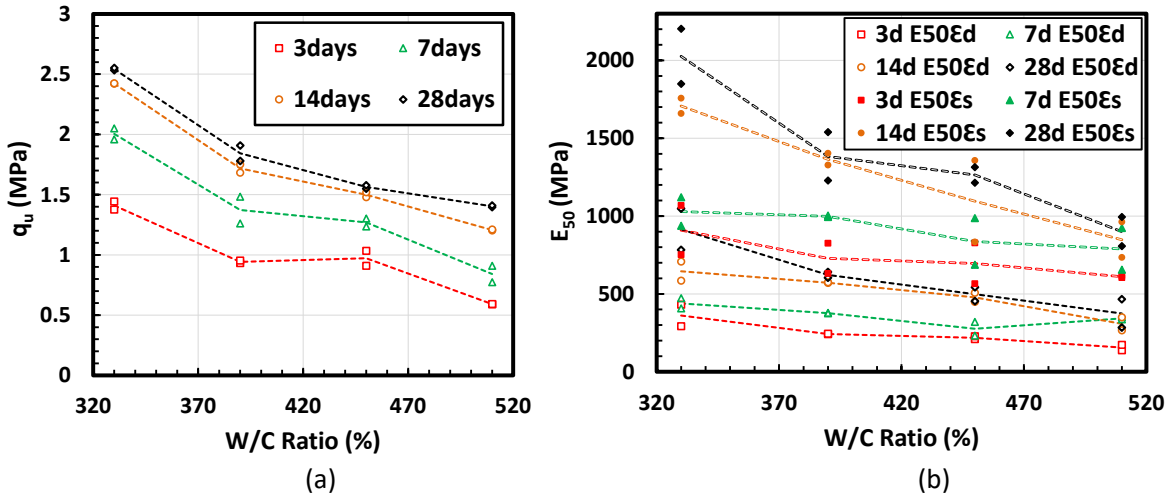

Figure 3.26 Variation of q_u and E_{50} for mud rocks made at different water cement ratios (w.c=39%)

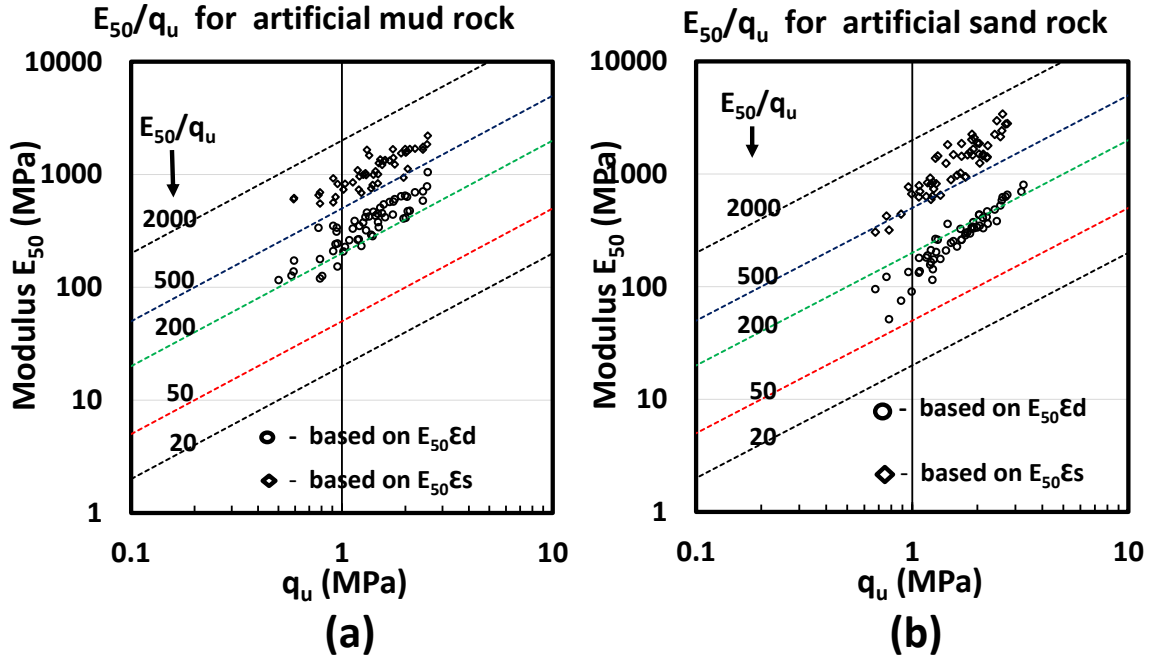

Figure 3.27 Relationship of E_{50} and q_u obtained from artificially made (a) mud and (b) sand rocks

Variation of q_u and E_{50} with water-cement ratio were investigated at different curing time intervals for mud rock specimens made at 39% moisture content and different water cement ratios. Graphical representation of the results are illustrated in Figure 3.26. From Figure 3.26 (a) it can be observed that the unconfined compressive strength of artificially made mud rock samples show almost linearly decreasing trend with the increment of water-cement ratio as observed from sand rocks. Secant modulus (E_{50}) of the artificially made mud rock specimens

were estimated based on averaged external strain ($E_{50}\_\varepsilon_d$) and averaged strain gauge ($E_{50}\_\varepsilon_s$) measurements. E_{50} also shows generally decreasing trend with the increase of water-cement ratio as shown in Figure 3.26 (b) but the variation of E_{50} is no much significant as observed from sand rocks also the results are showing good repeatability. From the comparison of the results obtained by $E_{50}\_\varepsilon_d$ and $E_{50}\_\varepsilon_s$ at the same curing time, it can be observed that the stiffness measured by strain gauges always greater than that of dial gauge measurements. From this analysis it can be concluded that the results observed from unconfined compression test always under predict the stiffness of the artificially made mud rocks.

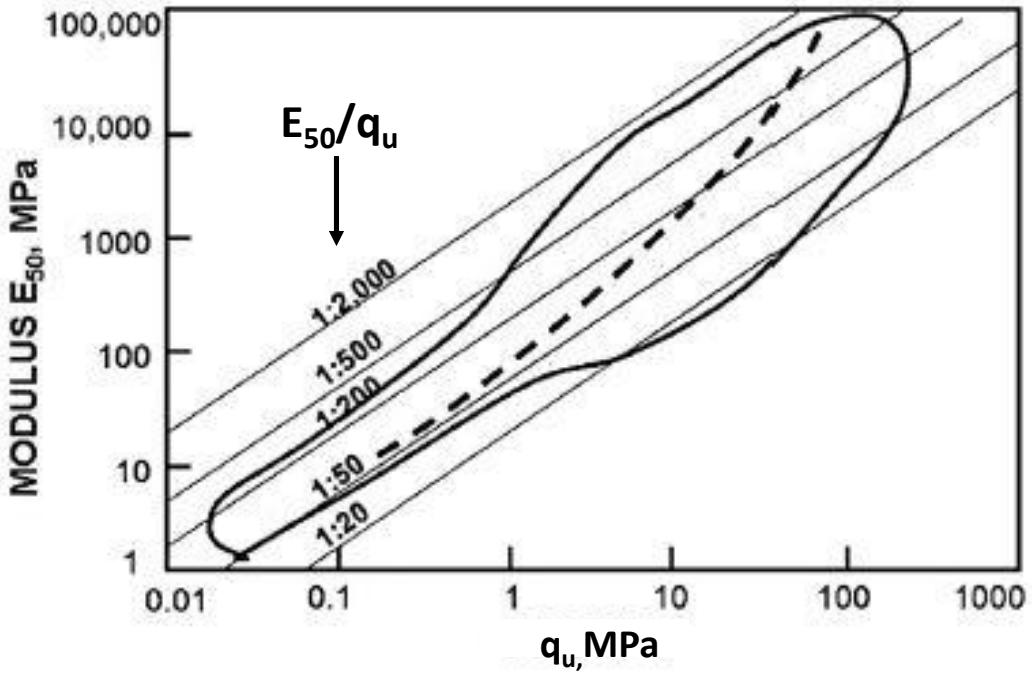

Figure 3.28 Relationship of E_{50} and q_u for most natural soils and rocks. The shadow area is the locus of the data (Modified after Deere(1968),Galvan(1999) and Kanji and Galvan(1998))

Figure 3.27 shows the relationship between E_{50} and q_u for artificially made soft rock samples. Comparing the results with the locus of natural rocks modified by Galvan and Kanji (1998) (Figure 3.28),it can be observed that the E_{50}/q_u ratios estimated based on ε_d are well fit within the locus whereas small fraction of E_{50}/q_u estimated based on ε_s are located on the edge and out of locus. From this investigation, observed good fit between the natural and artificially made soft rocks clearly indicates that, soft rocks can be modelled by using cement treated soils for further studies.

3.3 Design of centrifuge model for cantilever walls embedded in soft rock

3.3.1 Equipments /Apparatus

3.3.1.1 Soil mixer and mixing mould

Figure 3.29 Mixing mould and constituents of one batch mix (approximately 28L)

3.3.1.2 UC test machine and data logger

Figure 3.30 Utilized UC test machine and data logger

3.3.1.3 Sample holder and trimming

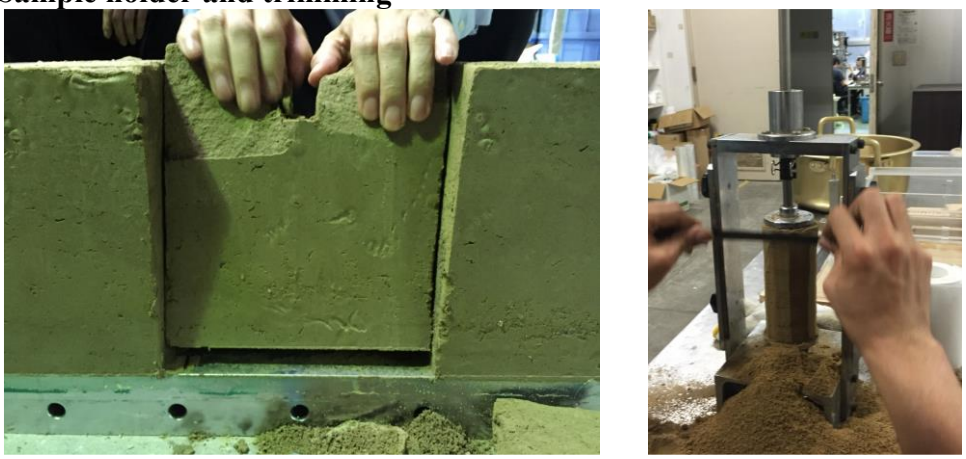

Figure 3.31 An example of centrifuge block sample and trimming process to make cylindrical specimen

3.3.1.4 Sensors

(a) Short range LDT
Measurable range is 3 to 5 cm

(b) Long range LDT
Measurable range is 6 to 14 cm

Figure 3.32 (a) Short and (b) Long range LDTs used in the experiments

Figure 3.33 Potentiometer

Figure 3.34 Pore pressure transduces (PPTs)

Figure 3.35 Solenoid valve

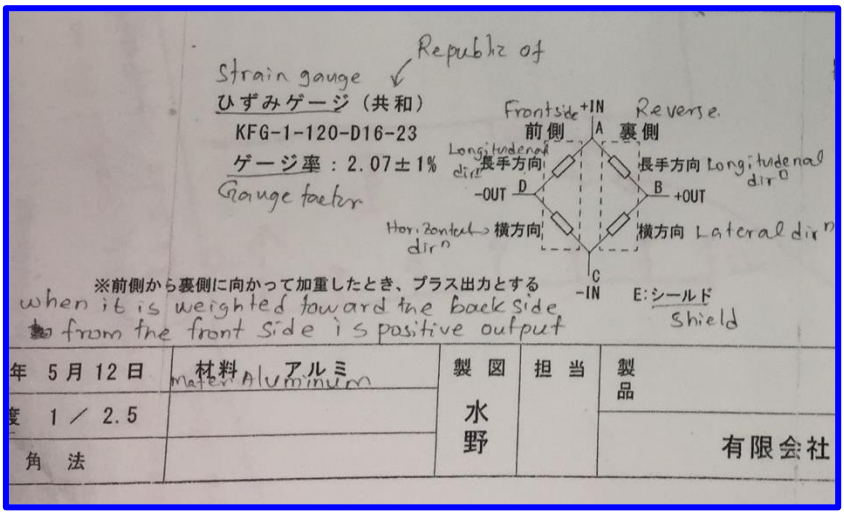

Figure 3.36 Bending strain measurement and type of strain gauge

3.3.1.5 Acrylic compaction plate and electric vibrator

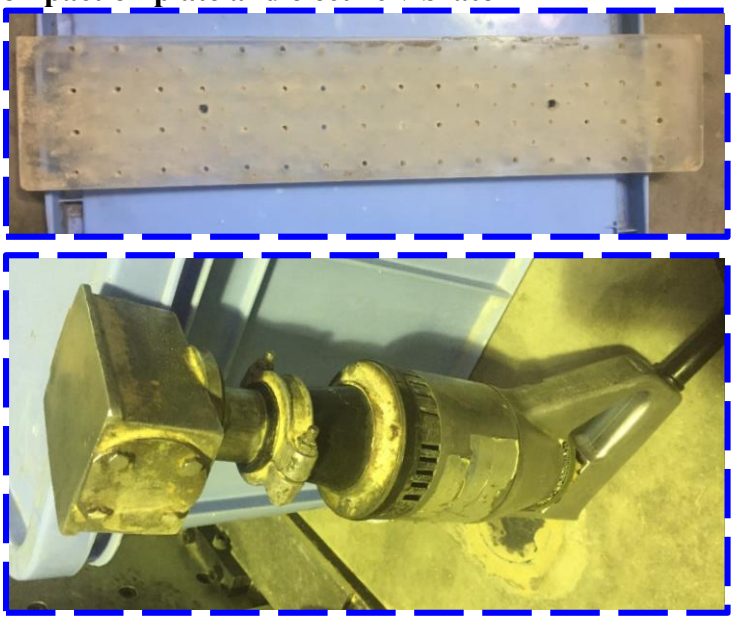

Figure 3.37 Acrylic compaction plat and electric vibrator

3.3.1.6 Sand hopper

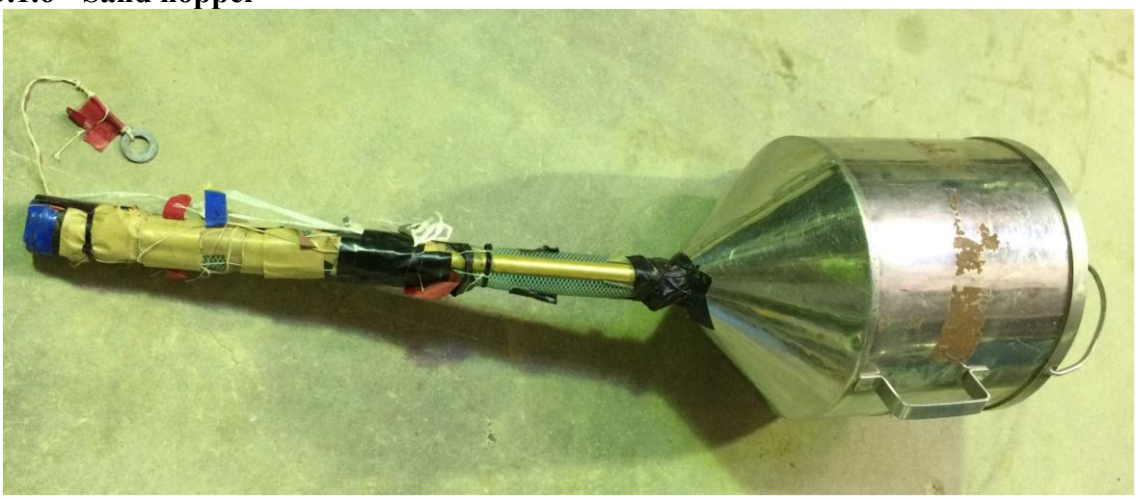

Figure 3.38 Sand hopper used in the centrifuge modelling of dry Toyoura sand at required density

3.3.1.7 Latex and Neoprene rubber bags

Figure 3.39 Neoprene (left) and Latex (right) rubber bags used in the test

3.3.2 Centrifuge model arrangement and modelling procedure

The experiments were conducted at 50 g centrifugal acceleration using TIT Mark III geotechnical centrifuge (Takemura et al., 1999). In the centrifuge model a cantilever sheet pile wall was embedded in artificially made soft rock. The wall was placed throughout the breadth of the container to secure plane strain conditions of the model. The soft rock model was prepared in a model container, which had the internal dimensions of 700 mm in length 150 mm in breadth and 500 mm in depth. The container was made up of a removable rear-side steel wall and a front-side transparent acrylic wall, and both wall plates were bolted with the main container body to form a rigid box. Unsolidified soft rock material was casted in the container. Prior to the casting, 0.5 mm thick Teflon sheets were pasted in the front and rear internal container wall faces and lubricated by silicon grease for easy detachment of wall from the hardened soft rock ground. The soft rock ground was then constructed by compacting the sand-clay-cement mixture layer by layer every 30 mm thickness, up to the depth of wall tip. After that, the sheet pile wall was rigidly fixed upright at the centre of container with the help of a guide plate as indicated in Figure 3.41.

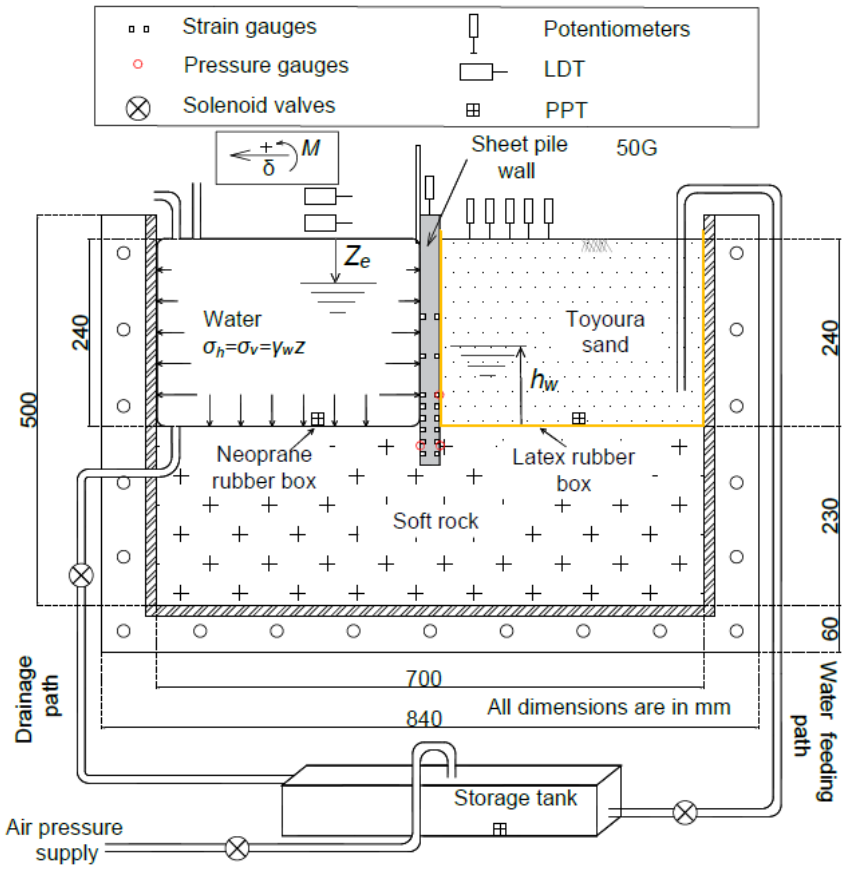

Figure 3.40 Schematic diagram of centrifuge model arrangement

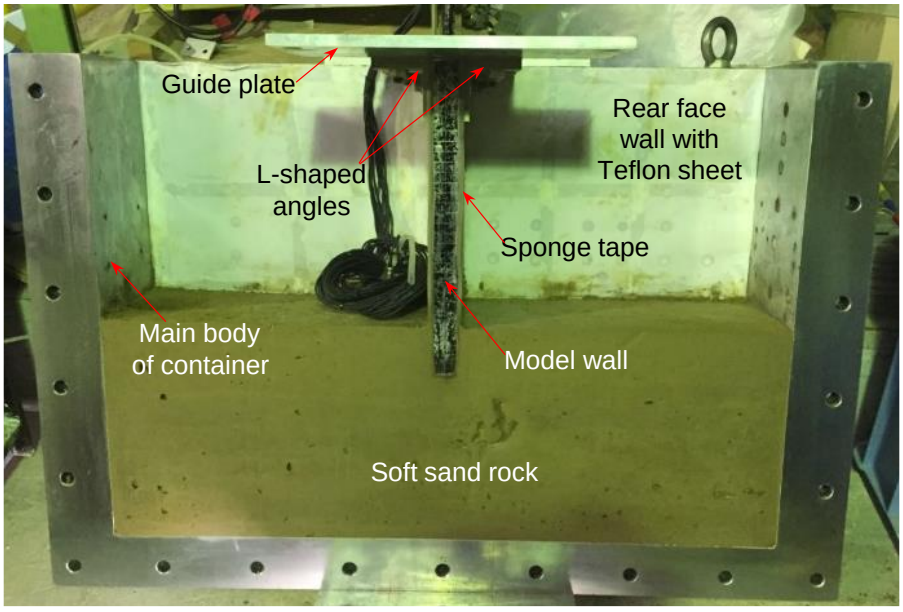

Figure 3.41 Typical centrifuge model preparation

Thereon, the soft rock material was compacted at either side of the wall separately up to the targeted height. The density of compacted mixture was carefully controlled by the volume of each compacted layer and the required mass of the mixture for the layer. Upon casting, the unsolidified soft rock material surface was covered by wet towels and conserved under room temperature for curing.

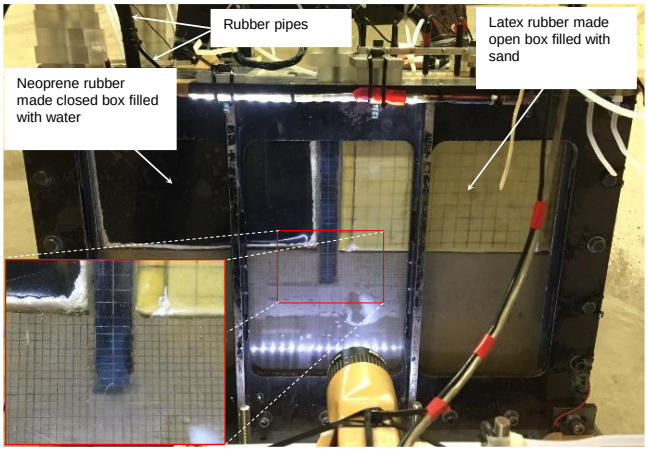

Figure 3.42 Typical centrifuge model ready for testing

After 14 days curing time the guide plate was unbolted from the container and the front wall was detached as shown in Figure 3.41, and the rear wall also detached. The Teflon sheet on the rear wall was replaced by a new one and lubricated with grease to minimize the friction. At the front side of the model soft rock, 5 mm or 10 mm square grids were drawn to visualize the ground deformation and then transparent silicon grease was smeared before attaching the front wall. The front and rear edges of the sheet pile wall were sealed with sponge tapes, which prevented an unfavourable friction at the wall edges by the intrusion of tiny particles between the model wall and the front and rear container wall.

An open rubber box with 250mm height was placed on the back side of the wall and 240mm thick dry Toyoura sand with 80% relative density was made in the box using a sand hopper as shown in Figure 3.42. Detail mechanical properties of Toyoura sand are described in (Fukushima and Tatsuoka,1984; Tatsuoka et al., 1986). The friction angle ϕ' =40o is assumed to calculate as-rest and active earth pressure coefficient in this study. The rubber box was made from thin sheets of latex rubber (t=0.5mm) with higher flexibility and tear resistance, which creates friction less condition on the contact to the wall and rock surface. Although the situation of the loading process by feeding the water into the sand contained in the box is not a realistic case, it can create a clear loading condition on the wall and rock surface without causing complexity or difficulty, such as the excess pore water pressure in the rock and water leakage from the side of the wall.

At the wall front, a neoprene made closed rubber box was placed, which had three rubber pipes. One at the bottom corner and remaining two at the top of the box (Figure 3.47). The bottom pipe was connected to the water storage tank via a solenoid valve (Figure 3.40). Water was then fed in the bag from the top pipe until the water level reach the same height of the retained sand (240mm).

The third pipe was used to remove the trapped air while feeding the water. The water in the bag has two functions, one is to maintain the equilibrium of wall with less unbalance to the earth pressure acting from the retained dry sand during the centrifugation and prior to the excavation, and the other to simulate the excavation, which is considered as the ordinary design loading condition. The neoprene rubber has higher stiffness, tear resistance and less flexibility compared to the latex rubber which helps to bear higher stresses and water tight conditions even at the connection of bottom pipe.

In the centrifuge model the interface friction between rubber boxes, the retaining wall and inner wall of the container was minimized by means of silicon-grease lubrication. Both rubber boxes

were equipped with a pair of pore pressure transduces (PPTs) at the bottoms (Figure 3.40) to capture the water heights. A pair of laser displacement transducers (LDTs) and a series of potentiometers were also equipped to track the lateral movement and rotation of the wall top and monitor the surface settlements of the retained sand.

3.3.3 In-flight simulation of excavation and loading

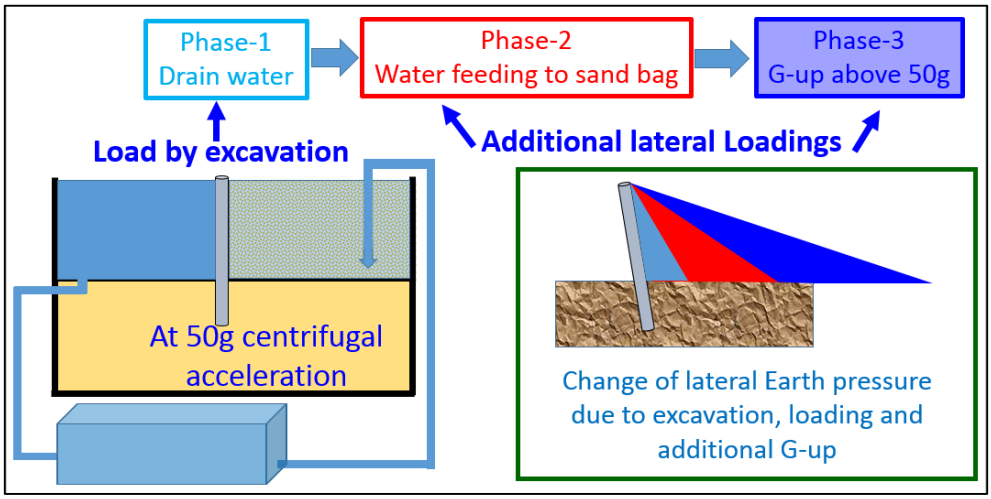

Figure 3.43 Loading mechanism in-flight

A main objective of this model study is to develop the testing system to investigate the stability of cantilever type retaining walls embedded in relatively hard mediums, and the influence of embedment depth on the wall behavior from the ordinary design loading condition (which could be at the end of excavation) to ultimate loading condition, which causes the failure or large deformation of the wall. Figure 3.43 depicts the loading mechanism utilized in-flight. Considering the limitations and difficulties of different techniques for the modelling of excavation employed in the previous studies, the technique of draining fluid from the rubber bag at the wall front was adopted in this study. This technique has two advantages, one is simple but clear stress (loading) condition in modelling process, and the other is reuse of the drained water to impose large lateral load from the retained side. On the other hand, as discussed by Takemura et al. (1999), there are several discrepancies between the liquid pressures acting on the wall and the pressure from the real soil at the wall front in the excavation process. For example, the difference of hydrostatic water pressure and at-rest soil pressure as the initial condition, and the difference of isotropic stress of liquid and variation of horizontal/vertical stress ratio from the at-rest condition to the passive conditions. In the previous studies, heavy fluid with the identical density of the excavated soil was commonly used to create identical stresses at the front and back side of the wall below the excavation bottom. However, plain water was used as a draining liquid in the model of this study. This is because the effects of horizontal stress discrepancy was larger than that of vertical stress in this model. Even for the plain water, the hydrostatic pressure acting on the wall as the initial condition was little larger than the at-rest earth pressure of the retained dry sand used in the model. Furthermore, the strength and stiffness of model rock were quite large with the negligible stress dependency which was confirmed from the triaxial compression tests by the unconsolidated and undrained (UU), consolidated and undrained (CU) conditions. Considering these material conditions and the easiness in handling water, the plain water was used rather than the heavy liquid.

The completion of water drainage or excavation process is considered as a kind of ordinary design loading condition, which causes relatively small wall displacement below the allowable one. To observe the large movement of the wall as the ultimate conditions, an additional load was imposed to the model wall by feeding the water from the storage tank to the retained side of the wall. As compared to dry sand with active earth pressure coefficient of about 0.2, large lateral and moment loads can be imposed to the retaining structure in centrifuge by means of water feeding technique. Khan et al., (2001 and 2006) used this technique to observe failure behavior of double steel sheet pile wall cofferdam under high water. In the real field, the failure of retaining walls are mostly associated with the rise of water table behind the retaining walls (D'Andrea and Day, 1998). Though several situations should be considered, which cause the ultimate failure of the wall, such as large earthquake, the water rise behind the wall can be one of the critical conditions.

3.3.4 Modelling of soft rocks for centrifuge study

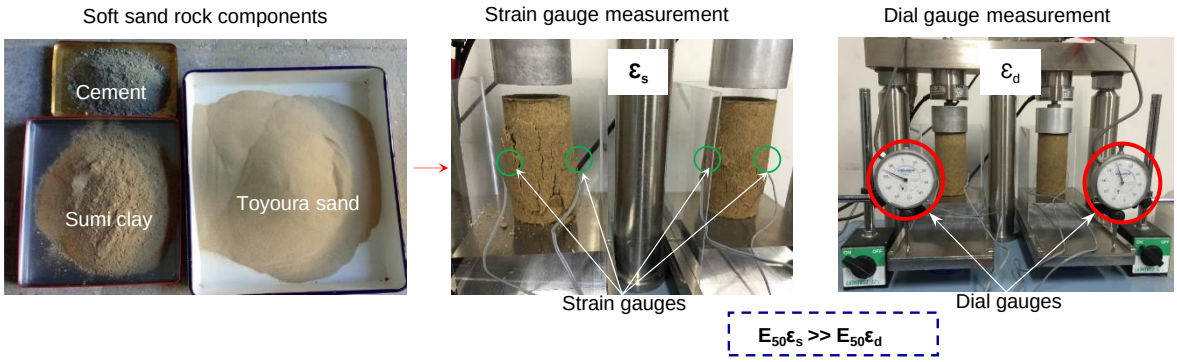

Figure 3.44 Unconfined compression test and sensor arrangements

Table 3-3 Physical and mechanical properties of model soft rocks

Property	Sand rock	Mud rock
Clay: Sand (wt. %)	30:70	100:0
Cement/dry soil (wt.%)	5.7	8.3
Water/solid ratio (%)	21.5	39
Water/Cement ratio (%)	395	510
Bulk density (kg/m^3)	2060	1820
Dry density (kg/m^3)	1715	1320

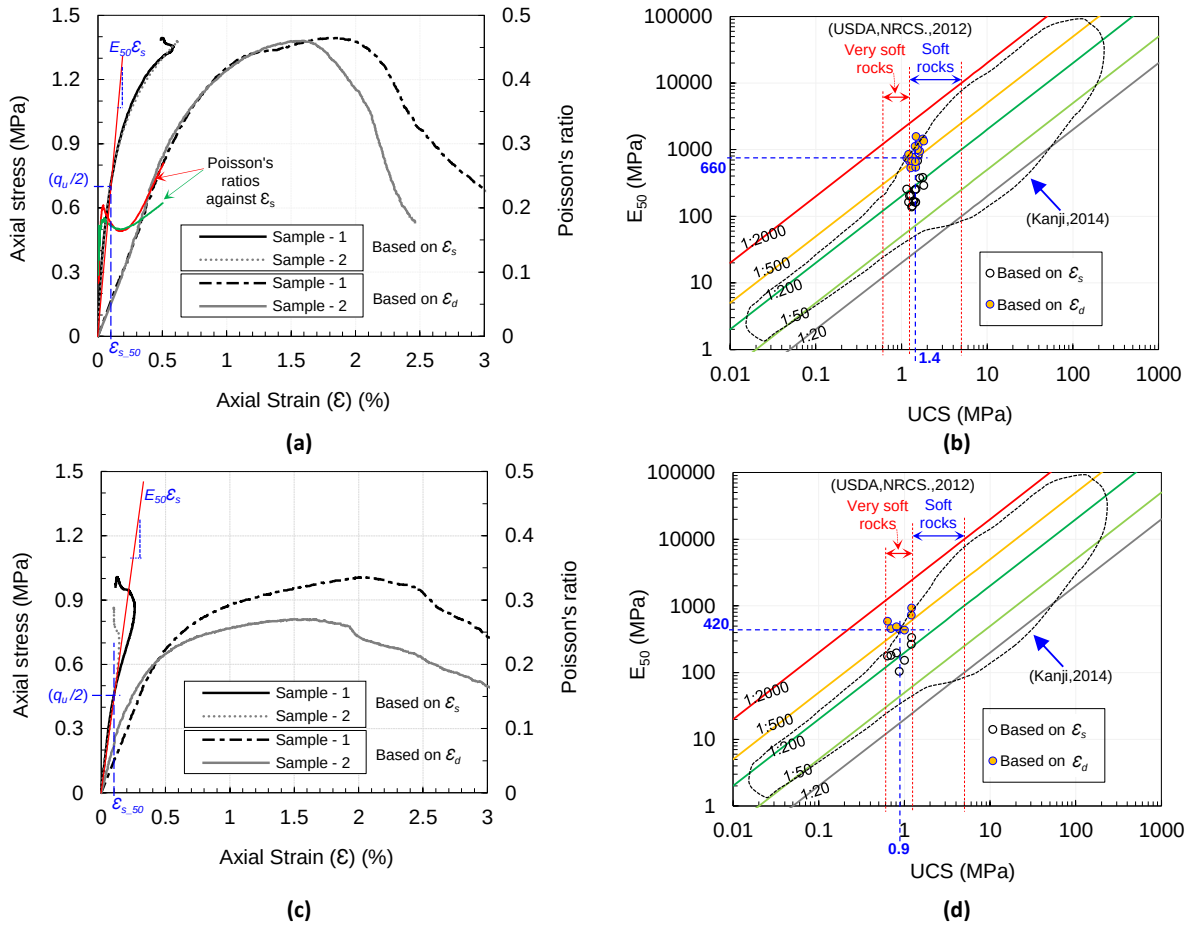

Figure 3.45 Stress-strain relation for model sand and mud rocks

According to Blyth and de Freitas (1984), soft rocks can be divided in to sandstones (Arenaceous), mudstone (Argillaceous) and calcareous rocks. The original constituent of mudstone is clay or muds, showing relatively low strength and stiffness as its existing state. Sandstone is a sedimentary rock formed by consolidation of sand cemented with clay and other minerals, which could exhibit a wide range of strength and stiffness depending on its moisture content, composition and degree of cementation (Irvine et al., 2015; Kanji, 2014). Based on the engineering classification (USDA- NRCS.,2012), rock materials with the unconfined compressive strength (UCS) of 0.6 MPa -1.25 MPa and 1.25 MPa - 5.0 MPa are defined as very soft rocks and soft rocks. The modelling of synthetic soft rock for experimental investigations has a long history (Johnston and Choi., 1986; Indraratna, 1990; Choo and Kim., 2016). The most of them have used cement treated soils to represent the mechanical properties of soft rock. As a part of the centrifuge study on CSTP walls, artificial soft sand rock was made by using Toyoura sand, Sumi clay (Sumitomo Osaka Cement Co., Ltd.), and high early strength Portland cement (Taiheiyo Cement Corp.) mixtures as shown in Figure 3.44(a). The model soft rock was made from the mixtures with mixing ratio shown inTable 3-3. The detailed procedures of modelling soft rocks are described in Kunasegaram et al., (2015). The mechanical properties of artificial soft rock samples were investigated by unconfined compression (UC) tests as shown in Figure 3.44 (b) and Figure 3.44 (c). The secant modulus (E50) of the rock samples were estimated based on strain gauge (Ɛs) (Figure 3.44 (b)) as described in Figure 3.45(a,c). It is important to note that the strain measured by dial gauge (Ɛd) (Figure 5(c)) substantially underestimate the real stiffness of the specimen due to bedding error as shown in Figure 3.45(a,c). Poisson's ratio of the model soft rock was measured by means

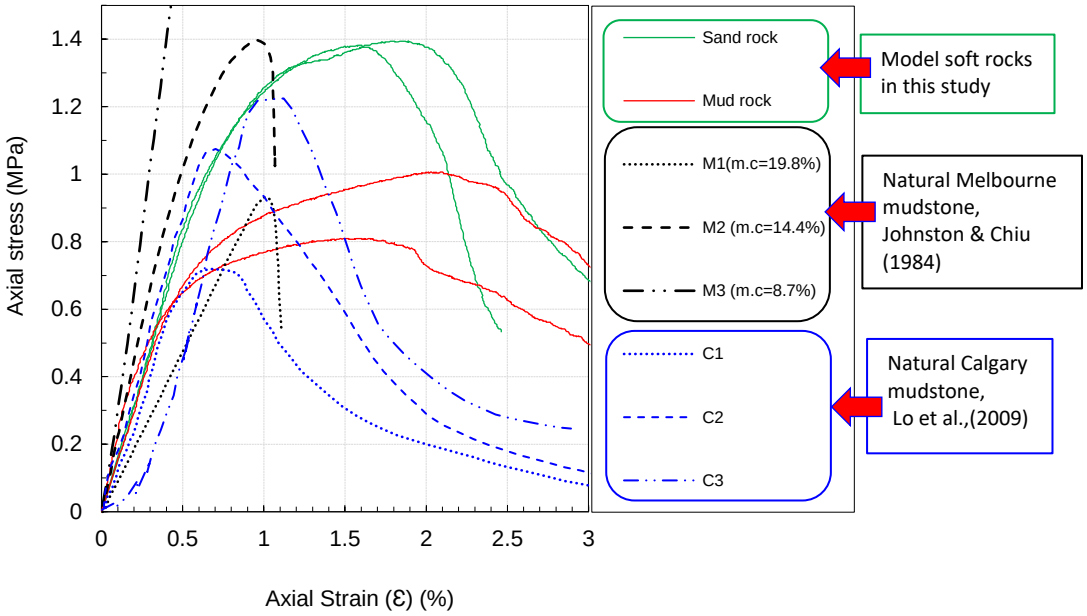

Figure 3.46 Comparison between natural soft rocks and model soft rocks in this study

of axial and transverse strains using the strain gauges. The estimated non-linear variation of Poisson's ratio against the axial strain ($Ɛ_s$) is illustrated in Figure 3.45(a). The observation reveals a contractive nature of model soft rocks up to $Ɛ_s$ =0.2% and dilative beyond the strain. Based on the estimated variation of Poission's ratio, a value of 0.2 was chosen for the estimation of shear modulus as described in the following section. The relationships between the strength and stiffness of soft rock measured from the UC tests are plotted with the locus of E50-UCS relation (Kanji, 2014) obtained from different soils and natural rocks in Figure 3.45(b,d).From Figure 3.45 (b) and Figure 3.45 (d) it can be confirmed that the strength and stiffness of the model rock corresponds to lower bound of soft rock. The average unconfined compression strengths (UCS) of 1.4 MPa (for sand rock),0.9MPa (for mud rock), and the corresponding secant stiffness (E50) of 660 MPa, 420 MPa of the model soft rocks also were obtained, which are used to calculate the indices described in the next section.

It should be emphasized that the model soft rocks in this study could be considered as a uniform rock mass with simple material properties in terms of strength and stiffness. Rocks are often fractured in real field conditions with more discontinuities, fissures and clay-filled joints due to several geological processes. These rock joint conditions make rock mass behavior very complicated, such as scale effects, stress dependency, anisotropy. Even in the weak rock, the dip direction affects the mechanical properties of rock mass (Richard et al., 2004). However, the effects of these complex behavior are out of the scope of this study and the model soft rock used in this study is considered as unweathered soft rock materials without clear discontinuities or joints.

The stress-strain behavior based on unconfined compression tests of model soft rocks in this study and natural soft rocks investigated in Melbourne (Johnston and Chiu.,1984) and Calgary (Lo et al.,2009) are illustrated in Figure 3.46. Three different Melbourne mudstone specimens (54mm diameter core samples) illustrated in the figure had different moisture contents at their existing state, the moisture content is about 19.8%,14.4% and 8.7% for the samples M1, M2 and M3 respectively. From the figure the influence of moisture content on the strength and stiffness of the specimen can be observed, smaller the moisture content larger the strength and stiffness can be seen as a common behavior while comparing the samples. The soft rocks tested

in Calgary was cube samples, the sample C1 (43x44x76), C2(37x45x69) and C3(38x33x67) had different dimensions in length, width and height respectively. From Figure 3.46 it can be seen that the sample C3 is highly influenced by the bedding error up to about 0.15 MPa axial stress and strain of 0.3%, beyond which a real initial stiffness of the specimen can be considered for the comparison purpose.

Comparing the behavior of natural rocks and the model Sand rock, Mud rock in this study quiet good agreement between model and natural rock can be seen up to an axial strain of 0.5%. beyond this level the model rocks exhibit more ductile behavior and the observation for natural rocks are more brittle. The strain level of 0.005 is much larger than the allowable design shear strains at the embedment level for the retaining walls (0.0001-0.001) as described in **Figure 2.33**. From this it can be confirmed that the behavior of model soft rocks in this study could be comparable under working loads or the allowable strain levels. However, at relatively large strain levels (>0.005) and the post peak behavior of model soft rocks showing more ductile deformations comparing to the natural rocks, which indicates that the failure behavior in natural rocks would be a catastrophic collapse than the model rocks. Furthermore, the observed steep post peak reduction in the natural rocks could be reduced under real field conditions, where certain confining pressures (either self-confinement of the rock or the confining pressures from surcharge pressures) could control the deformation characteristics of the rock.

3.3.5 Test conditions and retaining wall models

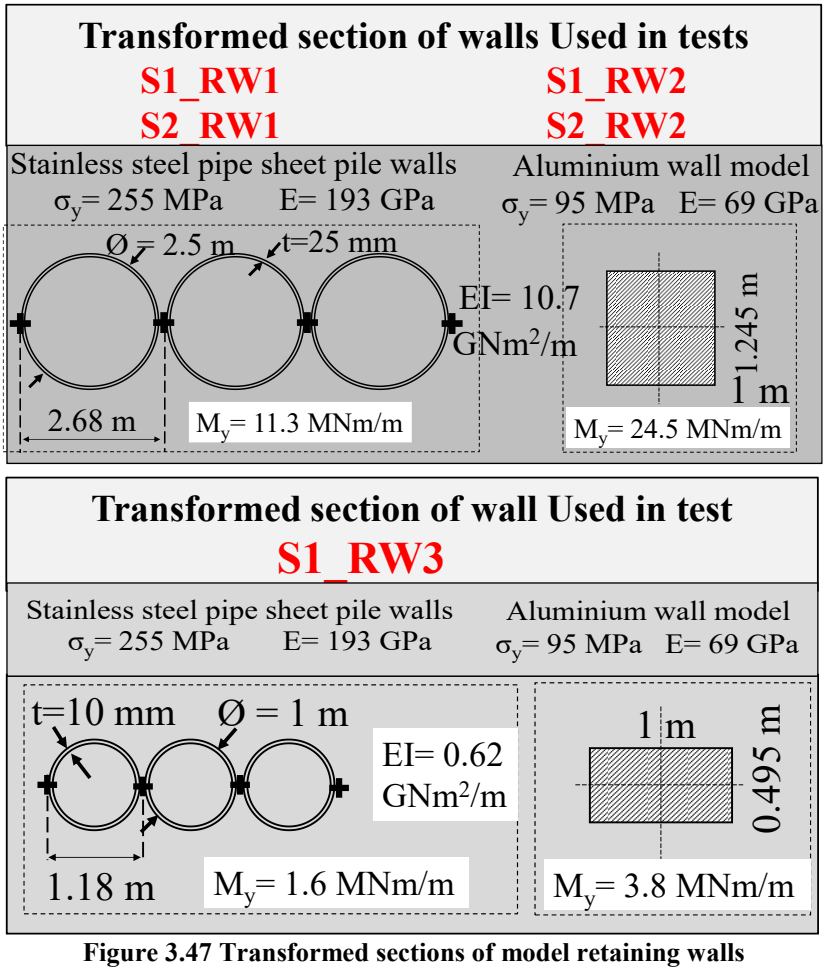

Figure 3.47 Transformed sections of model retaining walls

Table 3-4 Test conditions

Test code	Retain height, H (m)	Embedment depth, d_e (m)	Wall EI (GNm^2/m)	Rock q_u (MPa)	Rock E_{50} (MPa)	Chang's β value (1/m)	$3/\beta$ (m)	E_e/G^* (Randolph, 1981)	d_{e_r} and d_{e_s} (m) (Randolph,1981) (Carter&Kulhawy,1992)	d_e/β
S1_RW1	12	2.5	11.1	1.4	660	0.35	8.7	44	0.9 ~ 7.4	0.88
S1_RW2	12	3.0	11.1	1.4	660	0.35	8.7	44	0.9 ~ 7.4	1.05
S1_RW3	9	1.8	0.65	1.4	660	0.7	4.3	40	0.3 ~ 2.9	1.26
S2_RW1	12	2.5	11.1	0.9	420	0.3	9.7	69	1.0 ~ 8.4	0.75
S2_RW2	12	3.0	11.1	0.9	420	0.3	9.7	69	1.0 ~ 8.4	0.90

This chapter reports the results of five centrifuge model tests on large diameter CSTP walls embedded in soft sand rock as described in

Table 3-4. All dimensions and the properties of the model walls given in the table are described in a prototype scale for 50 g models. The sheet pile wall models represent a stiff CSTP wall with a retaining height (H) of 12 m, 9m and the embedment depths (d_e) of 2.5 m, 3 m and 1.8m respectively. Model sheet pile wall was made up of an aluminium (*A5052-O*) alloy plate having the yield strength (σ_y) of 95 MPa and the Young's modulus (E) of 69 GPa. A detail description of the sheet pile wall and the sensor arrangements are illustrated in Figure 3.48 and Figure 3.49.

The model sheet pile wall was designed to replicate the flexural rigidities (EI) of steel tubular pile walls with the diameter (Ø) of 2.5 m, thickness (t) of 25 mm and(Ø) of 1.0 m, thickness (t) of 10 mm as shown in Figure 3.47. Considering the currently available technology for the installation of large diameter piles such as Gyro-press method (IPA, 2016), 0.18 m gap between two piles is inevitable. Therefore, in the modelling of equivalent rectangular section, an effective width of 2.68 m,1.18 m was considered for one pile. With this simplification from actual CSTP wall to the model wall with solid aluminium plate, yielding bending moment (M_y) of the model wall was larger than that of the CSTP as shown in Figure 3.47.

The investigated model embedment depths in this study were much smaller than the minimum requirement ($3/\beta$) estimated from the Chang's design method (ASP, 2009). Otherwise the large wall movement could not have been created in the model setup used. The β-values derived from Chang's method (Chang, 1937), which is widely known in Japan, is calculated by Equation 1.

$$\beta = \left(\frac{k_H}{4EI} \right)^{1/4} \quad \text{.....equation 3.5}$$

$$k_H = k_{Ho} \left(\frac{B_H}{0.3} \right)^{-3/4} \quad \text{.....equation 3.6}$$

$$k_{Ho} = \frac{4}{0.3} E_s \quad \text{.....equation 3.7}$$

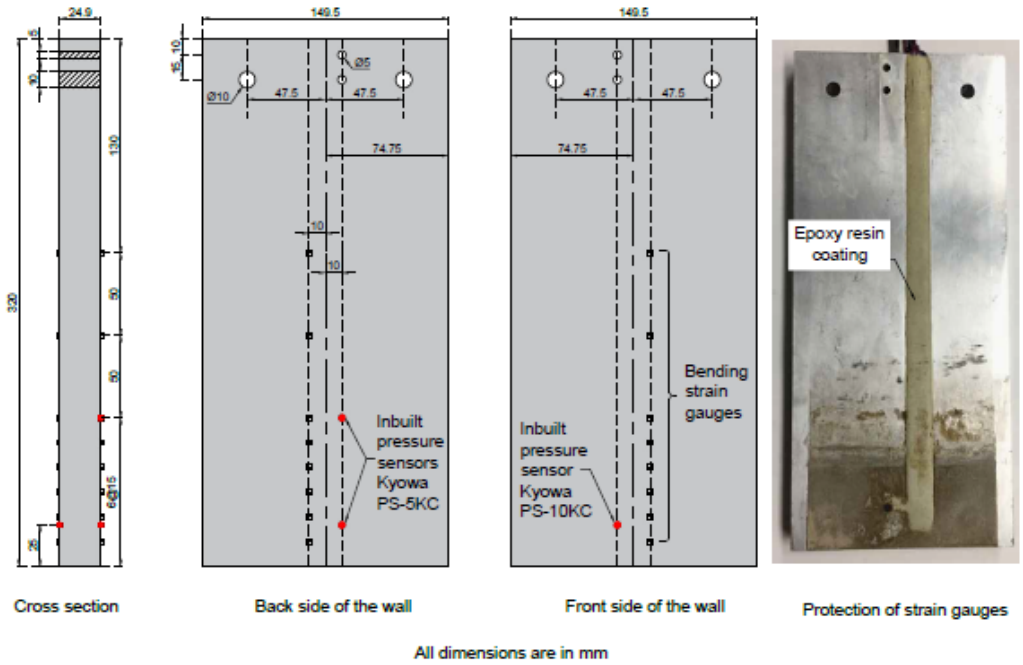

Figure 3.48 Model walls used to retain 12 m backfill

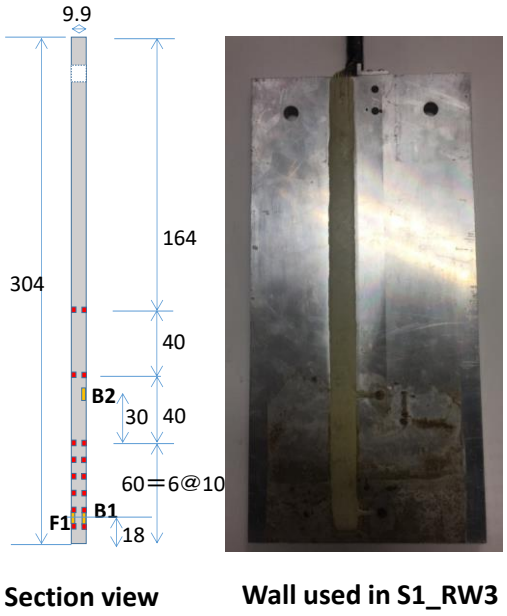

Figure 3.49 Model sheet pile used to retain 9 m backfill

Where k_H is the coefficient of horizontal subgrade reaction in uniform semi-infinite elastic medium (geo-material), B_H is wall width, k_{H0} is the k_H value measured by plate loading with 0.3m width, and E_s is Young's modulus of the geo-material. In ASP (2009) design code, B_H = 10m is assumed as the upper limit of the wall width in the estimation of β –values for the

cantilever type sheet pile walls. Using the material properties and dimensions, β value was calculated and shown in

Table 3-4 together with minimum required embedment depth in the design ($3/\beta$). Randolph (1981) proposed a critical pile length and diameter ratios (D/B), over which the pile behave as a flexible slender pile, as a function of relative pile stiffness ratio to that of soil (E_e/G^*, E: effective Young's modulus of pile, G*: equivalent shear modulus of soil). While Cater and Kulhawy (1992) proposed another critical D/B ratio, below which the pile behaves as a rigid body. The E_e/G^* value obtained from the model conditions and the critical pile depths for rigid and slender piles (d_{e_r} and d_{e_s}) assuming the B=2.5 m, 1 m are also shown in

Table 3-4. It can be confirmed from the table that $3/\beta$ value is quite close to the critical depth of slender pile and the d_e of the model walls are almost in the mid value of the two critical depths.

3.4 Experiment procedures and observed behaviors

3.4.1 Excavation and water feeding

In the experiment, the model was gradually accelerated and the equilibrium condition was achieved at 50 g centrifugal acceleration at an effective radius of 2.09 m. While maintaining the equilibrium conditions over a certain period of spinning, the excavation in the wall front was simulated by draining out the water from the wall front rubber bag to the storage tank by opening the solenoid value (Figure 3.40). The sequence of excavation (water draining) and loading (water feeding) processes are illustrated in Figure 3.50 (a). Upon completion of the excavation process, the model wall subjected to the pressure from the retained sand was in equilibrium by the horizontal resistance of the embedment part with certain amount of induced strains in the wall. Thereon to study the behavior of walls under the ultimate loading conditions, the additional load was applied by feeding the drained water from the storage tank to the backside rubber box. The water feeding was done by the application of air pressure to the storage tank manually with the monitoring of water pressure at the bottom of the rubber box (Figure 3.40). The excavation depths (Z_e) and the loading heights (h_w), as well as the change of tank pressure were monitored using PPTs (Figure 3.40). Figure 3.40 (c) illustrates the variation of water height behind the wall against the applied air pressure in the inflight storage tank. The air pressure was increased by a manual operation while monitoring the PPT responses in the backside sand bag as well as inside the storage tank. The water pumping or feeding required certain head difference in 50g environment, to pump the water from a low elevation tank to the upper elevation of backside rubber bag. The required head difference was about 300kPa, which can be observed from the onset of increment in loading height from a value of zero as shown in Figure 3.40(c). Meanwhile the wall top displacements and the surface settlements also were recorded using LDT and potentiometers respectively. The variation of measured excavation depth (Z_e) and loading height (h_w) with time, and the relationship between the loading height and the tank pressure are illustrated in Figure 3.51(a), Figure 3.51(b)and Figure 3.51(c) respectively. The excavation process by draining water exhibits almost identical unloading rate as seen in Figure 3.51(a). On the other hand, the difficulty in monitoring and controlling the tank pressures resulted in noticeable differences in the time variation of loading height (Figure 3.51(b)). This difficulty is also seen from the difference in the tank pressure and h_w relation in Figure 3.51(c).

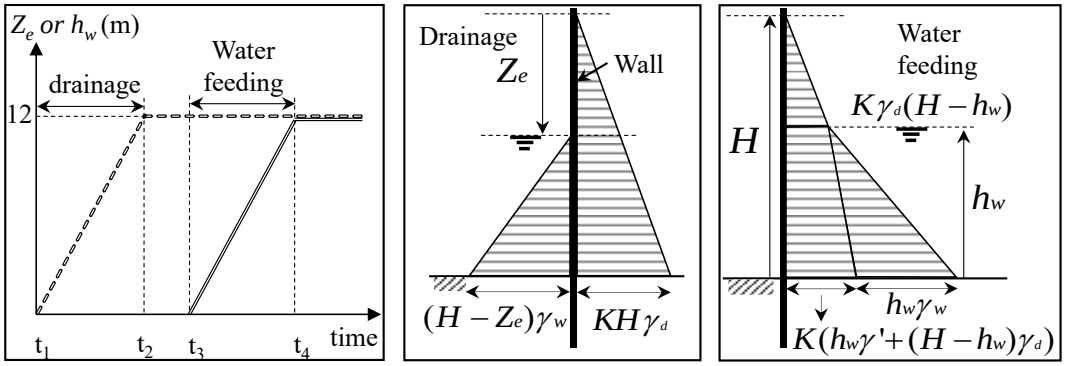

(a) (b) (c)

Figure 3.50 (a) Loading sequence and the change of earth pressure during (b) excavation,(c) loading

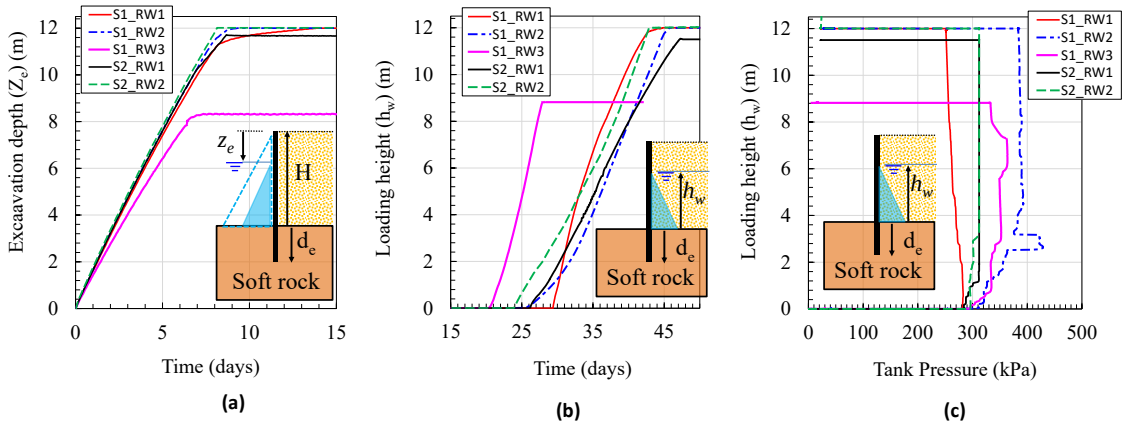

Figure 3.51 Variation of (a) excavation depth and (b) loading height against time and (c) the variation of loading height against tank pressure

3.4.2 Observed wall behaviors

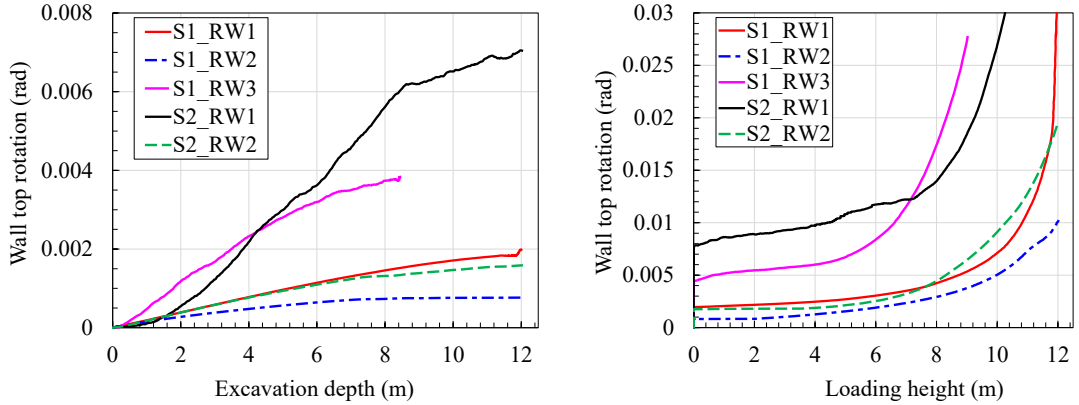

Figure 3.52 Change of wall top rotation with excavation depth and loading height

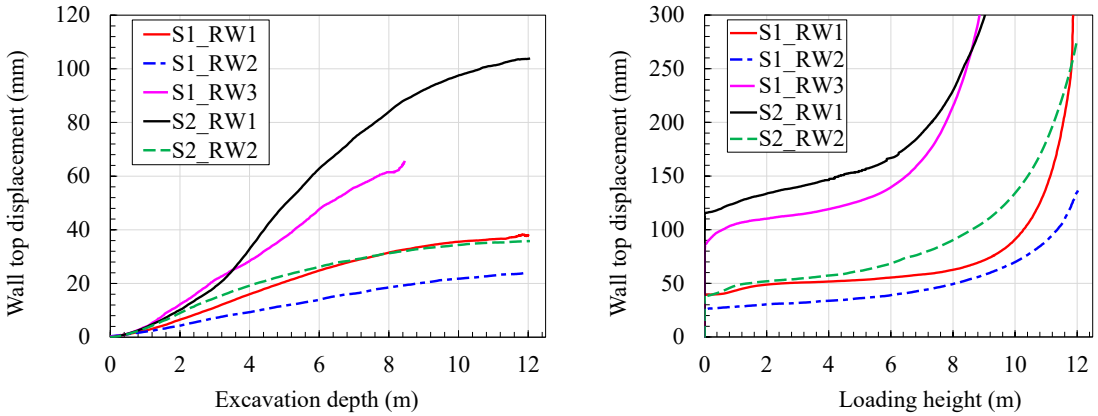

Figure 3.53 Variation of measured wall top displacement with excavation depth and loading height

The way of increasing wall top rotations and displacements with the excavation depth and loading height are shown in Figure 3.52 and Figure 3.53 respectively. Unlike a convex shape displacement and rotation profile with the increase of excavation depth in field, a concave shape behavior can be observed in all test cases. Attributing to the nature of excavation by draining a liquid with a constant lateral pressure coefficient of unity and zero stiffness, about 75% of the initial lateral load from water was removed in the first half depth (0-6 m) of excavation depth (Z_e). This loading nature caused relatively large wall displacement till Z_e=6 m and comparatively smaller displacements in the subsequent half of excavation process, resulting concave shapes of displacement and rotation curves. Considering the difference in unloading by fluid and the real field excavations, in real field excavation with the lateral movement of wall mobilized passive earth pressure also increases. Which could control the wall deflections at initial stage of excavation with a larger supporting height of earth in wall front. This phenomenon results a convex shape load displacement behavior in real field excavation. However, it cannot be expected from a fluid with zero stiffness. Considering the uncertainty in the initial condition of the modelling process in this study, a nonlinear variation of earth pressure coefficient with the excavation depth was selected as explained in subsequent sub chapters. There was an interval between the excavation and loading processes about 12mins. The creep displacement ($\Delta\delta_t$) and rotation ($\Delta\theta_t$) observed during the interval are discussed under a sub chapter in the following chapters.

3.4.3 Initial conditions

Measured bending moments from the initial condition to the end of loading for the walls embedded in sand rock and mud rock, representing 2.5m CSTP walls are illustrated in Figure 3.54 and Figure 3.55 respectively. Where the sub figures indicated by (a) and (b) are corresponding to the observations during excavation and loading (by water feeding) stages. Owing to the damage of 4th and 5th strain gauges from the bottom tip of the wall, reliable strain measurements could not be made at the locations closer to the excavation bottom (EB) in both experiments. However, in Figure 3.54 (a) and Figure 3.55(a) it can be confirmed that negative bending moments were generated near EB from the initial state. As the excavation and loading progresses, the bending moments above EB monotonically increase. While below the excavation bottom (embedded portion of the wall), a similar increment trend can be seen in the response of strain gauges located below the rock surface level and at very shallow depth (3rd gauge from the wall tip) during excavation and loading process from Figure 3.54 (b) and Figure 3.55(b). However, at deeper locations below the rock surface level, strain gauges showing much fluctuated variations. Measured bending moments by the 2nd and 1st gauges from the wall tip show, increase and decrease with different increment trend, resulting in "*S*" shape bending moment profile with depth below EB. There are

several reasons can be considered for this complicated moment variations. The strain gauges on the wall were coated by rigid epoxy resin with thickness about 1mm as shown in Figure 3.48 and Figure 3.49. It is important to emphasize that the coating portion ends with the deepest location of the strain gauge below the rock surface level as shown in the picture of model wall given in Figure 3.48 and Figure 3.49. Beyond this location to the bottom tip of the wall could be considered as kind of tapered section due to 1mm thickness of coating. Some force locally acting at this location on the coating from the rock might affect the strain measurement. The stress concentration on the bottom edge of coating can be caused by the relative vertical displacement between the wall and rock. As the vertical movements at the both side of wall surface tend to occur in opposite directions, the change of wall displacement mechanism from the translation dominated one to the rotation dominated one as discussed in subsequent chapters, could also affect the strain measurement.

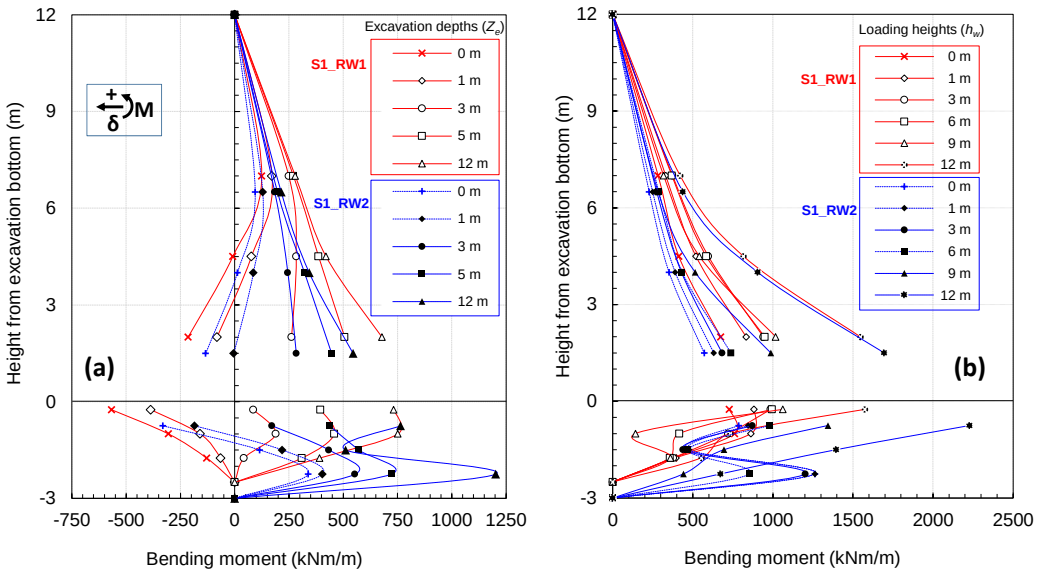

Figure 3.54 Measured bending moments of 12m height retaining walls in sand rock

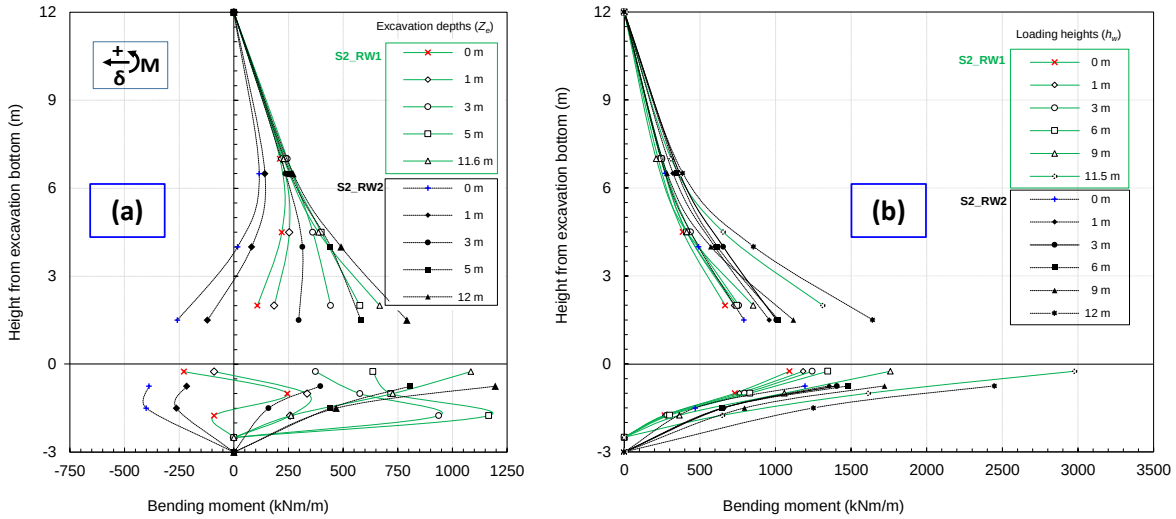

Figure 3.55 Measured bending moments of 12m height retaining walls in mud rock

As the rock-wall relative displacement increases in the embedded zone, the 'S' shape vanishes and a linearly increasing trend appears as shown in from Figure 3.54 (b) and Figure 3.55(b). Perhaps the observation from the beginning of excavation to the end of loading could be

attributed to the progressive dilation and mobilization of combined shear and adhesion in the rock-wall interface. As described in Williams and Pells (1981), the dilation in the rock socket interface increases with increasing shear stress and remains constant up on mobilization of peak shear. Williams and Pells (1981) also describes the loss of shear capacity due to the reduction of rock mass modulus from their vertical loading tests. In fact, the reduction of rock mass modulus would be much significant in the lateral loading and thereby the loss of side resistance due to the large deformations also could be considered in the abovementioned observations.

3.4.4 Estimation of lateral and moment load increments

As presented in previous chapters, due to the limitation of water drainage technique in modelling of excavation process, the small back ward movement occurred by the centrifugation. This movement made the wall earth pressure acting on the wall from the retained sand larger than the at-rest pressure and negative bending moment near the rock surface as shown in Figure 3.54 (a) and Figure 3.55(a) up to about 1m and 3m excavation depths respectively. These earth pressure and bending moments prior to the excavation are considered as the initial condition of the model before the excavation process.

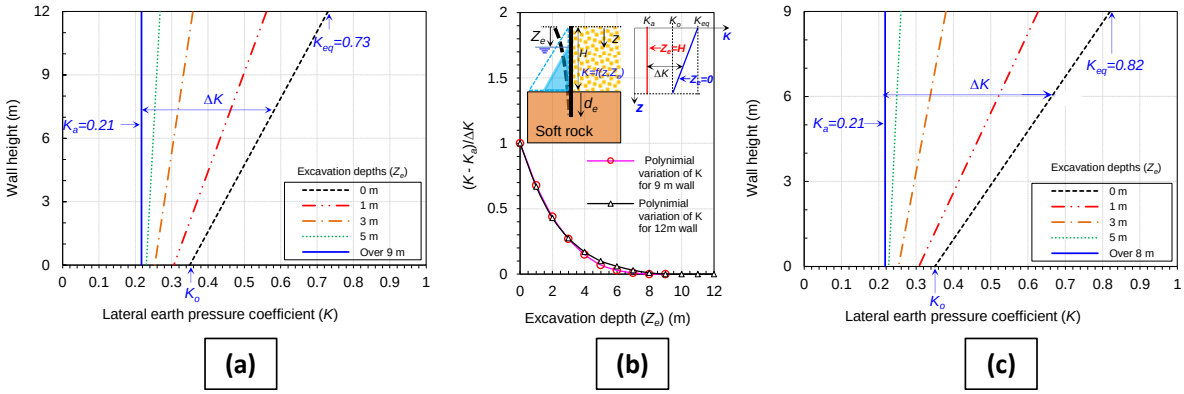

Figure 3.56 (a,c) Assumed variation of earth pressure coefficient along the wall and (b) Polynomial variation of (K-K_a)/ΔK against excavation depth

To estimate the lateral thrust force and moment load acting on the wall from the initial conditions in the excavation and loading processes, the following assumption is introduced. In the assumption, the lateral earth pressure coefficient (K) along the wall decreases linearly with depth from a value of K_{eq} at wall top to at-rest coefficient K_o ($(1-sin\Phi)$ = 0.35) at the excavation bottom as illustrated in Figure 3.56(a) and Figure 3.56(c). The backward wall elastic deflection due to centrifugation and only one known value, that is, the wall bending moment at the excavation bottom, is the base of the assumption. K_{eq}= 0.73(12m wall) and 0.82 (9m wall) of initial profiles were estimated from the moment equilibrium with the wall bending moment of -400 kNm/m(for 12m wall) and -88 kNm/m (for 9m wall) at the excavation bottom. Which was estimated by the extrapolation from the measured bending moments above the excavation bottom (Figure 3.54(a) and Figure 3.55(a)). The real earth pressure profile might not be so simple and some difference between four tests can be seen in Figure 3.54 (a) and Figure 3.55(a). However, as the measured bending moment profile is not so accurate to allow the more precise analysis, the simple common assumption (Figure 3.56(a) and Figure 3.56(c)) was employed in this study. But the initial earth pressure profile calculated from this assumption could capture the shape of bending moment profile. Furthermore, using the same profile for the two tests, the estimated load increment can be used as a common load index for the excavation and loading processes in the discussion.

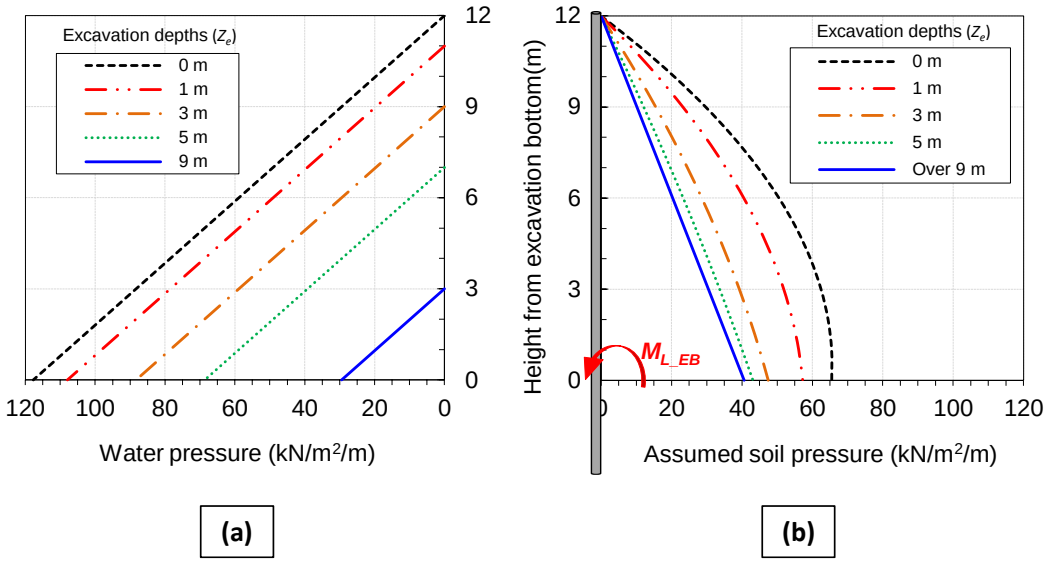

Figure 3.57 (a) Water pressure in the wall front and the (b) assumed earth pressure behind the wall at the initial condition prior to the excavation for 12m retained height wall

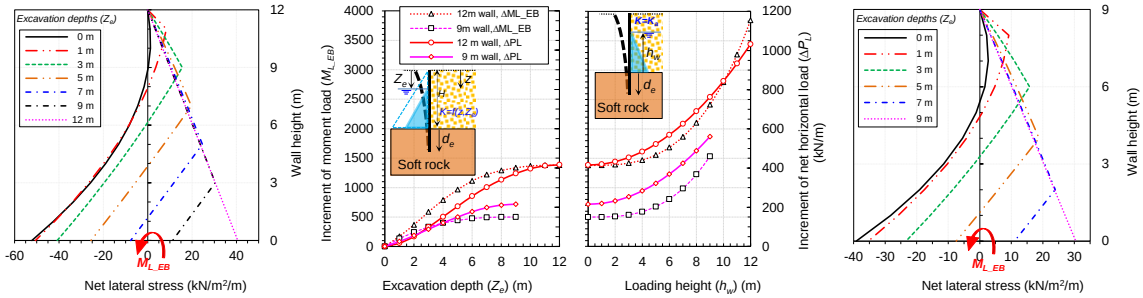

Figure 3.58 Calculated net pressure distributions at different embedment depths for (a) 12m wall, (c) 9m wall and the (b) increment of net horizontal and moment loads above the excavation bottom

Typical depth profiles of the assumed applied earth pressure behind the wall with 12m retained height at different excavation depths are drawn in Figure 3.57(b). Rankine's active state with earth pressure coefficient, (K_a = 0.21) along the wall is assumed to reach at the excavation depths of 9m and 7m for the walls with 12m retained height and 9m retained height respectively. Figure 3.57(a) describes the hydrostatic pressure in the wall front at different levels of excavation.

The Rankine's pressure can be reasonably used as active state, since the latex rubber back with lubrication can create the friction less condition on the wall surface. The transition of earth pressure coefficient at specific depth from the initial condition to the Rankine's active states during the excavation process was estimated based on the assumption that (K-K_a)/ΔK change with Z_e as a polynomial function (Figure 3.56(b)) till Z_e =9m, Z_e =7m for the walls with 12m and 9m retained heights respectively. Here ΔK is the difference between the initial K value and K_a. This polynomial function was captured from the nearest measured strains above the excavation bottom. Over Z_e=9m for 12m wall and 7m for 9m wall in the excavation process, Rankine's active state ($K = K_a$) is assumed for all subsequent processes. The variation of (K-K_a)/ΔK with Z_e is illustrated in Figure 3.56(b). Based on the abovementioned assumptions, net horizontal load (P_L) acting on the wall above the excavation bottom level was calculated as shown in Figure 3.58 (a) and Figure 3.58 (c) for the walls with 12m and 9m retained heights respectively.

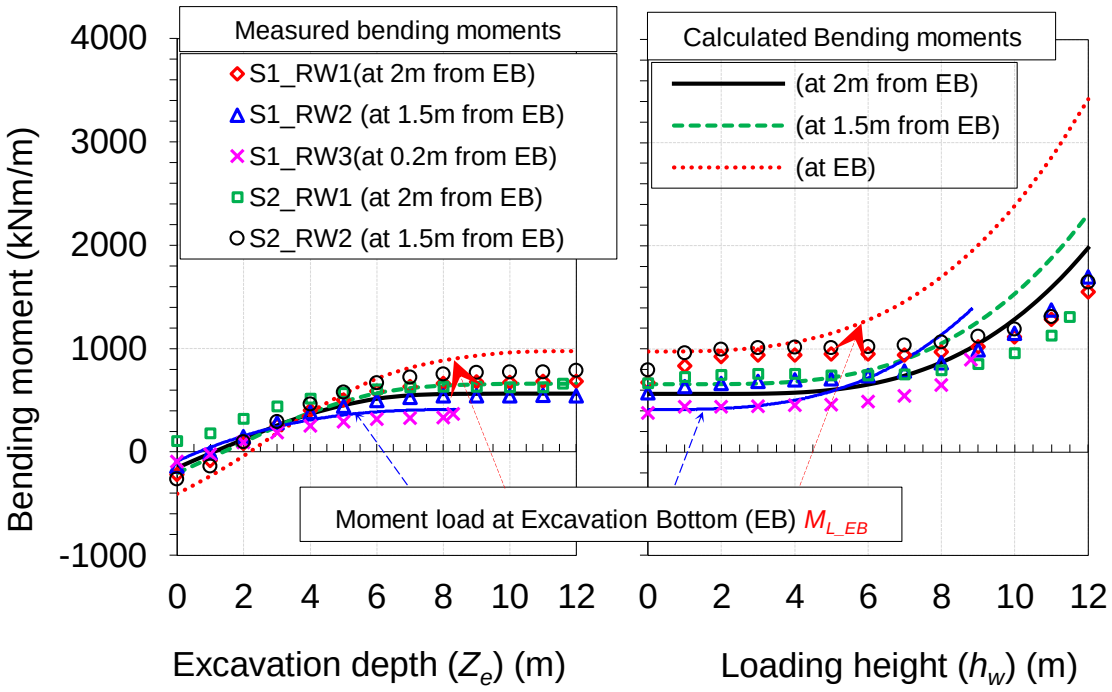

Figure 3.59 Comparison between the measured and calculated bending moments at different locations of the wall

Increment of horizontal load was estimated (ΔP_L) from the initial conditions (Z_e =0m) of net pressure distribution (Figure 3.58 (a and c)) to the end of excavation (Z_e =12m). The horizontal load during the loading process (water feeding behind the wall) also estimated by assuming K_a condition behind the wall during entire water feeding process. From the estimated increment of lateral load(ΔP_L), corresponding moment load increment (ΔM_{L_EB}) applied a the excavation bottom level also estimated. Variations of both increment of lateral load and moment loads are illustrated in Figure 3.58(b). From the loading mechanism adopted in this study, the lateral thrust on the wall can be increased by 2.5 times from the end of excavation to the end of loading as shown in Figure 3.58 (b).

Using the assumed earth pressure variation in the retained sand, bending moments of the wall were calculated and compared with the measured bending moment at the location of 2.0m (S1_RW1, S2_RW1), 1.5m (S1_RW2, S2_RW2) and 0.2m (S1_RW3) above the excavation bottom in Figure 3.59. Though some discrepancy can be seen at the early stage of loading of S1_RW1 and S2_RW2 till h_w=6m, the calculated bending moments well predict the variation of measured bending moments especially in the excavation process of all tests and the loading process of S1_RW2, S1_RW3 and S2_RW1. Based on this confirmation, the calculated bending moment at the excavation bottom (M_{L_EB}) will be used as a net applied moment load on the wall from the retained soil, which could be used as a common loading index bridging

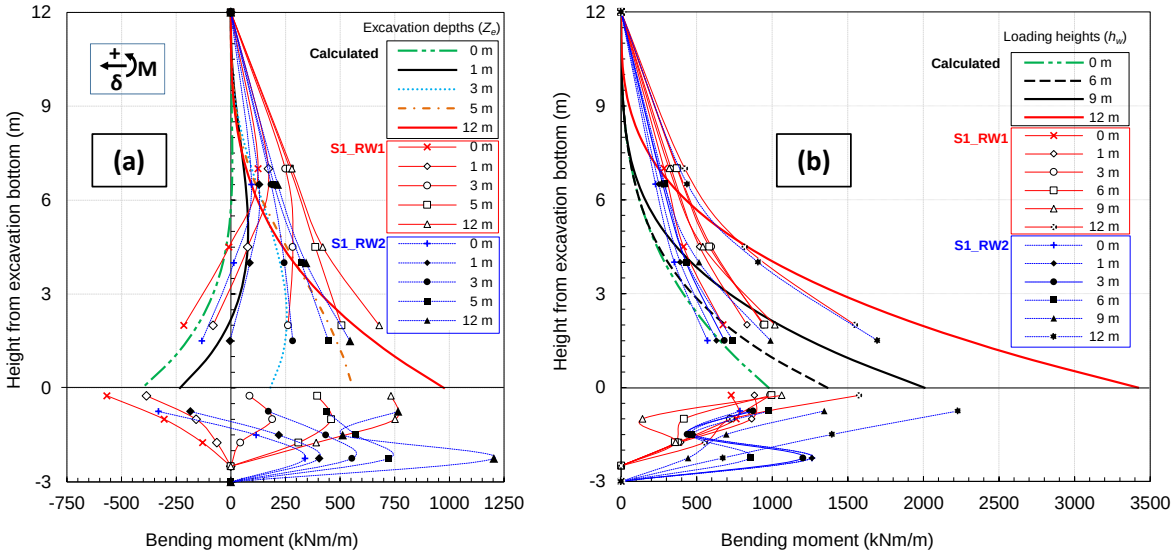

Figure 3.60 Measured and calculated bending moment profiles during (a) excavation and (b) loading for 12m walls embedded in sand rock

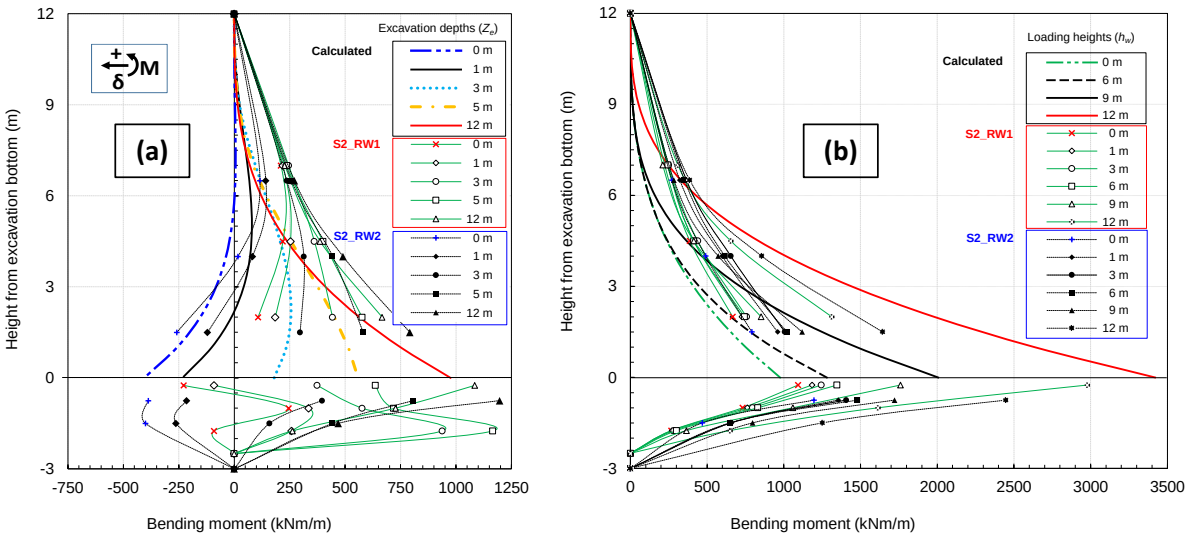

Figure 3.61 Measured and calculated bending moment profiles during (a) excavation and (b) loading for 12m walls embedded in mud rock

the excavation and loading processes. The variation of M_{L_EB} is also shown in Figure 3.59 for the walls with 12m and 9m retained heights. The calculated bending moment profiles above the excavation bottom and the measured bending moment profiles along the wall at different excavation depths and loading heights are plotted in Figure 3.60, Figure 3.61 and Figure 3.62. At the wall height from 0 to 2m, only theoretical bending moments are plotted due to the failure of the gauges in 12m wall. Based on Figure 3.60 and Figure 3.61, Although significant difference exists between the calculated and the measured bending moments in the upper half of the retained height (6-12m), the variation between measured and calculated bending moment is relatively small in the lower half (0-6m) potion of the retained height. Especially closer to the excavation bottom level, which can be confirmed by referring the available measured bending moments closer to the excavation bottom level from Figure 3.60, Figure 3.61 and Figure 3.62. It also compared in Figure 3.59 for the available bending

moment data closer to the excavation bottom level. The actual variation of initial earth pressure coefficient along the wall height above the excavation bottom level must be more nonlinear in the trend corresponding to the wall displacements at different heights above the excavation bottom, however for simplicity a linear trend was assumed to estimate the possible earth pressure distributions. This could be the possible cause in the variations between measured and calculated bending moments along the wall. Consideration of a non-linear variation of initial earth pressure coefficients behind the wall could provide more realistic bending profiles closer to the measured ones. The assumed linear variation of earth pressure coefficients along the wall height, closely predict the wall bending near the excavation bottom level. Having this level of accuracy, the bending moments corresponding to the damaged strain gauges near the excavation bottom level were derived from the calculated bending profiles and illustrated in terms of increment of bending moments in Figure 3.63 and Figure 3.64 for the walls with 12m retained height.

Thanks to the good response of strain gauges in the wall S1_RW3, the increment of measured bending moment profiles along the wall (Figure 3.62) was utilized to estimate the deflection profiles by means of moment area theorem. Referring to Figure 3.62(a) the end moment caused by unbalanced forces is much smaller for the wall S1_RW3 compare to the walls with 12m retained height. Observed small end moments in the initial conditions could be attributed to two facts. The former is the wall flexibility and the mobilization of large passive pressures in the backfill soil, which could provide relatively large lateral resistance from the backfill sand and reduces the unbalance moment. The second reason could be the loading nature of hydrostatic pressures, which increase as a square function of water height. This phenomenon causes relatively large water pressures in the case of walls with 12m retained height compare to the wall S1_RW3.

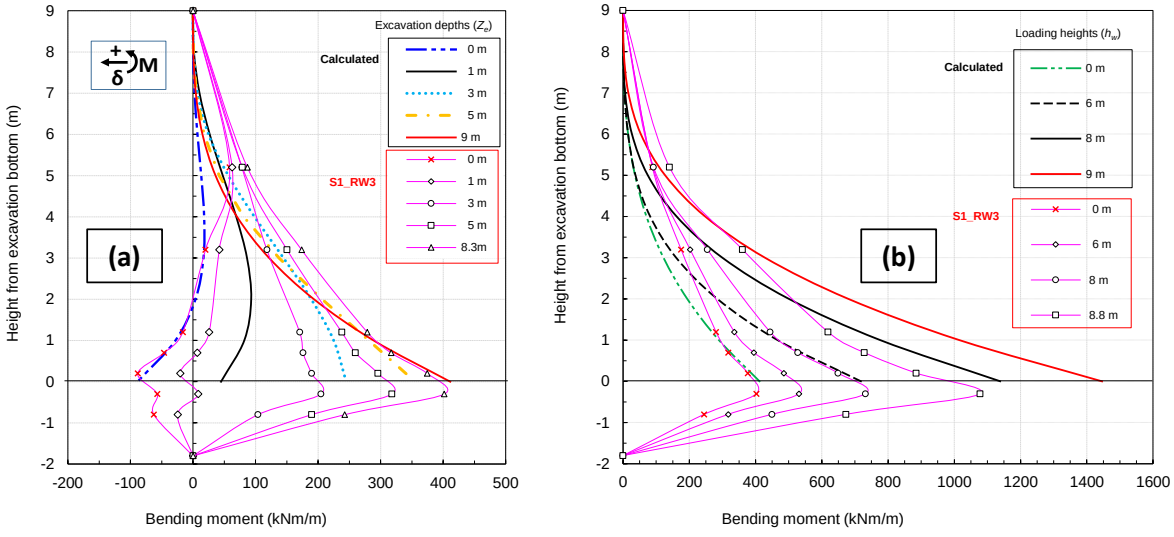

Figure 3.62 Measured and calculated bending moment profiles during (a) excavation and (b) loading for 9m wall embedded in sand rock

Comparing the measured and calculated bending moment profiles given in Figure 3.62, especially at the excavation bottom level, the variations are much are much smaller during excavation process (Figure 3.62 (a)) compare to the loading (Figure 3.62 (b)) process. Unlike the uncertainties in the excavation process, the lateral and moment load estimation in the loading process is more reliable and strait forward based on the measured PPT readings of water height and the assumption of full active pressure mobilization in the backfill sand.

However, significant difference in the calculated and measured bending moments at 6m,8m loading heights can be seen from Figure 3.62 (b) also the difference increases with the increasing loading height from 6 to 8m.

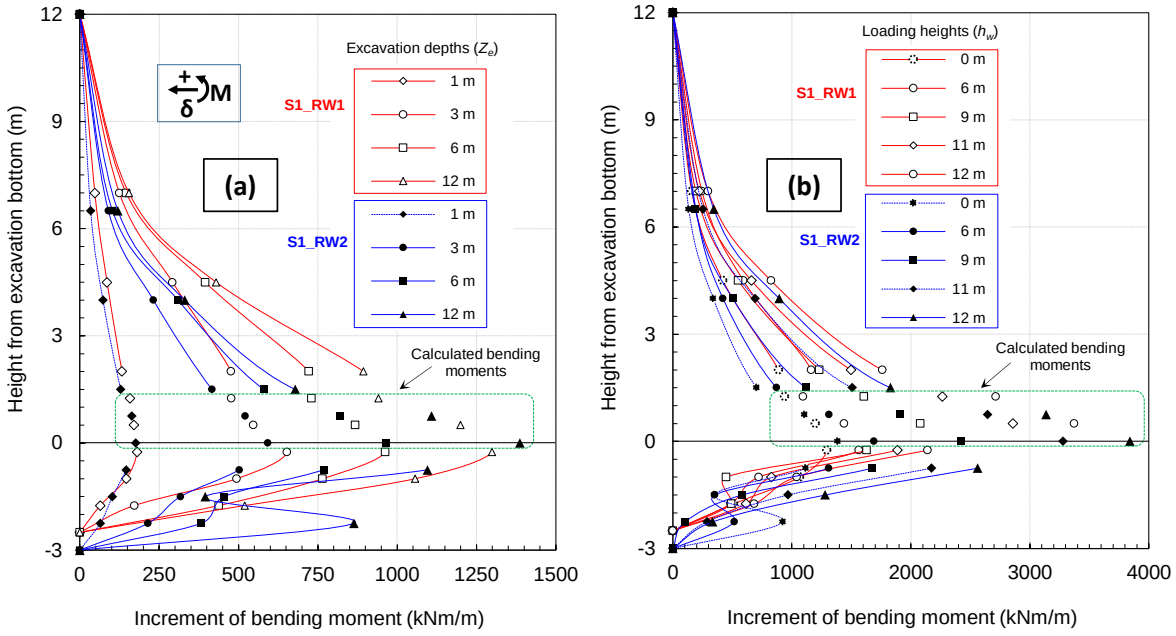

Figure 3.63 Increment of measured and calculated bending moment profiles during (a) excavation and (b) loading for 12m walls embedded in sand rock

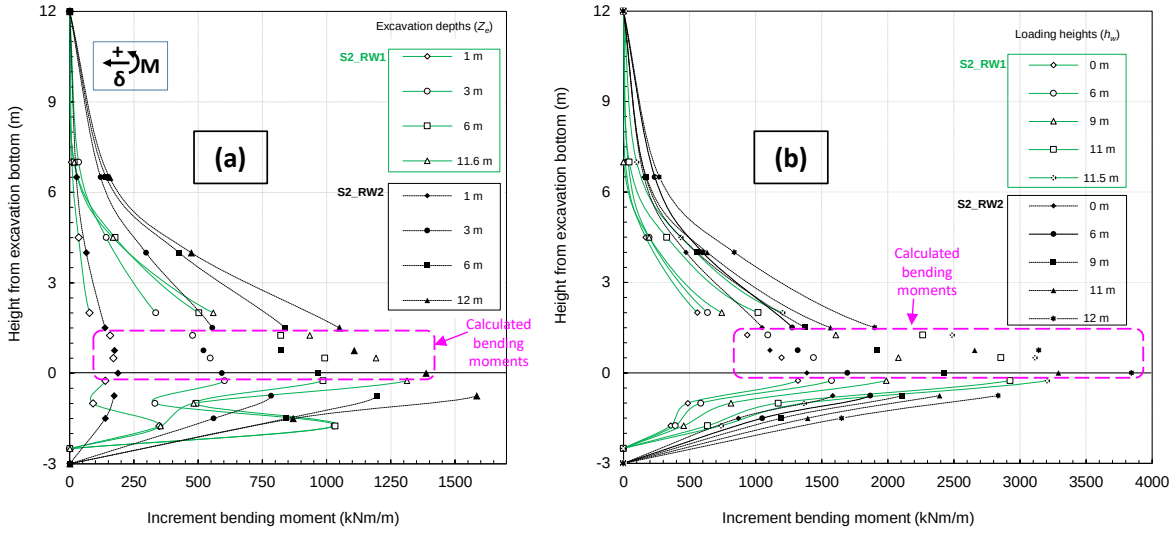

Figure 3.64 Increment of measured and calculated bending moment profiles during (a) excavation and (b) loading for 12m walls embedded in mud rock

The possible cause for this observation could be the lack of contact between the wall and the backside rubber bag, which expected to increase with the increasing rotations and the

displacement of the wall as a square function of the loading height, which can be observed from Figure 3.52.

Figure 3.63 and Figure 3.64 show the measured bending moment increment profiles merged with the calculated bending moment increments at the locations closer to the excavation bottom level, which are indicated with in a dotted box in Figure 3.63 and Figure 3.64. Meanwhile Figure 3.65 represents the increment of measured bending moment profiles from Z_e=0m to the end of loading for the wall with 9m retained height. Although some difference between measured and calculated ones are still seen in Figure 3.63 and Figure 3.64, overall trend of measured profile could capture by the variation of earth pressure profiles assumed in this chapter. The increment of calculated moment load acting at the level of the excavation bottom from the initial state before the excavation (ΔM_{L_EB}) is used as a common loading index to the increment of observed values, such as wall displacements and rotations, in the following section. Also for the estimation of deflection profiles based on moment are method, the measured bending moment profiles merged with the calculated one as described in Figure 3.63 and Figure 3.64 was used. It is important to emphasize that the calculation process by moment area method includes the observed 'S' shape variations below the excavation bottom level as shown in Figure 3.63(a) and Figure 3.64(b), which was the cause of certain local influences as described earlier. However, these 'S' shape bending profiles has no significant influence on the deflection profiles and the estimated deformations in the subsequent chapters attributing to a rigid body behavior of high stiff walls.

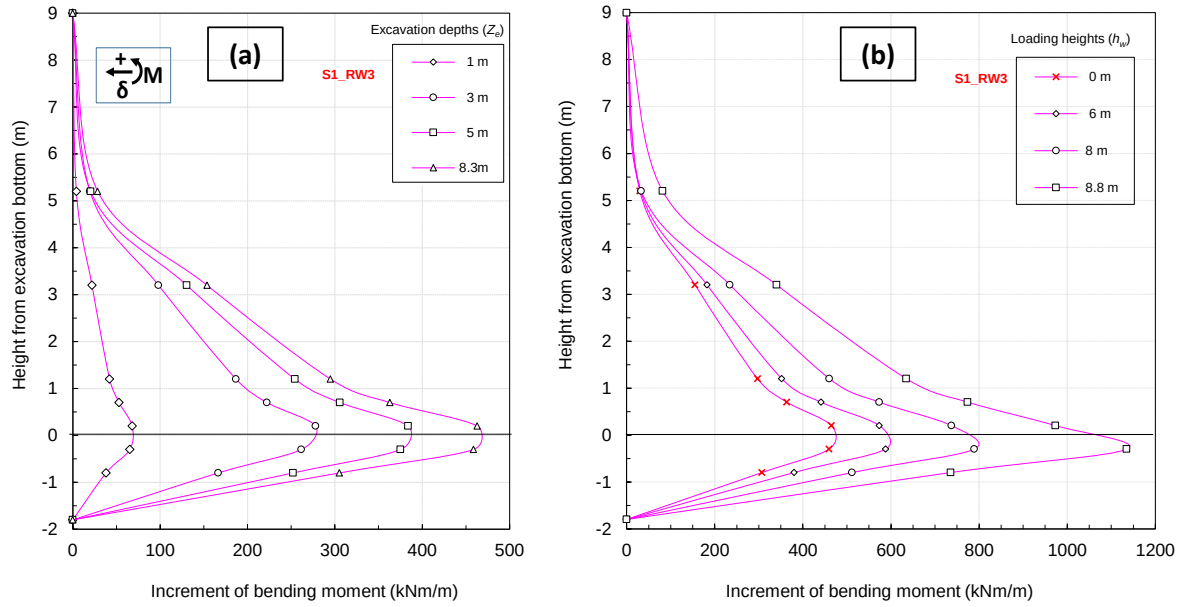

Figure 3.65 Increment of measured bending moment profiles during (a) excavation and (b) loading for 9m wall embedded in sand rock

3.5 Results and discussion

3.5.1 Wall deflection

Figure 3.66 illustrates the typical deflection profile of cantilever type retaining wall with the notations of displacements and rotations at the wall top (WT), the excavation bottom (EB) and the wall tip (BT) levels. As shown in the figure, wall top displacement (δ_t) can be divided into three components, i) displacement at EB, δ_{EB}, ii) displacement caused by the rotation at EB, $\theta_{EB}H$, and iii) displacement caused by the bending of wall above EB, δ_{t_b}. The

displacements and rotations included in the components can be obtained from the wall deflection curves estimated using measured increments of δ_t and θ_t from the initial conditions, at the wall top level and the bending increment profiles.

Variations of calculated increment of rotations and displacements at wall top (WT), excavation bottom (EB) and bottom tip (BT) against ΔM_{L_EB} are shown in Figure 3.67 and Figure 3.68 for walls with 12m retained height (S1_RW1,S1_RW2)in sand rock.

Similar variations of δ_t and θ_t against ΔM_{L_EB} and the estimated displacements and rotations at EB and BT for the walls in mud rock are presented in Figure 3.69 and Figure 3.70. Figure 3.71 depict the above mentioned variations for 9m thin wall embedded in sand rock. The estimated deflection profiles at different excavation depths and loading heights are depicted in Figure 3.72 for the walls S1_RW1, S1_RW2 and in Figure 3.73 for S2_RW1, S2_RW2. Meanwhile the Figure 3.74 illustrates the profiles of wall S1_RW3. The estimated displacements and rotations at EB, BT and rotational component of wall top displacement ($\theta_{EB}H$) are also shown in Figure 3.68, Figure 3.70 and Figure 3.71. ΔM_{L_EB} = 400 kNm/m in Figure 3.67(a) and Figure 3.68(a) corresponds the point that the bending moment at the excavation bottom was zero and the displacements before this point is considered as the elastic rebounds from the overstressed condition to the at-rest condition. These elastic rebounds were 9 mm, 6 mm for δ_t and 0.0004 rad, 0.0003 rad for θ_t in S1_RW1 and S1_RW2 respectively.

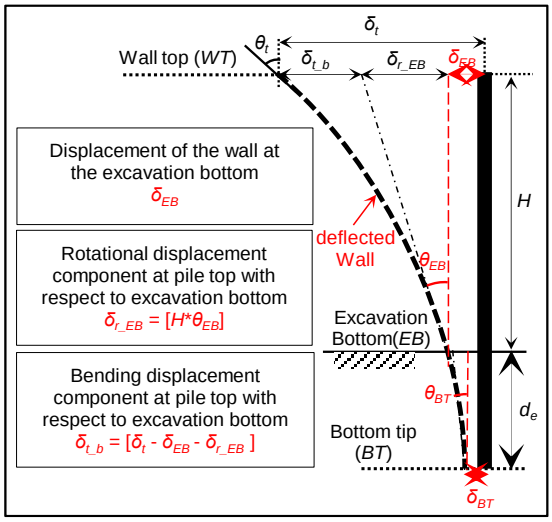

Figure 3.66 Typical deflection profile of cantilever type retaining wall

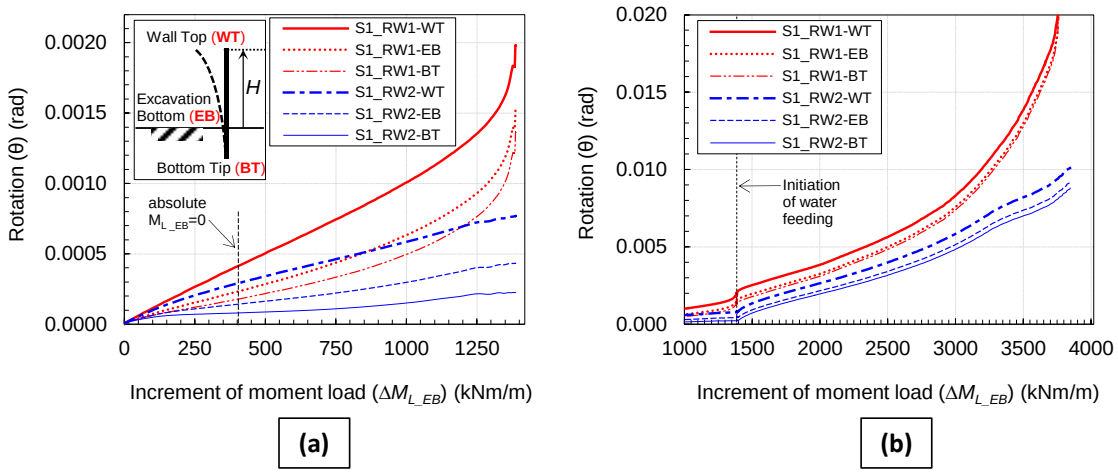

Figure 3.67 Variation of rotations at the wall top, excavation bottom and bottom tip against the increment of moment load during (a) excavation and (b) loading processes for 12m walls in sand rock

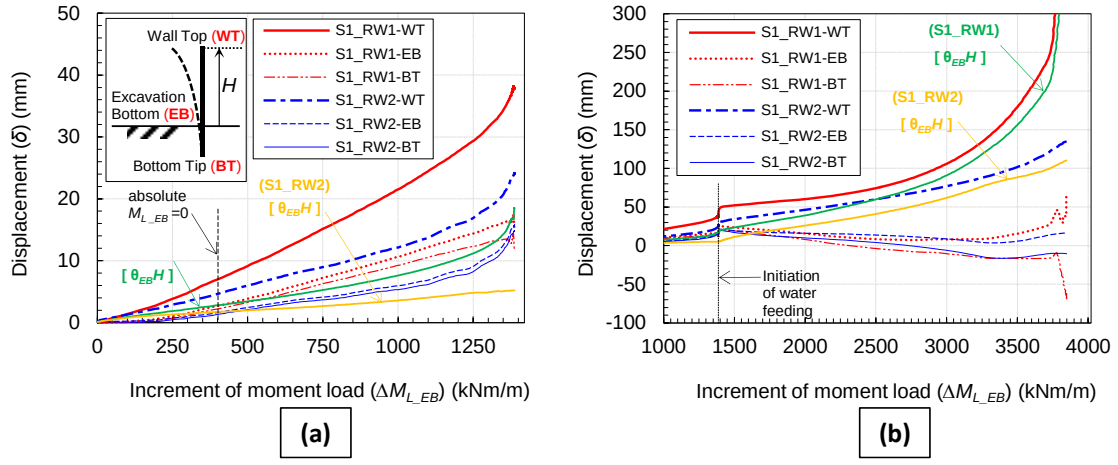

Figure 3.68 Variation of displacements at the wall top, excavation bottom and bottom tip against the increment of moment load during (a) excavation and (b) loading processes for 12m walls in sand rock

Increment of moment load about ΔM_{L_EB} = 300 kNm/m in Figure 3.69(a) and Figure 3.70(a) corresponds the point that the bending moment at the excavation bottom was zero for the walls in mud rock. These elastic rebounds were 8 mm, 7 mm for δ_t and 0.0004 rad, 0.0003 rad for θ_t in S2_RW1 and S2_RW2 respectively. The wall S1_RW3 showed the approximately zero bending moment at the excavation bottom at a moment load increment of 160kNm/m as indicated by the vertical dotted line in Figure 3.71.Where the elastic rebounds were 7 mm for δ_t and 0.0005 rad for θ_t. Even though, several features can be seen in the displacement behavior from the figures, it should be noted that due to high sensitive of the estimated displacement to the measured data, especially θ_t and uncertainty of bending moment profiles as explained before, there are relatively large error in the estimated displacement in the early stage ($Z_e \leq 1$m) of excavation process.

Considering the walls in sand rock, all displacement indexes, the displacements and rotations at three specific points (WT, EB and BT) were all smaller for S1_RW2 (d_e=3.0m) than S1_RW1 (d_e=2.5m) during the excavation process, e.g., 24mm and 38mm of δ_t. Subtracting the elastic rebound displacement, these values become 18mm and 29mm and 0.15% and 0.24% of the wall height, which are less than the commonly used allowable wall top displacement (50mm in IPA(2016)). These observations could suggest the applicability of the large diameter CSTP wall with relatively small embedment depth in hard medium.

During the excavation process, in S1_RW2 all rotations almost linearly increase with ΔM_{L_EB}, while in S1_RW1 the increasing rate of rotations against the moment load shows the gradual increase from ΔM_{L_EB} = 900kNm/m (Figure 3.67(a)). This trend of S1_RW1 is reflected in the increase of $\theta_{EB}H$ (=δ_{r_EB}) and δ_t (Figure 3.68(a)). In S1_RW2, nonlinear increase of δ_t can be seen from ΔM_{L_EB} = 1,100 kNm/m, but it could be attributed to the translational movement of wall (δ_{EB}). The difference of δ_t at the end of excavation of the two model is almost the same as that of $\theta_{EB}H$, 18.5mm for S1_RW1 and 5mm in S1_RW2. The above discussion points can confirmed from Figure 3.72(a). It can be confirmed from Figure 3.72 that, the walls deflected almost as a rigid body with small bending deformation especially in the loading process, which can be also confirmed from the same increments of rotation at the three location (Figure 3.67(b)).

Figure 3.69 and Figure 3.70 illustrates the above mentioned explanations for the walls embedded in mud rock. Corresponding deflection profiles are illustrated in Figure 3.73. Based on the observation of these figures the wall S2_RW1 could be characterized as a kind of unstable wall, which exhibits large rotations even with small increment of moment load as shown in Figure 3.69(a). The narrowing trend of rotations at EB and BT even during excavation process and almost no difference between the rotations at these two locations in the loading process clearly indicates the instability of the wall with a normalized embedment depth $d_e\beta$=0.75. However, the wall S2_RW2 exhibits relatively small rotations and the behavior is more or less similar to that of S1_RW1 in sand rock. Which can be even confirm from the observations in Figure 3.52 and Figure 3.53.

Observed clear difference between the rotations at EB and BT for the thin wall S1_RW3 in Figure 3.71(a) clearly indicates the influence of less stiffness and the relatively higher bending of the wall compare to the rigid walls, which can be observable from Figure 3.74(a). It also indicates the requirement of large diameter piles with higher flexural stiffness to resist the loads from relatively large retained height of earth.

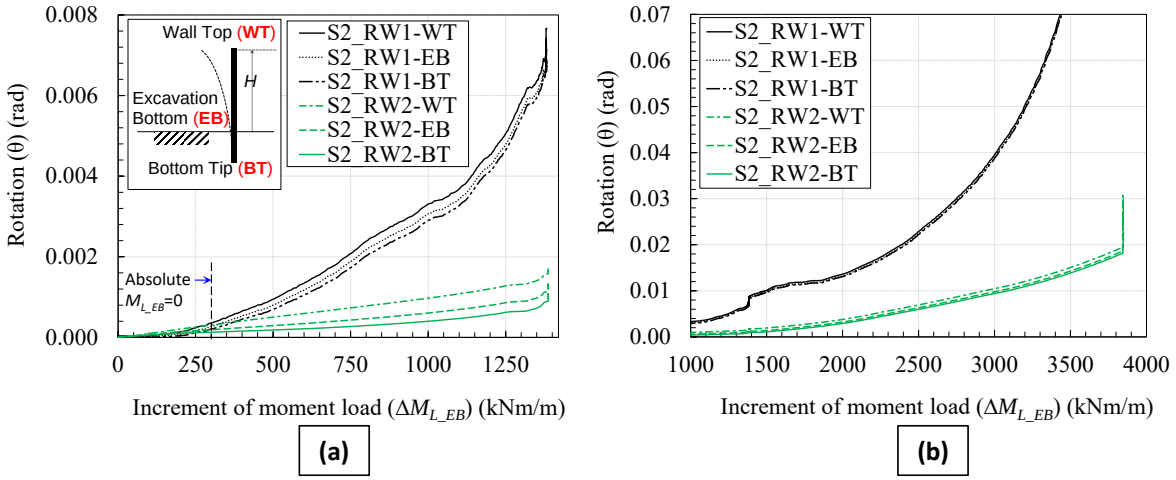

Figure 3.69 Variation of rotations at the wall top, excavation bottom and bottom tip against the increment of moment load during (a) excavation and (b) loading processes for 12m walls in mud rock

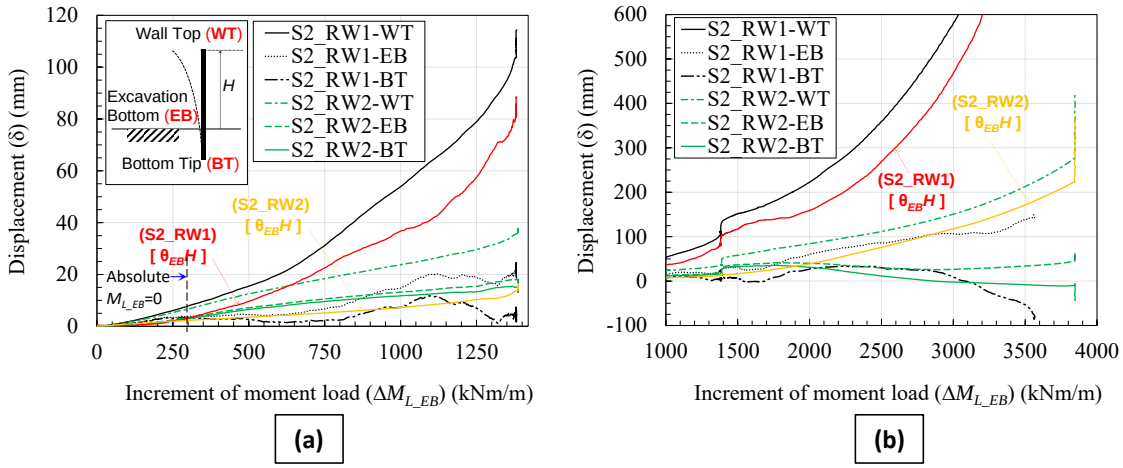

Figure 3.70 Variation of displacements at the wall top, excavation bottom and bottom tip against the increment of moment load during (a) excavation and (b) loading processes for 12m walls in mud rock

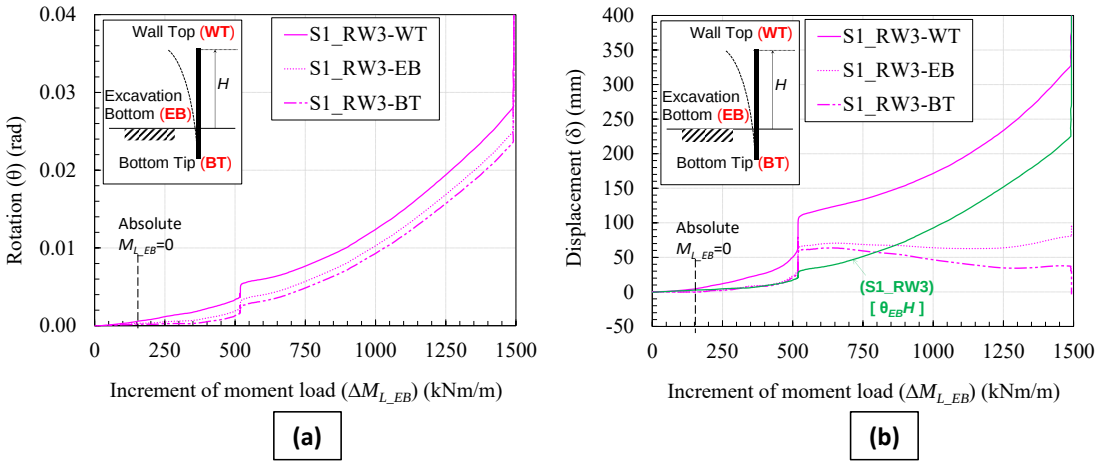

Figure 3.71 Variation of (a) rotations and (b) displacements at the wall top, excavation bottom and bottom tip against the increment of moment load during excavation and loading processes for 9m wall in sand rock

3.5.2 Deflection profiles at different stages

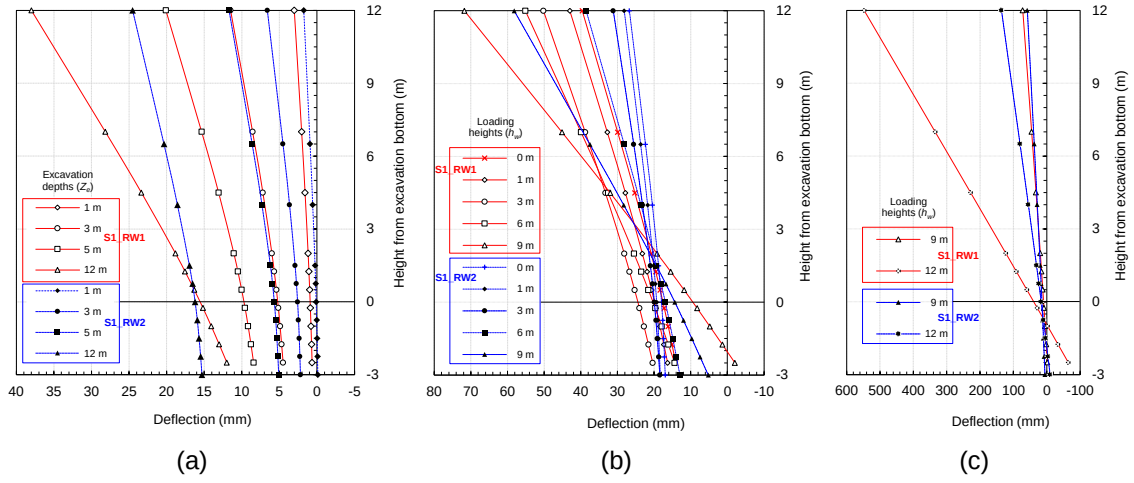

Figure 3.72 Deflection profiles of the walls S1_RW1 and S1_RW2 during (a) excavation and (b,c) loading processes

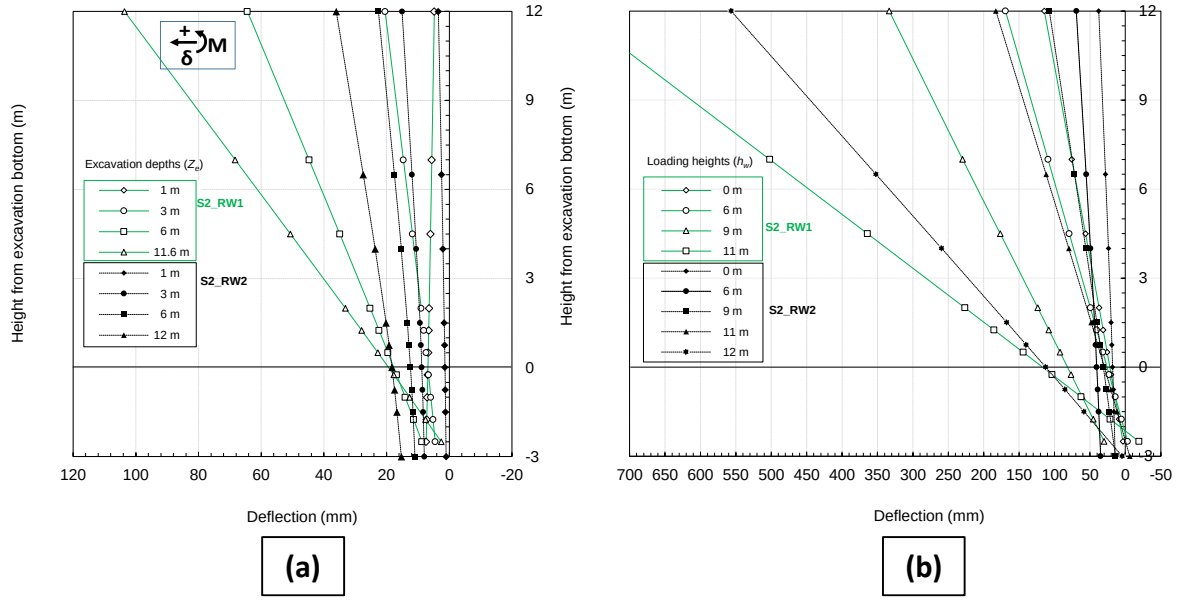

Figure 3.73 Deflection profiles of the walls S2_RW1 and S2_RW2 during (a) excavation and (b) loading processes

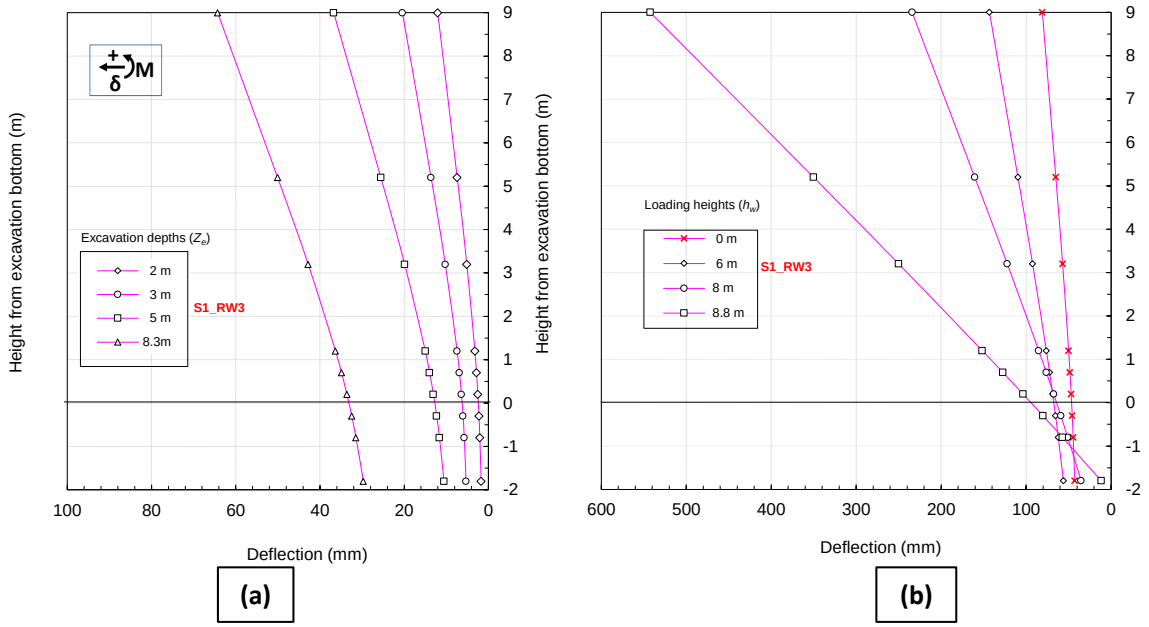

Figure 3.74 Deflection profiles of the wall S1_RW3 during (a) excavation and (b) loading processes

3.5.3 Deformation and failure mechanism

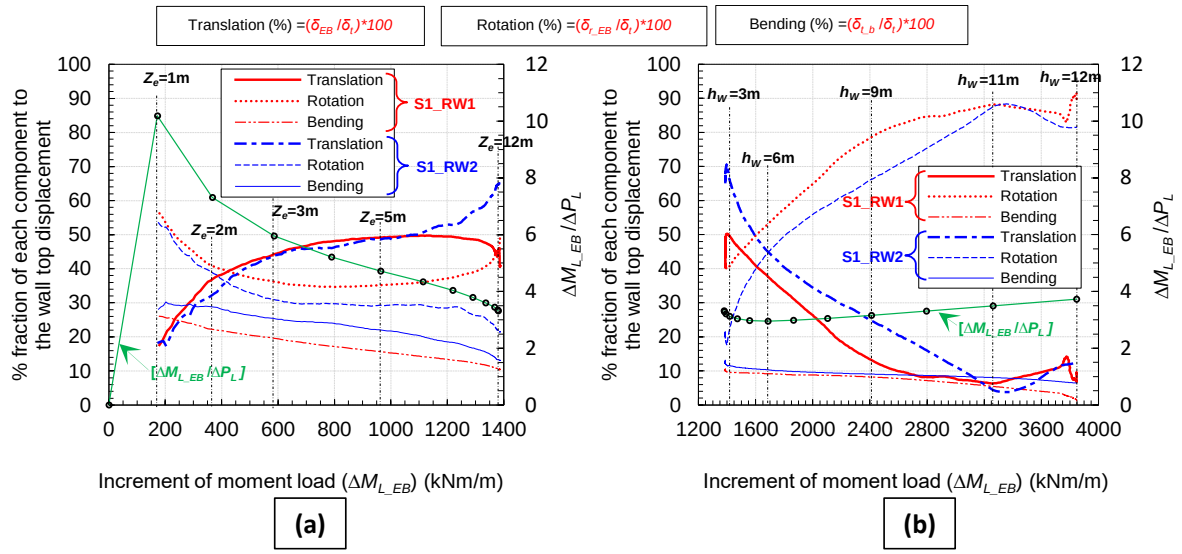

Figure 3.75 Variation of % fraction of displacement components of wall top displacement, the ratio between moment load and horizontal load against the increment of moment load during (a) excavation and (b) loading processes for the walls S1_RW1 and S1_RW2

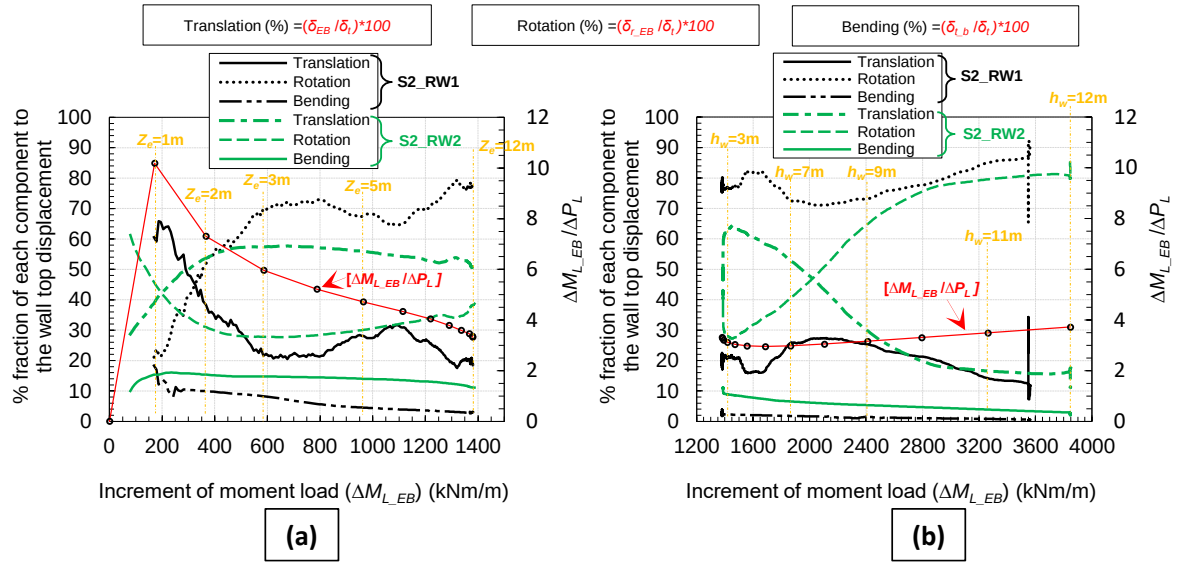

Figure 3.76 Variation of % fraction of displacement components of wall top displacement, the ratio between moment load and horizontal load against the increment of moment load during (a) excavation and (b) loading processes for the walls S2_RW1 and S2_RW2

The three components of wall top displacement shown in Figure 3.66 are considered as indexes representing the effects of translation, rotation and bending of the wall. To visualize the fraction of three components of wall top displacement during the excavation and loading processes, the variation of % fractions of the components are plotted against ΔM_{L_EB} in Figure 3.75 for walls S1_RW1, S1_RW2 and in Figure 3.76 for walls S2_RW1, S2_RW2 with the ratio of the moment load and horizontal load ($\Delta M_{L\_EB} / \Delta P_L$) . Figure 3.77 shows the %fractions for the wall S1_RW3. Owing to the relatively large measurement errors in the beginning of excavation process with very small displacements, the variations are shown from the point Z_e=1m.

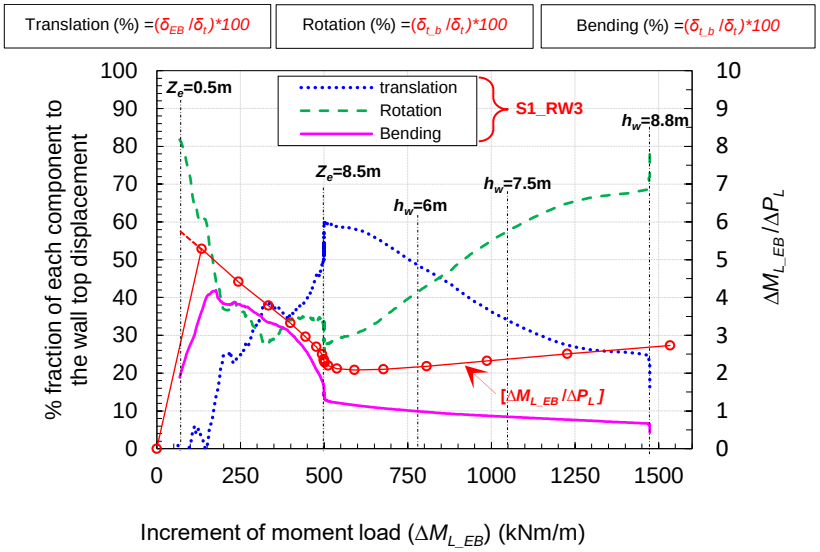

Figure 3.77 Variation of % fraction of displacement components of wall top displacement, the ratio between moment load and horizontal load against the increment of moment load during (a) excavation and (b) loading processes for the wall S1_RW3

Considering the walls S1_RW1, S1_RW2 except at the early excavation stage when $\Delta M_{L\_EB}/\Delta P_L$ was relatively large, the translation components are 15 – 20 % larger than the rotation one in the mid process of excavation. But in S1_RW1, the fraction of rotation component starts increasing from about ΔM_{L_EB} = 900kNm/m becomes almost the same as that of the translation. This rotation dominant trend further progress in the loading process, which can be confirmed from not only the increase of the fraction but also the decrease of δ_{EB} which is confirm from the deflection profiles of h_w=3m and 6m in Figure 3.72. In S1_RW2, this change of the translation dominant mode to rotation dominant mode occurs in the loading process. The variations of the fractions are similar with slight difference of ΔM_{L_EB}, 200-400 kNm/m larger in the latter test than the former for the same % fraction. The difference of δ_t between two tests is kept almost constant with linear increase until ΔM_{L_EB} = 2,500 kNm/m (Figure 3.68(b)). However, over this moment load, the wall rotations and wall top displacement of S1_RW1 show the exponential increase departing from the linear trend and a failure occurred near the end of loading as confirmed from Figure 3.67(b), Figure 3.68(b) and Figure 3.72 (c). The small displacement at excavation bottom (δ_{EB}) and the gradual increase of backward displacement at the bottom tip (δ_{BT}) from ΔM_{L_EB} = 3250 to 3700 kNm/m along with the exponential rise of wall top displacement reveals the compression of the toe back of the embedded medium and rigid body rotation about the pivot point closer to the excavation bottom. Rapid rise of rotations and the backward movement of bottom tip beyond ΔM_{L_EB} = 3750 kNm/m clearly indicates the ultimate collapse of S1_RW1 caused by the brittle deformations of the embedded medium at the backside of the wall. The rigid body rotation about a pivot point located at 0.9 m below the excavation bottom can be detected from Figure 3.72 (c). The wall front compression and the toe back shear failure for S1_RW1 at the ultimate collapse can be confirmed from the photo taken after the test shown in Figure 3.78 (a). While in S1_RW2, the liner increasing trend of δ_t can be seen except of small non-linear increase near the end of loading stage, ΔM_{L_EB} over 3,300 kNm/m (Figure 3.68(b)). After M_{L_EB} = 3,300 kNm/m, a decreasing trend of rotations and a certain increase of δ_{EB} can be detected as illustrated in Figure 3.67(b), Figure 3.68(b) respectively. Thanks to the contribution of 0.5 m increase of the wall embedment depth, even after this non-linear behavior of S1_RW2 and a clear large residual deformation achieved through the additional loading by the increase of centrifugal acceleration up to 95 g, failure in the embedded medium was not observed.

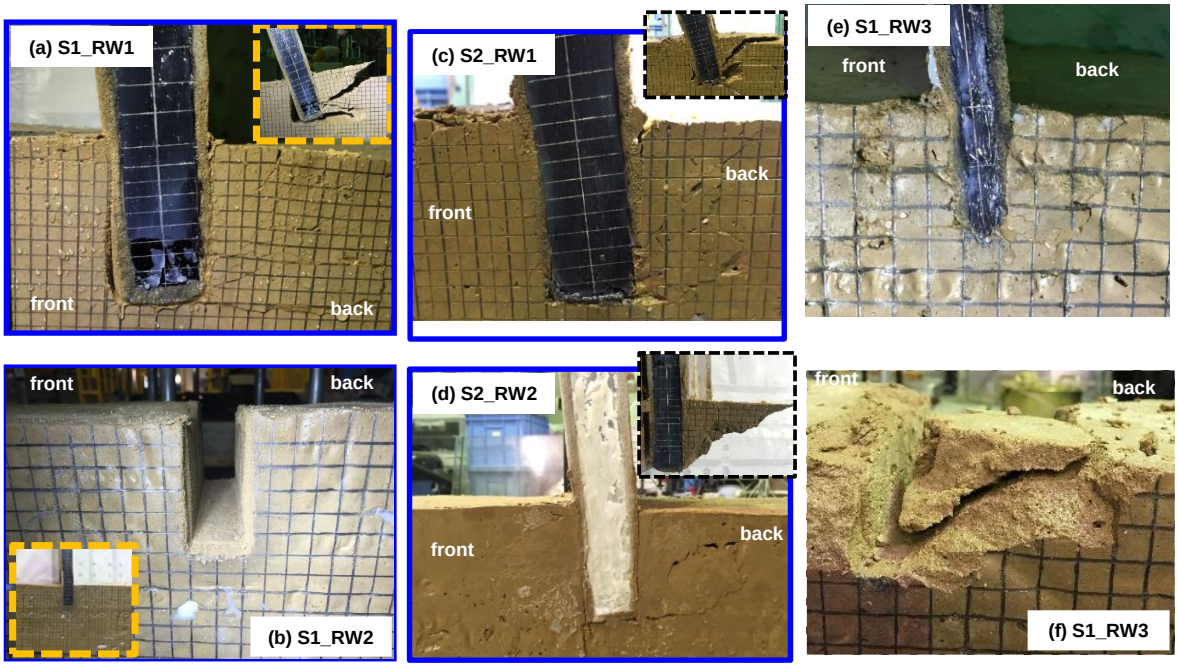

Figure 3.78 Observed deformations of embedded medium

It can be also confirmed from Figure 3.78 (b), showing the embedded medium upon removal of the wall in S1_RW2. The pivot point of wall rotation estimated from the displacement profile at the end of loading process (Figure 3.72 (c)) was 1.85 m below the excavation bottom, which is lower than that of S1_WR1.

3.5.4 Influence of embedment depth

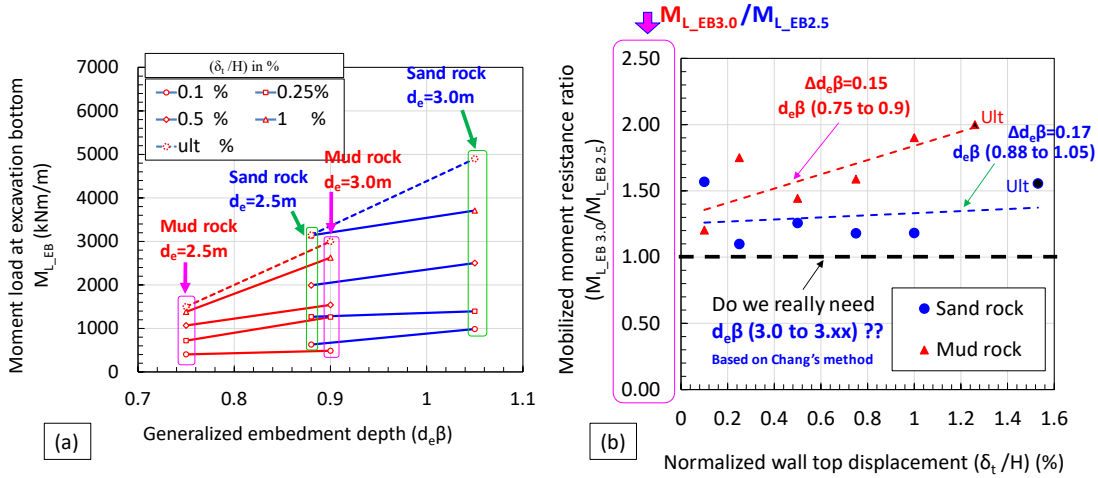

Figure 3.79 Moment load resistance of walls with different generalized embedment depths

Figure 3.79(a) illustrates the variation of moment load resistance against the generalized embedment depths ($d_e\beta$) at different levels of wall top displacements in terms of the percentage of wall retained heights ($100*\delta_t/H$). Comparing the walls with 2.5m and 3m embedment depths in mud rock and sand rocks as indicated in Figure 3.79(a) significant influence of 0.5m embedment depth increment can be observed at relatively large wall top displacements and ultimate failure conditions. However, at relatively small displacement levels up to δ_t/H =0.1% for the walls in mud rock and up to δ_t/H =0.25% for the walls in sand rock, influence of embedment become minimal. In order to discuss the behavior in more detail a mobilized moment resistance ratio between the walls with 2.5 m and 3m embedment depths are

introduced separately for sand and mud rocks in Figure 3.79(b). Where y-axis indicates mobilized moment resistance ratio and x-axis representing the normalized wall top displacements (100*δ_t/H).

Observing the circle (Sand rock) markers in Figure 3.79(b), almost constant trend up to δ_t/H =1% (120mm) and a large increment in the mobilized resistance ratio at ultimate condition can be seen for the walls in sand rock except the a single point at δ_t/H =0.1%. Meanwhile the triangular (Mud rock) markers in Figure 3.79(b), illustrating a linearly increasing trend up to ultimate condition except the single point at δ_t/H =0.25%. This linearly increasing trend clearly indicates the higher dependency of wall stability on the increment of embedment depth ($\Delta d_e\beta$=0.15), at relatively small $d_e\beta$ (< 0.9) values. However, the observed constant trend up to δ_t/H =1% (120mm) for the walls in sand rock with the similar increment of embedment depth ($\Delta d_e\beta$=0.17) suggest that different deformation mechanism tend to play a major role at relatively large $d_e\beta$-values closer to 0.9 or over. It can also be confirmed by referring the walls in mud rock given in Figure 3.76(a).Where a rotational dominant behavior at smaller $d_e\beta$ condition and a combined (rotation and translation) deformation mechanism closer to a $d_e\beta$ of 0.9 for the walls can be observed. In Figure 3.76(a), the wall S2_RW1 is corresponding to a $d_e\beta$=0.75 and the $d_e\beta$ for wall S2_RW2 is 0.9. The possible cause for the observation in sand rock could be attributed to the influence of shallow rock layers on the lateral resistance of walls up to certain level of displacement prior to a significant deterioration of rock stiffness. This displacement level is about 1% at the wall top in terms of wall height.

From Figure 3.79(b), either by considering the circle and triangular maker points or corresponding trend lines a declining tendency in the moment resistance ratio can be observed for almost same increment ($\Delta d_e\beta$=0.15&0.17) of $d_e\beta$ values from a $d_e\beta$=0.75 and a $d_e\beta$=0.88. From this observation it can be confirmed that the increment of moment resistance tends to decrease with the increasing $d_e\beta$ values over 0.9.

Attributing to the lack of experimental evidence for the embedment depths over the $d_e\beta$=1.05, the following paragraph is drawn based on my engineering judgement.

If we could further increase the embedment from $d_e\beta$=1.05 (wall S1_RW2) with the same increment rate ($\Delta d_e\beta$=0.15), after two or three times the increment (approximately, $d_e\beta$=1.5) we could achieve the moment resistance ratio of unity at any displacements induced under the implemented loading conditions in this study. This limiting depth of embedment could be considered as optimum embedment depth for this specific condition. Over which, further increment of embedment could not have any influence on the deformation and failure of the considered wall in this study. This embedment level could be expected to be between $d_e\beta$=1.5-2.0.

Finally, from the observations the following conclusions can be derived as follows;

At relatively small $d_e\beta$-values (0.7 - 0.9) the influence of embedment depth become eminent at all range (small to large) of wall top displacements, i.e., moment resistance ratios between two walls having the embedment depth ($d_e\beta$) in this range of $d_e\beta$ = 0.7-0.9, could be expected to increase linearly with wall deformations from small displacement up to failure. In other words, higher dependency of wall stability on the increment of embedment could be expected in this range.

Over the value of $d_e\beta$ = 0.9, the wall deformation mechanism is governed by the influence of shallow layers from initial condition to certain level of wall top displacement, which is about 1% of the retained height. Which can also be considered as an alarming point prior to the catastrophic failure of a wall with $d_e\beta$ = 0.9.

As a general conclusion, the normalized embedment depth for the wall considered in this study can be categorized in to three different zones. The first zone can be considered where the $d_e\beta <$ 0.9, in this zone the wall response highly controlled by the loading level than the embedment or the shallow layer contribution, it can be regarded as an unstable zone where catastrophic failures could be expected.

The second zone can be defined from $d_e\beta$ = 0.9 to 1.5 or 2, here the upper limit is based on the engineering judgement, it must be confirmed from physical or numerical studies. In this zone the influence of shallow rock layer provides large lateral resistance prior to the significant deterioration of stiffness. Yielding of rock or significant deterioration of rock stiffness took place at about 120mm (δ_t =1%H) wall top displacement which is far above the allowable displacement concept (50mm) of most of the design codes. The third zone can be considered with the $d_e\beta$ values over 2, where the ultimate failure can be expected only due to the structural deformation.

As a recommendation the boundary value of $d_e\beta$ between second and third zone must be investigated physically or numerical studies, until that this boundary value must be treated with caution. Also this study can be applicable only for a uniform mass of soft rock where no clear planes of weakness or discontinuities are present.

The variation of normalized wall top displacement (δ_t /H) and rotation (θ_t /H) against the applied increment of moment load at the excavation bottom (M_{L_EB}) are illustrated in Figure 3.80(a) for the walls S1_RW1 and S1_RW2. Owing to the sound lateral confinement in the embedded portion of the wall in S1_RW2, the failure could not be achieved by the loading process (water feeding to the retained dry sand) in this study. Therefore, in order to create the failure or large deformations, the Gravity Turn On (GTO) technique (Craig, 2014) was adopted at the end of loading (water feeding) stage. It is important to note that, only stress change due to centrifugation was considered while the wall dimensions remain constant in the estimation of the moment load during GTO. At very small rotations (θ_t < 0.02%H) and displacements (δ_t < 0.1%H), significance influence of d_e could not be detected. At small displacements the influence of shallow rock layer is expected to be higher, which could mainly confine the wall by the large initial stiffness of the intact rock.it can be confirmed from Figure 3.79 as well at a displacement of δ_t = 0.1%H. This phenomenon might relatively reduce the effect of d_e prior to the deterioration of shallow layers. However, with the increment of moment load, owing to the deterioration of shallow layers in the wall front as well as the deformation of toe back rock portion a clear deviation in the rotation and displacement of walls can be seen. It also reflect in the moment load resistance observed in Figure 3.79 at relatively large displacements. The wall in S1_RW1 exhibits an increasing rate of displacement from the initiation of the water feeding, which implies the gradual deterioration of the fixity in the embedment portion. The ultimate failure at a displacement of 2.25%H can be considered as a result of full mobilization of the resistance or yielding of rock in the entire embedment depth. The wall and ground deformation captured by in-flight photo at the ends of excavation and the loading processes of S1_RW1 are given in Figure 3.80(b-1) and Figure 3.80 (b-2) respectively. The observed brittle failure of the wall S1_RW1 could be attributed to the toe back shear failure observed in Figure 3.78(a) and Figure 3.80 (b-2).

Figure 3.80 (b-3) and Figure 3.80 (b-4) indicate the deformation of the wall and embedded soft rock in S1_RW2 at the end of loading process and at the loading of 95 g centrifugal acceleration respectively. Although large displacements of the wall S1_RW2 was created by means of GTO technique, it is important to emphasize that the failure of the embedded medium could not be achieved even at 95 g as portrayed in Figure 3.80 (b-4). The significance of 0.5 m increase of embedment depth on the deformation and failure behavior of CSTP walls in soft rock can be

reconfirmed from these photos. The 0.5m addition could decrease the deformation under the ordinary design loading and increase the ultimate failure load significantly. Furthermore, increase the redundancy against the failure changing the failure behavior from brittle one to rather ductile one. From the above discussion, a safety factor in terms of the embedment depth could be proposed, as a safety margin in the design of this type wall for the ultimate condition.

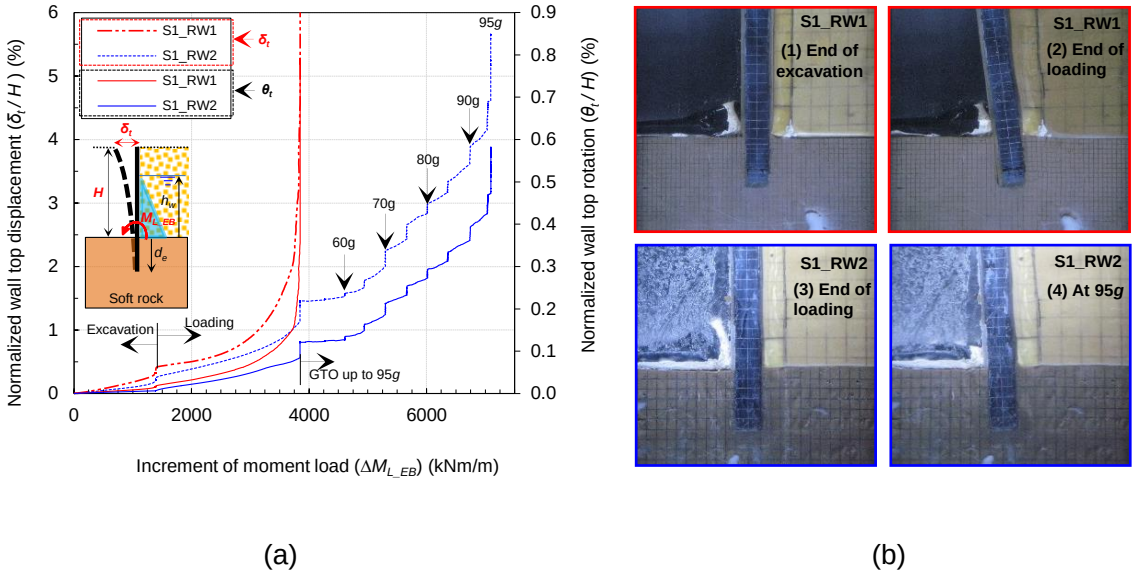

(a) (b)

Figure 3.80 Influence of embedment depth (a) normalized wall top displacement and wall top rotation against the moment load, (b) photos of wall and ground deformation taken inflight after excavation and loading processes for the walls S1_RW1 and S1_RW2

3.6 Summary

A centrifuge modelling system was developed to model the behavior of cantilever type retaining walls embedded in soft rocks from a design loading condition to the ultimate failure conditions under a constant centrifugal (50 g) acceleration.

From the centrifuge model experiments done by using the developed system, the following are confirmed,

1) Stability of cantilever type retaining walls with large stiffness equivalent to 2.5 m diameter steel tubular pile wall could be secured with relatively small embedment depth in soft rock against relatively high wall height of 12 m in the design condition, and could pose reasonable safety margin against ultimate failure.

2) Deflection of the cantilever retaining wall is generated by the combination of translation and rotation in the embedded part, and bending of wall under the ordinary design load. As the load from the retained soil further increases, the rigid body rotation becomes dominant displacement mode and the wall fails by the rotational failure mode with a pivot point at the location near the excavation bottom.

3) A relatively small increment of embedment depth (e.g. 0.5m (20%)) from 2.5m embedment depth could decrease the deformation under the ordinary design loading and increase the ultimate failure load significantly, and furthermore, increase the redundancy of the wall against the failure, changing the failure behavior from brittle one to ductile one.

The following summaries can be derived based on generalized embedment conditions;

At relatively small deβ-values (0.7 - 0.9) the influence of embedment depth become eminent at all range (small to large) of wall top displacements, i.e., moment resistance ratios between two walls having the embedment depth (deβ) in this range of $d_e\beta$ = 0.7-0.9, could be expected to increase linearly with wall deformations from small displacement up to failure. In other words, higher dependency of wall stability on the increment of embedment could be expected in this range. Over the value of $d_e\beta$ = 0.9, the wall deformation mechanism is governed by the influence of shallow rock layers from the initial condition to a wall top displacement of about 1% of the retained height (*H*). This *1%H* also can be considered as an alarming point prior to the catastrophic failure of a wall with $d_e\beta$ = 0.9.

The normalized embedment depth for the wall considered in this study can be categorized in to three different zones. The first zone can be considered where the $d_e\beta$< 0.9, in this zone the wall response highly controlled by the embedment depth under a load of interest, it can be regarded as an unstable zone where catastrophic failures could be expected.

The second zone can be defined from $d_e\beta$ = 0.9 to 1.5 or 2, here the upper limit is based on the engineering judgement, it must be confirmed from further physical or numerical studies. In this zone the influence of shallow rock layer provides large lateral resistance prior to the significant deterioration of stiffness. Yielding of rock or significant deterioration of rock stiffness took place at about 120mm (δ_t =1%H) wall top displacement which is far above the allowable displacement concept (50mm) of most of the design codes.

The third zone can be considered with the $d_e\beta$ values over 2, where the ultimate failure can be expected only due to the structural deformation.

As a recommendation the boundary value of $d_e\beta$ between second and third zone must be investigated physically or numerical studies, until that this boundary value must be treated with caution. Also this study can be applicable only for a uniform mass of soft rock where no clear planes of weakness or discontinuities are present.

3.7 References

ArcelorMittal, 2008. Piling Handbook, 8th ed, ArcelorMittal, Esch-sur-Alzette, Luxembourg, Installation of sheet piles. Ch-11, pp.284-337.

Association of Steel Pile (ASP), 2009, Design manual of self-standing steel sheet pile wall.

(In Japanese)

Bica, A.V.D. and Clayton, C.R.I., 1998. An experimental study of the behavior of embedded lengths of cantilever walls. Geotechnique, 48(6), pp.731-745.

Blyth, F.G.H. and de Freitas, M.H., 1984. A geology for engineers 7th ed. Edward Arnold, London.

Bolton, M.D. and Powrie, W., 1987. The collapse of diaphragm walls retaining clay. Geotechnique, 37(3), pp.335-353.

Bolton, M.D. and Powrie, W., 1988. Behavior of diaphragm walls in clay prior to collapse. Géotechnique, 38(2), pp.167-189.

Bransby, P.L. and Milligan, G.W.E., 1975. Soil deformations near cantilever sheet pile walls. Geotechnique, 25(2), pp.175-195.

Carter, J.P. and Kulhawy, F.H., 1992. Analysis of laterally loaded shafts in rock. Journal of Geotechnical Engineering, 118(6), pp.839-855.

Chang, Y.L. ,1937. Lateral pile loading tests. Transaction of ASCE, 102,pp. 273-276.

Chen, J.J., Zeng, F.Y., Wang, J.H. and Zhang, L., 2017. Analysis of laterally loaded rock-socketed shafts considering the nonlinear behavior of both the soil/rock mass and the shaft. Journal of Geotechnical and Geoenvironmental Engineering, 143(3), p.06016025.

Choo, Y.W. and Kim, D., 2016. Experimental Development of the p-y Relationship for Large-Diameter Offshore Monopiles in Sands: Centrifuge Tests. Journal of Geotechnical and Geoenvironmental Engineering, 142(1), p.04015058.

Craig, W.H., 2014. Modelling slope failures by 'gravity turn-on', Proceedings of the 8th International Conference on Physical Modelling in Geotechnics, Perth, pp.1203-1209.

D'Andrea, R. and Day, R.W., 1998. Discussion and Closure: Design and Construction of Cantilevered Retaining Walls. Practice Periodical on Structural Design and Construction, 3(2), pp.87-88.

Fukushima, S. and Tatsuoka, F., 1984. Strength and deformation characteristics of saturated sand at extremely low pressures. Soils and Foundations, 24(4), pp.30-48.

Indraratna, B., 1990. Development and applications of a synthetic material to simulate soft sedimentary rocks. Geotechnique, 40(2), pp.189-200.

International Press-in Association (IPA), 2016. Press-in retaining structure: a handbook, 1st ed.

Irvine, J., Terente, V., Lee, L.T. and Comrie, R., 2015. Driven pile design in weak rock. In Proc. Int. Symp. Frontiers in Offshore Geotechnics III, ISFOG 2015 (pp. 569-574).

Johnston, I.W. and Chiu, H.K., 1984. Strength of weathered Melbourne mudstone. Journal of Geotechnical Engineering, 110(7), pp.875-898.

Johnston, I.W. and Choi, S.K., 1986. A synthetic soft rock for laboratory model studies. Geotechnique, 36(2), pp.251-263.

Kanji, M.A., 2014. Critical issues in soft rocks. Journal of Rock Mechanics and Geotechnical Engineering, 6(3), pp.186-195.

Khan, M.R.A., Takemura, J. and Kusakabe, O., 2006. Centrifuge model tests on behavior of double sheet pile wall cofferdam on clay. International Journal of Physical Modelling in Geotechnics, 6(3), pp.01-23.

Khan, M.R.A., Takemura, J., Fukushima, H. and Kusakabe, O., 2001. Behavior of double sheet pile wall cofferdam on sand observed in centrifuge tests. International Journal of Physical Modelling in Geotechnics, 1(4), pp.01-16.

Kimura,T., Takemura,J., Hiro-oka,A., Suemasa,N.and Kouda,N., (1993) Stability of unsupported and supported vertical cuts in soft clay. Proceedings of the 11th SEAGC, Singapore, pp. 61–70.

Kunasegaram,V., Akazawa,S., Takemura,J., Seki,.S, Fujiwara,K, Ishihama,Y. and Fujii,Y.,2015. Modeling of soft rock for a centrifuge study, Proceedings of 12th GeoKanto,Tokyo,Japan, pp. 15-19.

Kunasegaram,V., Hsiao, W.H. and Takemura, J., 2018. Behavior of a large diameter piles subjected to moment and lateral loads, Proceedings of the 1st International Conference on Press-in Engineering 2018, Kochi, Japan,pp.133-140.

Lam, S.Y., Elshafie, M.Z., Haigh, S.K. and Bolton, M.D., 2012. A new apparatus for modelling excavations. International Journal of Physical Modelling in Geotechnics, 12(1), pp. 24-38.

Leung, C.F., Ong, D.E. and Chow, Y.K., 2006. Pile behavior due to excavation-induced soil movement in clay. II: Collapsed wall. Journal of Geotechnical and Geoenvironmental Engineering, 132(1), pp.45-53.

Lo, K.Y., Micic, S., Lardner, T. and Janes, M., 2009. Geotechnical properties of a weak mudstone in downtown Calgary. GeoHalifax'09.

Long, M., 2001. Database for retaining wall and ground movements due to deep excavations. Journal of Geotechnical and Geoenvironmental Engineering, 127(3), pp.203-224.

Lyndon, A. and Schofield, A.N., 1970. Centrifugal model test of a short-term failure in London clay. Geotechnique, 20(4), pp.440-442.

Madabhushi, S.P.G. and Chandrasekaran, V.S., 2005. Rotation of cantilever sheet pile walls. Journal of Geotechnical and Geoenvironmental Engineering, 131(2), pp.202-212.

Miyanohara,T., Kurosawa,T., Harata,N., Kitamura,K., Suzuki,N. and Kajino,K., 2018. Overview of the Self-standing and High Stiffness Tubular Pile Walls in Japan, Proceedings of the 1st International Conference on Press-in Engineering 2018, Kochi, Japan,pp.167-174.

Ong, D.E., Leung, C.E. and Chow, Y.K., 2006. Pile behavior due to excavation-induced soil movement in clay. I: Stable wall. Journal of Geotechnical and Geoenvironmental Engineering, 132(1), pp.36-44.

Ou, C.Y., Hsieh, P.G. and Chiou, D.C., 1993. Characteristics of ground surface settlement during excavation. Canadian Geotechnical Journal, 30(5), pp.758-767.

Padfield, C.J. and Mair, R.J., 1984. The design of propped cantilever walls embedded in stiff clays. CIRIA Rep, 104.

Powrie, W., 1996. Limit equilibrium analysis of embedded retaining walls. Géotechnique, 46(4), pp.709-723.

Randolph, M.F., 1981. The response of flexible piles to lateral loading. Geotechnique, 31(2), pp.247-259.

Reese, L.C., 1997. Analysis of laterally loaded piles in weak rock. Journal of Geotechnical and Geoenvironmental Engineering, 123(11), pp.1010-1017.

Richards, D.J. and Powrie, W., 1998. Centrifuge model tests on doubly propped embedded retaining walls in overconsolidated kaolin clay. Géotechnique, 48(6), pp.833-846.

Richards, D.J., Clayton, C.R.I., Powrie, W. and Hayward, T., 2004. Geotechnical analysis of a retaining wall in weak rock. Proceedings of the Institution of Civil Engineers-Geotechnical Engineering, 157(1), pp.13-26.

Suzuki,N. and Kajino,K.,2018. Issues for the Reduction of the Embedded Length of Cantilevered Steel Tubular Retaining Wall Pressed into Stiff Ground, Proceedings of the 1st International Conference on Press-in Engineering 2018, Kochi, Japan,pp.159-166.

Takemura, J., Kondoh, M., Esaki, T., Kouda, M. and Kusakabe, O., 1999. Centrifuge model tests on double propped wall excavation in soft clay. Soils and Foundations, 39(3), pp.75-87.

Tatsuoka, F. and Kohata, Y., 1995. Stiffness of hard soils and soft rocks in engineering applications. In pre-failure deformation of geomaterials. Proceedings of the international symposium, 12-14 September 1994, Sapporo, Japan. 2 vols.

Tatsuoka, F., Goto, S. and Sakamoto, M., 1986. Effects of some factors on strength and deformation characteristics of sand at low pressures. Soils and Foundations, 26(1), pp.105-114.

USDA-NRCS, United State Department of Agriculture, Natural Resource Conservation Service, 2012. National Engineering Handbook. Engineering Classification of Rock Materials. Part 631.Ch- 4. (210–VI–NEH, Amend. 55, January 2012).

Williams, A., & Pells, P. J. N. (1981). Side resistance rock sockets in sandstone, mudstone, and shale. Canadian Geotechnical Journal, 18(4), 502-513.

Whittle, A.J. and Davies, R.V., 2006, June. Nicoll Highway Collapse: Evaluation of Geotechnical Factors Affecting Design of Excavation Support System. International Conference on Deep Excavations, Singapore, 16p.

4 Behavior of Large Diameter Steel Tubular Piles in Firm Ground Subjected to Lateral Loads

4.1 Introduction

Large diameter steel tubular piles are being used in several civil engineering applications as Describe in Figure 4.1. The main purpose of the applications given in Figure 4.1 is the retaining of backside sand or water in case of cofferdams. The behavior of these retaining structures governed by the behavior of single piles and their interaction between adjacent piles and the embedded medium. Therefore, it's important to understand the behavior of these structures in an elementary level, prior to the investigations on a complicated soil-structure interaction. This chapter mainly focused on the behavior of single piles and influential factors related to embedment depth, embedded medium and loading conditions.

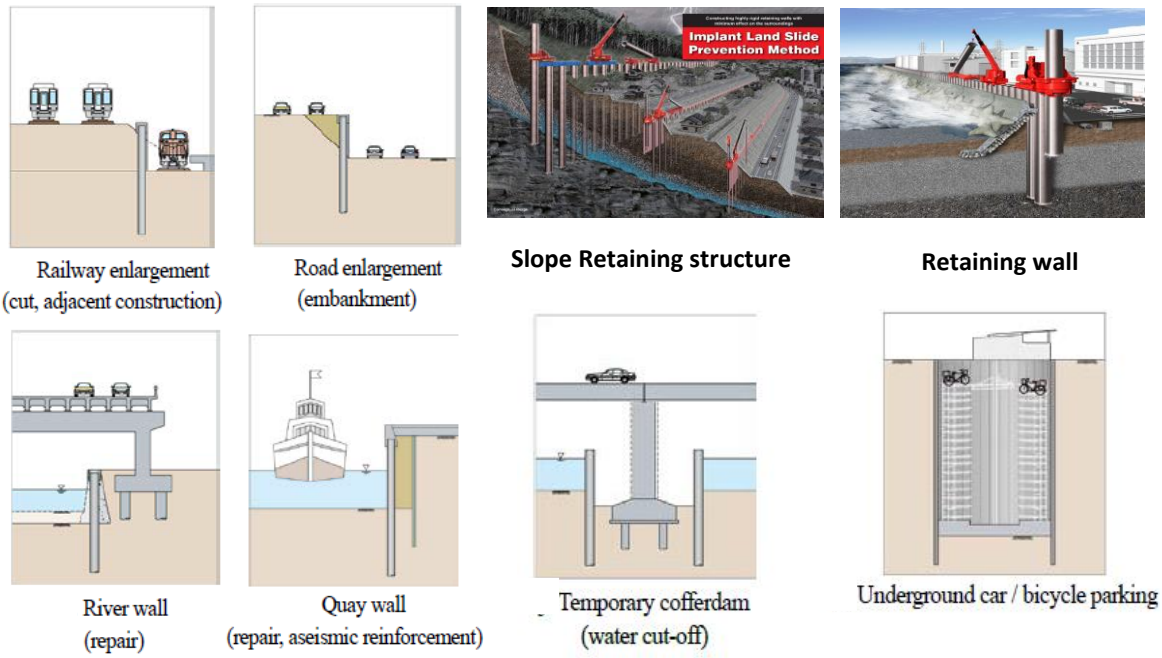

Figure 4.1 Applications of Large diameter steel tubular piles in civil engineering constructions (Source :IPA-handbook)

Besides the applications described in Figure 4.1, relatively larger diameter piles (4 m -10 m diameter) are utilized in the wind farm industry as a mono-pile foundation, depending on the capacity of the wind turbine, required diameter also varies in order to prevent the structural deformation. Although this chapter mainly focus on the behavior of single piles as an element of CSTP walls, certain outcomes from this study could be applicable to assess the behavior of large diameter mono-piles as well. According to Doherty and Gavin (2012), mono-piles are typically design to a serviceability tolerance of 1° rotations during its entire lifespan including the installation tolerance of 0.5° in most common situations. Although the serviceability requirements of mono-pile foundations could be satisfied based on the loading combinations incorporated in the current design methods, the behavior of mono-piles under an earthquake loading event is unforeseeable. Relatively large lateral and moment loads compare to the design loads could be expected in a short period of time, which might induce large rotations and permanent deformations of mono-pile foundation there by the wind turbine as well. Under these extreme loading events the stability and the behavior of mono-piles are governed by the embedded medium, embedment depth and the flexural rigidity of the mono-pile foundation.

4.2 Modelling perspective

Applications of embedded piles in rock under lateral loading and relevant documented investigations are barely encountered (Guo and Lehane, 2016) in the past compare to the rock socketed shafts (Carter and Kulhawy, 1988; Chen et al., 2011), where substantial thickness of overburden soil govern the deformation characteristics of piles which yields negligible displacements at the underlying rock surface. However, recent infrastructure development nearby mountain sites (Xing et al., 2014; Ishihama et al., 2018; Miyanohara et al., 2018) or the application of onshore (Guo, 2015) and offshore (Kallehave et al., 2015) mono-pile foundations often encounter the rock surface near or at the ground level. In such situations the lateral resistance is mainly controlled by the rock embedment. To the best of writer's knowledge, the lateral response of large diameter steel tubular piles embedded in rock (Fragio et al., 1985) has not well studied by physical models or real field tests to observe the critical behavior, which is controlled by several influential factors such as pile properties (diameter, stiffness, embedment depth), ground factors (strength and stiffness), and loading conditions (loading height, monotonic and cyclic) (Arany et al., 2017). On the other hand, few field tests using concrete shafts (Digioia and Rojas-Gonzalez, 1994; Kahle and Brown, 2002; Guo and lehane, 2016) and numerical solutions are available based on continuum approach (Randolph 1981; Carter et al., 1992; Zhang et al., 2000; Chen et al., 2016) and non-linear p-y curves (Reese, 1997; Gabr et al., 2002; Erbrich, 2004) for laterally loaded shafts in rock. Therefore, this chapter aims to investigate the behavior of single steel tubular piles embedded in soft rock, soft rock overlain by medium dense sand, the piles embedded in medium dense and dense sand under lateral load by means of 50g centrifuge and 1g model tests. Investigating the influence of embedded medium, embedment depth, loading history and the applicability of 1g model tests for the piles embedded in rock type material are the major objectives of this chapter.

4.2.1 Model ground conditions

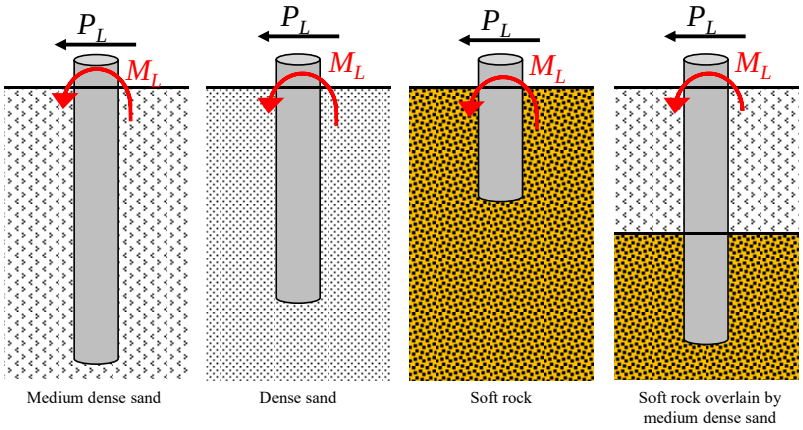

Figure 4.2 Target ground conditions and pile embedment considered in this study

Soil profiles and its variation in the real filed are more complicated, although modelling of such complicated profiles in the centrifuge could be possible up to certain extent for a physical study, the applicability of outcomes can be used only for a specific ground condition. This is the reason why researchers often study the behavior of structures under simplified models under more or less a uniform soil condition. This chapter also focused on the behavior of single piles embedded in well-defined boundary conditions and the embedded mediums. Four different types of embedment conditions are considered in this study, which are often encountered in the real practice. Such as the piles embedded in sand, rock and socketed in to rock and overlain by a granular medium. Although existence of overlain medium could be a cohesive material (clay) in real field applications, which is out of the scope of this study.

4.2.2 Target structure and loading conditions

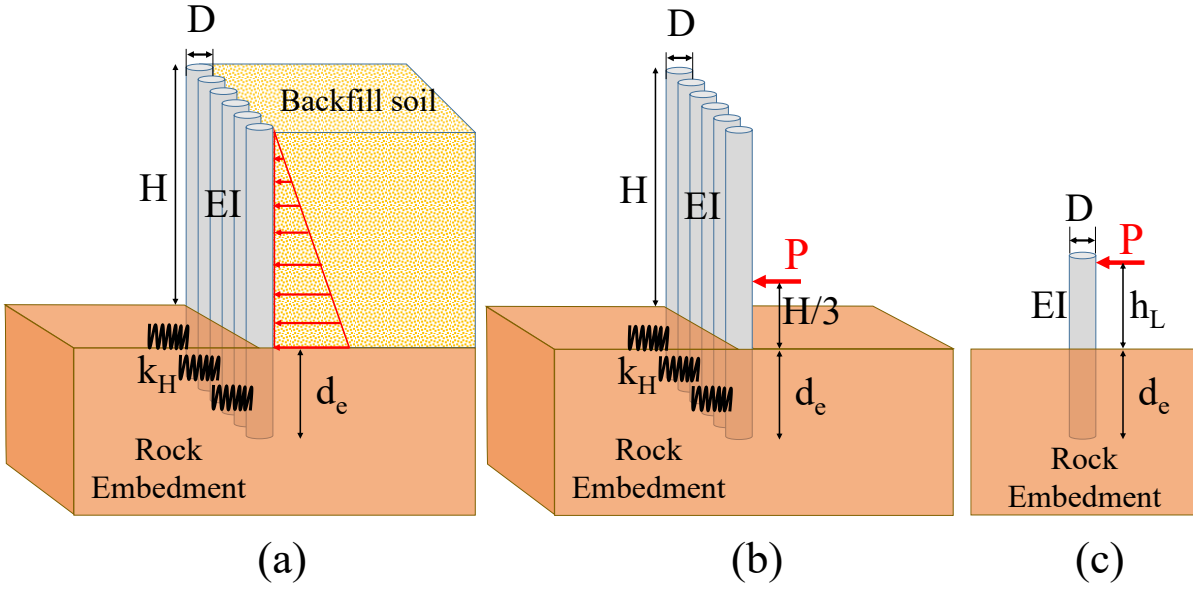

Figure 4.3 Target structure and simplified models

The major objective of this thesis is the development of a rational design method for the application of CSTP walls embedded in soft rock as shown in Figure 4.3(a). In order to investigate the influential factors on the behavior of CSTP walls, each factor must be assessed in different centrifuge models. However constructing a whole wall model as described in Figure 4.3(a) for each experiment is an expansive solution and more time consuming. Therefore the experiment process using tubular pile models in the centrifuge was divided in to three stages. In the first stage it was decided to conduct the single pile loading tests as described in Figure 4.3(c) to investigate the influential factors on the behavior of large diameter steel tubular piles. Which is the main theme of this chapter. Upon analysing the outcomes of single pile loading, the required embedment depths for the tubular pile wall models under lateral loads (as described in Figure 4.3(b)) was decided. Which is included in the chapter -5, it describes the results of 4 CSTP walls embedded in soft rock and layered (Soft rock overlain by sand) profile. The third stage of the experiment process is the dynamic stability of CSTP wall (as described in Figure 4.3(a)) embedded in soft rock. Besides these three series the chapter-3 describes the behavior of a simplified CSTP wall under ordinary design loading and ultimate loading conditions.

4.2.3 Influential factors to be investigated

Based on the dimensionless analysis, Randolph (1977) found that the behavior of a pile is simply govern by the stiffness E_p/G ratio and the embedment depth of the pile, where E_p is the effective young's modulus of the pile and G is the shear modulus of soil. Besides these strength and stiffness parameters, Arany et al., (2017) indicated that the pile properties (diameter, stiffness), loading conditions (loading height, monotonic and cyclic) also influence on the behavior of large diameter piles. Attributing to the cost and available time, it is difficult to investigate all the influential factors by physical models, however investigation of some key factors and the validation of observed behaviors could open a path to investigate the all influential factors by numerical modelling up to certain accuracy. In this chapter the following influential factors are investigated by physical models either 1g or 50g centrifuge model;

- Influence of Embedment depth and embedded medium on the lateral resistance
- Influence of loading cycles and imposed displacement

- Effect of confining pressure on the pile behavior in soft rock
- Influence of loading height

4.2.4 Model conditions and model arrangement

Table 4-1 Centrifuge models, Notation of piles, Embedment and loading conditions

Model condition	Properties of embedded medium	Pile notation	Embedment depth (d_e) (m)	Loading height (h_w) (m)	Pile properties EI (GNm^2/m) M_y, M_p (MNm)
Model-1 Toyoura sand Dr=80% 50G model	Medium dense Sand γ_{ds}=15.5 kN/m³ ϕ'=40°	SP-MS-6.5	6.5 (130 mm)	6.5 m (130 mm)	Ø=2 m (40 mm) t = 25 mm (0.5 mm) EI=7.3 ($1.17x10^{-6}$) M_y=19.3 ($0.154x10^{-3}$) M_p=24.8 ($0.198x10^{-3}$)
		SP-MS-9	9 (180 mm)		
		SP-MS-11.5	11.5 (230mm)		
Model-2 Toyoura sand Dr=95% 50G model	Dense Sand γ_{ds}=16 kN/m³ ϕ'~45°	SP-DS-6.5	6.5 (130 mm)	6.5 m (130 mm)	
		SP-DS-9	9 (180 mm)		
		SP-DS-11.5	11.5 (230mm)		
Model-3 Soft sand rock 1G model	Soft Rock γ_{dR}=16.8 kN/m³ q_u=1.3-1.4 MPa E_s= 400-600MPa	SP-SR-40	(40 mm)	(130 mm)	
		SP-SR-60	(60 mm)	(130 mm)	
		SP-SR-60#	(60 mm)	(130 mm)	
		SP-SR-40□	(40 mm)	(80 mm)	
		SP-SR-60□	(60 mm)	(80 mm)	
Model-4 Soft sand rock (SR) 50G model	γ_{dr}=16.8 kN/m³ q_u=1.4 Mpa E_s=660 MPa	SP-SR-2*	2 (40 mm)	6.5 m (130 mm)	
		SP-SR-3	3 (60 mm)		
		SP-SR-4	4 (80 mm)		
Model-5 Soft Sand rock Overlain by Toyoura sand Dr=80% 50G model	γ_{ds}=15.5 kN/m³ ϕ'=40° γ_{dR}=16.8 kN/m³ q_u=1.3-1.4 MPa E_s= 400-600 MPa	SP-MS-SR-2	6.5 in MS, 2 in SR	6.5 m (130 mm)	
		SP-MS-SR-3	6.5 in MS, 3 in SR		
		SP-MS-SR-4	6.5 in MS, 4 in SR		
Model-8 Soft sand rock (SR) 50G model	γ_{dr}=16.8 kN/m³ q_u=1.4 Mpa E_s=660 MPa	SP-SR-2×	2 (40 mm)	6.5 m (130 mm)	
		SP-SR-3×	3 (60 mm)		
		SP-SR-4×	4 (80 mm)		

* Preloaded prior to the test without instrumentation # Rock filled up to the pile top
All dimensions are given in prototype scale model scales are given in parenthesis
M_y: Yielding bending moment of the pile M_p: bending moment causing plastic failure of the pile

4.2.5 Modelling process of centrifuge model

This chapter reports the behavior of single steel tubular piles subjected to lateral and moment loads, based on 50g and 1g centrifuge model tests. Influences of embedment depths, embedded mediums and loading history on the behavior of single piles embedded in stiff grounds were investigated. Besides, 1g model also discuss the influence of loading height and the confining pressures on the behavior of piles embedded in rock. Four different ground conditions were made in the centrifuge models, three uniform single-layer grounds with medium dense sand (Toyoura sand with relative density Dr =80%), dense sand (Toyoura sand Dr =95%) and soft sand rock, and one model for two-layers ground with the soft rock overlaid by the medium sand. Setups of centrifuge model tests for piles embedded in Toyoura sand, soft sand rock, and the two layers ground are shown in Figure 4.4, Figure 4.5, Figure 4.6, and Figure 4.7 respectively.

4.2.5.1 Model - 1&2 (Piles embedded in Toyoura sand at two different densities)

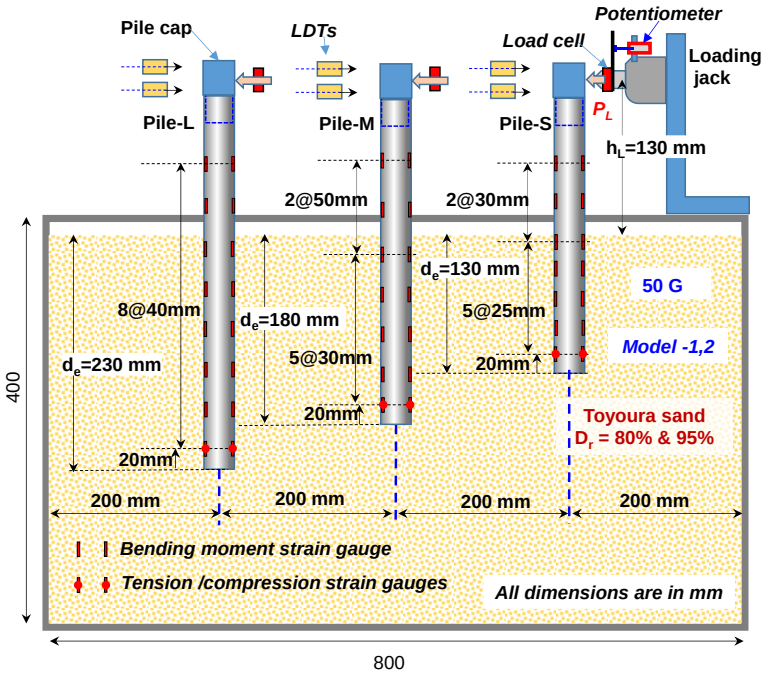

Figure 4.4 Centrifuge model setup for piles embedded in Toyoura sand at 80% and 95 % relative densities (Model 1 &2)

Different containers were used for the sand models and the models with the rock (Figure 4.12(b)), with the internal dimensions of 802mm length, 400mm depth and 250mm width, and 700mm length, 500mm depth and 150mm width respectively. Model tubular piles used in this study were thin wall pipes with 40mm outer diameter and 0.5mm thickness, made of stainless steel (SUS304) having the young's modulus (E) of 193 GPa and yield stress (σ_y) of 255 MPa. At the pile top, aluminium made solid circular pile cap with 30mm socketed depth was tightly fixed to form a solid loading head as shown in Figure 4.12(a). Sectional and mechanical properties of steel tubular piles are described together with the other test conditions in Table 4-1. Detailed mechanical properties of Toyoura sand were reported by Tatsuoka et al., (1984,1986) including the effects of density, and the mechanical properties of model soft rock used was described in Kunasegaram et al.,(2015).

4.2.5.2 Model - 3 (Piles embedded in rock 1g model)

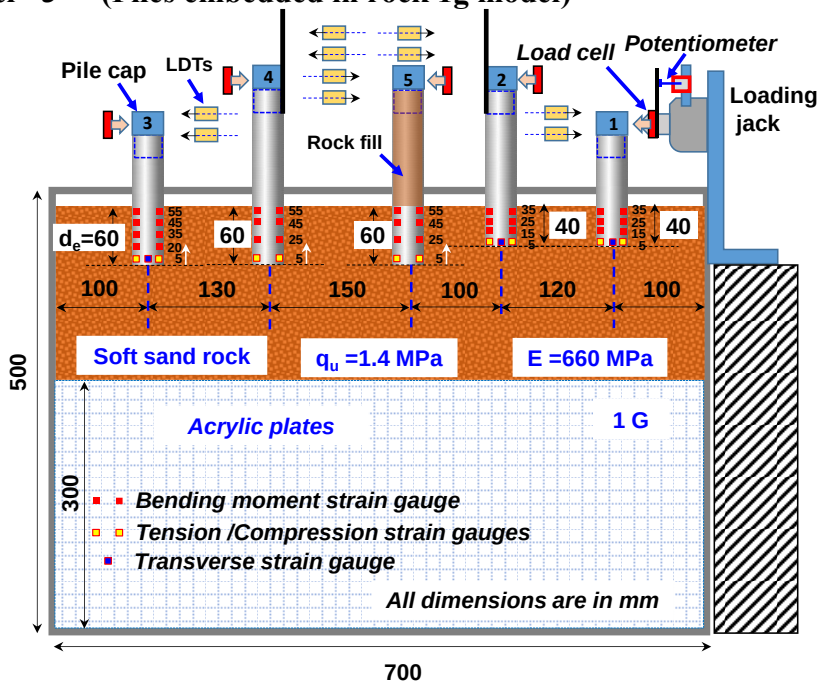

Figure 4.5 Model arrangement for piles embedded in soft rock for 1g model test (Model 3)

4.2.5.3 Model - 4&8 (Piles embedded in rock 50g model)

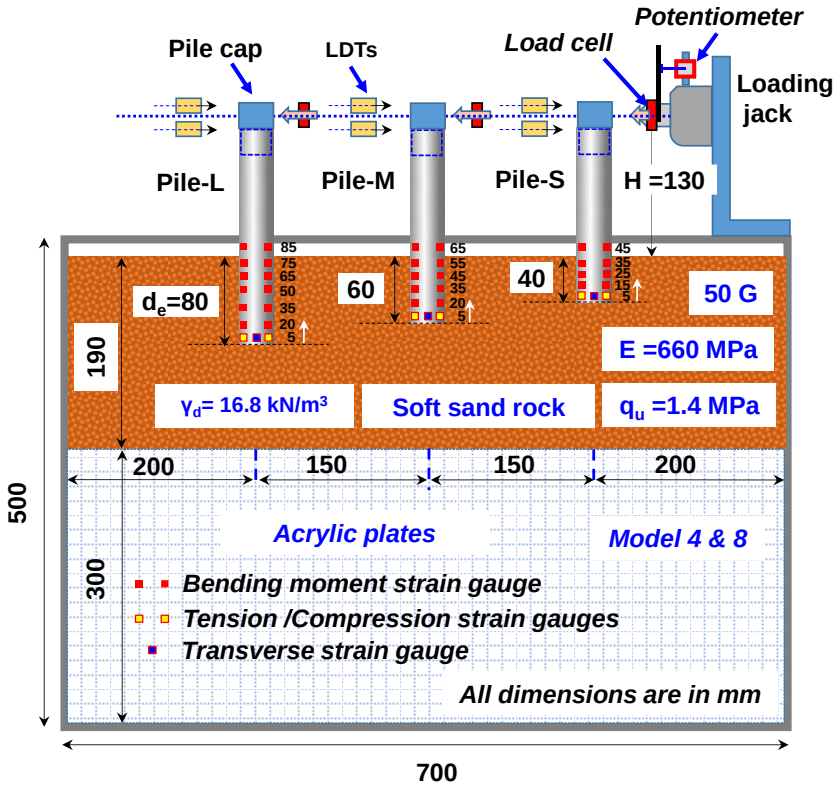

Figure 4.6 Centrifuge model setup for the piles embedded in soft rock (Model-4&8 at 50g)

4.2.5.4 Model – 5 (Rock socketed piles)

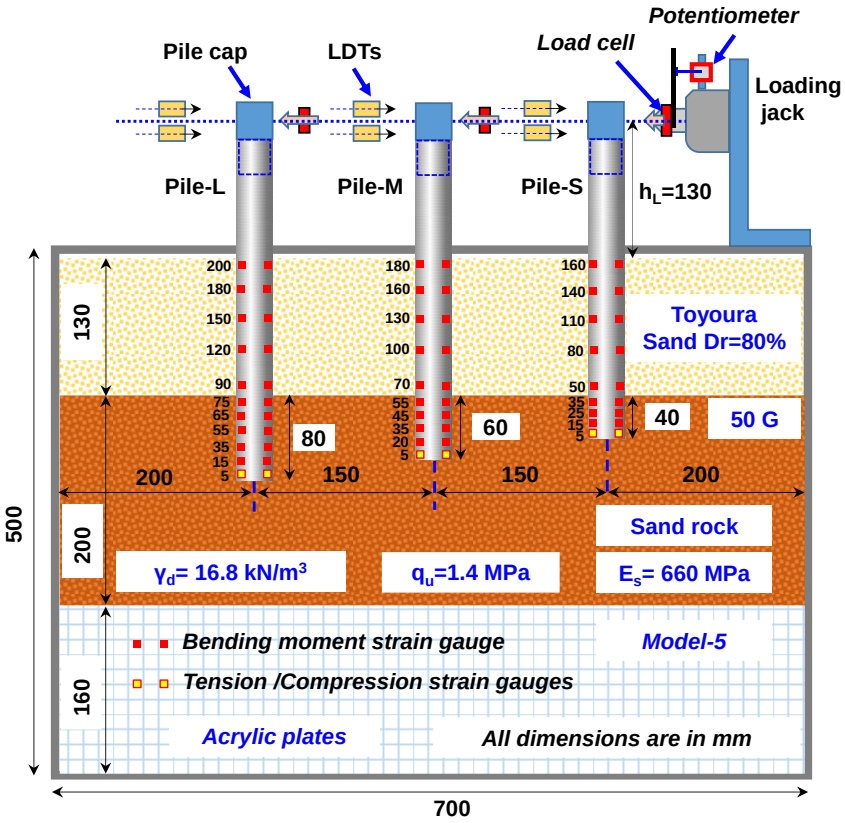

Figure 4.7 Centrifuge model arrangement for rock socketed piles (Model-5)

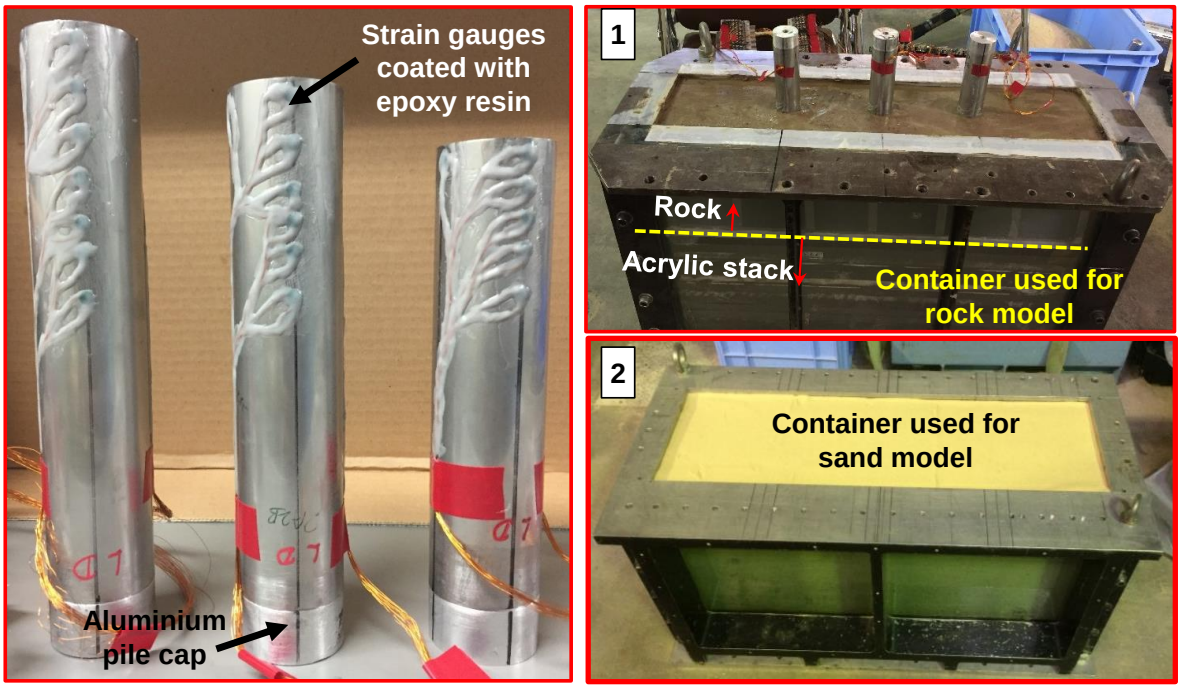

(a) Instrumented piles (b) Utilized containers for sand and rock model

Figure 4.8 (a) Model piles (For Model-3) and (b) Used containers for (1)rock and (2) sand models

The model piles were equipped with bending strain gauges on both sides of the pile along the loading direction, and Wheatstone circuits were made with the help of bridge boxes. Bending strains were measured by using full bridge circuits along the pile, while at the pile tip a pair of half bridge circuits were utilized to measure the axial strains at the loading and the opposite sides independently.

For the sand model, model grounds with 390 mm thickness were made using Toyoura sand with relative densities of 80% (Model-1) and 95% (Model-2) by air-pluviation as shown in Figure 4.12(b-2). Upon completion of the model ground with desired densities, three model piles with different embedment depths (d_e=130mm, Pile-S; 180mm, Pile-M; 230mm, Pile-L) were installed vertically in the model ground with the help of pile guide as shown in Figure 4.11-(1,2). By the static pile installation, the sand was filled in the pile to the level of ground surface. The section and mechanical properties of piles which were used in Model-1 and Model-2 are identical.

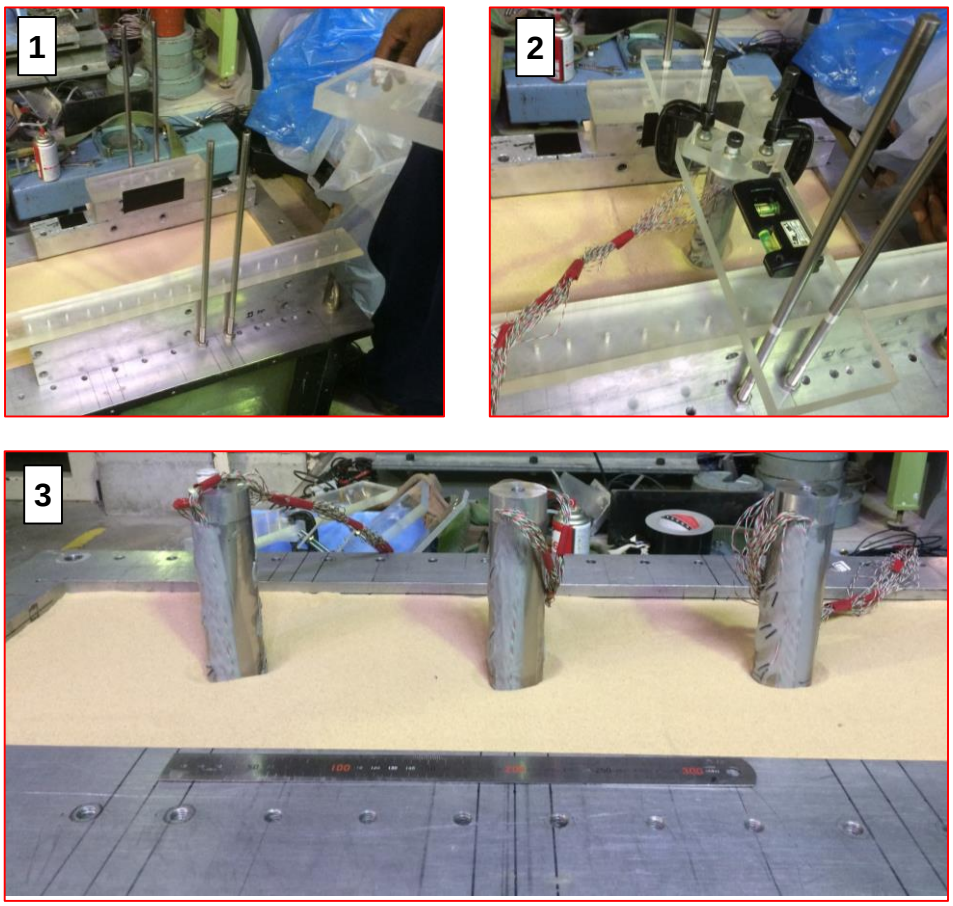

Figure 4.9 Static pile installation technique used in this study for pile installation in sand

Centrifuge model arrangement for three single piles embedded (d_e=40mm, Pile-S; 60mm, Pile-M; 80mm, Pile-L) in soft sand rock (Model-4&8) is described in Figure 4.6. In the preparation of soft rock model, 300mm thick acrylic plates stack was tightly placed in the container bottom to reduce the depth to 200mm (Figure 4.12(b-1)). A 190 mm thick layer of soft sand rock was made by compacting sand-clay-cement mixture layer by layer with 30mm thickness, confirming the target unit weight of each layer of compacted mixture. Immediately after casting the mixture, the model tubular piles were installed vertically into the unsolidified mixture with a pile guide (Figure 4.13) to the specified depth, and fixed the pile position. The casted

mixture was cured for 14 days in order to achieve the targeted strength (q_u) and stiffness of the embedded medium. The detailed preparation procedures and mechanical properties of the soft sand rock material are reported by Kunasegaram et al. (2015). It is important to note that sand and soft rock was filled inside the pile up to the rock surface level with the pile installation process employed in the model preparation stage, which was confirmed by means of physical measurements. In the preparation of Model-5 with two-layers ground, 160mm thick acrylic plates stack was placed at the container bottom to make 340mm depth for the sample. Then 200mm thick soft rock layer was made and the model piles were installed in the soft rock layer with the rock socked depths (d_R) same as the d_e of Model-3. After 14 days curing for the soft rock, 130mm thick top sand layer with Dr=80% was made by air pluviation. Upon completion of the model, the loading jack and laser displacement sensors (LDTs) were mounted on the container. Thereon the container moved to centrifuge platform and rigidly fixed, then the centrifugal acceleration was increased up to 50g.

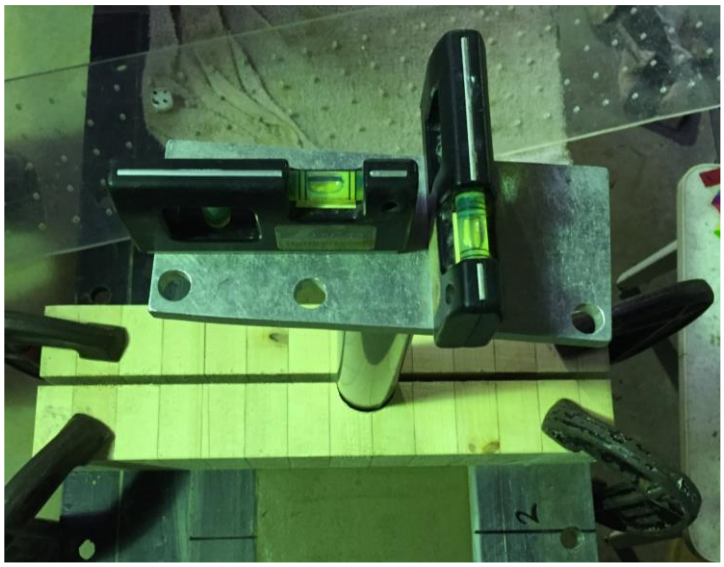

Figure 4.10 Pile installation method and wooden pile guide for rock models

4.3 Loading mechanism and the loading sequence

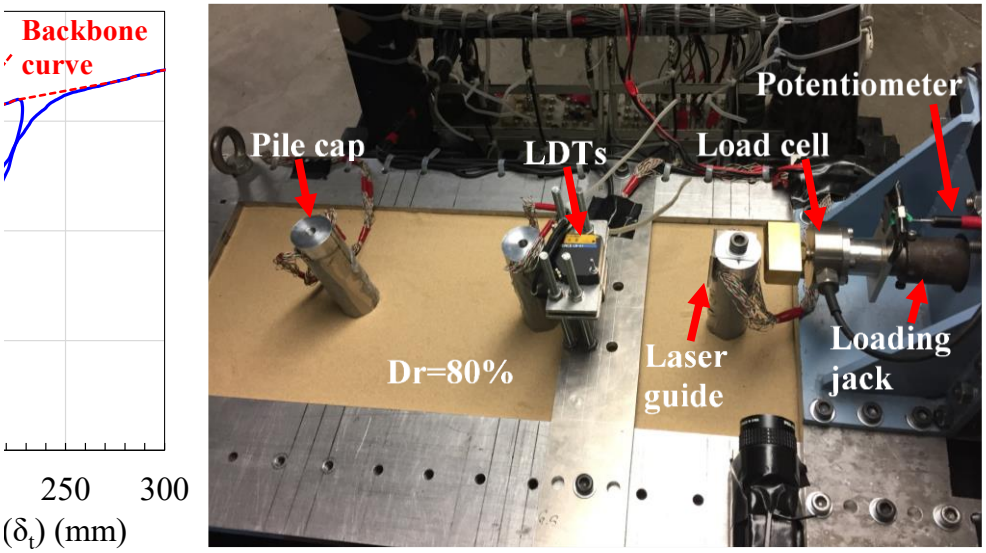

Figure 4.11 Loading mechanism and sensor arrangement in centrifuge

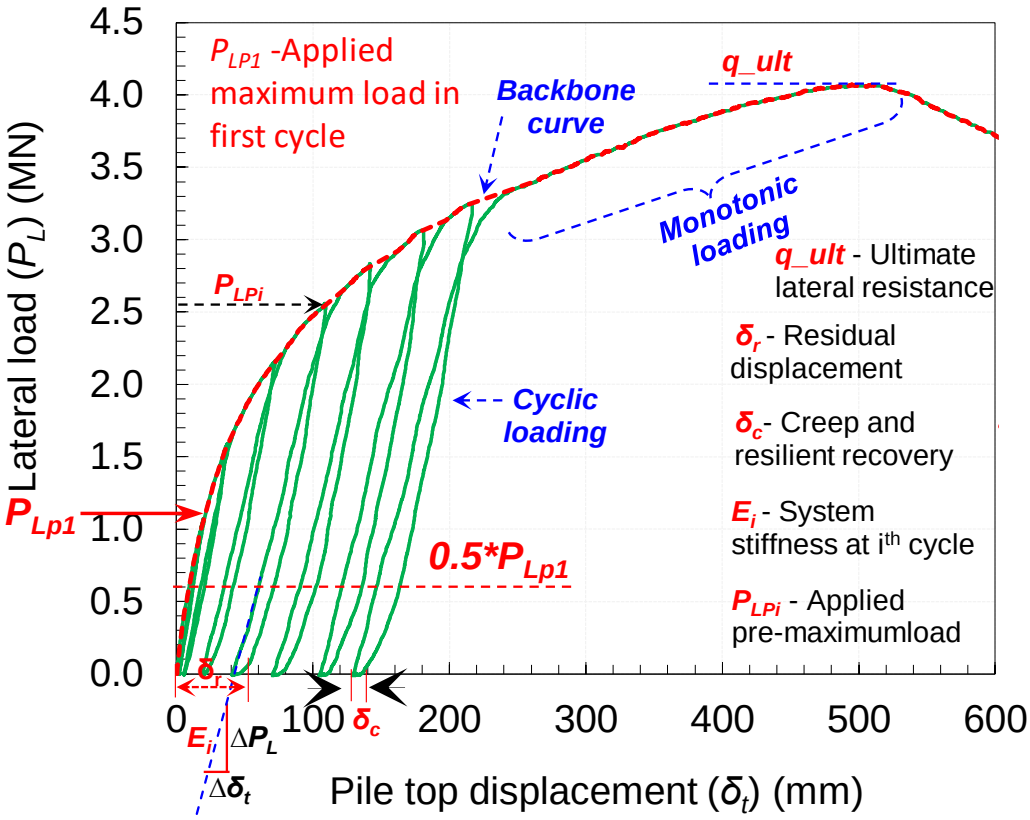

Figure 4.12 Typical loading sequence and definitions of load displacement parameters

In the centrifuge, one way horizontal load cycles were applied by the jack from small to large pile top displacements as described in Figure 4.11 and Figure 4.12 at 50g environment. Applied horizontal load at the pile top (P_L) was measured by a load cell and horizontal displacement (δ_t) and rotation (θ_t) at the pile top was obtained by means of LDTs at two elevations as described in Figure 4.11. Figure 4.12 describes a typical one way cyclic loading sequence implemented in this study, where the variation of applied lateral load in each cycle and subsequent monotonic loading period is illustrated against the pile top displacement. Figure 4.12 also describing the estimation method of system stiffness in the each cycle. Although system stiffness can be defined based on several ways of definitions, the system stiffness considered in this study focused on the stiffness deterioration induced by the additional loading in each cycle. Therefore, the initial stiffness in each cycle was the main interest in this estimation method. As a common rule for all the cycle the stiffness corresponding to 50% of the load applied in each cycle was estimated in this chapter and the rule is common for the subsequent chapter as well. In Model-3 (1g model), due to the less accurate measurements by LDTs, the pile top displacements were only measured by using the potentiometer attached to the loading jack as described by a similar loading arrangement in Figure 4.11. Having completed one pile loading test, the centrifuge was once stopped and the loaded pile was removed. Resetting the jack and LDTs to the next pile and the same horizontal loading was repeated. The loading was conducted in the sequence of 6.5m, 9m and 11.5m embedment in sand and it was 2m, 3m and 4 m for rock models. In the loading of Pile SP-MS-11.5 of Model 1, due to the trouble of loading jack, unloading at the small displacements could not be made. While the pile SP-SR-2* of Model 4 was accidently preloaded about 1mm prior to the test without instrumentation, the stiffness and resistance could not be obtained in the intact condition for the small displacement range. In the following chapter, the test results are shown in prototype scales. Except the comparisons related to the 1g model.

4.3.1 Observed loading sequences in centrifuge models

The variation of Imposed displacements at pile head against the time, are illustrated in Figure 4.13,Figure 4.14,and Figure 4.15.Which are representing the time variation of one way cyclic loads. As describe above the loading of pile SP-MS-11.5 of Model 1, due to the trouble of loading jack, unloading at the small displacements could not be made, it can be noticeable in the Figure 4.13. For the comparison of identical embedment piles in Model-4 and Model-8 with different imposed displacements in each cycle, the time variation of imposed displacement for each pile pairs are given separately in Figure 4.14. Also to compare the rock socketed piles with non-socketed one the loading sequence of pile SP-MS-6.5 also merged in the Figure 4.15.Where the imposed displacements of non-socketed pile is almost twice that of socketed ones.

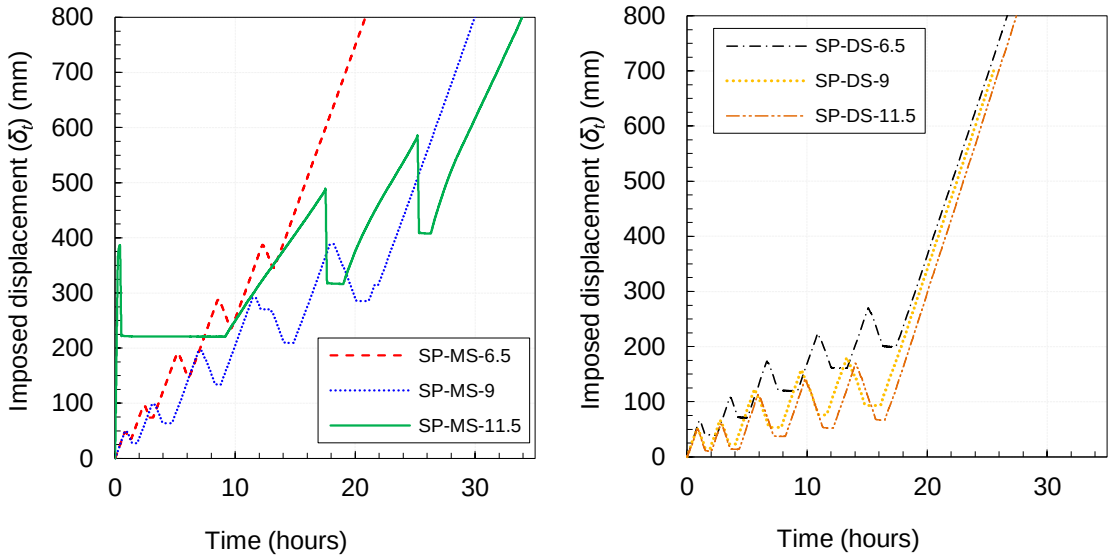

Figure 4.13 Loading sequence in Model-1 and Moldel-2

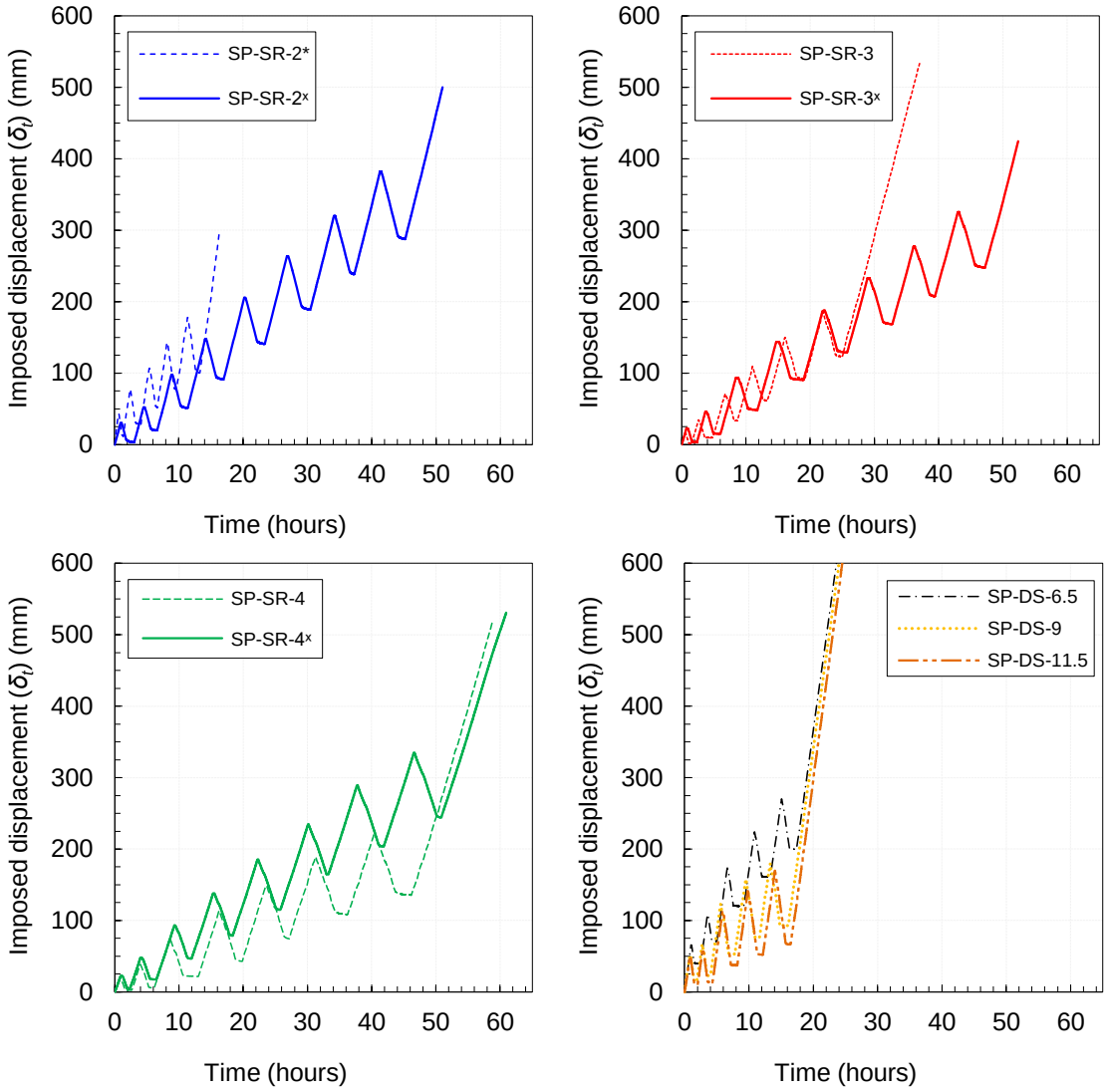

Figure 4.14 Loading sequence of piles in Model-3 & 8 with Model-2

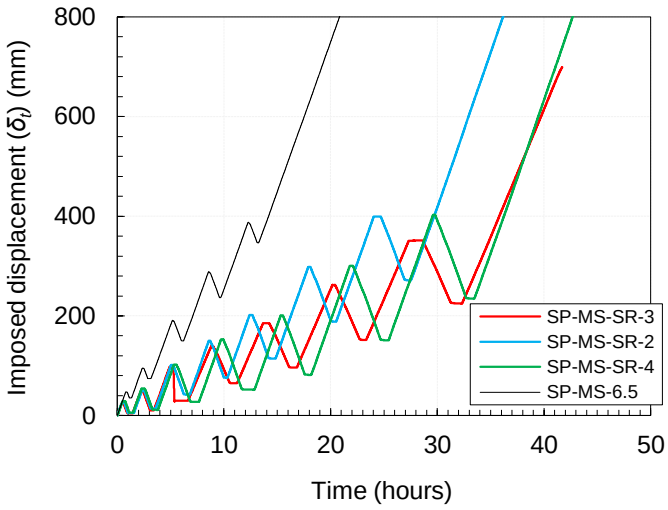

Figure 4.15 Loading sequence of rock socketed piles in Model-5 with non-socketed pile

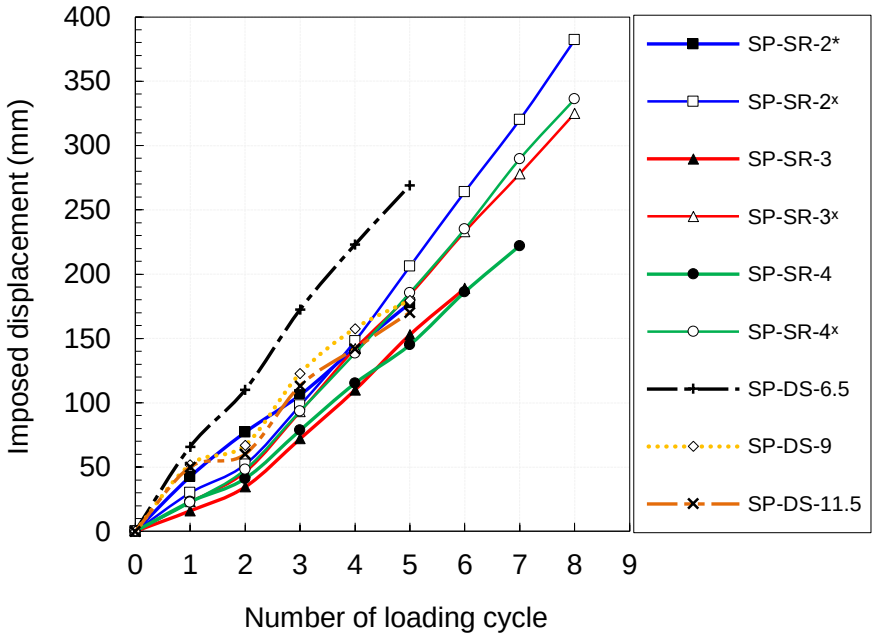

Figure 4.16 Variation of imposed displacements at the end of each loading cycle for the piles embedded in dense sand and soft rock

4.4 Results and discussion

4.4.1 Observed typical load-displacement-rotation behaviors

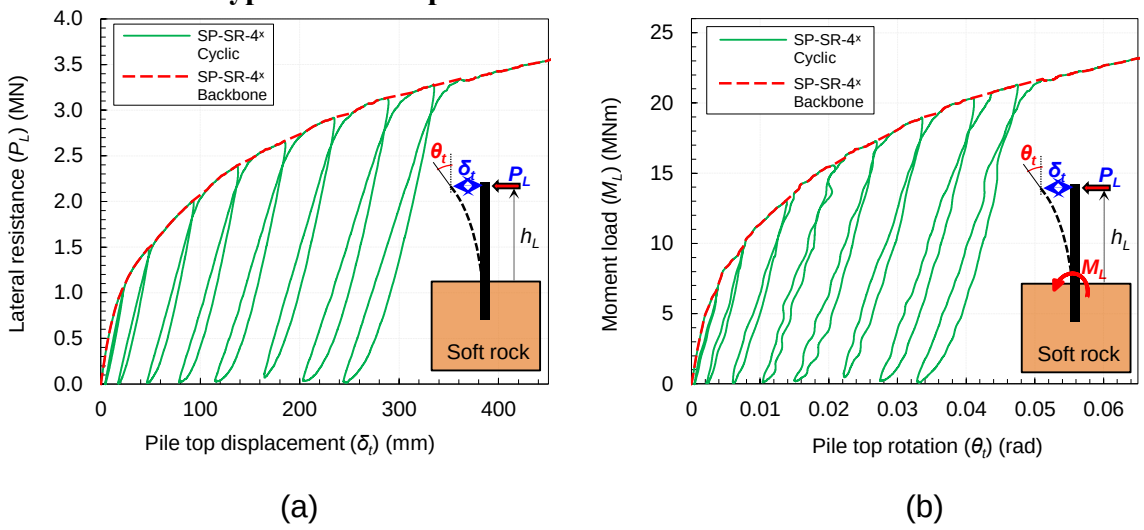

Figure 4.17 Target structure and simplified models

A typical observed cyclic load (P_L) - displacement (δ_t) and moment load (M_L) - rotation (θ_t) curve is presented in Figure 4.17. In each cycle, certain amount of residual displacements can be seen after unloading. However, in the reloading processes the P_L- δ_t curves return to a unique curve, which is the envelope of cyclic load-displacement behavior. Here onwards the envelope curve will be written as a backbone curve.

4.4.2 Behavior of large diameter piles embedded in sand and two-layer profile

Figure 4.18 illustrates the cyclic load-displacement (Figure 4.18(a,c)) and moment load-rotation (Figure 4.18(b,d)) relations and corresponding back bone curves (Figure 4.18(e,f)) of piles embedded in medium dense (SP-MS) and dense Toyoura sand (SP-DS) with different embedment depths of 6.5m (SP-MS-6.5 and SP-DS-6.5) ,9m (SP-MS-9 and SP-DS-9) and 11.5m) (SP-MS-11.5 and SP-DS-11.5). Similar illustrations for the case of socketed piles (Model-5) with 2m(SP-MS-SR-2), 3m(SP-MS-SR-3) and 4m(SP-MS-SR-4) socketing depths and non-socketed pile with same embedment and identical density of overlain sand (SP-MS-6.5) also given in Figure 4.19.

Referring to the observed load – displacement and moment load rotation relations for the piles with identical embedment depth [(SP-MS-6.5 and SP-DS-6.5), (SP-MS-9 and SP-DS-9), (SP-MS-11.5 and SP-DS-11.5)] and loading conditions the influence of embedded medium can be clearly confirmed from Figure 4.18(e,f). Similarly comparing the piles with different embedment depths in medium dense (SP-MS-6.5, SP-MS-9 and SP-MS-11.5) and dense Toyoura sand (SP-DS-6.5, SP-DS-9 and SP-DS-11.5) influence of embedment depth also can be confirmed from Figure 4.18(e,f). As expected, the lateral and rotational resistance of the piles increases with increasing embedment depths in both mediums (MS, DS), however denser the ground higher the lateral and moment resistance achieved for the identical embedment depths (e.g. SP-MS-6.5 and SP-DS-6.5).

From Figure 4.19 (c,d), similar comparisons based on load –displacement and moment – rotation relation for the piles with different socketing depths under identical loading conditions clearly indicates the influence of socketing depths on the lateral and rotational resistance of piles embedded in a layered profile. From Figure 4.19 (c,d), significantly larger contribution of 2m socketing could be observed while comparing non-socketed pile (SP-MS-6.5) and the pile with 2m socketing (SP-MS-SR-2). However, the additional 1m socketing increment has no significant contribution on the lateral and moment resistance. Especially the piles with 3m and 4m socketing exhibits almost identical load displacement and moment rotation behavior.

The post peak reductions in load displacement behavior of piles SP-MS-11.5, SP-DS-9 and SP-MS-11.5 could be attributed to the observed structural buckling failures. The deformed shape of piles in medium dense (Model-1) and dense sand (Model-2) are shown in Figure 4.20. Figure 4.23 describes the condition of rock sockets up on removal of overlain sand after finishing the tests and the observed failures of the piles and the relative location of the point of pile buckling from the top surface of the sand layer.

Based on Figure 4.18 (e) and the piles SP-MS-6.5, SP-MS-9 and SP-MS-11.5, deeper the embedment is, the larger the mobilized resistance of pile can be observed. However, this observation is not true while comparing the behavior of piles SP-DS-11.5 and SP-DS-9, there is no significant difference between the two piles, implying less effects of embedment depth increase from 9 m to 11.5 m in the dense sand. Similar behavior can be observed while comparing the socketed piles SP-MS-SR-3 and SP-MS-SR-4. Although increasing the socketing depth from 3m to 4m has no significant influence on the lateral resistance of socketed piles, comparison between SP-MS-6.5 and SP-MS-SR-2 clearly indicates the contribution of 2m socketing in to relatively hard layers, increasing the lateral resistance of piles more than twice that of the non-socketed pile. Structural failures of the socketed pile were confirmed with clear local buckling at a point below the ground level as shown in Figure 4.23 (b). Deeper the socketing depth, the relative point of buckling from sand surface also deeper, which can be confirmed from the comparison of buckling locations of piles SP-MS-SR-3, SP-MS-SR-4 from Figure 4.23 (b). Comparing the observed buckling

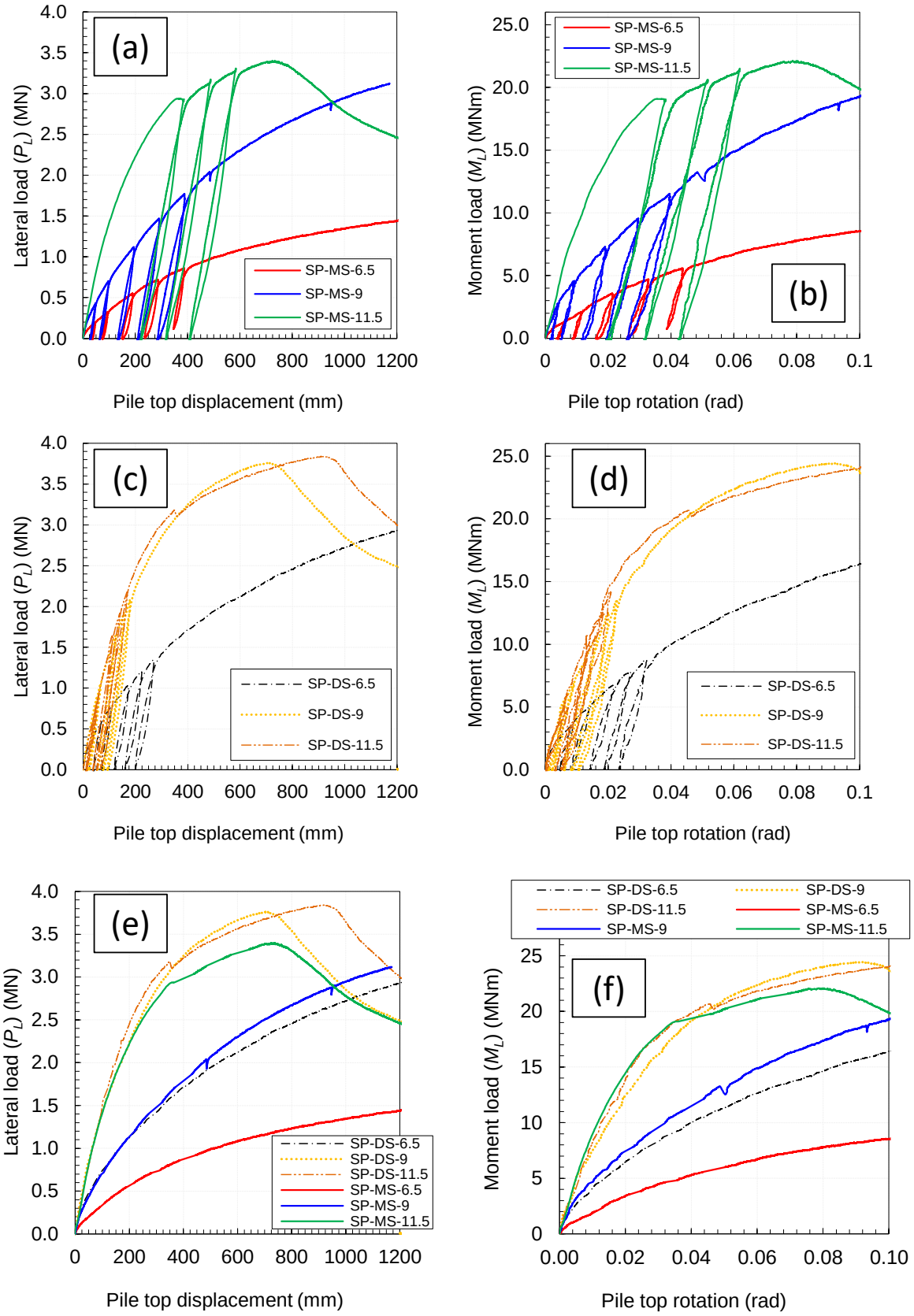

Figure 4.18 Comparison of observed load –displacement – rotation behaviors for the piles in medium dense (Model-1) and dense (Model-2) sand

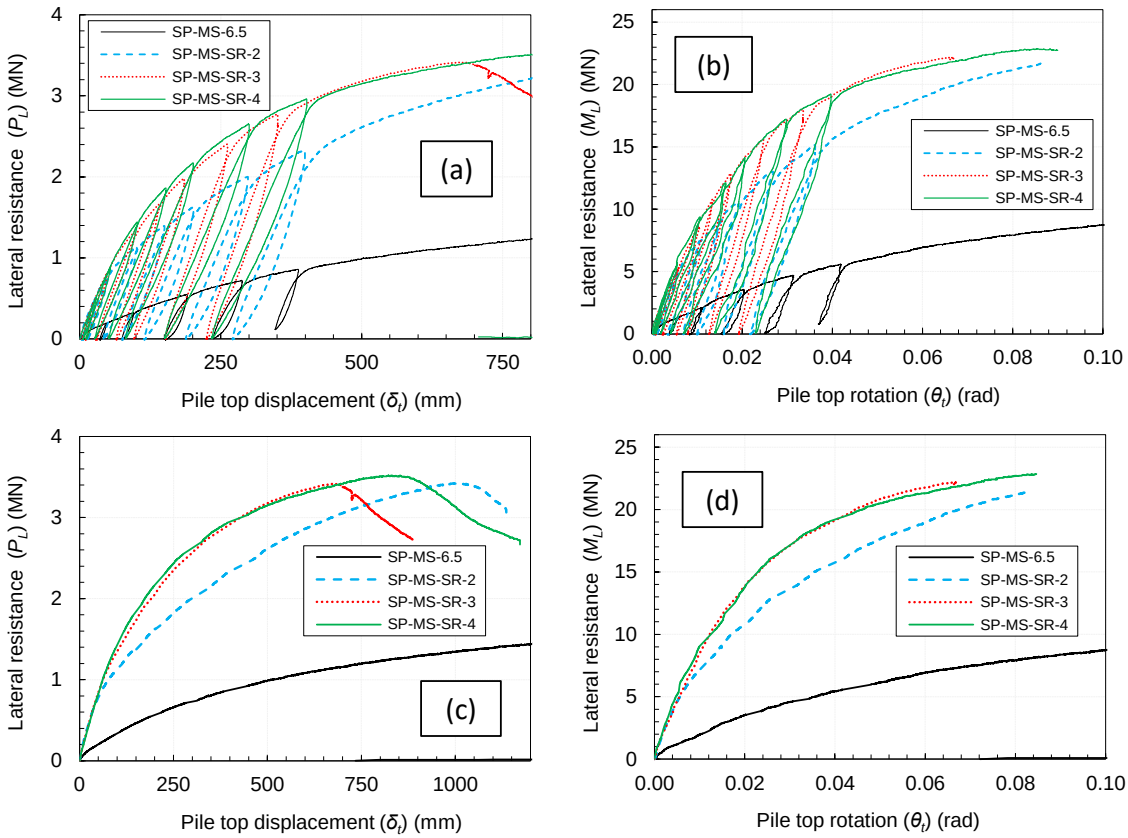

Figure 4.19 Comparison of observed load –displacement – rotation behaviors for the piles socketed in soft rock and overlain by 6.5 m Toyoura sand (Model-5) and non-socketed pile in sand with 6.5m embedment depth (zero socketing depth) (Model-1)

points of piles embedded in medium dense sand (SP-MS-11.5) and dense sand layer (SP-MS-11.5) as the confinement increases the location of buckling point moves closer to the embedment level. Which can be confirmed from the location of observed structural buckling for the case of rock embedded pile (SP-SR-4) given in Figure 4.24, which is described in the subsequent sub chapter. Once the pile failed by the structural buckling, the further increase of embedment or socketing depth (de >11.5 m for medium dense, de >9m for dense sand and d_R >3m for socketed piles) could have no significant influence on the lateral resistance of piles for abovementioned

loading conditions. The reductions of resistance after the peak load are the indication of clear structural failure, while for SP-MS-6.5, SP-MS-9, and SP-DS-6.5 piles, the resistance increased until large pile top displacement over 50% of pile diameter (Φ) without showing peak resistance also no structural failure can be observed from Figure 4.20 (a,b).

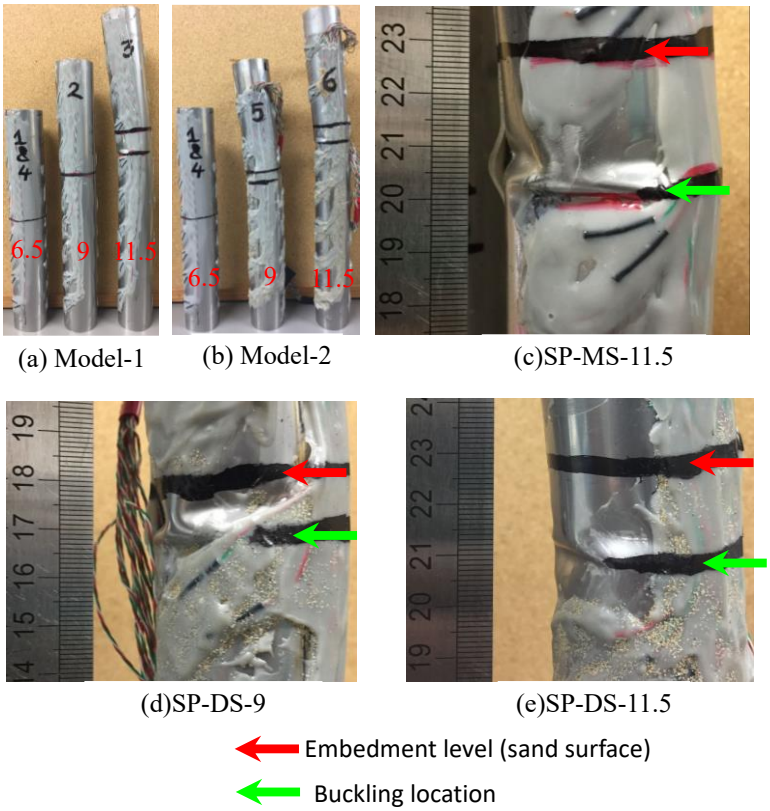

Figure 4.20 Observed deformation of piles in medium dense (Model-1) and dense sand (Model-2)

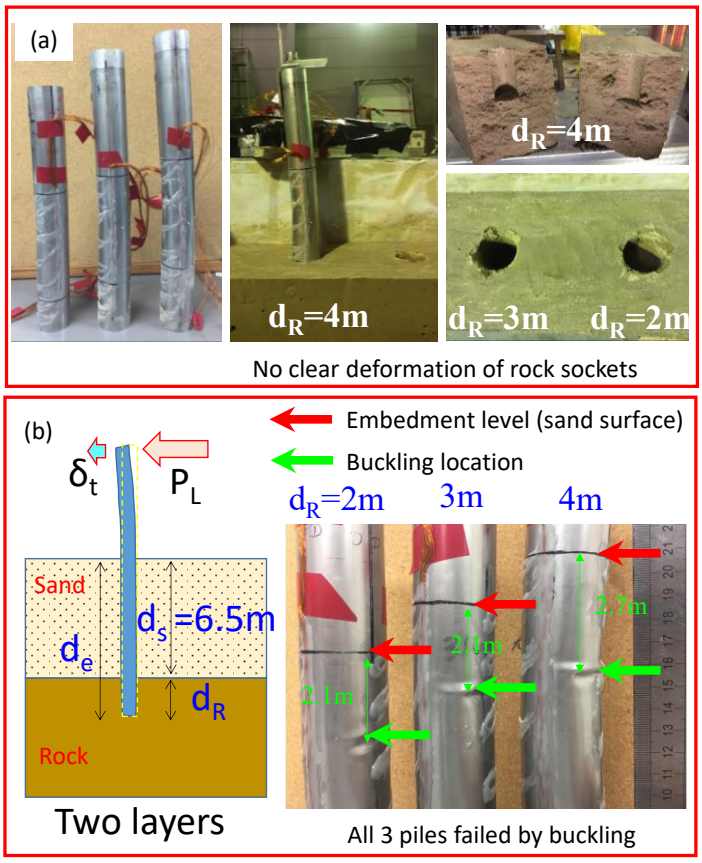

Figure 4.21 Observed deformation of piles in two layer profile (Model-5)

4.4.3 Behavior of laterally loaded large diameter piles embedded in rock

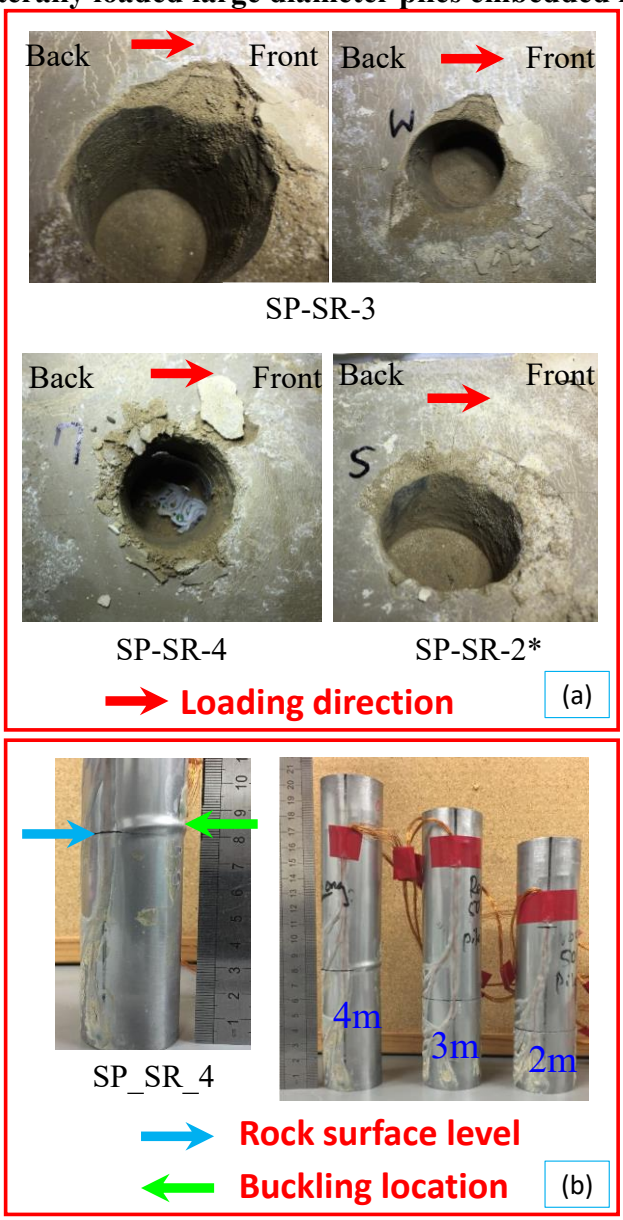

Figure 4.22 Observed ground failures and deformation of piles embedded in soft rock (Model-4)

Figure 4.23 illustrates the cyclic load-displacement and moment load-rotation relations and corresponding back bone curves of piles embedded in soft rock for 50g centrifuge models (Model-4 and Model-8). Similar illustrations for the case of 1g model piles (Model-3) embedded in soft rock are shown in Figure 4.24. From Figure 4.23 and Figure 4.24 the influence of embedment depth, loading height and the imposed displacements on the behavior of piles embedded in soft rock could be confirmed. For the piles embedded in the soft sand rock, 1 m increment in embedment depth can significantly increase the ultimate lateral resistance up to d_e=4m. As a clear structural failure with local buckling was observed slightly above the ground level for SP-SR-4 with d_e=4m as shown in Figure 4.25 (a-2) it can be inferred that further increase of the embedment could not contribute to the increase of pile lateral resistance. The depth over which the effect of embedment increment cannot be obtained is considered as an "optimum embedment depth (OED)". The difference between the OED in the medium dense sand, dense sand, soft rock and socketed piles can be attributed to their rigidity

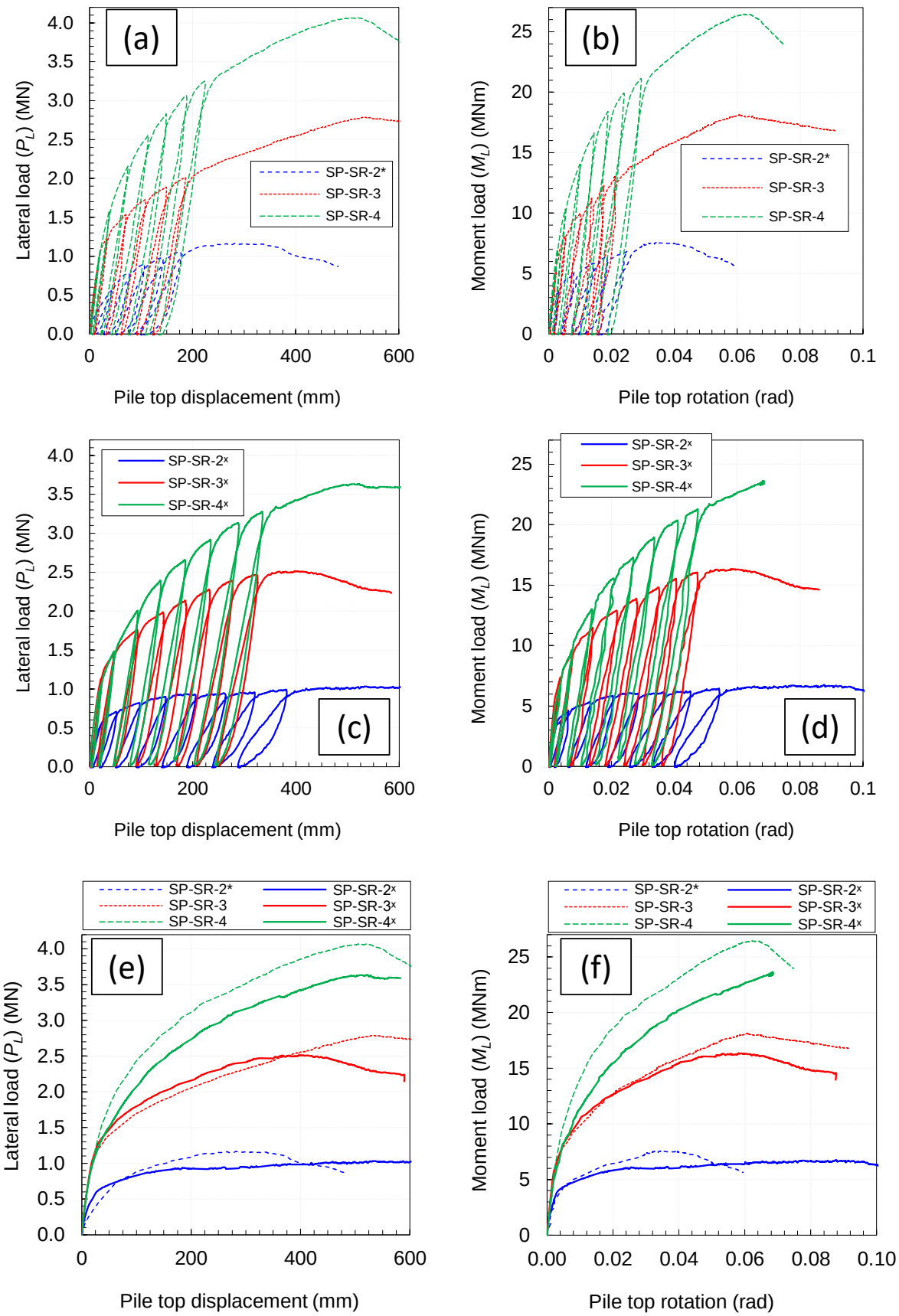

Figure 4.23 Observed load –displacement – rotation behaviors for the piles in soft rock (Model-3&8)

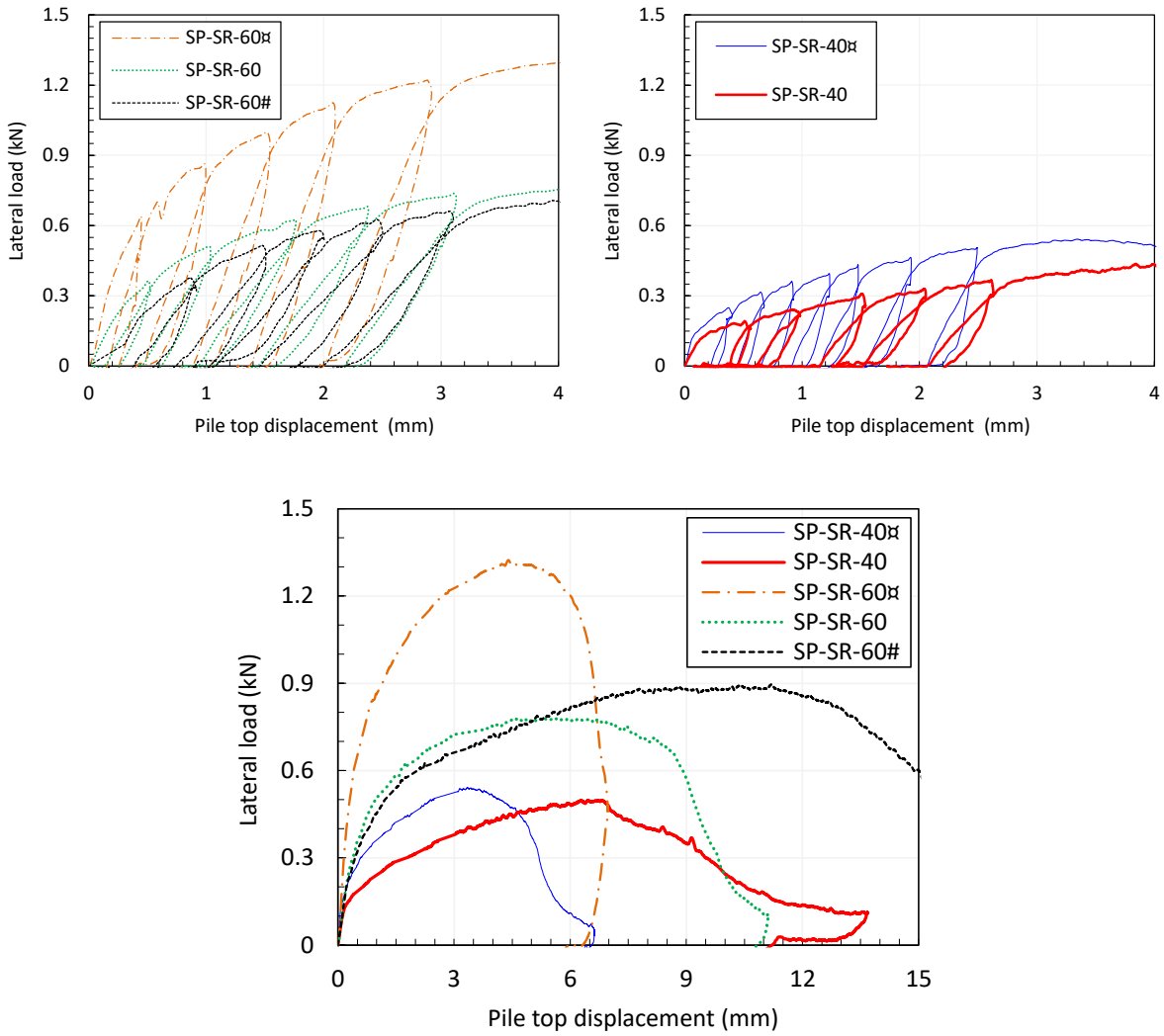

Figure 4.24 Observed load –displacement behavior for the piles in soft rock (1g (Model-3))

or confinement. The soft rock can effectively hold the pile at shallow depth even for the relatively stiff large diameter pile. Observed buckling point of SP-SR-4 is located at the ground surface level which could be attributed to the large lateral confinement of soft rocks and the plugged portion of the rock inside the piles. No structural failures were observed for the piles SP-SR-2* and SP-SR-3 in the soft rock as shown in Figure 4.22(b), but the load displacement curves of the two piles also showed clear peak resistance and the reduction. The observed post peak reduction could be attributed to the rock failure in the embedded zone as described in the Figure 4.22(a). In theoretical point of view, this increase of strain even with the reduction of applied load could be attributed to the strain softening of stress-strain relationship of the rock material and smaller d_e of the soft rock model than that of sand model. Although the piles with structural failure and the piles embedded in the soft rock with relatively small embedment depth showed strain softening behavior in the load-displacement curves, the post peak resistance reduction are different between the piles failed by the structural failure and the ground failure. Once the structural buckling initiated a sudden reduction of load against the displacements can be seen, while comparing the behavior of piles SP-SR-4 and SP-SR-3 from Figure 4.23. On the other hand, the observed post peak behavior related to ground failures (SP-SR-2*, SP-SR-3) exhibited smaller post peak stiffness and much more ductile especially for the deeper embedment case (SP-SR-3).

The peak load displacement of SP-SR-2 was smaller than that of SP-SR-3. These behavior of the piles with no pile failure but ground failure of the soft rock as shown in Figure 4.22(a) is different from that of the sand. The pile behavior with sand failure did not exhibit a clear post peak reduction in sand, rather a continuous increase in the resistance more than 50% of the pile diameter could be seen as shown in Figure 4.18(e).

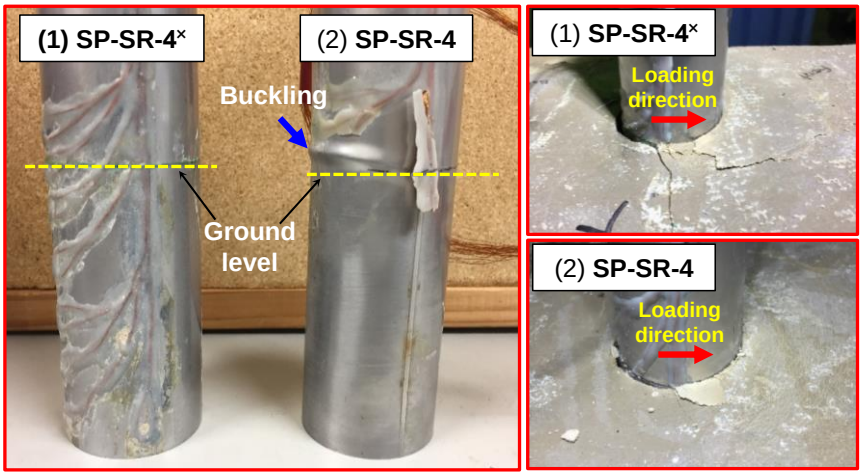

Observed failure mode of the piles with 80 mm embedment depth and 50g model

Figure 4.25 Observed ground and structural deformation of piles with 4m embedment in soft rock

4.4.4 Influence of embedment and socketing depths

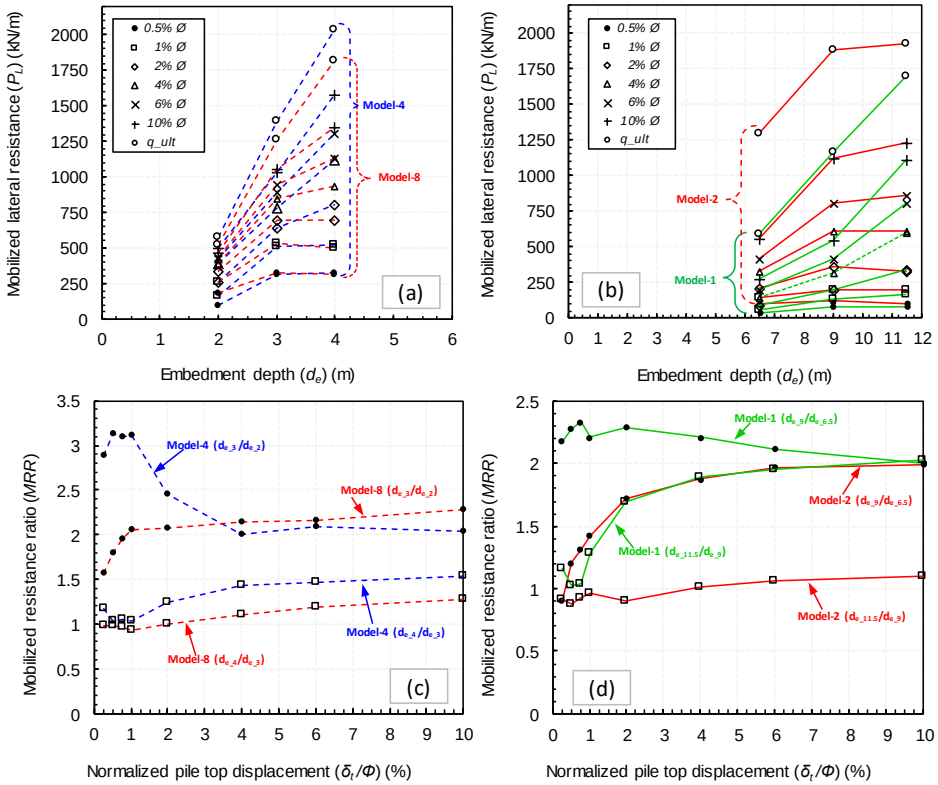

Figure 4.26 Influence of embedment depth on the lateral resistance of piles

The influence of embedment depth (d_e) on the lateral resistance of piles embedded in soft rock and sand from small to large pile top displacements (δ_t) are depicted in Figure 4.26 (a) and Figure 4.26 (b) respectively. It is important to note that, for the piles without peak resistance, the-ultimate resistance (P_{ult}) was obtained based on double tangent method using the backbone load - displacement relation (Figure 4.18(e)).From Figure 4.26 a distinctive behavior of piles at different displacement levels depending on the stiffness of embedded medium can be observed. Based on Figure 4.26 (b), in Model -1 (MS), as the embedment depth increases, the lateral resistance also increases from small to large displacements. However, the increment trends of resistance from d_e =6.5m to 9m depth and d_e =9m to 11.5m change with imposed displacement. At the small displacement (δ_t <2% Ø) the resistance increases linearly with d_e, while at δ_t =4~10% Ø, the larger resistance increase can be seen for the increment of d_e from 9m to 11.5m than that of 6.5m to 9m. However, the effect of former depth increment on P_{ult} become less significant than that of the latter increment. This is a clear evidence that the horizontal resistance of the pile or system stiffness was governed by mobilized soil resistance in the early stage of loading but controlled by the strength and stiffness of pile at the ultimate conditions as described for the pile SP-SR-4 with the structural buckling in sand rock (Model-4). Referring to Figure 4.26 (b), in Model-2 (dense sand), the piles with d_e=9 m and 11.5 m show almost no difference in the mobilized resistance from small displacement to ultimate values. The horizontal resistance of piles embedded in the soft rock also increased with d_e. But the trend is quite different from that in sand. Large increase of lateral resistance can be attained by increasing d_e from 2m to 4m, and the trend is almost linear with d_e for all displacements, except the piles with d_e over 3m at small displacements. The resistance of 4m (SP-SR-4) embedment pile is almost the same and slightly larger than that of 3m (SP-SR-3) embedment piles at δ_t =1% Ø and 2% Ø respectively for the piles in Model-4. At the small pile displacement, the shallower depth of the rock (less than 3m) could mainly confine the pile by the large initial stiffness of intact rock. But the softening of rock by the displacement deteriorates the subgrade reaction in the shallow layers of rock as shown in Figure 4.25(b-2) and Figure 4.35(b-2), which cause the difference in the mobilized resistance between the piles SP-SR-3 and SP-SR-4 at larger displacement levels.

In order to discuss the optimum values of embedment depth for the model piles studied in this chapter, the mobilized resistance ratio (*MRR*) between two piles of interest was estimated and illustrated against the normalized pile top displacement in Figure 4.26 (c) and Figure 4.26 (d) for the piles embedded in soft rock and sand respectively. Where the separate notations given in figures are describing two piles of interest and indicating the corresponding variations of *MRR* by an arrow mark. For example, the meaning of Model-4(d_{e-4} /d_{e-3}) is that, the piles with 4m and 3m embedment depth was considered for the calculation of *MRR* in Model-4 and the *MRR* was calculated by dividing the resistance of 4m embedment by the 3m embedment pile under the same displacement level. A value of *MRR*=1 for two piles with different embedment depth is the indication of the optimum embedment depth, which is corresponding to the smaller embedment among two piles. From Figure 4.26 (c) and Figure 4.26 (d), observing the variations of *MRR* for the piles with relatively large embedment depths in sand ($d_{e-11.5}$ /d_{e-9}) and soft rock (d_{e-4} /d_{e-3}), the pile behavior dictates two different optimum embedment depths depending on the stiffness. In other words, depends on the level of displacement, which governs the stiffness deterioration of embedded medium and thereby the system stiffness as described in subsequent chapter 4.4.6.

From Figure 4.26 (c), an *MRR* of unity for d_{e-4} /d_{e-3} can be observed up to a pile top displacement of δ_t =1% Ø, beyond this level a gradual increasing trend of *MRR* can be seen for the piles of interest. As discussed earlier the intact condition of model soft rock tends to deteriorate beyond this displacement level, thereby the mobilized resistance of pile with 3m

embedment depths becomes smaller than that of 4m beyond this level, which causes an increment in *MRR*. From the observation it can be concluded that, up to δ_t=1%Ø (20mm) the 3m embedment depth ((d_e/Ø) =1.5) could be considered as an optimum embedment for the piles embedded in sand rock with specific loading height considered in this study. This embedment depth is a kind of optimum embedment depth for relatively larger initial stiffness of soft rock more or less in the intact condition. Furthermore, from the observed buckling of the pile with 4m embedment ((d_e/Ø) =2) in soft rock (Model-4), it can be considered that the optimum embedment depth could be closer to 4m embedment depth for this specific loading condition. Similarly, referring to the piles with 9m and 11.5m embedment depths in Figure 4.26 (d), the optimum embedment depth for the piles in medium dense and dense sand could be derived. Referring to the *MRR*-($d_{e\text{-}11.5}$ /$d_{e\text{-}9}$) in Model-1, up to δ_t=0.5%Ø (10mm) an *MRR* of unity can be seen. Beyond this stage a steep increasing trend of *MRR* up to δ_t=6%Ø and a constant variation over this displacement can be observed. However, the piles with same embedment depths in Model-2 indicates the *MRR* of unity or less than one up to a displacement of δ_t=4%Ø. Beyond this level a small increment and a constant trend can be seen from Figure 4.26 (d). Based on these observations 9m embedment depth ((d_e/Ø) =4.5) can be defined as an optimum embedment depth in medium dense (Model-1) and dense sand (Model-2) up to δ_t =0.5%Ø (10mm) and δ_t =4%Ø (80mm) respectively. Beyond these displacement levels the optimum embedment also increases depending on the deterioration of ground stiffness for the considered cross section of the pile.

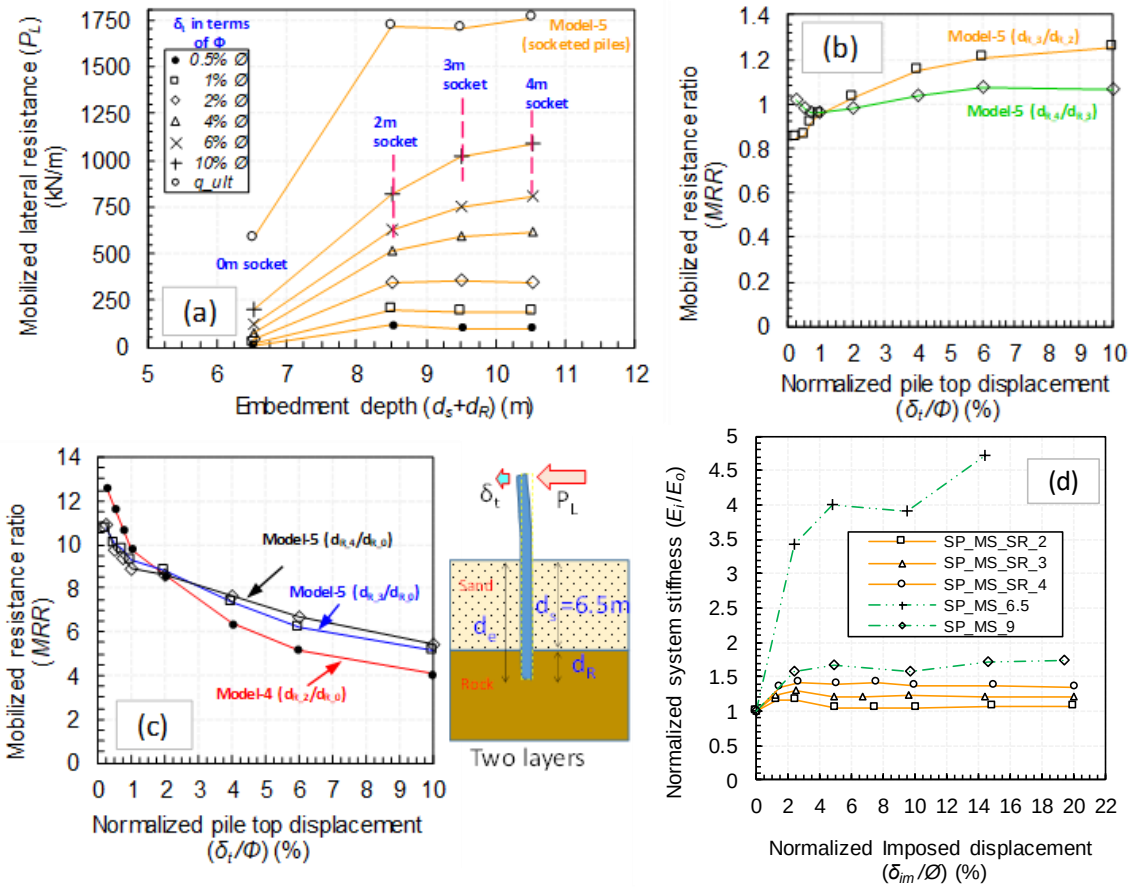

Figure 4.27 Influence of socketing depth on the lateral resistance of piles

Influence of socketing depth on the lateral resistance of piles embedded in a two layer profile can be expressed by referring the Figure 4.27. Where Figure 4.27(a) illustrates the variation of lateral resistance against the embedment depths (d_s+d_R) at different levels of imposed pile top

displacements. Figure 4.27(b) describes the mobilized resistance ratio (*MRR*) between the pairs of 3m,2m socketing and 4m,3m socketing against the normalized pile top displacement. In order to discuss the influence increment in the socketing depth, the MRR between 2,3 and 4m socketing depths and non-socketed pile are drawn against the normalized pile top displacement in Figure 4.27(c). Figure 4.27(d) describing the variation of system stiffness in each loading cycle against the normalized maximum imposed displacement in previous cycle for socketed piles and the piles in Model-1 with 6.5m and 9m embedment depths. From Figure 4.27(a), it can be seen that the rock socketing over 2m has no significant influence on the lateral resistance up to 2% Ø of pile top displacements which could be attributed to the combination of mobilized resistance at shallow layer of rock and the densification of the overlain sand overlaying sand.

However, beyond this displacement level a clear influence of socketing can be seen from the pile top displacement of 4% to 10%Ø as shown in Figure 4.27 (a). Referring to Figure 4.27 (d), beyond the imposed displacement of 2% Ø, a sudden reduction in the system stiffness can be observed for the socketed piles. However, the pile SP-MS-9 exhibits more or less a constant system stiffness beyond this displacement level, which could be attributed to the achievement of limiting passive pressures in the pile front and this contribution of stiffness could be expected even up to large imposed displacements not only for SP-MS-9 but also for the socketed piles. Referring to the behavior of pile SP-MS-9 and socketed piles the observed sudden reduction in the system stiffness of socketed piles could be attributed to the deterioration of shallow layers of rock. Comparing the discussions based on Figure 4.27 (a) and Figure 4.27 (d), it can be concluded that the deterioration of underlain shallow layer rock stiffness took place at a pile top displacement of δ_t =2%Ø (40mm) for the specific embedment and loading condition in this study. Based on this study, limiting passive pressures in a 3.25Ø thick overlain layer could be expected to reach at δ_t =2%Ø, for the case of design conditions with an allowable pile top displacements δ_{all} >2%Ø, small strain stiffness of the underlain rock could not be expected.

Upon reaching the limiting passive pressures in the overlain sand, the deformation mechanism is mainly governed by the socketing depth of the piles for further increment of loading. Based on Figure 4.27 (a), a clear influence of 2m socketing (d_s+d_R=8.5m) at all displacement levels can be confirmed while comparing with the non-socketed condition (d_s+d_R=6.5m). However, the contribution of increment in socketing over d_R=2m become apparent only beyond δ_t =2%Ø, it can be confirmed from the *MRR* variations illustrated in Figure 4.27 (c). Furthermore from Figure 4.27(c), although significant difference between *MRR*(d_{R-2} /d_{R-0}) and *MRR*(d_{R-3} /d_{R-0}) could be observed, the observed difference for the case of *MRR*(d_{R-3} /d_{R-0}) and *MRR*(d_{R-4} /d_{R-0}) is negligible. This observation clearly indicates that, a 3m socketing (1.5 Ø) could be considered as an overall optimum socketing depth for initial stiffness and ultimate failure conditions. Which can be confirmed from the *MRR* value of unity for the piles with 3,4 m socketing depths in Figure 4.27 (b) as well as the observed structural buckling of the above-mentioned piles in Figure 4.21(b).

Although the deterioration of shallow layers took place, there is no significant influence of embedment or socketing depth on the ultimate resistance can be observed. The observation could be attributed to the observed structural buckling of all three socketed piles as shown in Figure 4.21(b) owing to the high lateral confinement of soft rock even with small socketing depths and after the shallow layer deterioration. As overall behavior it can be concluded that the lateral resistance of pile embedded in sand and soft rock increases with increasing embedment depth if the ground stiffness dominates the resistance. Influence of shallow layer of intact rock could alternate this conclusion at relatively small pile top displacements. Also, the effect of the embedment depth over the OED has no significant contribution on the lateral resistance of piles.

4.4.5 Bending behavior of single piles and influence soil or rock plugging

Measured bending moments along the pile at different pile top displacements (0.5%, 1%, 5%, & 10% Ø) for the piles embedded in dense sand (Model-2), soft rock (Model-3) and soft rock overlain by medium dense sand (socketed piles Model-5) are presented in Figure 4.28. Figure 4.29 describes the bending moment profiles at 1MNm and 5MNm applied moment loads for above mentioned model piles along with the piles embedded in medium dense sand (Model-1).

From Figure 4.28 and Figure 4.29(a), depths at the maximum bending moment for the piles embedded in sand (Model -1(MS), Model-2(DS)) are about -0.5 m for d_e=6.5 m pile,-2 m for d_e=9 m pile and -2.5 m for d_e=11.5 m pile. The bending moments of the pile in the sand models increase almost linearly with the distance from the loading point to the depth of maximum bending moment. The observation clearly indicates that the confining stresses from shallow layers of the sands has less significant influence on the lateral resistance of piles. On the other hand, the piles in the soft rock showing the maximum moment slightly above the ground surface and an abrupt change in the bending moments above and below the ground surface also can be observed. This observed bending behavior is another evidence of very high confinement of shallow layers of soft rock. Although rock socketed piles also exhibits a linearly increasing trend with the depth in sand layer at relatively small displacements (0.5-1% Ø), at large pile top displacements (5% Ø and 10% Ø) unlike the piles in sand, a clear non-linear variation of bending profiles below the embedment level can be observed. Though the shallow layers of sand has no significant confinement as observed in Model-1&2 the observed bending profile in Model-5 could be attributed to the high fixity of the piles in the socketed portion.

The depths of local buckling were -1.5m in SP-MS-11.5, -1.0m in SP-DS-9 & SP-DS-11.5, for the sand model and 0.15m above the ground surface for SP-SR-4, which were shallower than the depth of maximum bending moment. This could indicate the effect of infilled materials in the pile up to the ground surface. Therefore, without this plugging effect, ultimate resistance of the structurally failed piles could have been smaller than the observed resistance. It is important to note that the socketed piles have no infilling material above the rock surface since they installed prior to the sand pouring. In Model-5(Socketed piles) the measured maximum bending moment is located around -2.7 m for all three piles and the points of structural buckling was measured at -2.5m, -2.3m and -2.5m for MS-SR-2, MS-SR-3 and MS-SR-4 respectively. Comparing the observations with the observed structural failures in Model-1 and Model-2, the clear influence of plugging can be confirmed. From Figure 4.28 and Figure 4.29(a), up to δ_t =4%, 5% Ø (100 mm) all piles showing the bending moment smaller than the yielding moment (M_y). At δ_t =10% Ø (200 mm), SP-MS-9 and SP-MS-11.5 piles in the medium dense sand exhibit the bending moments slightly below and about the yielding moment respectively. However, at δ_t =10% Ø, the pile pairs SP-DS-9, SP-MS-SR-3 and SP-DS-11.5, SP-MS-SR-4 reached the bending moments corresponding to yielding and plastic hinge (M_p) respectively. At δ_t =20%Ø, piles SP-MS-11.5, SP-DS-9, SP-DS-11.5, SP-MS-SR-2 and SP-MS-SR-3 had already reached the plastic limit, this is a clear evidence for the structural deformation observed in Figure 4.20 and Figure 4.21(b). Embedded pile in rock SP-SR-4 and rock socketed pile SP-MS-SR-4 are showing the bending moment higher than the plastic limit at a pile top displacement of 10% Ø. As the stiffness of the ground increases from MS, DS to SR, the pile reaches its yielding and plastic limits at small displacement, which increases the possibility of structural failure over the soil failure in hard mediums and rock socketed piles. It can be also confirmed that the increasing embedment depth over the optimum

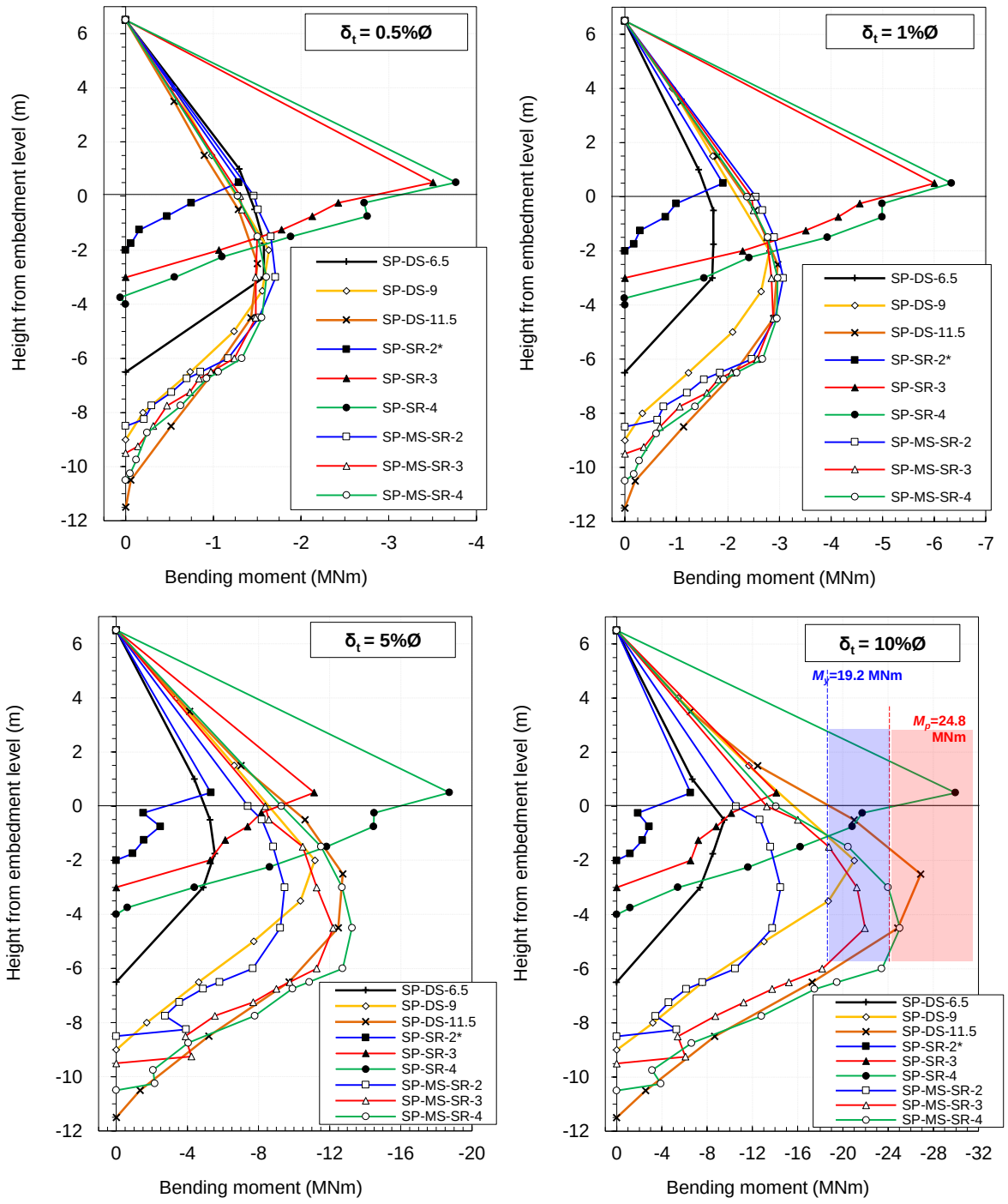

Figure 4.28 Comparison of pile bending behavior in dense sand, soft rock and two layer profile

depth in relatively hard embedment mediums cannot prevent the ultimate failure since it is caused by structural hinge. In other words, it can be said that the increasing section modulus can increase the optimum depth and the ultimate resistance. Measured bending moment profiles for the piles in medium dense sand (SP-MS), dense sand (SP-DS), soft rock(SP-SR) and socketed piles(SP-MS-SR) at the moment load of 1 and 5 MNm are given in Figure 4.29(b). Where the embedment depths in each models notated in the increasing trend as smaller, intermediate and larger to simplify the notation due to the space limitation in the plot. The moment load defined by horizontal load times the loading height at the ground surface is compared for all the piles in Figure 4.29(b).

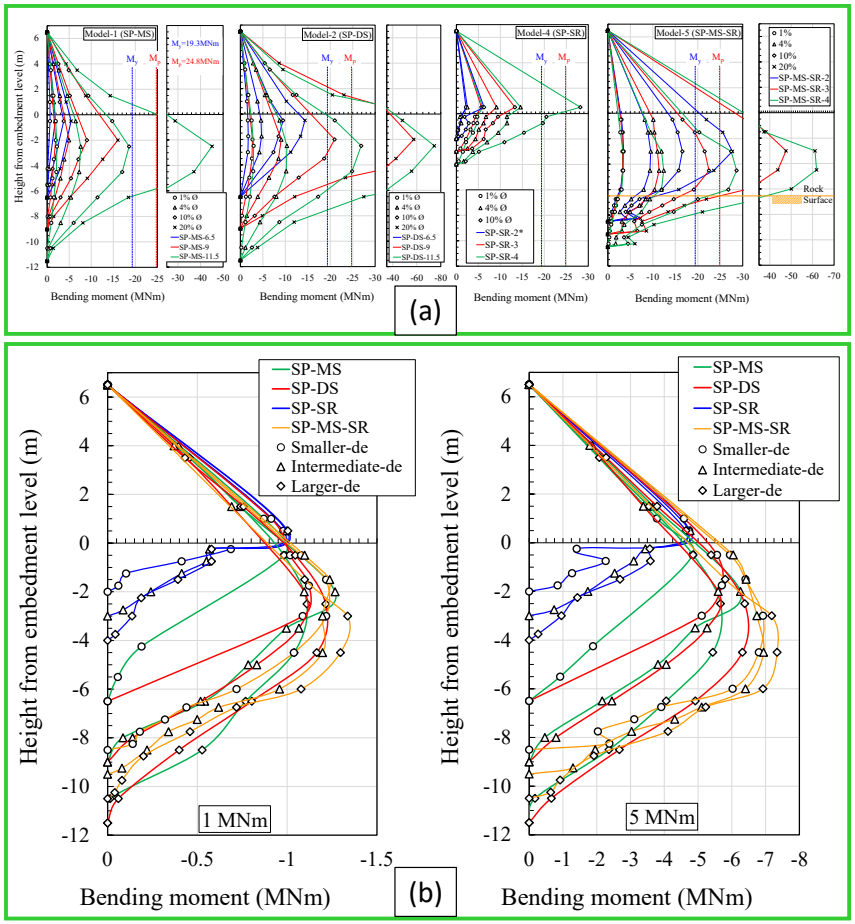

Figure 4.29 Bending moment profiles of piles (a) at different displacements in same embedded medium and different embedment depths (b) at applied moment loads of 1MNm and 5MNm

Some strain gauges of the short piles in the two sand models did not work. Excluding the short piles, similar bending moment profiles were measured in the medium and long piles in the two sands (SP-MS & SP-DS). The difference between the middle and long piles are more evident, i.e., the longer the piles are, the lager the moment in the deep portion becomes. This implies that as the load increases, the resistance mobilization at the deep depth becomes larger relative to the shallower depth. While in the soft rock model, 3m and 4m embedded piles showed almost the same bending moment from the loading point up to -2m till the moment load of 5MNm and very small bending below this depth. Thanks to the large stiffness and strength of the intact rock, a large horizontal resistance concentrated at the very shallow depth against relatively small load. Referring to the moment profiles of socketed piles at relatively small load levels (1MNm) the behavior is similar to the observation in sand even in the socketed portion, which implies that the behavior of socketed piles mainly governed by the upper layer at relatively small moment loads. Which can be confirmed from Figure 4.28 at small pile top displacements(0.5%,1% Ø) as well, all three socketing depths showing almost similar bending moment profiles at same pile top displacement. Unlike the behavior in sand, as the loading increases from 1 to 5MNm, the deviation between measured bending moments at same elevation decreases for the piles with different socketing depths. This clearly indicate the influence of socketed medium; owing to higher strength and large stiffness of soft rock, the applied moment energy is simply transferred in terms of bending strains in the pile especially above the rock surface with the mobilization of large horizontal resistance in the rock.

4.4.6 System stiffness and residual displacements

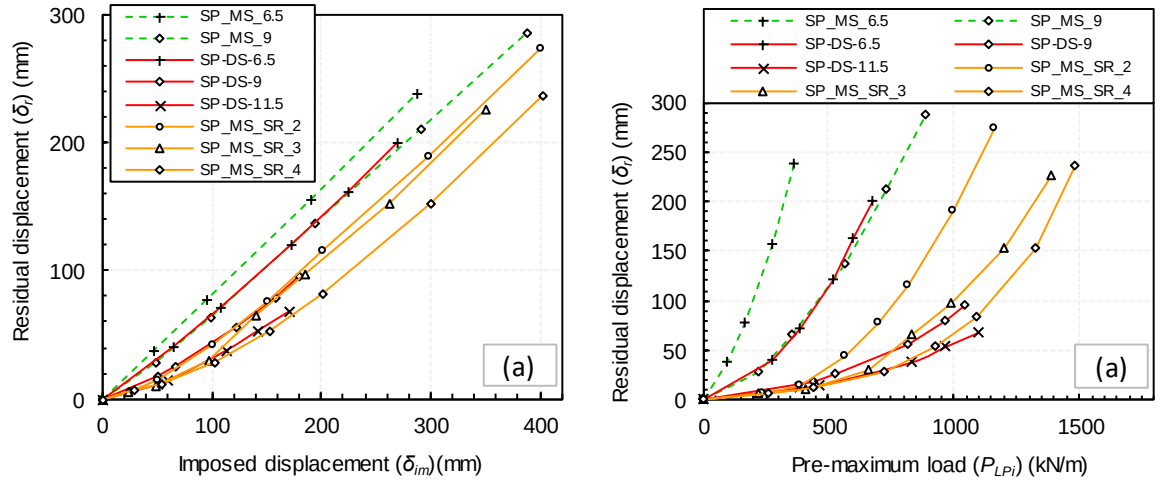

Figure 4.30 Variation of residual displacement against (a) Imposed displacement and (b) pre-maximum load for rock socketed piles and embedded piles in sand

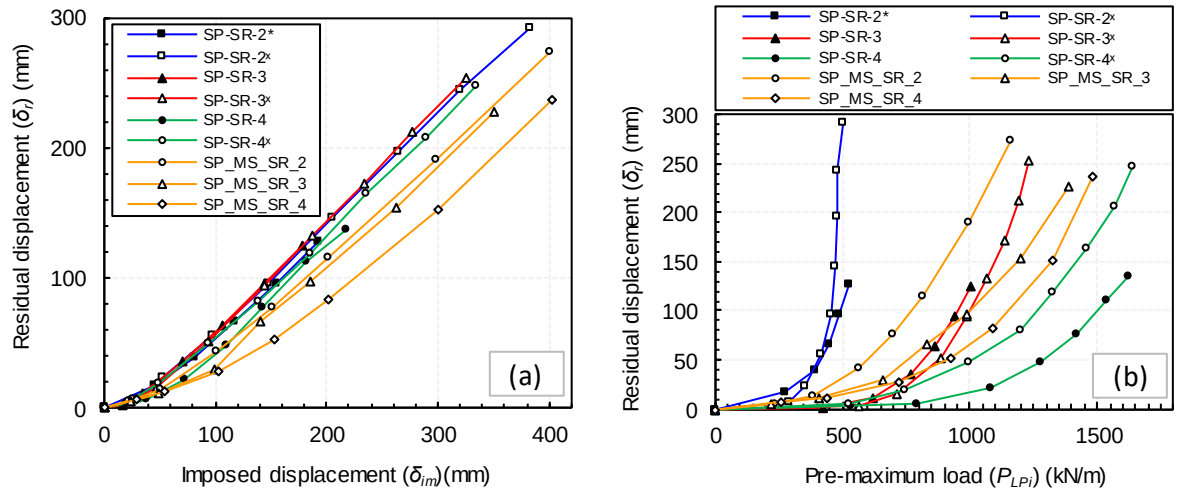

Figure 4.31 Variation of residual displacement against (a) Imposed displacement and (b) pre-maximum load for embedded piles in rock and dense sand

Although the objective of this research work highly focused on the application of retaining walls, the investigated variation of system stiffness and residual displacement of single piles in this chapter could provide some useful information to the geotechnical applications related to large diameter piles, such as mono pile foundation for wind turbines.

Large diameter piles are being used as mono-pile foundation for wind turbines, where one way cyclic loads by wind forces are the typical loading condition. Due to one-way cyclic loads, the accumulation of residual displacement and permanent movement of foundation and super structure could be a major concern for a long term stability of such large geotechnical structures. In order to discuss the ground stiffness and the influence of embedment depth on the permanent deformation of mono-pile foundations, the relationship between residual displacement at the pile top and the imposed displacement, normalized applied pre-maximum load (P_{Lpi}, see Figure 4.12) in previous cycle by the ultimate load (P_{ult}) is presented in Figure 4.30 and Figure 4.31, where P_{Lpi}/P_{ult} is a kind of load factor.

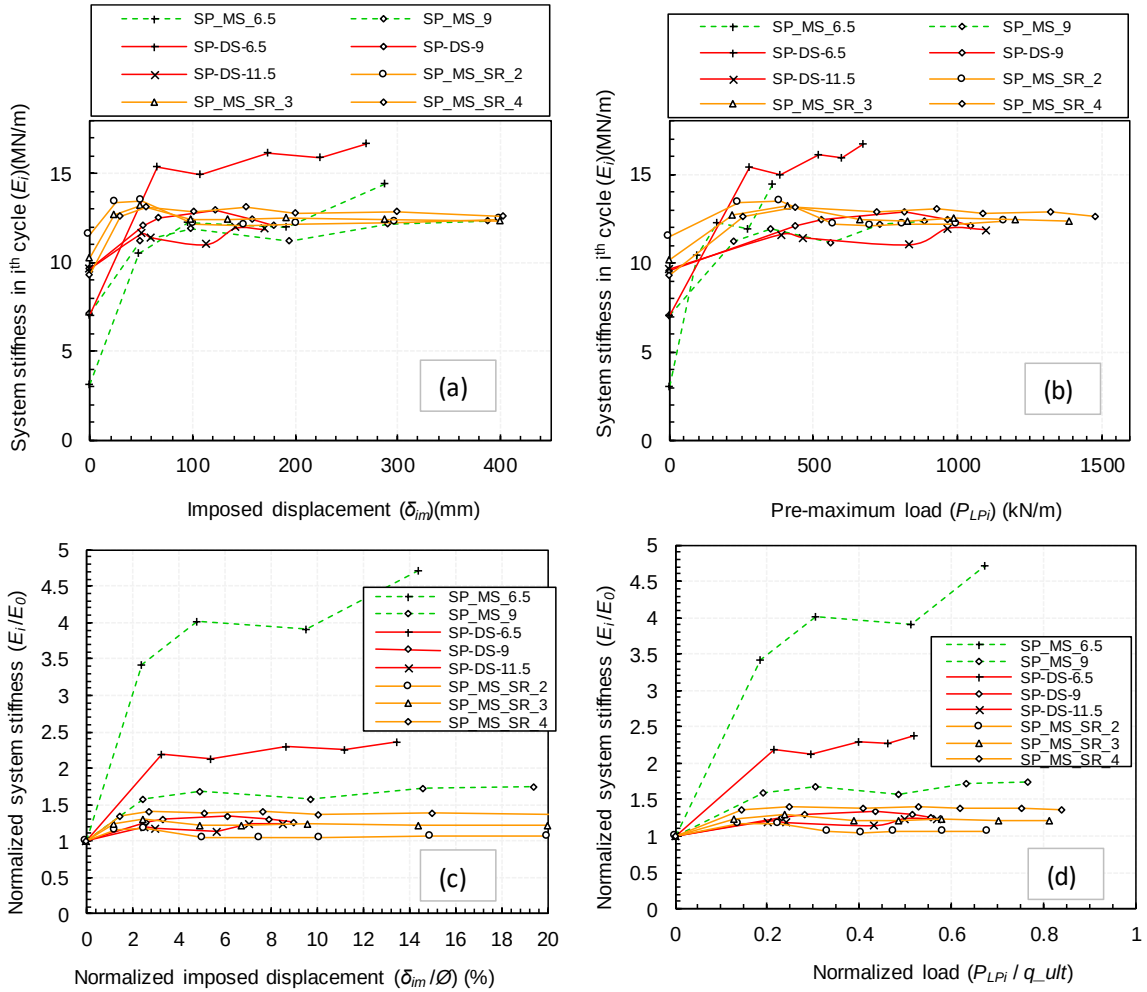

Figure 4.32 Variation of system stiffness against (a) imposed displacement and (b) pre-maximum load, (c,d) corresponding normalized variations for rock socketed piles and embedded piles in sand

From Figure 4.30 and Figure 4.31 as an overall trend, the residual displacements for the same load factor are reduced by increasing the ground stiffness from medium dense sand, dense sand to soft rock. From this trend, it can be said that the displacement should be the dominant factor compared to the ultimate failure for the soft ground, while for the stiff embedment medium, securing the factor of safety against failure tends to be a critical condition in the foundation design.However, the socketed piles lie between soft and stiff ground conditions it indicates the influence of both layers of embedded medium and the requirement of complex design procedures to control the deformation and failure of mono-piles.

Observed system stiffness (E_i) of each cycle is plotted against the applied pre-maximum load (P_{Lpi}) and the imposed displacement in the previous cycle as described in Figure 4.32 and Figure 4.33. It should be noted that in pile SP-SR-2* the observed stiffness was affected by the unintentional preloading, and in pile SP-MS-11.5 the stiffness under small load could not be measured, but only measured after the large loading history therefore the variation of system stiffness of pile SP-MS-11.5 is not included in Figure 4.32 . Nonetheless, effects of embedment medium and depth can be clearly confirmed from Figure 4.32 and Figure 4.33. The initial stiffness very much depends on the ground stiffness, much higher for the soft rock compared to sands, even though the embedment depth of the rock was about one third of that of the sand. However, the significant deterioration of the stiffness took place for the soft rock, compare to the sand.

To scrutinize the change of the system stiffness by the cyclic loading history, the normalized stiffness by initial one (E_i /E_0) is plotted against the normalized imposed displacement (δ_{im} /Ø) and normalized peak load (P_{Lpi} /P_{ult}) Figure 4.32(c,d) and Figure 4.33(c,d). From Figure 4.32(c,d), the larger increase of the stiffness, in other words the effect of hardening can be seen for the piles in medium dense sand than the dense sand, and also for the short pile than the long piles. For the socketed piles SP-MS-SR-2, SP-MS-SR-3 and SP-MS-SR-4 in Figure 4.32(c,d) a combined hardening and subsequent deterioration of stiffness can be seen. Initial hardening could be attributed to the intact condition of socketed portion which allows the strain hardening of the upper layer.

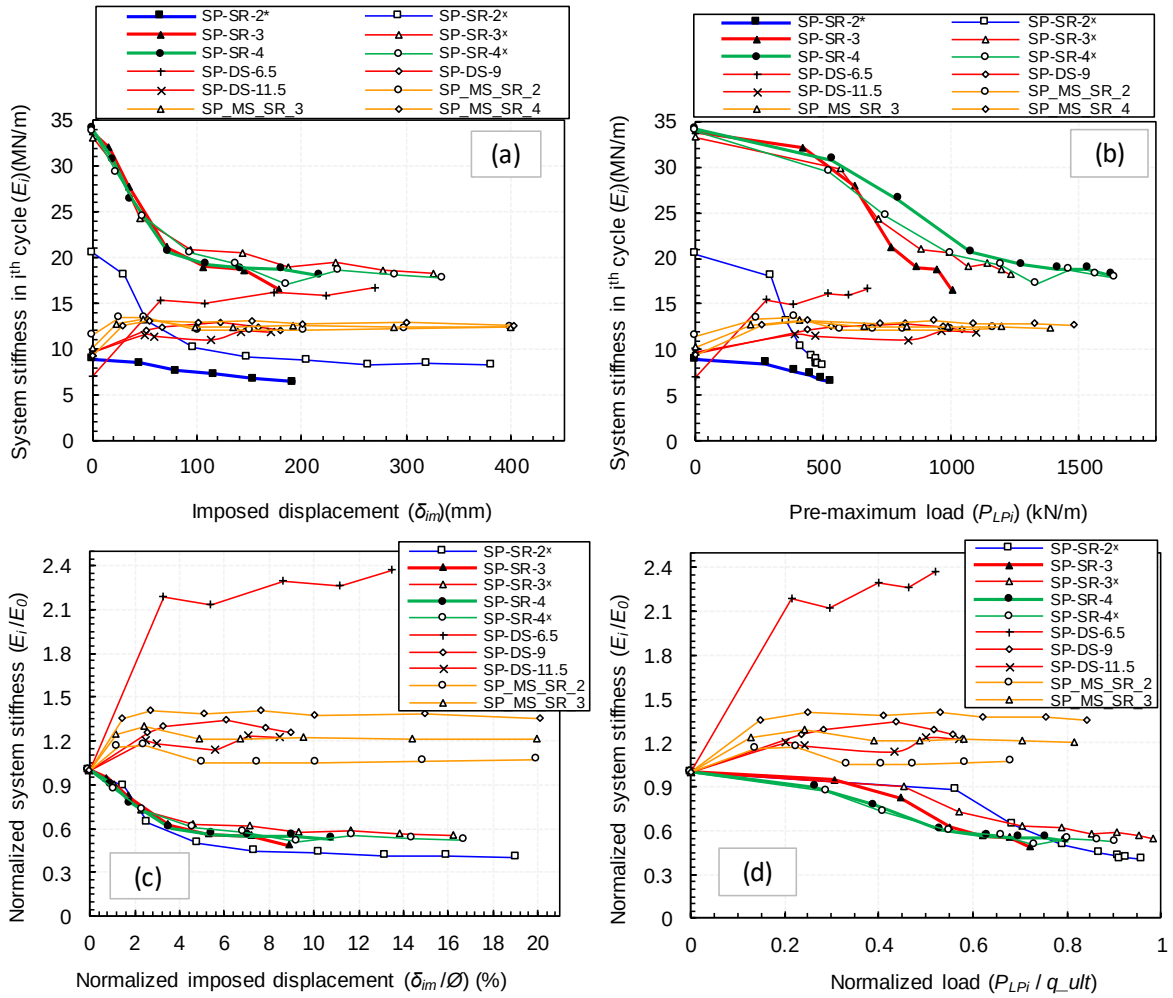

Figure 4.33 Variation of system stiffness against (a) imposed displacement and (b) pre-maximum load, (c,d) corresponding normalized variations for embedded piles in rock and dense sand

However, the deterioration of the shallow layers of rock, resulting the reduction in the system stiffness similar to the behavior of piles embedded in single rock layer (e.g. SP-SR-2*,SP-SR-3 & SP-SR-4) as illustrated in Figure 4.33(c,d) from the initiation of loading.

From the variation of system stiffness of the piles embedded in soft rock (Figure 4.33(c,d)), the initial stiffness of SP-SR-3, SP-SR-3^x (d_e=3m) and SP-SR-4^x, SP-SR-4 (d_e=4m) are almost the same, but the stiffness deterioration is more significant for piles SP-SR-3^x and SP-SR-4^x beyond about 20% stiffness reduction from the intact condition as shown in Figure 4.33(c), and corresponding loading level is about 40% of the ultimate resistance, which can be observed from normalized relation given in Figure 4.33(d), referring to the E_i/E_o= 0.8. Observed different behavior between the piles with same embedment depth could be attributed to the influence of

imposed displacements in each cycles for the same embedment conditions. Higher the imposed displacements in each cycle larger the deterioration of the rock stiffness, thereby the failure mode also could be alternated from structural buckling to rock failure as described in Figure 4.25. However, beyond an imposed displacement of 5% Ø no significant change in the system stiffness could be observed especially for the piles embedded in soft rock from Figure 4.33(c). Based on this observation and the observed structural failure of the pile SP-SR-4 it can be said that, after a pile top displacement of 5%Ø the lateral resistance is mainly controlled by the structure rather than the embedded medium.

4.4.7 Influence of confining pressure and loading heights on the pile behavior in rock

Figure 4.34 shows the backbone curves obtained from the piles in Model-3 (pile loading in 1g) and Model-4 (pile loading in 50g) in model scale. From Figure 4.34 the effects of loading conditions can be clearly confirmed. The deeper the embedment is, the larger resistance of piled is mobilized. Over all the lateral resistance of pile embedded in soft sand rock increases with increasing embedment depth and decreasing loading height.

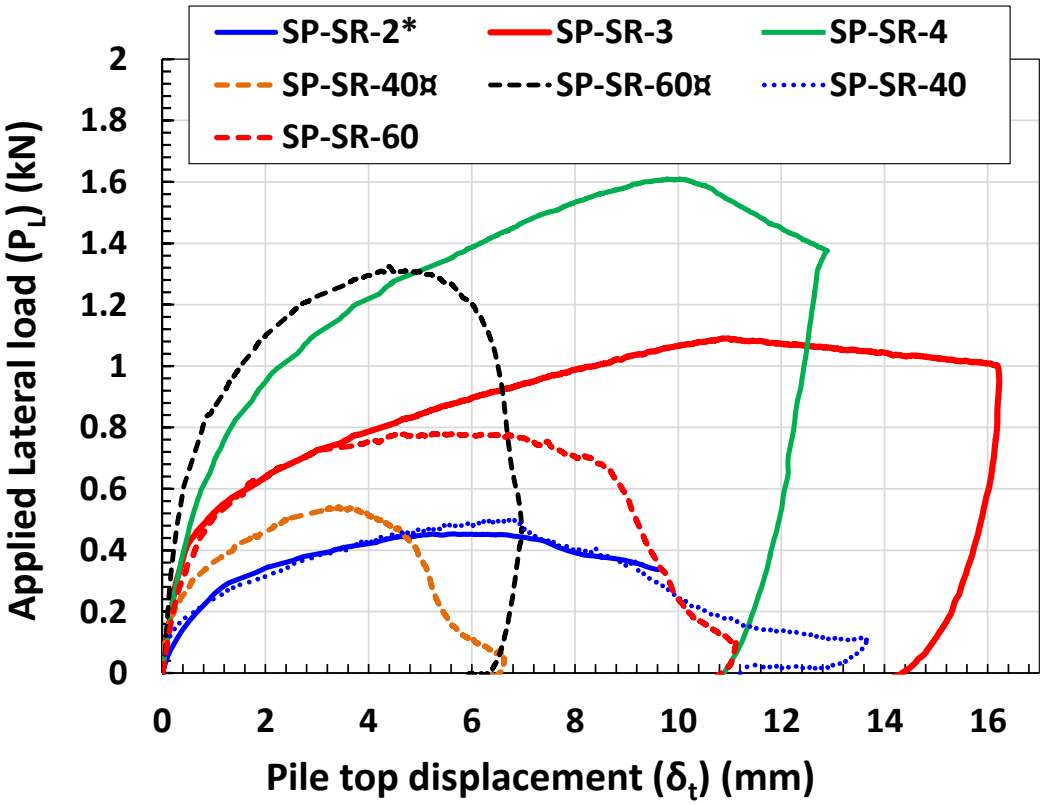

Figure 4.34 Back bone curves of piles embedded in rock comparison between 1g (Model-3) and 50g (Mmodel-4) models (Results are in model scale)

About the effects of confining pressure or the g-level, the 40mm embedment piles in 1g and 50g (SP-SR-40, SP-SR-2*) exhibit almost identical behavior along the entire load-displacement curve. This behavior clearly indicates that, confining stresses and materials self-weight have no significant influence at shallow depths for even relatively hard mediums. For the piles with 60mm embedment depth in 1g and 50g (SP-SR-60 & SP-SR-3) similar behavior can be seen up to pile top displacements of 4mm (10% Ø). However after this displacement, the SP-SR-60 curve deviates from that of SP-SR-3 and exhibits sharp drop of resistance at δ_t =20% Ø in the post peak behavior. From these difference, effects of confining can be confirmed

in the large displacement range. This effect can be expected from stress strain behaviors between unconfined and triaxial compression tests, showing similar peak strengths but different post peak softening. The difference in post peak behavior of model piles in 1g and 50g can be seen from the ground deformation as shown in Figure 4.35(b,c). Clear block type failure wedge was observed at the pile front ground surface for SP-SR-60, while for SP-SR-3 compression of the soft rock occurred at the pile front. Although there are clear difference in the post peak behavior, it could be considered that the behavior of 1g and 50g can be comparable before the peak for the soft rock model with about 10 % variation in the mobilized resistance. From the results between the piles with the different loading heights, namely SP-SR-40, SP-SR-40ᵍ and SP-SR-60, SP-SR-60ᵍ in Figure 4.34, it can be confirmed that the lateral resistance of piles significantly decreases with the increase of loading height. This implies that the moment load could be critical for the piles with relatively small embedment depth. Which can be confirmed from the observed rock failures of the pile with 60mm embedment depth and two different loading heights (130 mm , 80mm loading heights) as shown in Figure 4.35(c,e).The pile SP-SR-60 exhibits a clear wedge type in the front and significant rock deformation in the toe back. However in SP-SR-60ᵍ clear toe back failure could not be observed.

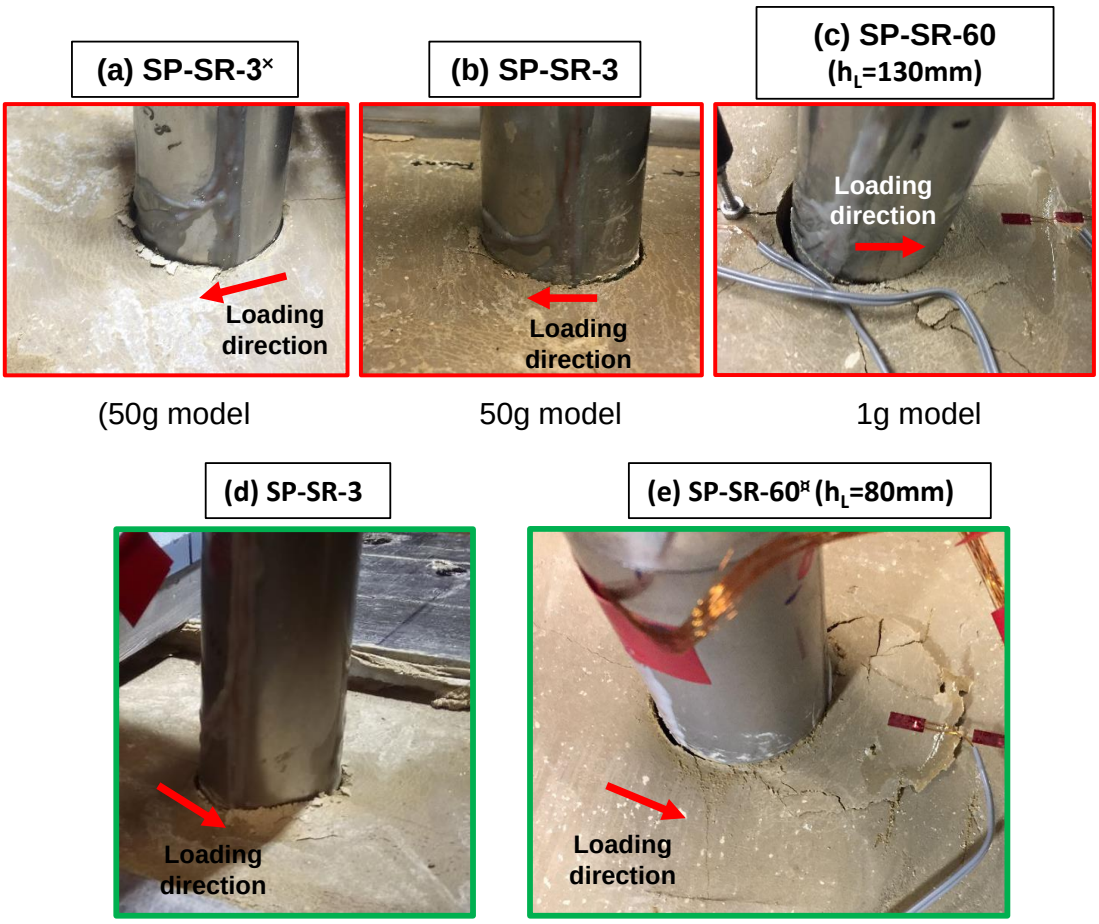

Observed ground failures of the piles with 60 mm embedment depth and different loading heights in 50g, 1g models

Figure 4.35 Observed ground failure of piles in 1g model and 50g centrifuge model

4.4.8 Effect of load cycles and imposed displacement on the ultimate bearing capacity

Measured bending moments of SP-SR-3, SP-SR-3× and SP-SR-4, SP-SR-4× at different loads and Imposed displacements are illustrated in Figure 4.36. From Figure 4.36, a clear matching

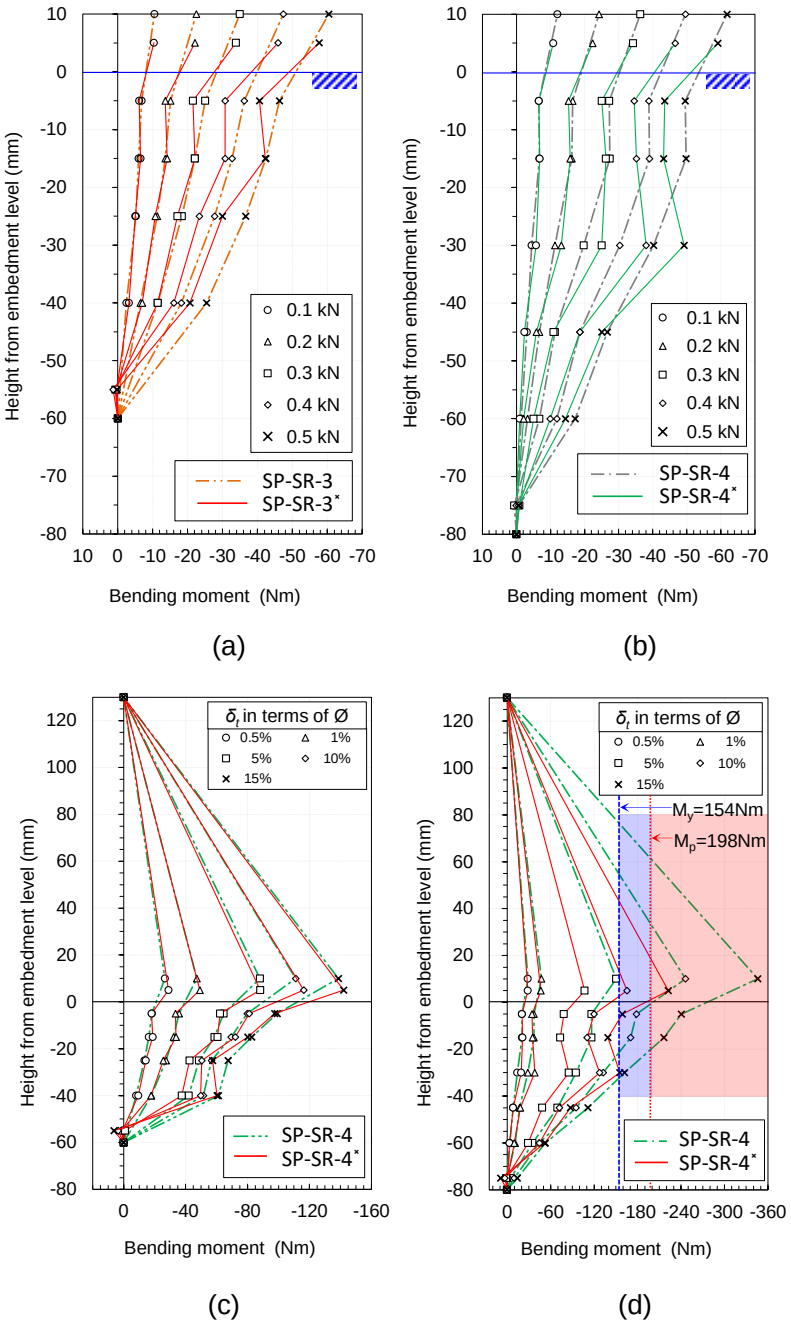

Figure 4.36 Bending moment profiles of piles with same embedment and loading conditions but different mode of ultimate failure

of the bending moment profiles in the embedded zone can be seen at different loads within the elastic bounds. Also from overall back bone curves (Figure 4.37(a)), clear difference between the piles (SP-SR-3, SP-SR-3× and SP-SR-4, SP-SR-4×) in two identical 50g models could not be confirmed at the early stage of the loading. Both evidences clearly indicate a good repeatability in the mechanical properties of embedded medium and steel tubular piles in Model-4 and Model-8, which are identical models with different imposed displacement cycles. The differences in the imposed displacement in each cycle for both models could be observable from Figure 4.16.

Although good repeatability exists in the initial stages of the loading, for the Model-8, in the latter stages of the loading smaller ultimate resistances (Figure 4.37 (a)) can be observed. This could be attributed to relatively large imposed displacement cycles of Model-8 from 4th load cycle to the final cycle as described in Figure 4.16. Furthermore, structural yielding and plastic failure of the piles SP-SR-4 and SP-SR-4× clearly visible from bending profiles in Figure 4.36(d). Figure 4.25. However from Figure 4.25 , clear buckling of pile SP-SR-4× could not be observed, indicating the post peak behavior of SP-SR-4× as a combined ground failure with pile yielding. This dictates supplementary deterioration of ground stiffness by additional imposed displacements in each cycle of pile SP-SR-4× and the reduction of confinement in subsequent monotonic loading (Figure 4.23(a,c)) compare to SP-SR-4.

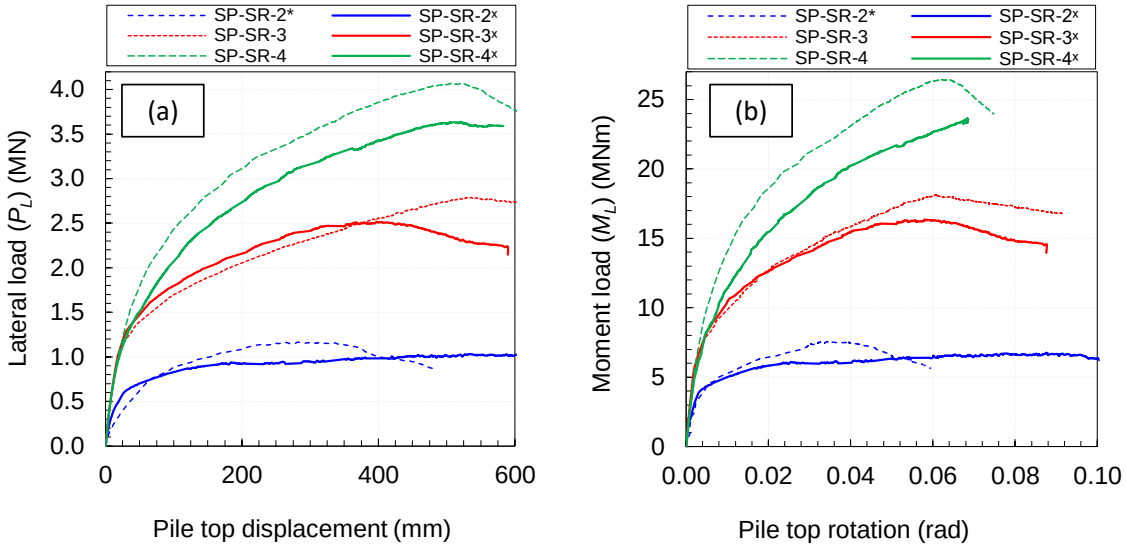

Figure 4.37 Back bone curves of piles with identical embedment depth and loading height with different imposed displacement cycles

4.5 Summary

Based on Figure 4.26 (a), at small displacement (1%Φ） level no significant influence of embedment depth in rock type grounds can be observed, which indicates large lateral confinement and contribution of shallow layers of rock on the lateral resistance.

In the stiff ground like the soft rock, the lateral resistance changes significantly in a small range of embedment depth. A small increment of embedment depth in soft sand rock highly controlled the displacement and failure behavior of the piles compared to the increment in the sand soil.

Over certain embedment depth, the increment of pile length becomes less significant on the increase of resistance. This depth can be considered as an optimum depth. On the other hand, due to the softening of ground materials and the change of failure mode from the ground failure to pile structural failure, the optimum embedment depth changes depending on the conditions of resistance, shallower for the initial stiffness than the ultimate bearing capacity in the soft rock.

For the cases with the ground failure as the ultimate condition, the failure behaviors of sand and rock become quite different, ductile and brittle respectively.

Based on the discussions of Figure 4.26, it can be concluded that, up to δ_t=1%Ø (20mm) the 3m embedment depth ((d_e/Ø) =1.5) could be considered as an optimum embedment for the piles embedded in soft rock with specific loading height considered in this study. This

embedment depth is a kind of optimum embedment depth for relatively larger initial stiffness of soft rock more or less in the intact condition. Furthermore, from the observed buckling of the pile with 4m embedment ((d_e/Ø) =2) in soft rock (Model-4), it can be considered that the optimum embedment depth covering the initial stiffness and the ultimate bearing capacity could be closer to 4m (2Ø) for this specific loading condition.

However, the ultimate lateral resistance associated with the pile-rock interaction could be alternated by the loading history. Higher the imposed displacements in each cycle larger the deterioration of the rock stiffness, thereby the failure mode could be alternated from structural buckling to rock failure.

Comparing the discussions based on Figure 4.27 (a) and Figure 4.27 (d), it can be concluded that the deterioration of underlain shallow layer rock stiffness took place at a pile top displacement of δ_t =2%Ø (40mm) for the specific loading condition in this study. Based on this study, limiting passive pressures in a 3.25Ø thick overlain layer could be expected to reach at δ_t =2%Ø. Based on this, for the design conditions with an allowable pile top displacements δ_{all} >2%Ø, small strain stiffness of the underlain rock could not be expected.

From Figure 4.33(c), beyond an imposed displacement of 5%Ø no significant change in the system stiffness could be observed especially for the piles embedded in soft rock. Based on this observation and the observed structural failure of the pile SP-SR-4 (in Figure 4.25) as an ultimate failure condition, it can be said that, after a pile top displacement of 5%Ø the lateral resistance is mainly controlled by the structure rather than the embedded medium for the piles with a specific loading condition in this study.

4.6 References

Arany, L., Bhattacharya, S., Macdonald, J. and Hogan, S.J., 2017. Design of monopiles for offshore wind turbines in 10 steps. Soil Dynamics and Earthquake Engineering, 92, pp.126-152.

Bhattacharya, S., Lombardi, D. and Wood, D.M., 2011. Similitude relationships for physical modelling of monopile-supported offshore wind turbines. International Journal of Physical Modelling in Geotechnics, 11, pp.58-68.

Carter, J.P. and Kulhawy, F.H., 1988. Analysis and design of drilled shaft foundations socketed into rock (No. EPRI-EL-5918). Electric Power Research Inst., Palo Alto, CA (USA); Cornell Univ., Ithaca, NY (USA). Geotechnial Engineering Group.

Carter, J.P. and Kulhawy, F.H., 1992. Analysis of laterally loaded shafts in rock. Journal of Geotechnical Engineering, 118(6), pp.839-855.

Chen, J.J., Wang, J.H., Ke, X. and Jeng, D.S., 2011. Behavior of large-diameter rock-socketed piles under lateral loads. International Journal of Offshore and Polar Engineering, 21(04).

Chen, J.J., Zeng, F.Y., Wang, J.H. and Zhang, L., 2017. Analysis of laterally loaded rock-socketed shafts considering the nonlinear behavior of both the soil/rock mass and the shaft. Journal of Geotechnical and Geoenvironmental Engineering, 143(3), p.06016025.

Digioia, A.M. and Rojas-Gonzalez, L.F., 1994. Rock socket transmission line foundation performance. IEEE transactions on power delivery, 9(3), pp.1570-1576.

Erbrich, C.T., 2004, January. A new method for the design of laterally loaded anchor piles in soft rock. In Offshore Technology Conference. Offshore Technology Conference.

Fragio, A.G., Santiago, J.L. and Sutton, V.J.R., 1985, January. Load tests on grouted piles in rock. In Offshore Technology Conference. Offshore Technology Conference.

Gabr, M.A., Borden, R.H., Cho, K.H., Clark, S.C., and Nixon, J.B. (2002). "P-y curves for laterally loaded drilled shafts embedded in weathered rock." FHWA/NC/2002-08, North Carolina Department of Transportation.

Guo, F. and Lehane, B.M., 2016. Lateral response of piles in weak calcareous sandstone. Canadian Geotechnical Journal, 53(9), pp.1424-1434.

Guo, F., 2015. Lateral response of single piles in cemented sand and weak rock (Doctoral dissertation, University of Western Australia).

Ishihama, Y., Fujiwara, K.,Takemura, J. and Kunasegaram,V., 2018. Evaluation of deformation of self-standing retaining wall using large diameter steel pipe piles into hard ground , Proceedings of the 1st International Conference on Press-in Engineering 2018, Kochi, Japan,pp.153-158.

Kahle, K.J. and Brown, D.A., 2002. Performance of Laterally Loaded Drilled Sockets Founded in Weathered Quartzite. Project No.B-425, Highway Research Center, Auburn University, Alabama 36849-5337.

Kallehave, D., Byrne, B.W., LeBlanc Thilsted, C. and Mikkelsen, K.K., 2015. Optimization of monopiles for offshore wind turbines. Philosophical Transactions of the Royal Society A: Mathematical, Physical and Engineering Sciences, 373(2035), p.20140100.

Kunasegaram,V., Akazawa,S., Takemura,J., Seki,.S, Fujiwara,K, Ishihama,Y. and Fujii,Y.,2015. Modeling of soft rock for a centrifuge study, Proceedings of 12th GeoKanto,Tokyo,Japan, pp. 15-19.

Miyanohara,T., Kurosawa,T., Harata,N., Kitamura,K., Suzuki,N. and Kajino,K., 2018. Overview of the Self-standing and High Stiffness Tubular Pile Walls in Japan, Proceedings of the 1st International Conference on Press-in Engineering 2018, Kochi, Japan,pp.167-174.

Randolph, M.F., 1981. The response of flexible piles to lateral loading. Geotechnique, 31(2), pp.247-259.

Reese, L.C., 1997. Analysis of laterally loaded piles in weak rock. Journal of Geotechnical and Geoenvironmental Engineering, 123(11), pp.1010-1017.

Takemura, J., Kondoh, M., Esaki, T., Kouda, M. and Kusakabe, O., 1999. Centrifuge model tests on double propped wall excavation in soft clay. Soils and Foundations, 39(3), pp.75-87.

Vijayakanthan, K., Takemura, J. "Deflection and failure of cantilever large stiffness walls embedded in soft rock", International Journal of Physical Modelling in Geotechnics (Submitted: IJPMG-D-19-00008).

Xing, H., Zhang, Z., Meng, M., Luo, Y. and Ye, G., 2014. Centrifuge tests of superlarge-diameter rock-socketed piles and their bearing characteristics. Journal of Bridge Engineering, 19(6), p.04014010.

Zhang, L., Ernst, H., and Einstein, H. H. (2000). "Nonlinear analysis of laterally loaded rock-socketed shafts", Journal of Geotechnical and Geoenvironmental Engineering.v. 126 issue 11, p. 955-968.

5 Deformation and Failure of Cantilever Large Diameter Steel Tubular Pile Walls Embedded in Soft Rock

5.1 Introduction

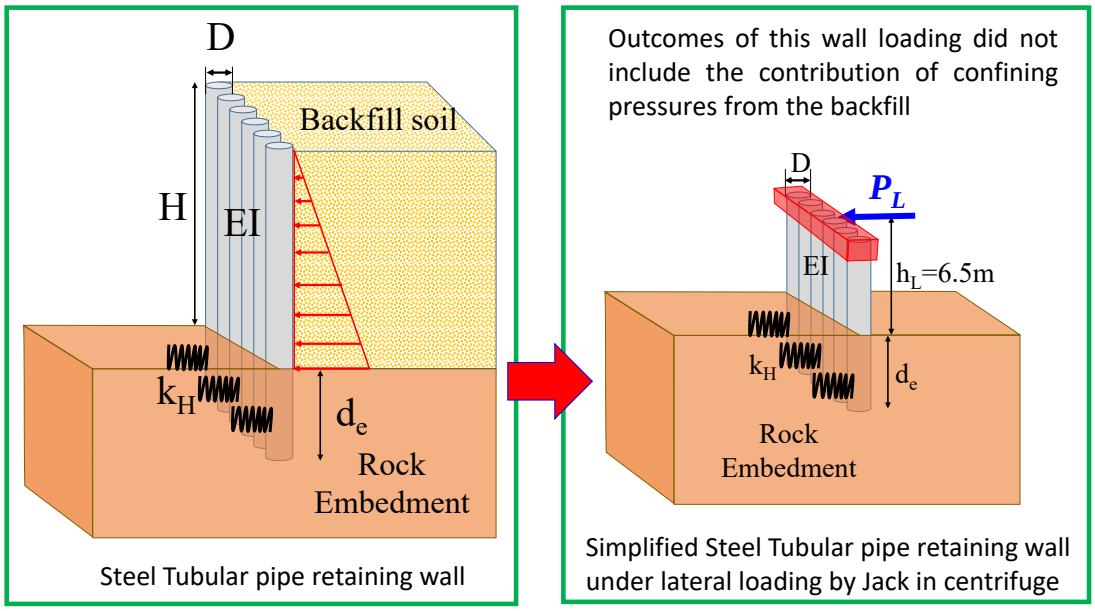

Figure 5.1 (a) Target structure and (b) simplified loading on steel tubular pile wall

This chapter discuss the behavior of steel tubular pile walls under two different embedment conditions. In the first experiment investigations were conducted on the walls embedded in soft rock and the second one is for the walls socketed in to soft rock with an overlain layer of sand. Although simulation of excavation and additional lateral loading as discussed in the chapter-3 could predict the real behavior of tubular pile retaining walls, attributing to the difficulties in the estimation of more realistic loading parameters with the wall deformation and required time and cost associated to that kind of more sophisticated investigations, the wall behavior was studied under a simplified lateral loading in centrifuge. In which the major benefit is that the loading mechanism is very simple and the applied lateral and moment loads can be exactly estimated unlike more complicated estimation of loading indexes in chapter-3. However the major drawback is the contribution of confining pressures from the backfill of the retaining wall is not present in this modelling concept as described in Figure 1.1. Which implies that the outcomes of this tubular pile wall loading must be verified to ensure the influence of confining pressures.

5.2 Design of tubular pile walls for centrifuge model

Steel pipes (SUS304) having the outer diameter Φ=40mm, and thickness t=0.5mm were used for the wall model. Steel tubular pipe wall models were made of three steel pipes, which were fixed at the top by aluminium block as shown in **Figure 5.2**(d). At the top of each pile a rigid aluminium cap was socketed to represent the socketing solid portion of 40mm (in model) below the loading point, which is identical to that of pile loading in chapter-4. In the model wall 3mm gap between piles was maintained to simulate the prototype conditions in the real file applications, where 0.18m gap between the piles is an inevitable gap attributing to the limitations in the pile installation machines. Attributing to the limitations in the model container this gap in the centrifuge model represents 0.15m in prototype corresponding to the

50g model. Model piles were fixed with the top loading frame shown in **Figure 5.2**(a) by means of six bolts as shown in **Figure 5.2**(d).Where two bolts are passing through the solid cap of middle pile. Upon arranging the wall model the gap between the wall edges and the container walls was confirmed prior to the strain gauge installation as indicated in **Figure 5.2**(c). Model walls with 6cm (3m in prototype) and 8cm (4m in prototype) embedment depths are shown in **Figure 5.2**(b) prior to the strain gauge installation. Up on bolting all three piles with the top loading frame, additional fixity between the piles and loading frame was provided by means of adding Scotch glue. After that the strain gauges were installed to measure the bending strains in the embedded zone and axial strains at the bottom tip of the walls. A typical completed wall model for 6cm embedment (3m in prototype) in soft rock is shown in **Figure 5.2**(d).

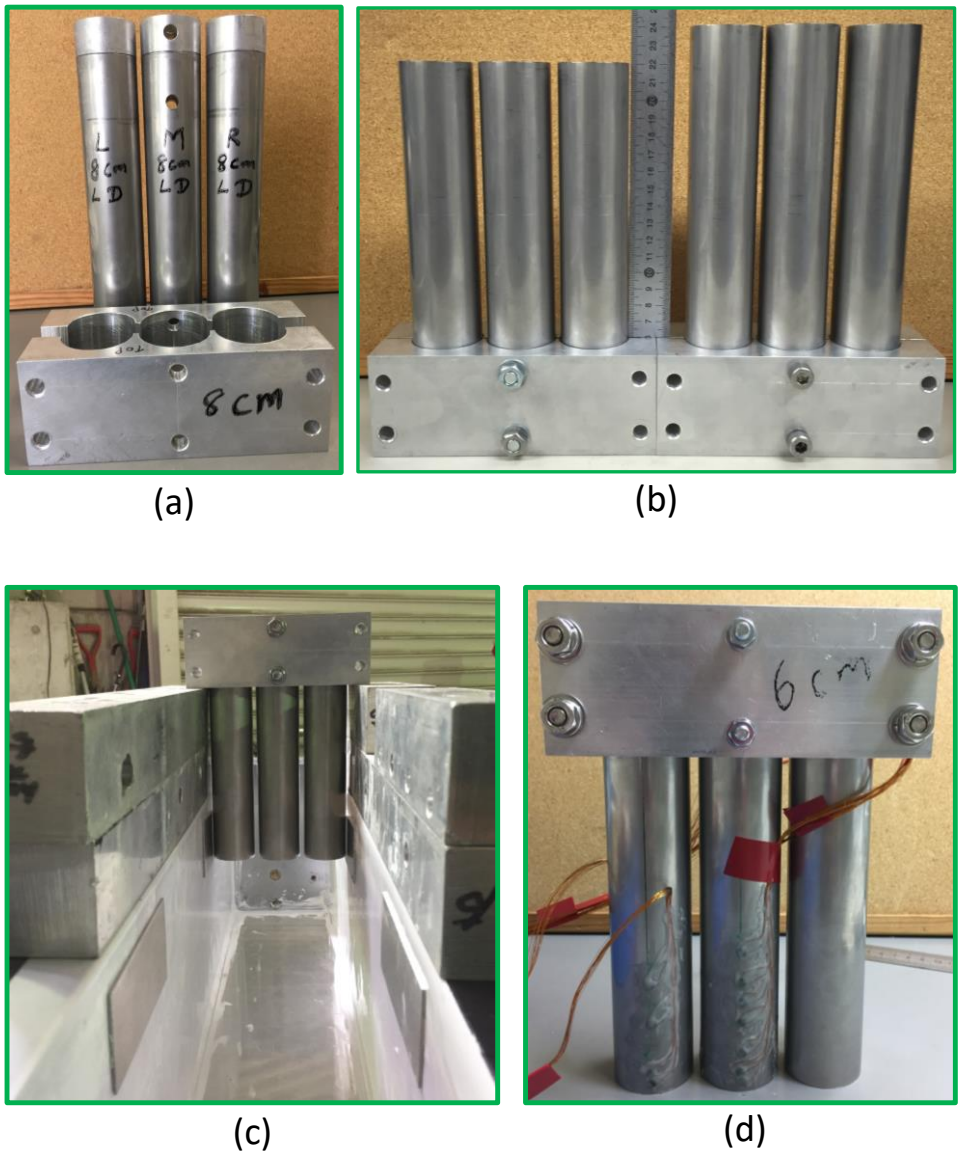

Figure 5.2 Tubular pile wall making process

5.2.1 Test conditions and tubular pile wall models

Totally four tubular pile walls were tested in two centrifuge models. In which two walls were embedded in single soft rock layer with 3m and 4m embedment depths as described in **Table 5-1** under the Model-6. Another two tubular pile walls were embedded in two layer profile

where the soft rock is overlain by 6.5m depth of Toyoura sand with 80% relative density. The embedment and loading conditions of the walls are describe in **Table 5-1**.

Table 5-1 Model conditions of tubular pile walls

Model condition	Properties of embedded medium	Pile notation	Embedment depth (d_e) (m)	Loading height (h_w) (m)	Pile properties EI (GNm^2/m) M_y, M_p (MNm)
Model-6 Soft sand rock (SR) 50G model	γ_{dR}=16.8 kN/m^3 q_u=1.4 Mpa E_s=660 MPa	RPW-SR-3 RPW-SR-4	3 (60 mm) 4 (80 mm)	6.5 m (130 mm)	Ø=2 m (40 mm) t = 25 mm (0.5 mm)
Model-7 Soft Sand rock (SR) Overlain by Toyoura sand Dr=80%(MS) 50G model	γ_{ds}=15.5 kN/m^3 ϕ'=40° γ_{dR}=16.8 kN/m^3 q_u=1.4 MPa E_s= 660 MPa	RPW-MS-SR-3 RPW-MS-SR-4	6.5 in MS, 3 in SR 6.5 in MS, 4 in SR	6.5 m (130 mm)	EI=7.3 ($1.17x10^{-6}$) M_y=19.3 ($0.154x10^{-3}$) M_p=24.8 ($0.198x10^{-3}$)

All dimensions are given in prototype scale model scales are given in parenthesis

M_y: Yielding bending moment of the pile M_p: bending moment causing plastic failure of the pile

5.2.2 Centrifuge model arrangement and modelling procedure

A model container with inner dimensions of 700 mm width, 150 mm breadth, and 500 mm depth was used in the modelling process of both Model-6 and Model-7. Thick acrylic plate stack was tightly placed in the container to reduce the depth to 340mm and 200mm for the two layer and single layer models respectively. After that the breadth of the container was reduced by means of adding a 20mm acrylic plate with the inner rear face of the container, which helps to reduce the breadth to 130mm and simulate the plane strain conditions of the steel tubular pile walls. Prior to the casting of unsolidified rock mix, 0.5mm thick Teflon sheet was added inner faces of the container. The soft sand rock was made by compacting sand-clay-cement mixture layer by layer with 30mm thickness. Immediately after casting the mixture, the model walls were installed vertically into the unsolidified mixture with a pile guide with the target embedment depth, and the mixture was cured for 14 days. With this wall installation process, soft rock was filled in the pile at the ground surface. For the two-layer model, dry Toyoura sand layer with Dr=80% was made by air pluviation. Detail description of the centrifuge model, model wall and strain gauge arrangements are described in **Figure 5.3** and **Figure 5.4** as follows.

5.2.2.1 Model – 6 (wall in rock)

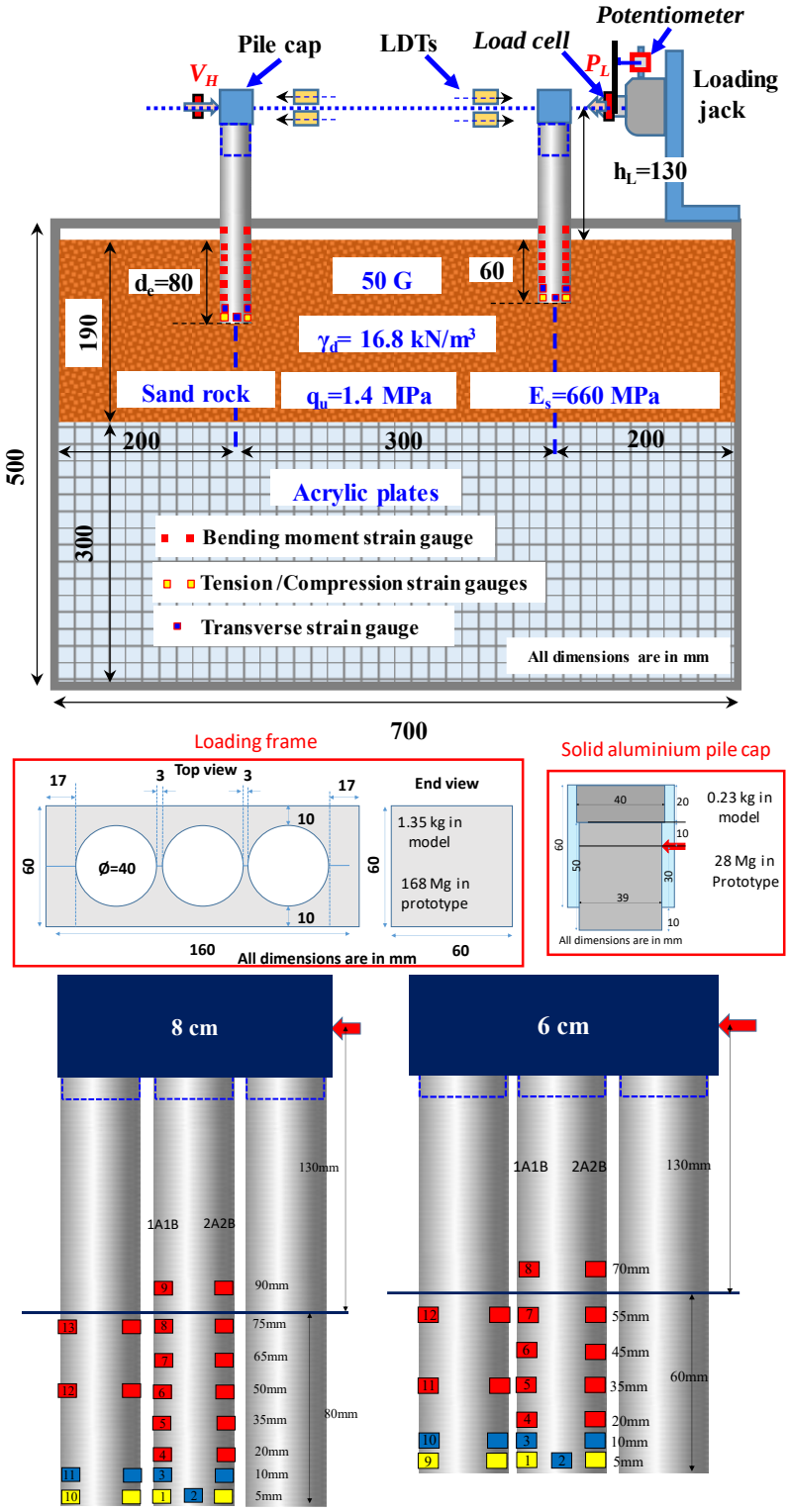

Figure 5.3 Centrifuge model arrangement and the description of strain gauge arrangement for the tubular pile walls embedded in soft rock (Model-6)

5.2.2.2 Model – 7 (Socketed wall)

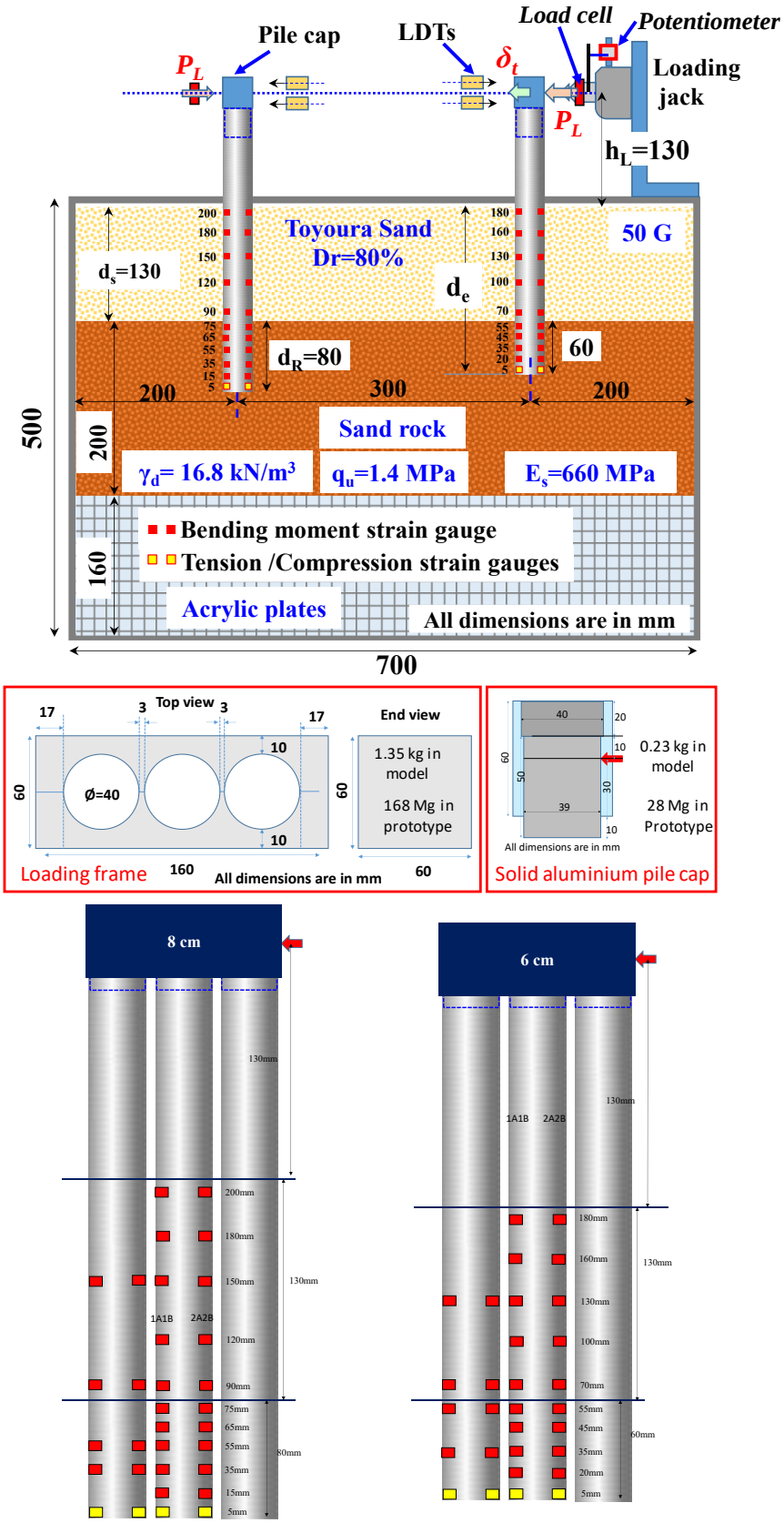

Figure 5.4 Centrifuge model arrangement and the description of strain gauge arrangement for the tubular pile walls embedded in soft rock (Model-7)

5.2.3 Loading sequence and mechanism

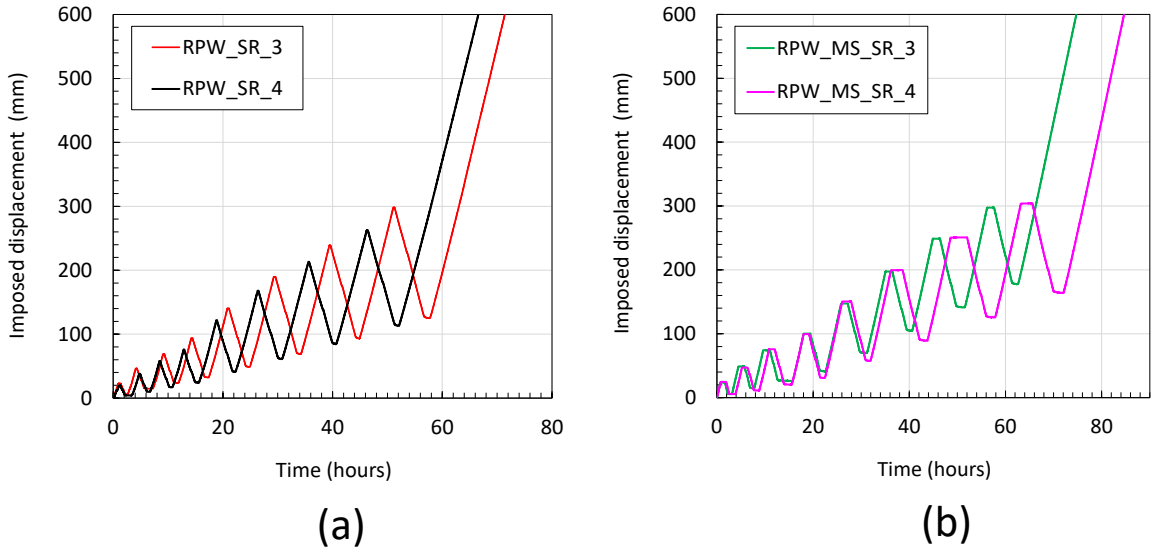

Figure 5.5 Loading sequence of (a) walls embedded in soft rock and (b) two layer profile

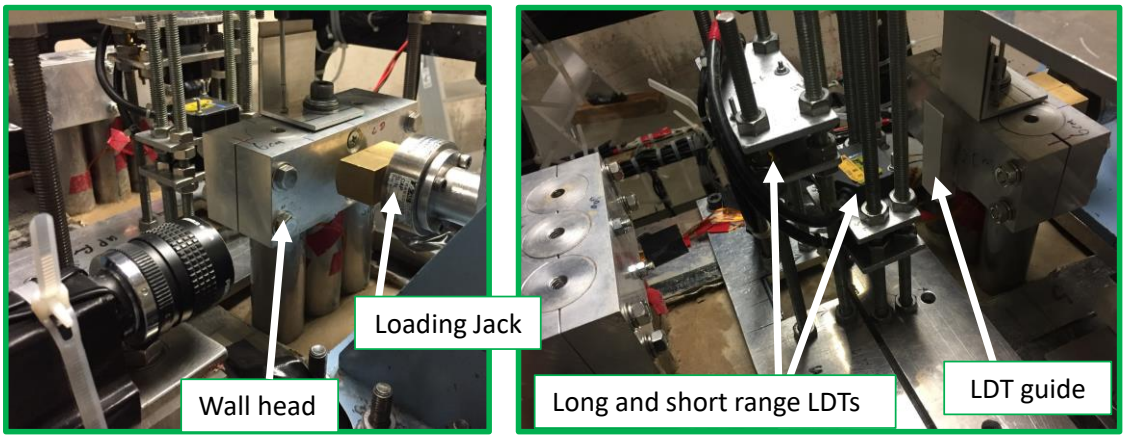

Figure 5.6 Loading mechanism in centrifuge

Figure 5.5 illustrates the variation of imposed displacements against time during the application of one-way cyclic loads. Where after certain number of load cycles the deformation of the wall was studied under a monotonic loading at a constant rate of displacement. The loading mechanism and the arrangement for the more precise displacement and rotation measurements are indicated in **Figure 5.6**. Cyclic lateral loading was conducted using electric jack and the imposed displacements were controlled manually from the centrifuge operation room. In the model attributing to the large horizontal subgrade reaction from the rock embedment and relatively small displacements at initial load cycles, to improve the accuracy and to have a backup measuring arrangement a pair of short range (3-5cm) LDTs and long range(6-14cm) LDTs were equipped as indicated in **Figure 5.6**.

5.3 Results and discussion

5.3.1 Load-displacement and Moment load-rotation relation

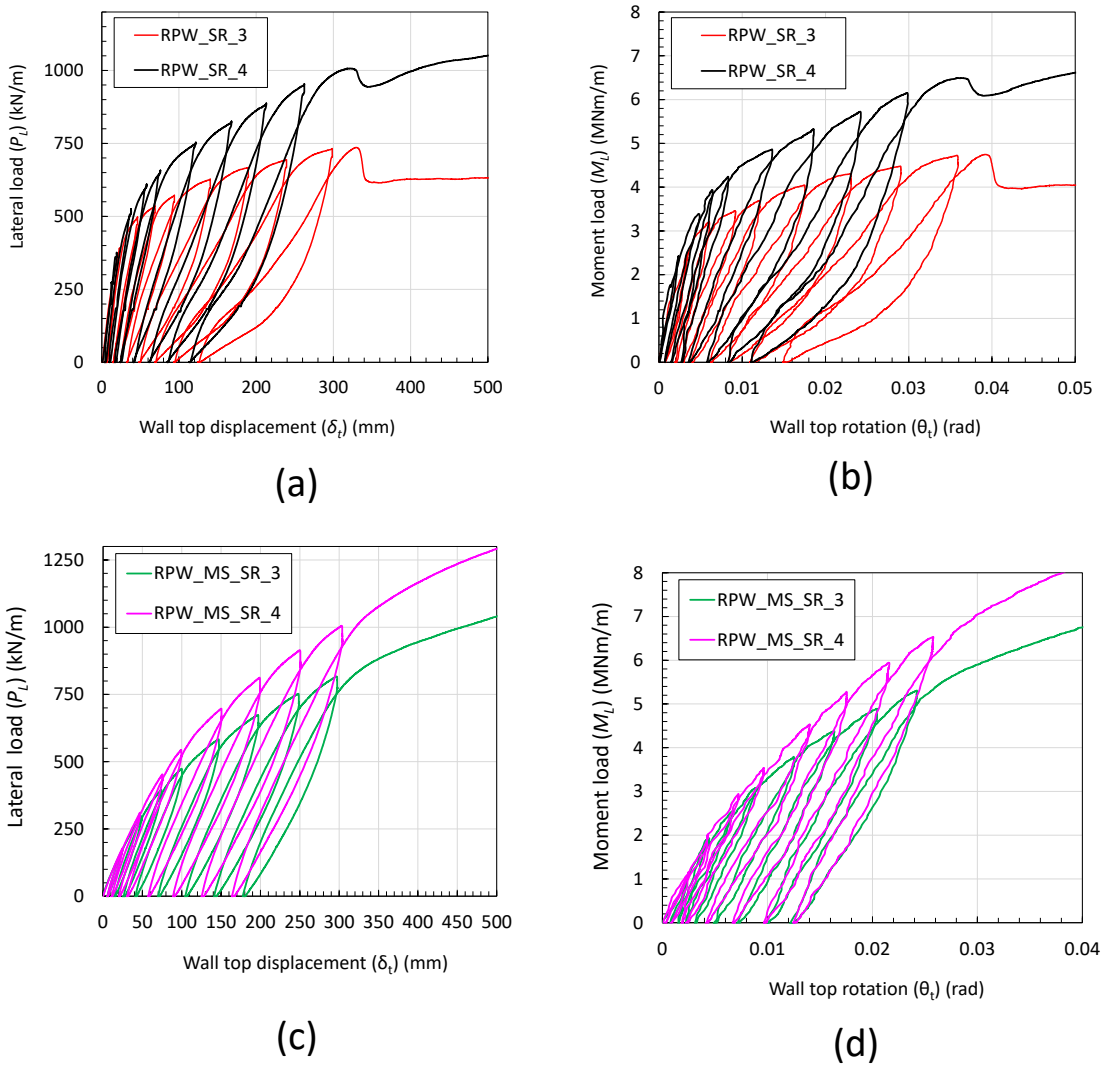

Figure 5.7 Observed cyclic load displacement and moment load rotation relations of tubular pile walls

Figure 5.7 illustrates the observed cyclic load- displacement and moment load-rotation relations for the steel tubular pile walls described in Model-6 and Model-7. Observed loads cycles in the case of rock socketed walls exhibits quiet linear trend in loading and unloading as described in **Figure 5.7** (c) and **Figure 5.7** (d). However, the both loading and unloading in portion of walls embedded in single rock layer is showing a complicated nonlinear trend with varying secant stiffness. Also the recovery percent of imposed displacements are much larger compare to the rock socketed walls.

Detail analysis of these cyclic loadings are describe in the latter part of the chapter and for the simple comparison, back bone curves of results given in **Figure 5.7** are illustrated in **Figure 5.9**. From **Figure 5.9**, referring to the initial portions of the curves the larger lateral confinement of single rock layer even with relatively small embedment depths can be confirmed. However, upon yielding of rock mass took place, a sudden reduction of load carrying capacity could be seen regardless of embedment depth. This trend is more gradual in the case of rock socketed

walls, perhaps it could be attributed to the contribution of overlain sand layer and the influence of confining pressures especially at large displacements.

5.3.2 Back bone curves

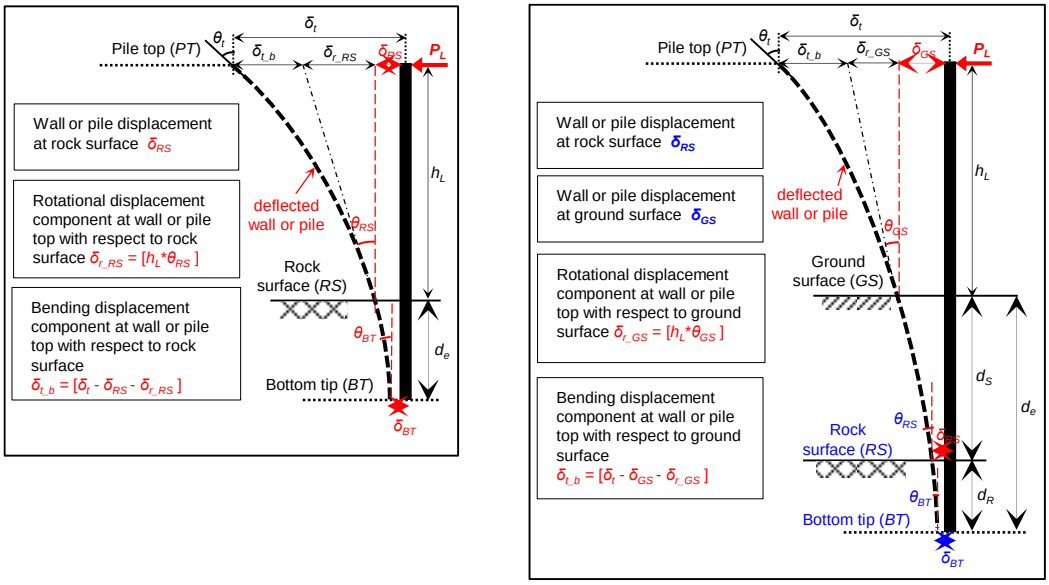

Figure 5.8 Definition and notations of displacement and rotations at different locations of the wall

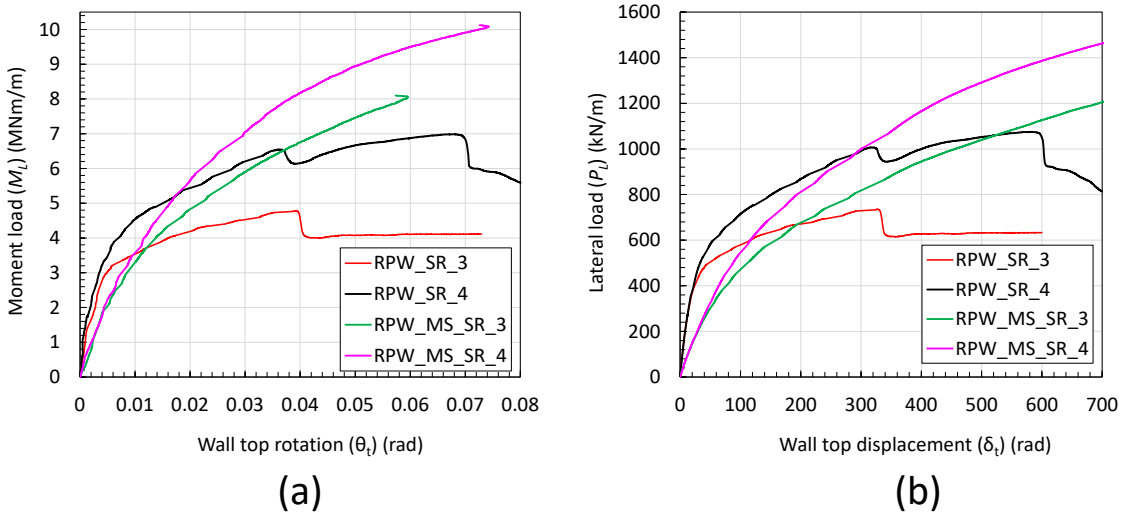

Figure 5.9 Back bone relations for lateral load-wall top displacement and moment load-rotation

In order to discuss the deterioration of the embedded zone in a quantitative manner the estimated rotations and displacements at different levels (**Figure 5.8**) of the wall are illustrated in **Figure 5.10** and **Figure 5.11**.From **Figure 5.11**(a) both walls with 3m (RPW_SR_3) and 4m (RPW_SR_4) embedment depths are showing the yielding of rock surface (RS) at about 3.2MNm/m moment load. However significant difference between walls can be seen in the yielding behavior at the bottom tip (BT) level. RPW_SR_3 exhibits the yielding at bottom tip almost at the same load level that of rock surface level and experiences large deformations with increasing moment loads. Which clearly indicates a combined failure mode of wall front compression and toe back shear failure, it can also be confirmed from **Figure 5.10** (a), referring

to the narrowing trend of rotation between RPW_SR_3(RS) and RPW_SR_3(BT). However yielding point of bottom tip level for the wall with 4m embedment is much larger than that of rock surface level which clearly indicates that the stability of this wall highly controlled by the additional 1m depth of soft rock. Furthermore, even after yielding at bottom tip level significant confinement exist, which reflects in the difference between the rotations RPW_SR_4 (RS) and RPW_SR_4(BT) given in **Figure 5.10** (a). Regarding to the influence of socketing depth similar discussions can be made for the cased of rock socketed walls as well, however major difference compare to the single rock layer is the limited yielding of underlain rock at rock surface and at the bottom tip level. Which can be observed from **Figure 5.11**(b).

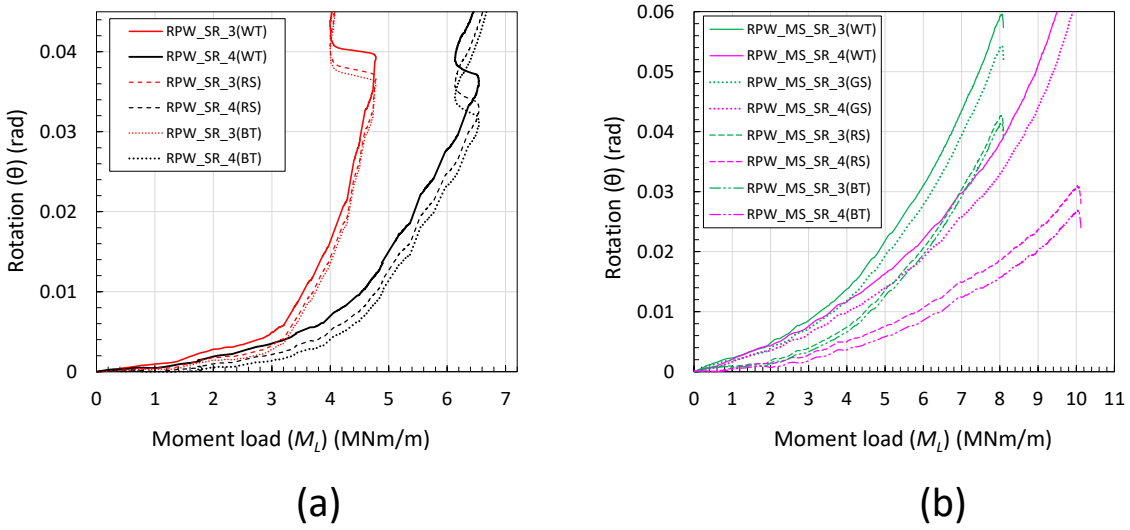

Figure 5.10 Calculated rotations against moment load at wall top, ground or rock surface and bottom tip levels for (a) Model-6 and (b) Model-7

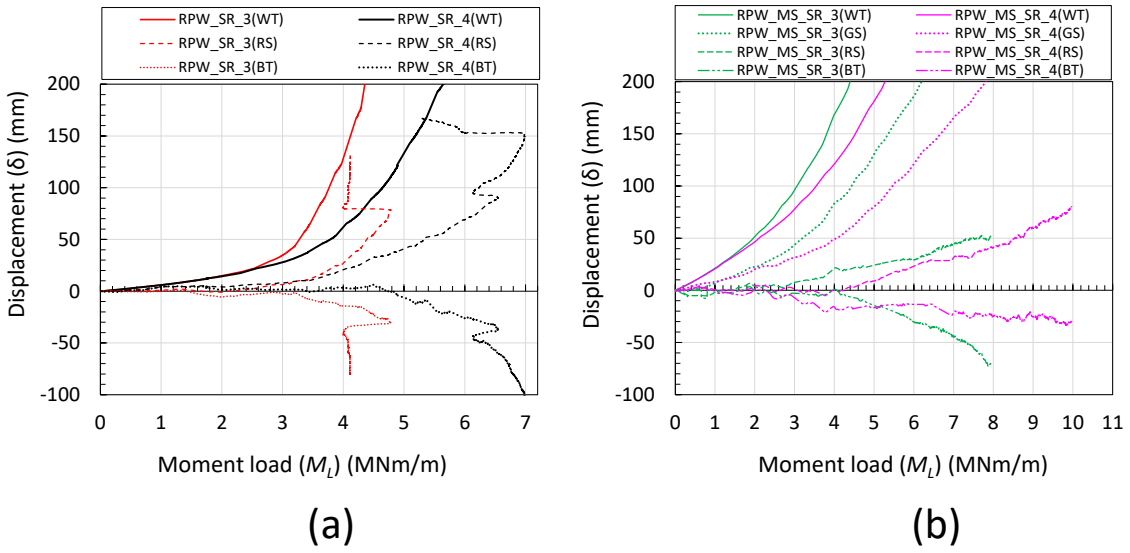

Figure 5.11 Calculated displacements against moment load at wall top, ground or rock surface and bottom tip levels for (a) Model-6 and (b) Model-7

5.3.3 Comparison between single pile and tubular wall behaviors

5.3.3.1 Load –displacement behavior

This subchapter aims to investigate the influence of boundary conditions by means of comparison between single pile loading and the loading of tubular pile wall model based on the results of chapter-4 and this chapter.

Figure 5.12 (a) illustrates the lateral load-wall or pile top displacement behavior of single piles and tubular pile walls embedded in rock with 3m, 4m embedment depth. Similarly **Figure 5.12** (b) compare the lateral load-pile or wall top displacement behavior in two layer profiles with 3m and 4m socketing depths in the underlain rock layer. The above mentioned variations at relatively small displacement (up to 80mm pile or wall top displacement) is given in **Figure 5.12** (c) and **Figure 5.12** (d) accordingly. Mechanism behind the lateral resistance of tubular piles and walls is a combined effect of the stiffness of the pile or wall (E_p), stiffness of the embedded medium (G_s), embedment depth (d_e) and the width of the pile or wall (B). Based on Randolph, (1981) the influential factors can be represented as a non-dimensional form of $G_s d_e/E_p B$.

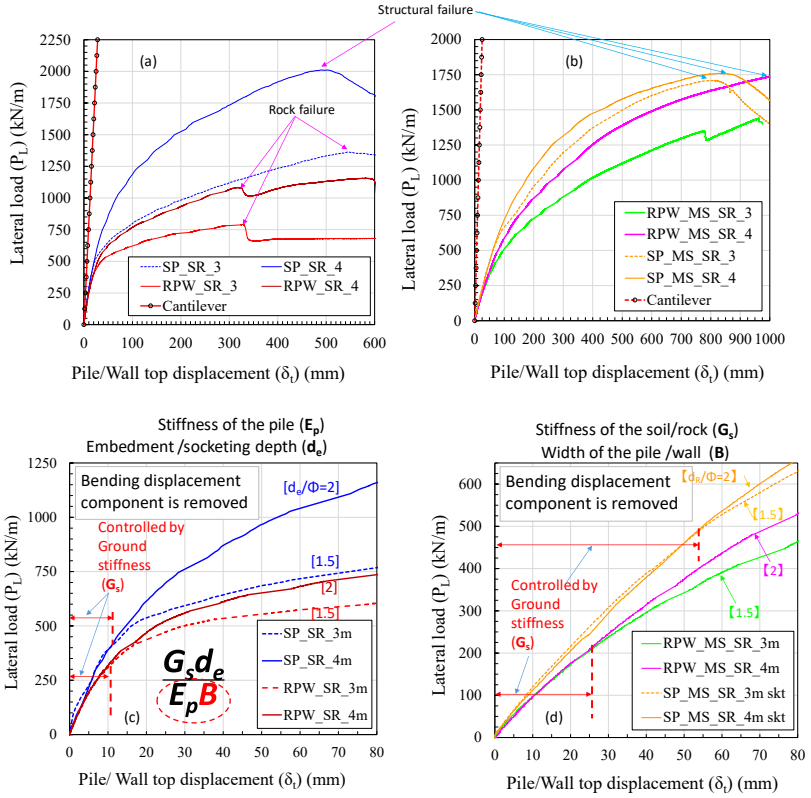

Figure 5.12 Comparison between single pile and tubular pile wall embedded in (a) single rock layer and (b) two layer profile

If we consider only single pile models or only wall models the denominator (E_pB) is constant for the piles or walls with different embedment depths. Implies that the overall behavior of the pile or wall will be governed by the stiffness of the embedded medium and the embedment depth of the pile or wall. Referring to the single piles (SP-SR-3,SP-SR-4) and tubular pile walls (RPW-SR-3,RPW-SR-4) in **Figure 5.12** (c), up to a wall or pile top displacement of 10mm (0.5% Ø) the influence of embedment depth cannot be confirmed. The observation indicates that, the

pile and wall behavior only controlled by the initial small strain stiffness of the rock. Up on certain deterioration take place in the embedded zone, clear deviation can be observed and the influence of embedment depth become eminent. Similar observation can be seen in the case of piles and walls in two layer profiles from **Figure 5.12** (b). However, the displacement at which the deviation in the load –displacement response took place between walls (RPW-MS-SR-3, RPW-MS-SR-4) or piles (SP-MS-SR-3, SP-MS-SR-4) with different embedment depth is relatively larger than that of single rock layer. Which is about 1% Ø for the walls an 2.5%Ø for the single piles. Although the increment of displacement level at which the ground yield is a desirable feature in the application of retaining walls, comparing the wall top displacements in **Figure 5.12** (c,d) under the same loading level for the walls in single rock layer (RPW-SR-3, RPW-SR-4) and the two layer (RPW-MS-SR-3, RPW-MS-SR-4) the walls in two layer even with larger embedment depths exhibits more redundancy in terms of displacements. This observation clearly indicates the requirement of additional lateral resisting measures in the application of cantilever type walls in layered profiles than the single rock layer.

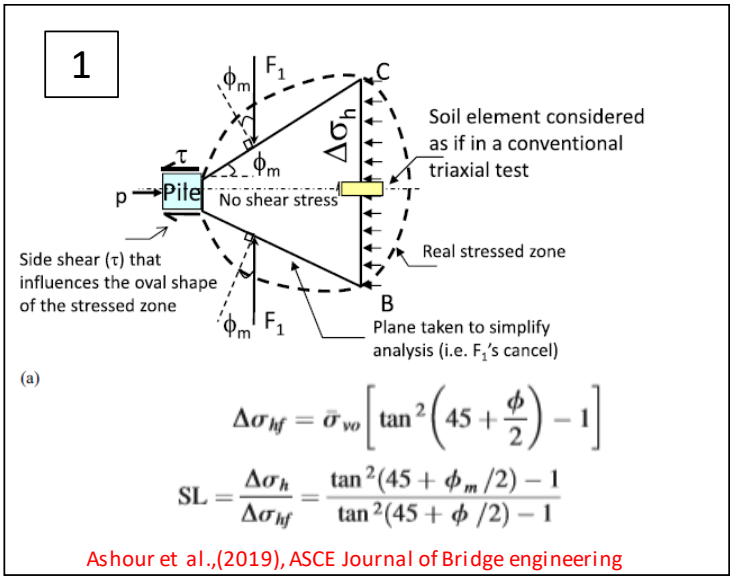

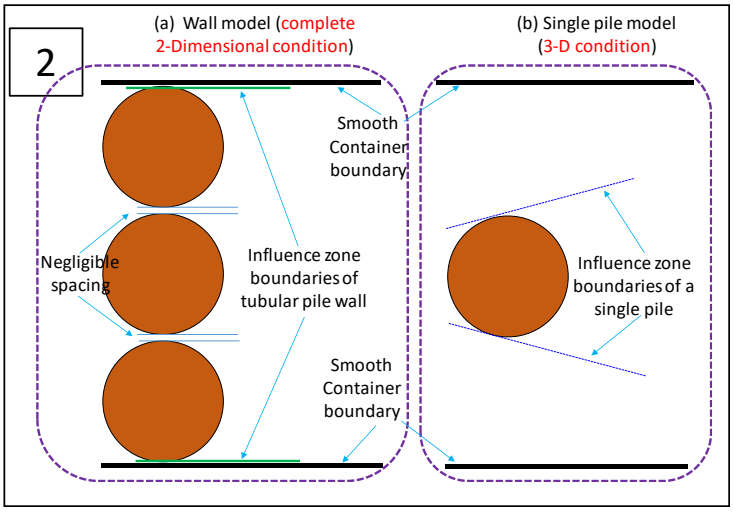

Figure 5.13 Influence zone of a single pile and wall model under lateral loading

The observed rock failure in the case of single pile and wall model is totally different, former exhibits more ductile and the latter is more brittle which can be confirmed from the abrupt reduction of RPW_SR_3 and RPW_SR_4 in **Figure 5.12** (a). Also the failure strains are much smaller for the case of wall than the single pile.

As discussed in 5.3.2 the deformation mechanism of these walls took place by wall front compression and toe-back shear failure. It can also be confirmed from the **Figure 5.19**(a) for both walls with 3m and 4m embedment depths. Observing from the failure pattern, the abrupt reduction at a wall top displacement of 330mm could be attributed to the backward slip failure. However, this displacement level for single pile is about 530mm at pile top and the reduction is gentler. Different failure patterns and failure strains could be discussed referring the **Figure 5.13**.

As explained in Ashour et al.,(2019), **Figure 5.13**-(1) describes the influence zones for an isolated single pile in a quantitative manner with the mechanical properties of the embedded medium, and their mobilization ratio.

According to Ashour et al., (2019), in a general design practice the p-y curves are being evaluated along the length of an isolated pile at a particular step of lateral loading. At that specific loading condition the mobilized strains in the soil/rock depending on the on the shape of the passive soil wedge, pile properties and the associated secant value of the modulus of subgrade reaction (E_s). They defined the stress level (SL) at a specific strain level and at a specific depth as a the ratio between horizontal stress change ($\Delta\sigma_h$) to the limiting stress ($\Delta\sigma_{hf}$) as describe in **Figure 5.13**-(1) to discuss the mechanism behind the stress mobilization around an isolated pile. The stress functions are correlated to the mobilized friction angle (ϕ_m) and the limiting angle of friction (ϕ). In a pile group with two or more raw of piles two different kind of influential zones can be considered according to Ashour et al., (2019), namely the shadow stress zone and the overlapping zone. According to Ashour et al., (2019), passive pressure wedge expands horizontally and vertically along the depth below the rock surface depending on the loading level on a pile or wall.

In case of a 2-dimensional condition, similar to the tubular pile walls (with about 0.18m spacing between 2m diameter piles) in Model-6 and Model-7 in this study, the width of the influential zones is equal to the wall width. Which is much narrower than the influence zone width of a single pile in a normalized form, such as per unit width. It can be observed from the **Figure 5.13**-(2).

In the single pile loading and tubular pile wall loading tests, Different failure modes were observed for the single pile (SP-SR-4) and tubular pile wall (RPW-SR-4) with the identical embedment (d_e=2Φ) and loading conditions in single soft rock layer as described in **Figure 5.12** (a). The former exhibited structural buckling and the latter was a clear wedge type ground failure. It reveals that the optimum embedment depth is deeper for the tubular pile wall than single pile, which indicates that the rational embedment for cantilever tubular pile wall is larger than single pile with same cross section.

In the case of wall model (RPW-SR-3) and single pile (SP-SR-3) with the embedment depth of 1.5Φ in single rock layer showed the ground failure as an ultimate failure condition as described in **Figure 5.12** (a). However, the normalized ultimate resistance for single pile is about 1.6times that of wall model and the wall model exhibited a clear wedge type ground failure, while the single pile showed more confined deformations.

The difference in the observed ground failures as an ultimate condition for the single pile and wall model embedded in single rock layer is highly influenced by the wall or pile width and thereby the mobilized subgrade reaction. Attributing to the 2-dimensional condition, the influence zone, which contribute to the lateral resistance for a unit width of the wall is much narrower compare to an isolated single pile. This phenomenon causes an increased stress level or strain in the shallow layer of the rock and resulting significant reduction in subgrade reaction

under same loading level. This mechanism causing large deflection of the wall compare to the condition of an isolated single pile. Due to the large deflection of the wall, eventual accumulation of wall deflection in the embedded zone, causing the deterioration of subgrade reaction along the wall embedded zone and eventually causing a wedge type ground failure at the ultimate resistance of the embedded medium.

5.3.3.2 System stiffness and residual displacement

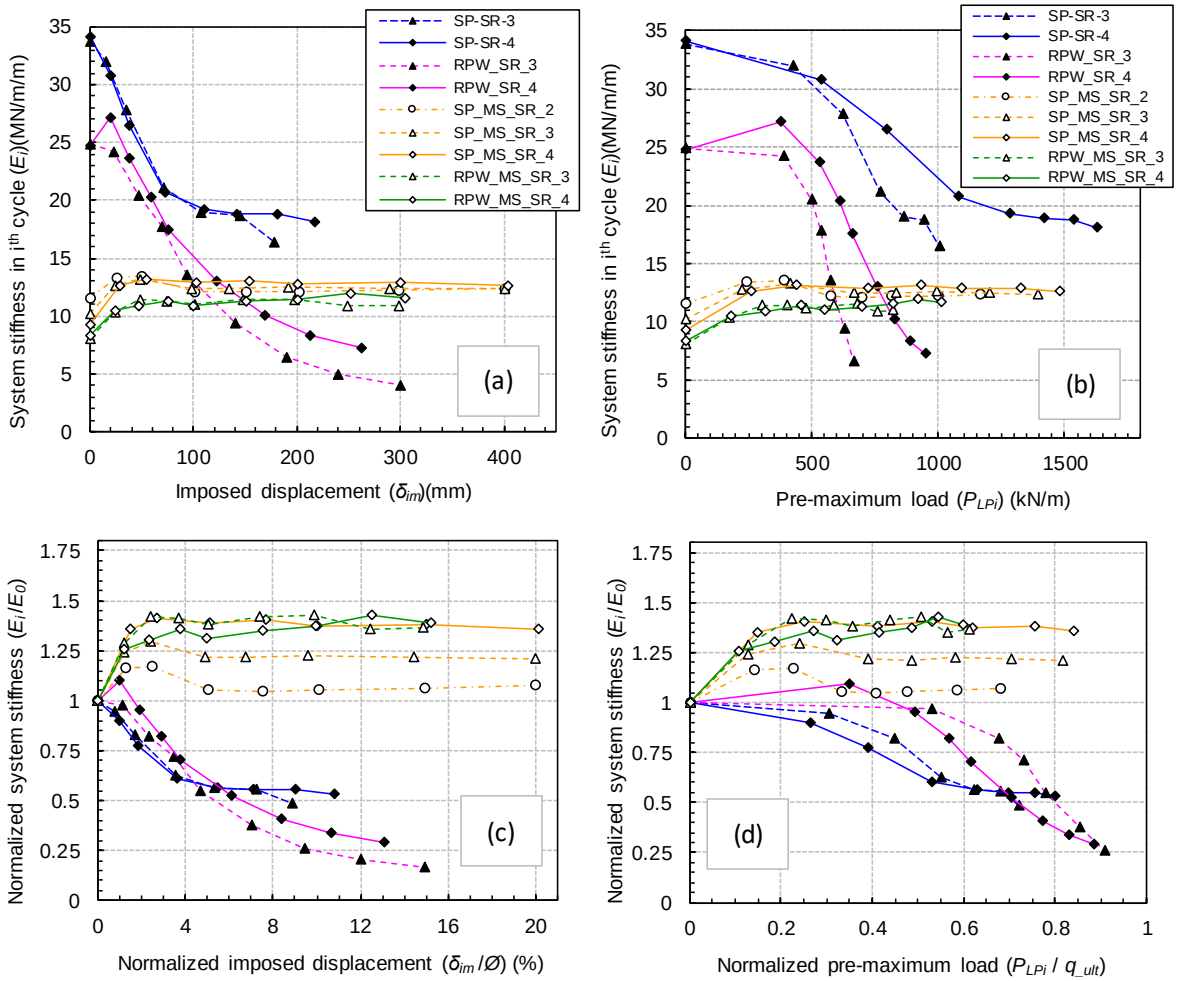

Figure 5.14 Variation of system stiffness of single pile and walls against the applied peak load in previous cycle

Estimated variation of system stiffness against the imposed displacement and applied peak load in the previous cycle is illustrated in **Figure 5.14**(a) and **Figure 5.14**(b) respectively. Corresponding variation of normalized stiffness in each cycle (E_i) based on the stiffness of initial cycle (E_0) is illustrated against the normalized imposed displacement and the normalized peak load in **Figure 5.14**(c) and **Figure 5.14**(d) for the single piles and wall models embedded in single rock layer and two layer profile. From **Figure 5.14**(a) and **Figure 5.14**(b) it can be seen that the initial stiffness of the piles and walls embedded in single rock layer is about 3 time larger than that of two layer profiles. Indicating the large lateral confinement of rock type ground even with relatively small embedment depths. From **Figure 5.14** (a) observed increment in the system stiffness of piles SP-MS-SR-3, SP-MS-SR-4 and the walls RPW-MS-SR-3, RPW-MS-SR-4 could be attributed to the densification of overlaying sand. As discussed earlier the observed reduction in the system stiffness of piles SP-MS-SR-3, SP-MS-SR-4 around a

displacement of 3%Ø is the fact of the stiffness deterioration in the shallow layer of rock. However, the wall models in two layer RPW-MS-SR-3, RPW-MS-SR-4, did not show a drop in the system stiffness. Showing about 40% increment from the initial stiffness in a gradually increasing trend up to the displacement of 3%Ø and a constant stiffness beyond the displacement of 3%Ø. Also no much deterioration even at large imposed displacements and showing a constant stiffness with load increment can be observed, which is a desirable feature in the real field to avoid the catastrophic failures. However from **Figure 5.15**(d), the accumulation of residual deformation is much more significant for the walls RPW-MS-SR-3, RPW-MS-SR-4 even at relatively small loading levels. Indicating the difficulties in achieving the allowable displacements under a cantilever condition of the wall.

However in the case of single rock layer (**Figure 5.14** (a,c)), deterioration rate is relatively larger for wall model than single pile in single rock layer. Observed deteriorations in the system stiffness could be attributed to the plastic deformations in the embedded rock medium. This kind of plastic deformations must be avoided in the life span of the cantilever type retaining walls since the stability of such walls highly depends on the mobilized passive pressures in the embedded zone. Stability of a retaining wall often defined based on the allowable displacement concept rather than the ultimate collapse. This allowable displacement (residual deformation) is generally defined based on the structures and service lines behind the retaining walls or in front of the walls. In the general design practice of this kind of walls in an urban environment, it is often expected to prevent the yielding of embedded medium or the retaining backfill, implies that the residual deformation of the structure must be kept within few mm.

Although a generalized conclusion cannot be derived from the limited number of experiments in this chapter, a specific conclusion can be written regrading to the allowable load and displacements to satisfy the stability or elasticity of the embedded medium, and the residual deformations. Referring to the walls RPW-SR-3 and RPW-SR-4 from **Figure 5.14**(c) and **Figure 5.14**(d), in order to satisfy the intact condition of the walls or to prevent the deterioration of system stiffness the an allowable wall top displacement of 1%Ø (20mm) from **Figure 5.14**(c) and an allowable load of $0.5q_{ult}$ could be defined. Referring to **Figure 5.15**(e), in order to remote the structure from permanent deformations the allowable load must be kept below $0.3q_{ult}$, while comparing the abovementioned requirements for the system stiffness and the residual deformations, an allowable wall top displacement of 1%Ø (20mm) and allowable maximum load of $0.3q_{ult}$ could be defined as the limiting values to prevent the plastic yielding of embedded medium or the failure of the walls under the specific loading condition implemented in this study.

The wall model shows an abrupt reduction in the system stiffness beyond a 10% reduction from initial stiffness. This is a clear indicator for the onset of yielding and the initiation of a catastrophic failure, which must be avoided in the life span of retaining structures. It can also be confirmed from the variation of residual displacements given in **Figure 5.15**(b) referring to RPW-SR-3 and RPW-SR-4. Although the walls in two layer profile showing relatively large residual deformation at initial cycles the overall observed residual deformations in two layer profile (**Figure 5.15**(a)) exhibits a gradually increasing trend. However the wall and single piles in single rock layer (**Figure 5.15**(b)) showing a sudden increase up on yielding took place, a large increment of residual displacement under small increment of load can be observed. Observed residual deformation characteristics and the deterioration of system stiffness in single rock layer indicates the design-risks related to the shortening of embedment depth as well as the evaluation method of strength and stiffness of the embedded medium.

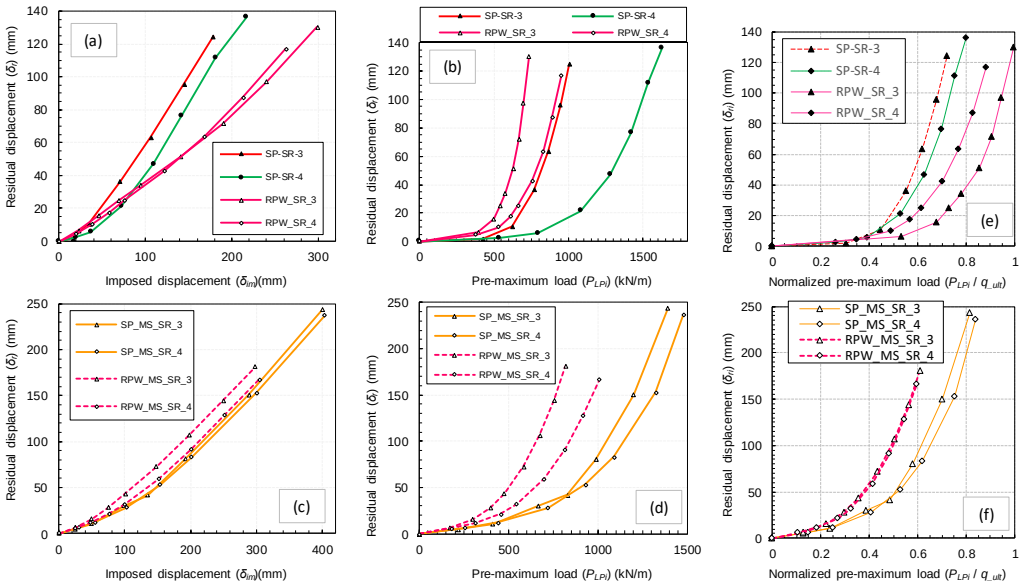

Figure 5.15 Variation of residual displacements of single pile and walls against the applied peak load in previous cycle

5.3.3.3 Structural failures and optimum embedment depths

Figure 5.16 summarize the influence of embedment depth based on the experiment models 4,5 in chapter-4 and models 6,7 in this chapter. As discussed in 4.6.4 similar influence of shallow layers can be confirmed at relatively small displacement levels for wall models as well.

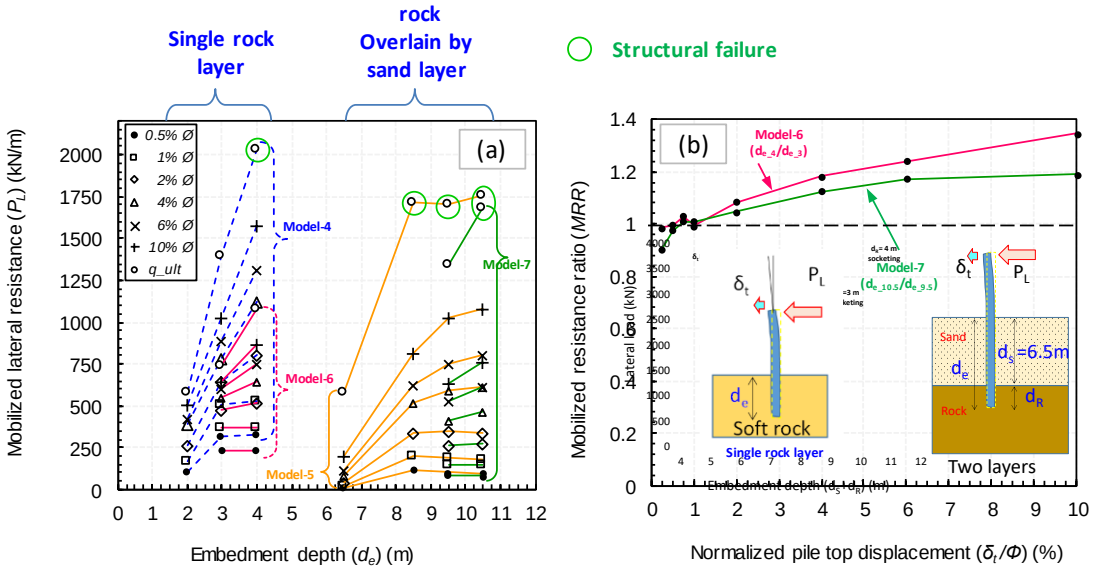

Figure 5.16 Influence of wall embedment depths

Based on the observed pile structural failures in single pile loading and the ground failure in wall model embedded in single rock layer it can be confirmed that the optimum embedment depth is deeper for the wall than single pile, which indicates that the rational embedment for cantilever tubular pile wall is larger than single pile with same section. When the failure take place by structural buckling, significant difference between the ultimate resistance of pile and wall models could not be observed in the case of two layers (Model-5 and 7). As an overall observation the variation of lateral resistance from small to large displacement depends on the

mode of failure either it take place by ground failure or structural buckling. Although structural buckling was observed as an ultimate failure of wall with 4m socketing, preventative measures must be taken in to account to control the residual deformations (**Figure 5.15**) under the design and ultimate loading conditions.

5.3.3.4 Bending behavior and observed failures and confining pressures

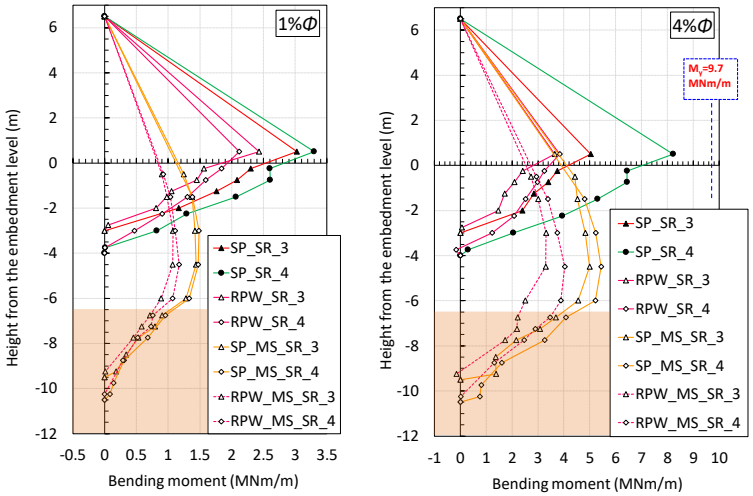

Figure 5.17 Observed bending moment profiles for single pile and wall models at small wall top displacements

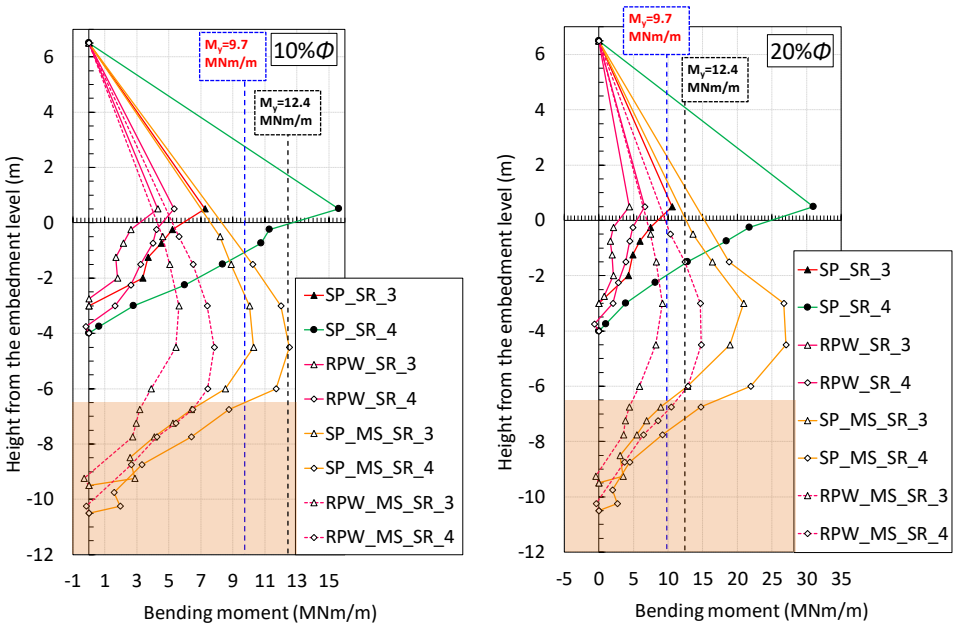

Figure 5.18 Observed bending moment profiles for single pile and wall models at relatively large wall top displacements

Observed bending profiles of single piles, walls embedded in single rock layer and two layer profiles are illustrated in **Figure 5.17** and **Figure 5.18** at relatively small and large displacements respectively. At small displacement levels a higher influence of overlain sand layer could be seen while comparing the bending moments at the rock surface for the piles and walls embedded in single rock layer and two-layer profile. However at large displacements (**Figure 5.18**) the lateral resistance from overlain sand tend to decrease (as the soil fails) and the

bending moment at the rock surface level keep increasing which can be confirmed from **Figure 5.17** and **Figure 5.18**. Furthermore from **Figure 5.18**, the experienced bending moments at rock surface level for the wall embedded in two layer (RPW_MS_SR_4) is much larger than that of single rock layer (RPW_SR_4).

5.3.3.5 Deformation and failure

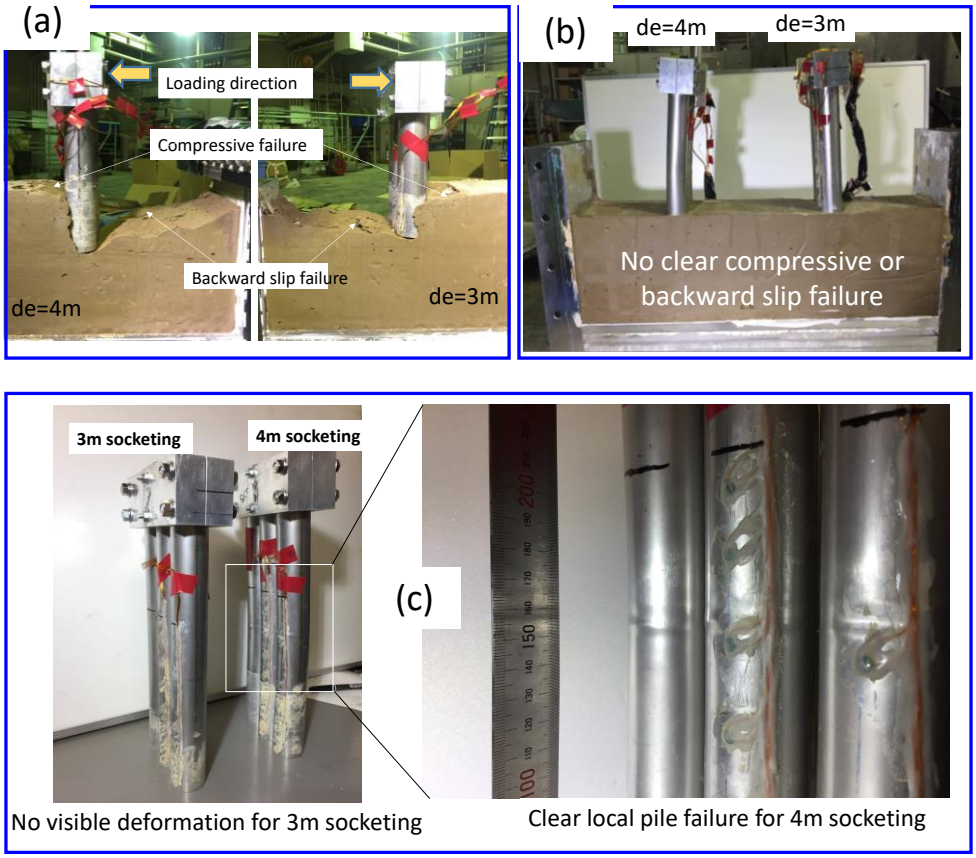

Figure 5.19 Observed failures of (a) Model-6 and (b,c) Model-7

However the wall RPW_MS_SR_4 did not exhibit the ground failure as observed for the single layer in **Figure 5.19**(a) for RPW_SR_4, rather structural buckling of the wall RPW_MS_SR_4 was observed as shown in **Figure 5.19**(b,c). Also, **Figure 5.19**(b) indicates no clear compression in wall front or toe back of the rock socketed zone, which could be attributed to the confining pressures cause by overlain sand layer.

From the observed failure mode of wall front compression and toe back shear failure as well as the load deformation characteristics explained in **Figure 5.11**(a), it can be confirmed that the rock failure initiated at the wall front and once the shallow layers fail and loose its capacity the toe back passive zone take its role to maintain the equilibrium. The deformation mechanism in two layer is quite different as described in **Figure 5.11**(b), where the deformation of wall front compression is limited, which can also observed from **Figure 5.20** (b). Thanks to the overlain sand in the wall front, this limited deformations in the wall front is the main governing mechanism in the two-layer profile, as far as the shallow layer of rock could resist the applied loads the failure of bottom tip passive zone can be prevented. Therefore, from the observations it can be concluded that the confining pressures in the wall front must play a major role in the deformation characteristics of walls in two-layer profile with the increment of applied loads.

5.3.3.6 Influence of confining pressure based on experiment outcomes

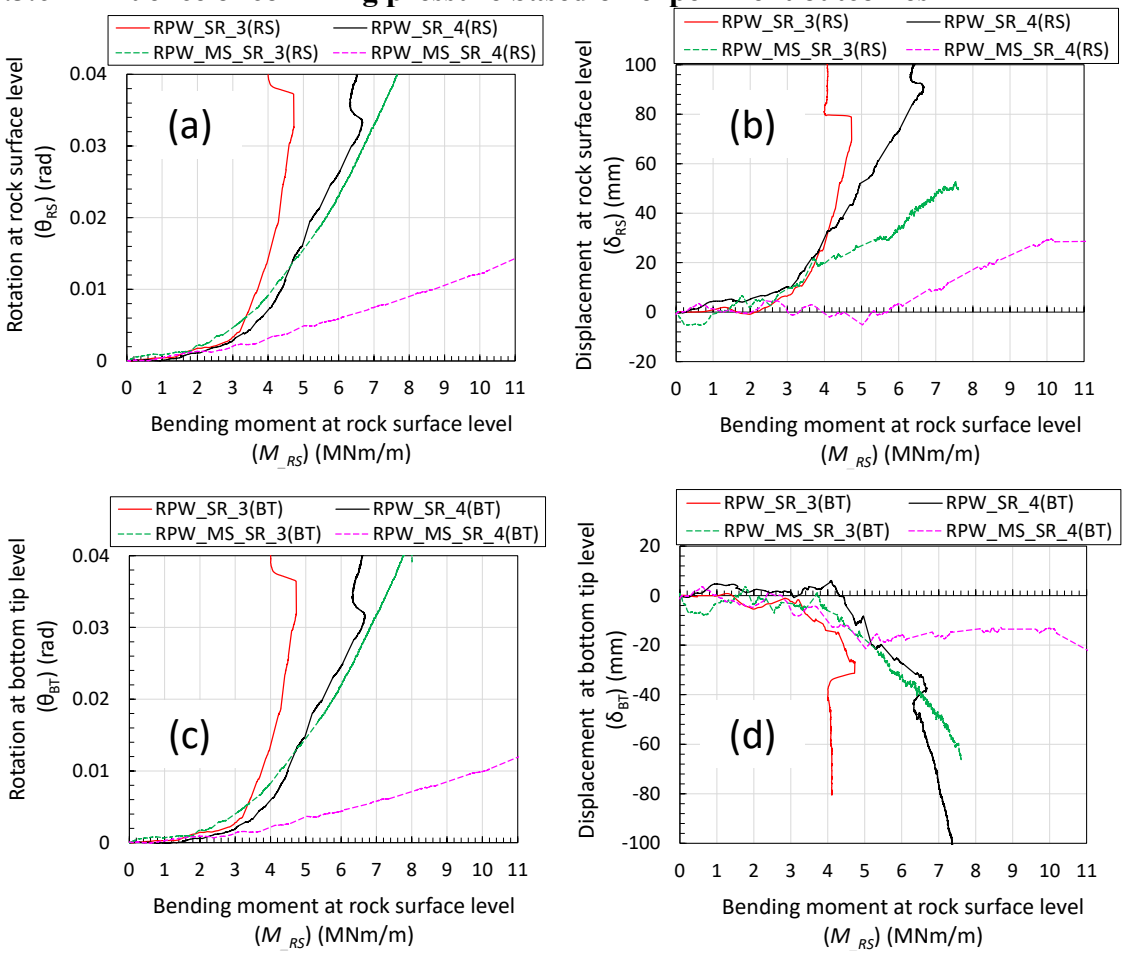

Figure 5.20 Calculated rotations and displacements at rock surface and bottom tip levels against the bending moment at the rock surface level

In order to investigate the influence of confining pressures on the deformation characteristics of the walls embedded or socketed in soft rock, the estimated rotations and displacements at the rock surface and bottom tip levels are illustrated against the measured bending moment at the rock surface level in **Figure 5.20**. Here the bending moment at the rock surface level is assumed as a moment load applied at this level. Referring to **Figure 5.20** (a,c), prior to the yielding point of rotation at rock surface and the bottom tip level no significant contribution of overlain layer can be observed. Observation in this region could be attributed to the self-confinement of rock materials which is much larger than the confining pressures of overlain sand. However up on yielding a clear influence of confining pressures can be seen while compare the walls with same embedment or socketing depth. The influence is much larger for the 4m socketing depth than the 3m which can be confirmed from **Figure 5.20** (b,d) as well. Perhaps this high influence might be attributed to the limited deformations and large resistance of shallow layers in the wall front and thereby the large self-confining pressure in the toe back at 4 m depth from the rock surface.

5.3.4 Numerical modelling of laterally loaded cantilever walls embedded in rock by Plaxis-2D

Numerical modelling was conducted by using Plaxis-2D finite element software. Prior to the modelling process the mechanical properties of embedded medium were estimated from the unconfined and triaxial test results, which were conducted on model soft rock specimens. The description about the model ground, mechanical properties and the loading type are described

in **Figure 5.21**. The loading was conducted by means of imposed displacements of 10mm at wall top level in each phase. Displacement increment of 10mm was introduced up to a maximum of 15 phases. It is important to emphasize that the wall behavior in rock type grounds mainly govern by the initial stiffness at relatively small imposed displacements, however with the deterioration of the rock the stiffness also changes, which could not be simulated in this assumed simple Mohr-Coulomb model. This is one of the major limitations in this modelling.

Used software	**Plaxis 2D**
Model condition	2D plane strain with 15 node triangular elements
Wall model	Modelled using plate element
Rock ground	Based on Mohr-Coulomb model (fully drained)
Loading type	Prescribed displacements of 10mm in each phase
Rock properties	Cohesion=330KPa,ϕ=31°,Poisson's ratio=0.2
Rock stiffness	Small strain stiffness was used E=2000MPa
Rock Unit weight	$\gamma_{d=16.8kN/m^3}$ and $\gamma_{sat=20.1kN/m^3}$
R_{inter}	0.8 ($tan\emptyset_{interface}=R_{inter}*tan\emptyset_{soil}$), ($C_{interface}=R_{inter}*C_{soil}$)

Figure 5.21 Information about the numerical model

5.3.4.1 Used mechanical properties of materials and justification for the selection

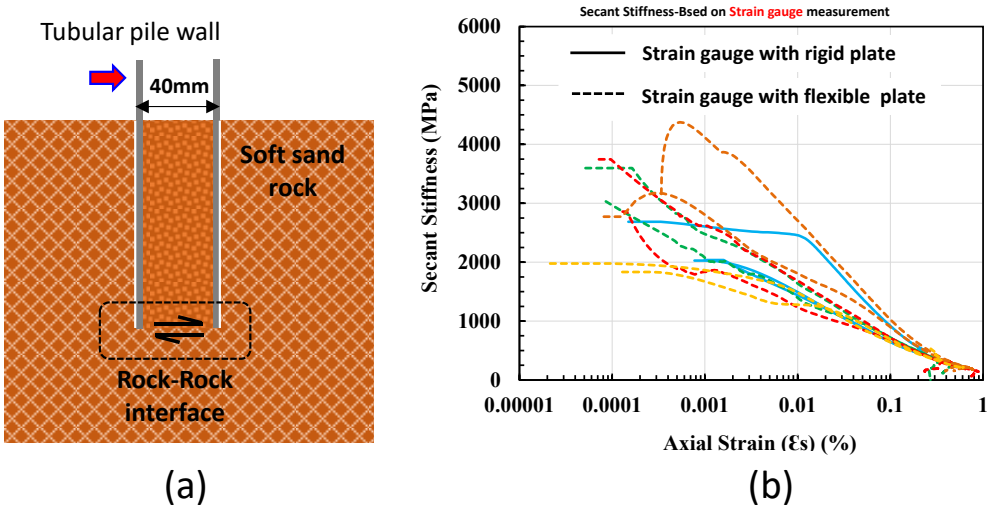

Figure 5.22 (a) Intact condition of tubular pile wall embedded in soft rock and (b) small strain stiffness measured by using flexible and rigid plate strain gauges

Figure 5.22(a) describes the intact condition of tubular pile wall embedded in soft rock, where the bottom boundary condition of the wall can be considered as a rock-rock interface attributing to the rock plugging portion. Therefore, from the initial condition to certain level of strain at which the rock failure take place at the interface, the interface friction coefficient would be

closer to unity. Considering this phenomena, the R_{inter} value for the modelling was assumed as 0.8. Furthermore, as we observed from the experimental outcomes of system stiffness against the load in 5.3.3.2, the variation is much more non-linear and modelling of such variations using adopted Mohr-Coulomb model is impossible. Therefore at least to capture the initial linear portion of load displacement behavior observed in the centrifuge model studies, which is corresponding to the small strain (0.001%) stiffness of the model rock, the modelling was conducted using initial stiffness measured by flexible strain gauges as described in **Figure 5.22**(b). Although the initial stiffness showing a large range of variations from 2000-3000MPa, in this study 2000MPa was considered as the initial stiffness, which is the lowest stiffness measured among several specimens given in **Figure 5.22**(b). Besides the stiffness of soft rock the effective shear strength and friction angle of the model soft rock was derived from consolidated undrain triaxial tests conducted by an outside company. From the results an effective cohesion of 330kPa and a friction angle of 31° were estimated as described in **Figure 5.23**.

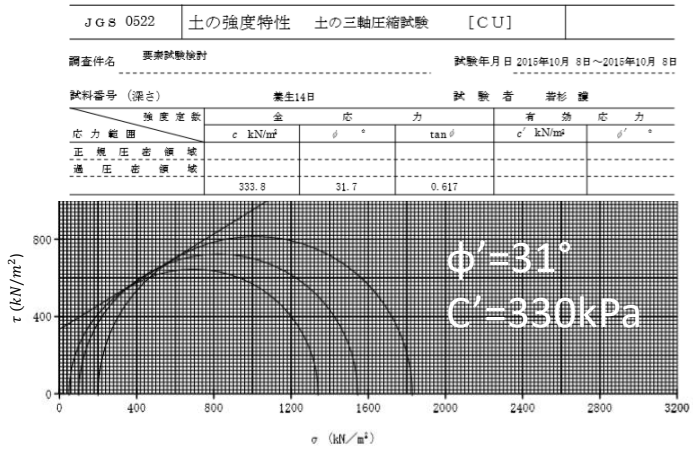

Figure 5.23 Triaxial test results and strength parameters

5.3.4.2 Model conditions and backbone curves

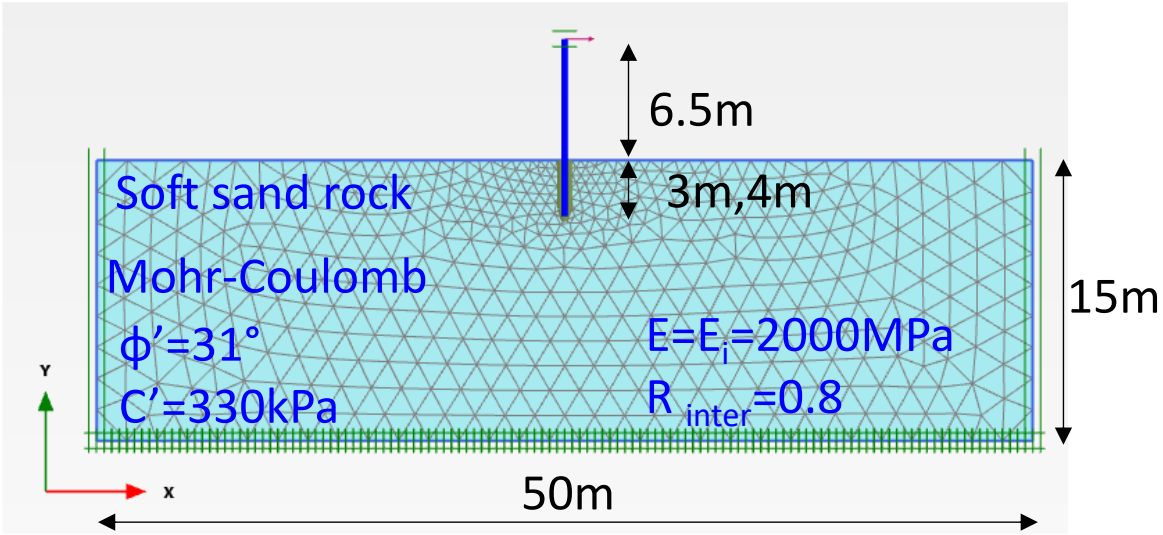

Figure 5.24 Typical numerical model used for the analysis in Plaxis-2D with 3m embedment depth

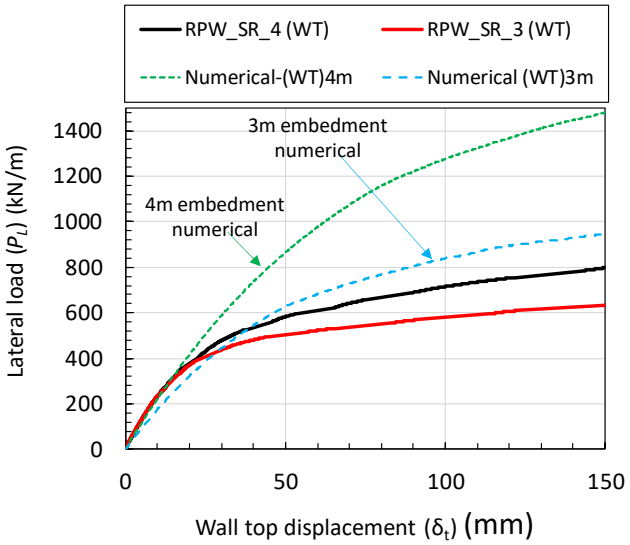

Figure 5.25 Load-displacement behavior observed from numerical and centrifuge models

Figure 5.24 describe a typical model and the shape of fine-mesh created with 15-noded triangle elements in Plaxis-2D. Where the equivalent sections of steel tubular pile walls were modelled as steel plate elements with a loading height of 6.5m. The analysis was conducted under drained conditions using Mohr-Coulomb linear elastic –perfectly plastic model, and model soft rock had the unit weights of γ_d=16.8kN/m^3 and γ_{sat}=20.1kN/m^3. The loading was conducted using prescribed displacement option with staged construction feature. In the analysis, totally 15 phases were considered with the increment of 10mm wall top displacement in each phase. It means the maximum analysed wall top displacement is 150 mm, which is 7.5% of the pile diameter.

Relatively large displacements are not studied in this modelling attributing to the reliability of the outcomes since the model using a constant stiffness throughout the loading process. Initially two models with 3m and 4m embedment depths were studied with abovementioned model parameters to compare the outcomes with the results of centrifuge models describe in Model-6 (Walls embedded in single rock layer) and to ensure the applicable range.

Observed lateral load-wall top displacement from numerical model is illustrated with the outcomes of centrifuge model is given in **Figure 5.25**. From **Figure 5.25** quiet good agreement between the numerical and experimental results can be seen up to a wall top displacement of 25mm, beyond which the numerical model overestimate the lateral resistance at a considered displacement. The observation is as expected since the Mohr-Coulomb (Linear elastic-perfectly plastic) model did not consider the deterioration of rock stiffness based on the strain level.

5.3.4.3 Validation of numerical model

The observed displacements at three different locations of the wall namely wall top (WT), rock surface (RS) and bottom tip (BT) are compared with experimental outcomes at the same locations as illustrated in **Figure 5.26** for the walls with 3m and 4m embedment depths. Measured bending moments at 10, 20, 50 and 100mm wall top displacements also illustrated with the numerical outcomes in **Figure 5.26**. Comparing the displacements at all three locations, prior to the yielding displacements of experimental outcomes at RS and BT, the numerical model could provide reliable outcomes where the wall top displacement is about 25mm for both walls.

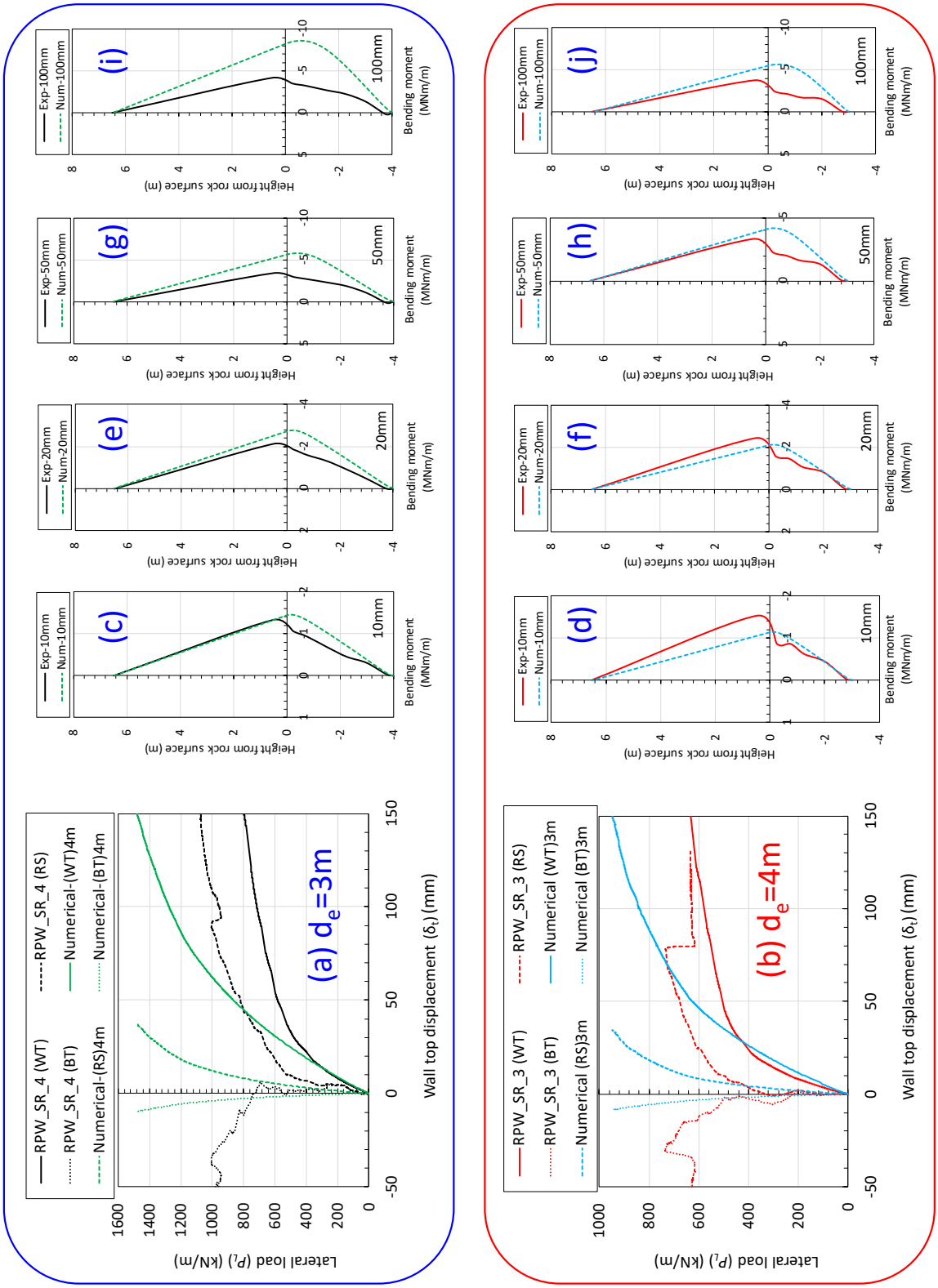

Figure 5.26 Comparison between the load-displacement and bending behaviors observed from experiment and numerical models

Below this displacement level quiet good relation between measured bending moments and the numerical ones can be seen as shown in **Figure 5.26**(c,d and e,f). However, at relatively large displacement level the difference between measured bending moments and numerical ones are much more significant especially for the wall with 4m embedment depth. Furthermore,

measured bending moment profiles below the rock surface could not be perfectly captured in the simplified model. Which clearly indicates that the real local behavior of actual tubular piles cannot be captured from the simplified plate models.

With the confirmation of some similarities in the small displacement range and differences at relatively larger imposed displacements between numerical and experimental outcomes, further analysis was conducted to investigate the influence of confining pressures caused by overlain mediums as describe in subsequent sub chapter 0

5.4 Influence of confining pressure based on numerical outcomes

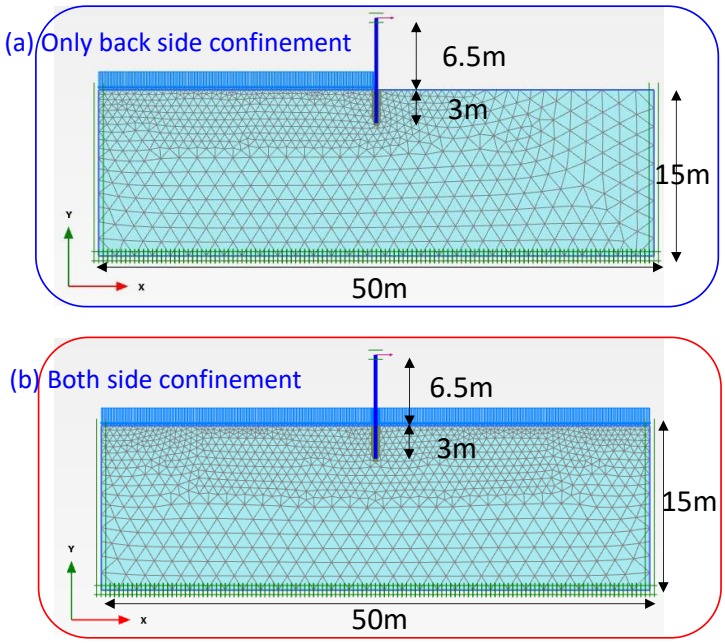

Figure 5.27 Used model conditions to investigate the influence of confining pressures (a) scenario-2 and (b) scenario-3

Influence of confining pressure was investigated under three different scenarios for a wall with 3m embedment depth. In the first scenario (scenario-1) no surcharge load on the rock surface was considered as described in 5.3.4.2, aiming to simulate the tubular pile walls embedded in single rock layer as described in subchapter 5.2.2.1 (Model-6). The second scenario (scenario-2) aims to investigate the confining pressures on the backfill side only as described in **Figure 5.27**(a), which is the common condition of a cantilever type retaining wall investigated in chapter-3. In the third scenario (scenario-3) the surcharge loads on either sides of the wall was considered as describe in **Figure 5.27**(b), which is the condition of Model-7 described in sub chapter5.2.2.2. It also helps to understand the similarities and differences in the stress mobilization of scenario-1 (Model-6) and scenario-3 (Model-7).

Observed load displacement relation for scenario-2 and scenario-3 at different confining pressures are illustrated in **Figure 5.28**(a) and **Figure 5.28**(b) respectively. Where the results of 0kPa represents the scenario-1, and RPW_SR_3(WT) indicates the experiment result of the wall with 3m embedment depth. **Figure 5.30** describe the mobilized passive pressure zones in the wall front and toe back regimes at relatively small (10mm) and large (150mm) wall top displacements. Influence of confining pressures on the lateral resistance of walls at different wall top displacements are summarized in **Figure 5.29**. From **Figure 5.28**(a) and **Figure 5.29**(b) it can be confirmed that the confining pressures in the backside of the wall has no significant influence on the lateral resistance of the wall at any displacement range. Observed behaviors

could be attributed to the expansion of shallow layer shear zone in the wall front as described in **Figure 5.30** (a,b) and the wall deformations are mainly controlled by the mobilized passive pressures in the wall front.

Confining pressure in the wall front has significant influence on the wall behavior and the mobilized passive pressures especially at wall front shallow layers. From **Figure 5.28**(b) and **Figure 5.29**(a) it can be observed that the confining pressures in the wall front has no significant influence at relatively small displacements 1%Φ-2%Φ, but as the displacement level increases the influence become eminent. Which can also be confirmed from the comparison of mobilized zone of earth pressures and the pattern of mobilization at 150mm wall top displacement in **Figure 5.30** (c) and **Figure 5.30** (a,b).

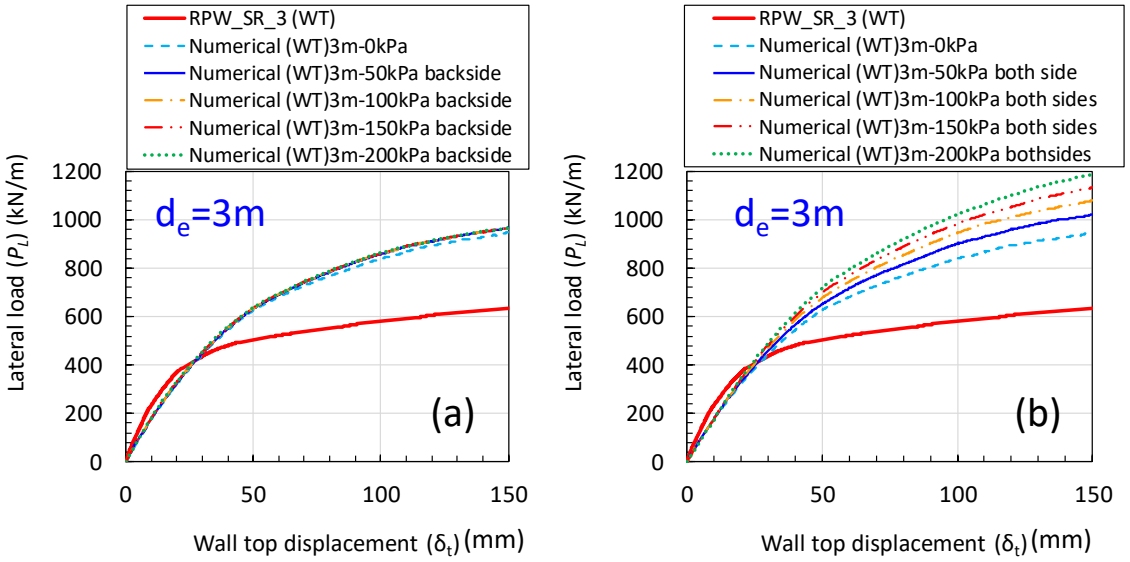

Figure 5.28 Numerical analysis results for (a) scenario-2 and (b) scenario-3

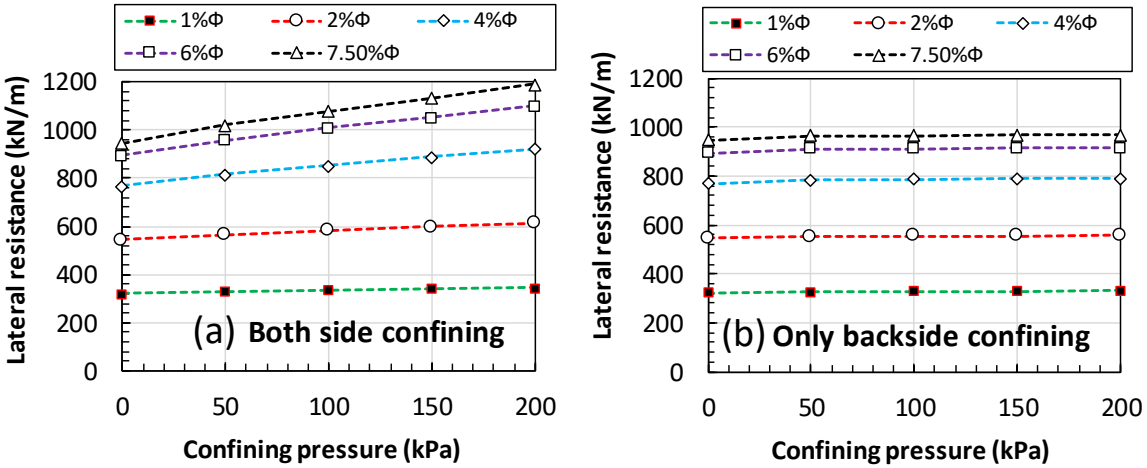

Figure 5.29 Influence of confining pressures under (a) scenario-3 and (b) scenario-2

5.5 Mechanism behind the failure of walls in single rock layer

In order to investigate the stress mobilization and deformation mechanism of the walls with (Model-7) and without surcharge (Model-6), the mobilized pressure envelop around the wall at relatively small (10mm) and large (150mm) wall top displacement is compared under the

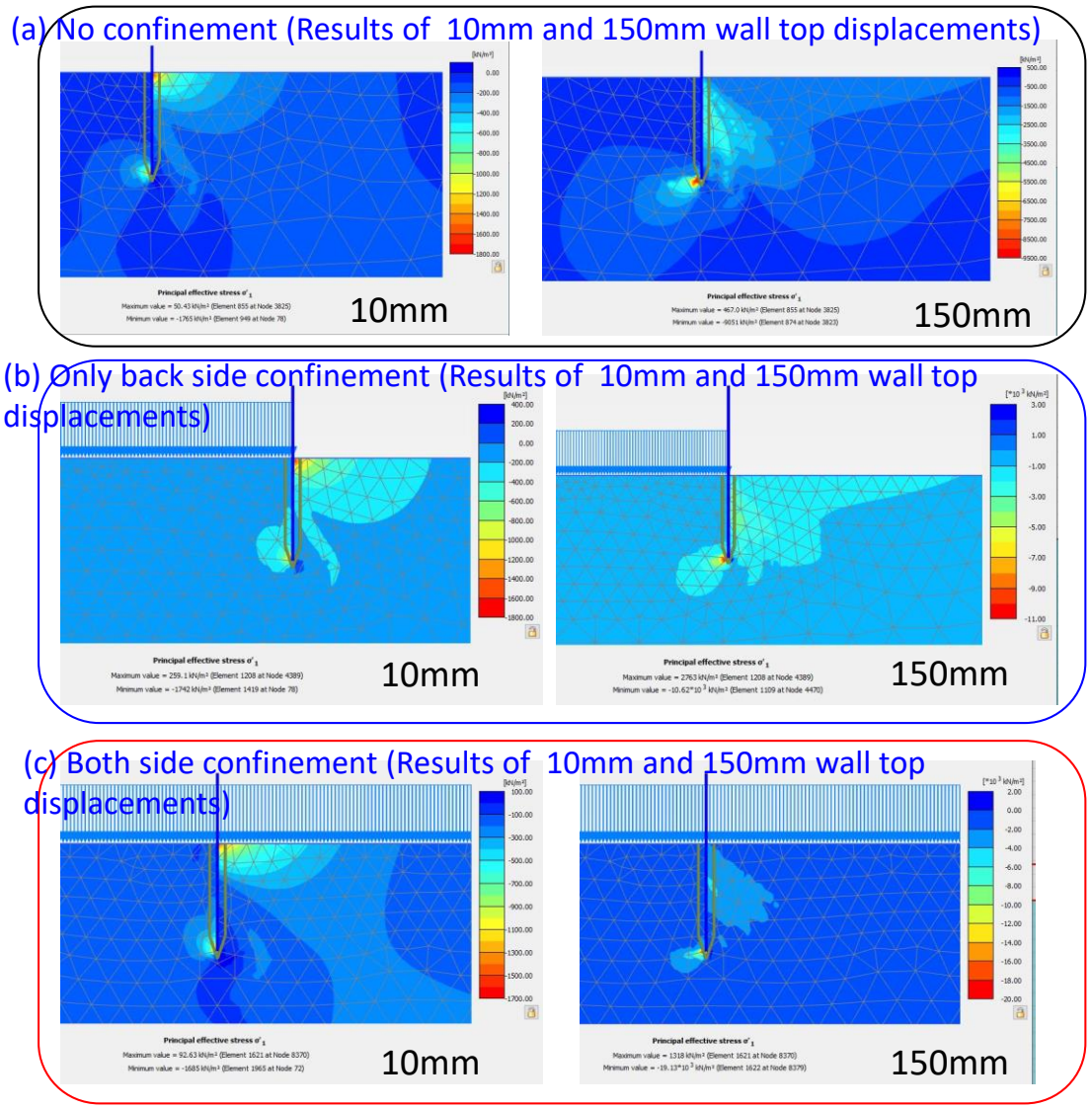

Figure 5.30 Observed passive pressure mobilizations at (a) 0 kPa and (b,c) 100kPa confining pressures

abovementioned three different scenarios as given in **Figure 5.30**. Comparing **Figure 5.30**(a) and **Figure 5.30**(b) at 10mm wall top displacement no significant difference in the mobilized pressures and the pattern of mobilization can be seen. However, at 150mm wall top displacement adding a surcharge pressure of 100kPa behind the wall highly increase the mobilized pressures on the shallow layers (about twice) and also expand the influence zone. Which could increase the possibility of wall front shallow layer failures in the case of one side surcharge loads similar to the retaining walls.

Mechanism behind the deformation and failure of wall models in Model-6 and Model-7 could be expresses referring to **Figure 5.30**(a) and **Figure 5.30**(c).Which are identical to the Model-6 and Model-7 respectively and the 100kPa confining pressure is representing a 6.5m layer of Toyoura sand with 80% relative density. From **Figure 5.30**(a) and **Figure 5.30**(c), at 10mm wall top displacement no significant difference in the mobilized pressures and the pattern of mobilization can be seen which could be attributed to the self-confinement of rock type materials at relatively small deformations. While comparing the pressure mobilization pattern at 150 mm wall top displacement, mobilization of large passive pressures in the wall front shallow layers (**Figure 5.30**(a)) are prevented in the case of wall with surcharge as shown in **Figure 5.30**(c). Furthermore, passive pressure mobilization took place at wall front deeper

location and the failure of shallow layers can be controlled which also helps to control the toe back shear failures or large deformations. This mechanism can be attribute to the observed deformation and failure of the walls in centrifuge Model-6 and Model-7.

5.6 Summary

At small displacement 1%Ø level no significant influence of embedment depth for the walls embedded in single rock layer can be observed, which indicates large lateral confinement and contribution of shallow layers of rock on the lateral resistance.

There is an optimum embedment depth from which the ultimate failure changes from ground failure to structural failure. From the observed ultimate failure conditions of single pile (structural failure) and tubular pile wall (shear wedge type failure) it can be concluded that the optimum embedment depth is deeper for the wall than single pile, which indicates that the rational embedment for cantilever tubular pile wall is larger than single pile with same cross section.

Based on observed system stiffness and residual deformations of tubular pile walls in single rock layer, an allowable wall top displacement of 1%Ø (20mm) and allowable maximum load of $0.3q_{ult}$ could be defined as the limiting values to prevent the plastic yielding or the failure of the walls embedded in single rock layer under the specific loading condition implemented in this study.

In the single pile loading and tubular pile wall loading tests, different failure modes were observed for the single pile (SP-SR-4) and tubular pile wall (RPW-SR-4) with the identical embedment (d_e=2Φ) and loading conditions in single rock layer. The former exhibited structural buckling and the latter was a clear wedge type ground failure. It reveals that the optimum embedment depth is deeper for the tubular pile wall than single pile, which indicates that the rational embedment for cantilever tubular pile wall is larger than single pile with same cross section.

In the case of wall model (RPW-SR-3) and single pile (SP-SR-3) with the embedment depth of 1.5Φ in single rock layer showed the ground failure as an ultimate failure condition as described in **Figure 5.12** (a). However, the normalized ultimate resistance for single pile is about 1.6times that of wall model and the wall model exhibited a clear wedge type ground failure, while the single pile showed more confined deformations. The difference in the observed ground failures as an ultimate condition for the single pile and wall model embedded in single rock layer is highly influenced by the wall or pile width and thereby the mobilized subgrade reaction.

Mechanism behind the difference in the ground failure of single pile and wall could be attributing to the 2-D and 3D boundary condition and associated influence zones. The influence zone, which contribute to the lateral resistance for a unit width of the wall is much narrower compare to an isolated single pile. This phenomenon causes an increased stress level or strain in the shallow layer of the rock and resulting significant reduction in subgrade reaction under same loading level. This mechanism causing large deflection of the wall compare to the condition of an isolated single pile. Due to the large deflection of the wall, eventual accumulation of wall deflection in the embedded zone, causing the deterioration of subgrade reaction along the wall embedded zone and eventually causing a wedge type ground failure at the ultimate resistance of the embedded medium. However, for the case of walls in two-layer profile, large passive pressure mobilization in the shallow rock layer is prevented due to the confining effect of overlain sand and the mobilized passive pressures in the sand layer. Also it shifts the zone of mobilization to deeper locations in the wall front as observed in the **Figure**

5.30(c). This mechanism helps to prevent the shallow rock layer failure as well as reduce the plastic deformations in the toe back passive zone as observed in **Figure 5.19**(b).

5.7 References

Ashour, M., Abbas, A.I. and Boskovic, S., 2019. Pile Cap Interaction with Bridge Pile Foundations under Lateral Loads. Journal of Bridge Engineering, 24(6), p.04019053.

Brinkgreve, R.B.J. and Broere, W., 2015. PLAXIS 2D Reference Manual 2015. *Delft, Netherlands2010*.

Brinkgreve RBJ, Broere W, Waterman D (2008) PLAXIS 2D-tutorial manual: Version 9.0, The Netherlands.

Randolph, M.F., 1981. The response of flexible piles to lateral loading. Geotechnique, 31(2), pp.247-259.

6 Dynamic Response of Cantilever Steel Tubular Pile Wall Embedded in Soft Rock by Centrifuge Modelling

6.1 Introduction

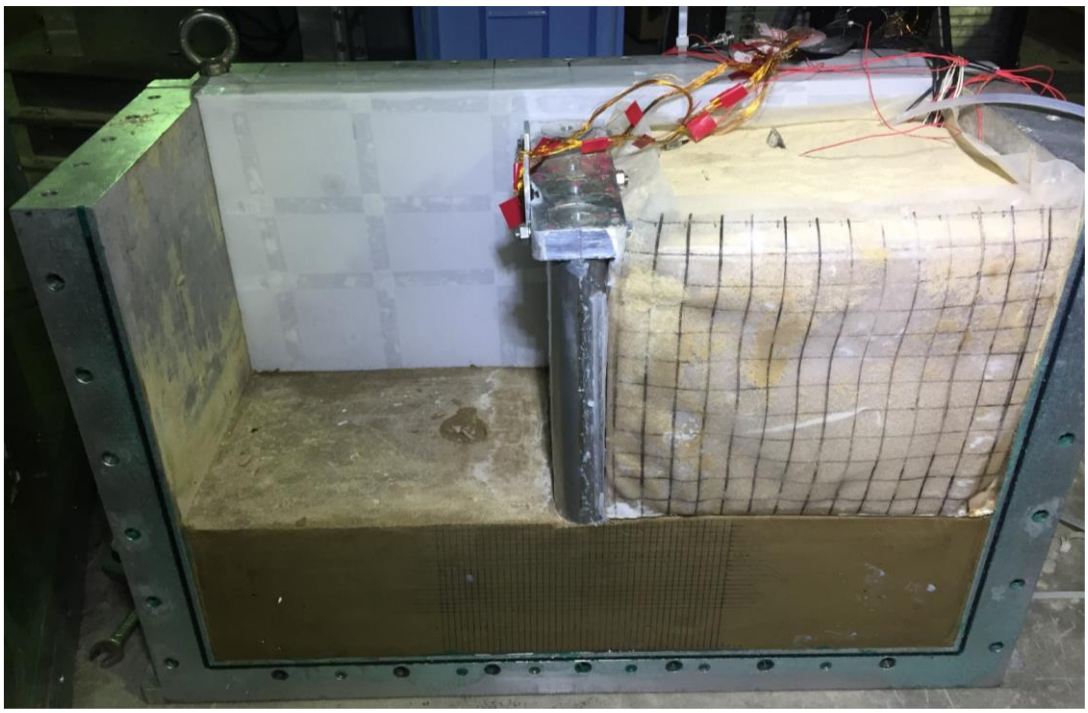

Figure 6.1 Cantilever steel tubular pile (CSTP) wall embedded in soft rock

Cantilever type retaining walls has several advantages. It can be constructed in very simple process in very narrow space, which is a common condition in highly populated urban area. However, when we call for a rationalized embedment depth, which is smaller than the current design method the risk against failure tend to increase. Therefore, it is essential to have an additional safety margin over the design and ultimate loads as well as against the unforeseeable embedment ground conditions (Such as, discontinuities, fissures and clay-filled joints in rock embedment) to ensure the safety and serviceability of the structure in its life span.

The major objective of this chapter is to understand the deformation and failure behavior of Cantilever type Steel Tubular Pile walls (CSTP) under different levels of dynamic excitations, which vary from lower to high hazard level under two different back fill conditions, that is the dry granular backfill and the partially submerged backfill. These two backfill conditions could be expected during the life span of the structure depending on the drainage conditions as well as the % of fine particles present in the backfill. The outcomes from this study could provide useful information to improve the rationalized design method and to ensure the reliability of new design method.

6.2 Earth pressure theories related to dynamic behavior of retaining walls

6.2.1 Mononobe-Okabe Theory for dry back fill

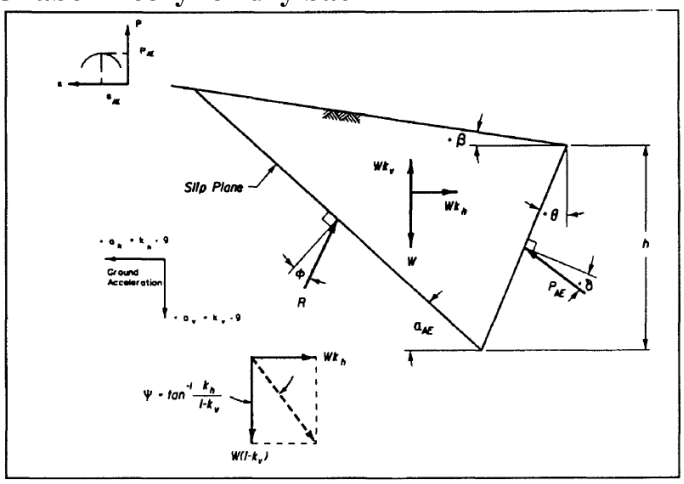

Figure 6.2 Mononobe-Okabe (active) wedge (Ebeling and morrison1993)

Mononobe-Okabe theory provides a combined solution to estimate the total earth pressure acting on a retaining structure during seismic excitations. Total in the sense the addition of the static active pressures as well as the dynamic earth pressure caused by the backfill soil acceleration. The dynamic active pressure **force** acting on the wall based on Mononobe-Okabe method is described by Ebeling and Morrison, (1993) as shown in Equation 6.1. In which

$$P_{AE} = 0.5K_{AE}[(1 - k_v)\gamma_t]H^2 \quad \text{..... Equation 6.1}$$

$K_{AE} =$ Dynamic active earth pressure coefficient

$k_v =$ vertical seismic coefficient

$\gamma_t =$ Total unit weight

$H = Wall\ Height$

$$K_{AE} = \frac{cos^2(\emptyset - \varphi - \theta)}{cos^2\theta cos\varphi cos(\varphi+\theta+\delta)\left[1+\sqrt{\frac{sin(\emptyset+\delta)sin(\emptyset-\varphi-\beta)}{cos(\delta+\varphi+\theta)\cos(\beta-\theta)}}\right]^2} \quad \text{..... Equation 6.2}$$

The dynamic active earth pressure coefficient for a wall with the inclined back face (θ) and a sloping backfill having an angle β to the horizontal as described in Figure 6.2 is given in Equation 6.2. In which

$$\varphi = Seismic\ inertia\ angle\ given\ by\ \left[\varphi = tan^{-1}\left[\frac{k_h}{(1-k_v)}\right]\right]$$

$\emptyset = Friction\ angle\ of\ soil$

$k_h = horizontal\ seismic\ coefficient\ (a * g)$

$\delta = An\ angle\ at\ which\ the\ resultant\ force\ P_{AE}\ acting\ from\ the\ normal\ to\ the\ wall$

The Equation 6.2 can further be simplified for a vertical wall and level backfill as described in Equation 6.3.

$$K_{AE} = \frac{\cos^2(\emptyset-\varphi)}{\cos\varphi\cos(\varphi+\delta)\left[1+\sqrt{\frac{\sin(\emptyset+\delta)\sin(\emptyset-\varphi)}{\cos(\delta+\varphi)}}\right]^2}$$ …….. Equation 6.3

According to Ebeling and Morrison, (1993), the Mononobe-Okabe (M-O) theory did not explain the point of action of this resultant force on the wall. However based on the analysis of **M-O method, Kramer, (1996) indicates that the total active thrust should act at a point H/3 above the wall base**. This analytical outcome contradict with the experiment al observations. According to Kramer, (1996), Seed and Whitman (1970) recommended the point of action at 0.6H from the wall base. Based on Ebeling and Morrison, (1993), analytical studies conducted by Prakash and Basavanna (1969) and some model wall tests conducted by other researchers indicates that the point of actin entirely depends on the wall movement and the mode at which it occurs. From these limited number of experiments they indicated that the point of action varies from 0.4 to 0.55 times the wall height from the base of the wall. The variation of the point of action with horizontal seismic coefficient based on Prakash and Basavanna (1969) is described in Figure 6.3.

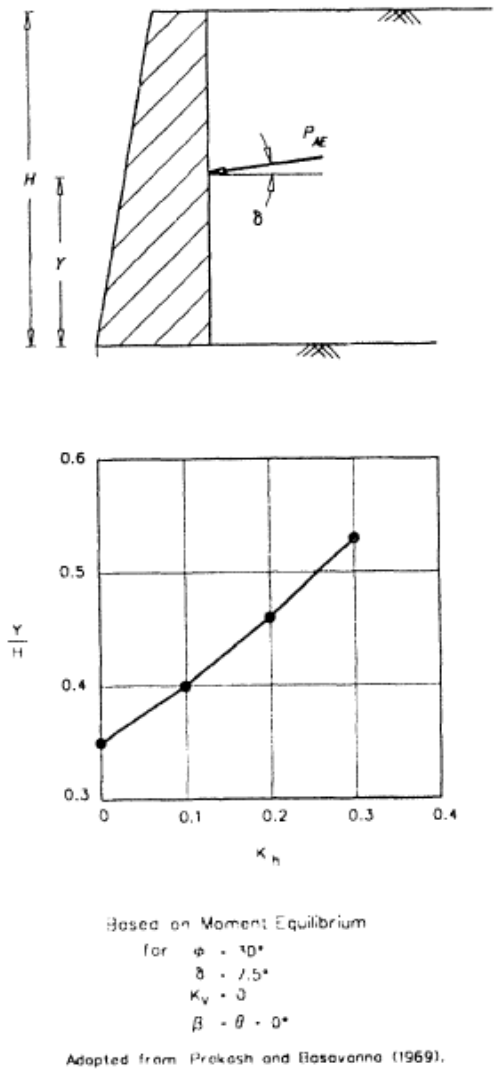

Adopted from Prakash and Basavanna (1969).

Figure 6.3 Point of action of resultant force by Prakash and Basavanna (1969) (From Ebeling and Morrison, (1993))

6.2.2 Application of M-O theory for submerged backfills- Restrained water case

For a submerged backfill condition, based on the assumption of pore water pressures does not vary due to the horizontal accelerations, Matsuzawa et al., (1985) describe the method to estimate the dynamic earth pressures. In which they considered a Coulomb active wedge, while subtracting the static pore water pressures the horizontal inertia force is proportional to the $\gamma_t k_h$ and the vertical force is proportional to the buoyant unit weight γ_b of the backfill soil when the vertical acceleration is absence.

In this method the seismic inertia angle is given by Equation 6.4.

$$\left[\varphi = tan^{-1}\left[\frac{\gamma_t k_h}{\gamma_b}\right]\right] \quad \text{..... Equation 6.4}$$

Where the equivalent horizontal seismic coefficient k_{he} is:

$$\left[k_{he} = \frac{\gamma_t k_h}{\gamma_b}\right]$$

Using the equivalent seismic coefficient k_{he} on M-O theory (Equation 6.1 and 6.2) together with the buoyant unit weight γ_b for the submerged zone will give dynamic active earth pressure force P_{AE} in which the static component of the earth pressure must be added separately as described in **Figure 6.4**.

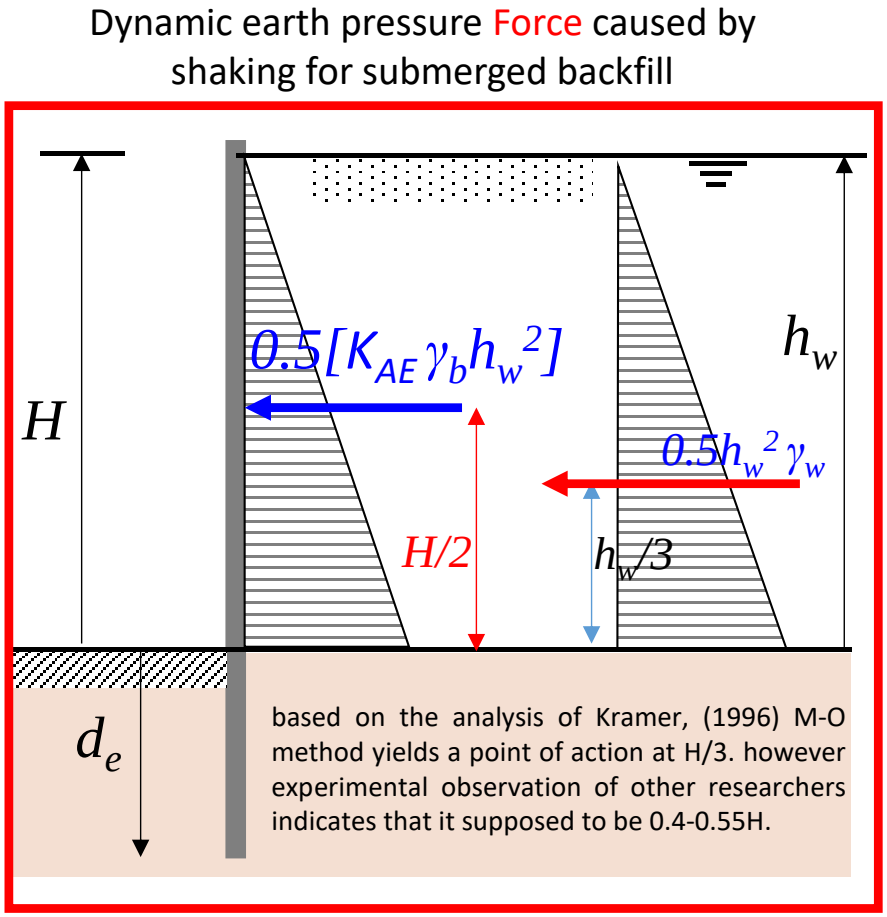

Figure 6.4 Application of M-O theory for submerged backfill- restrained water case

6.2.3 Japanese Road Bridge (JRB) Standard approach for dry back fill

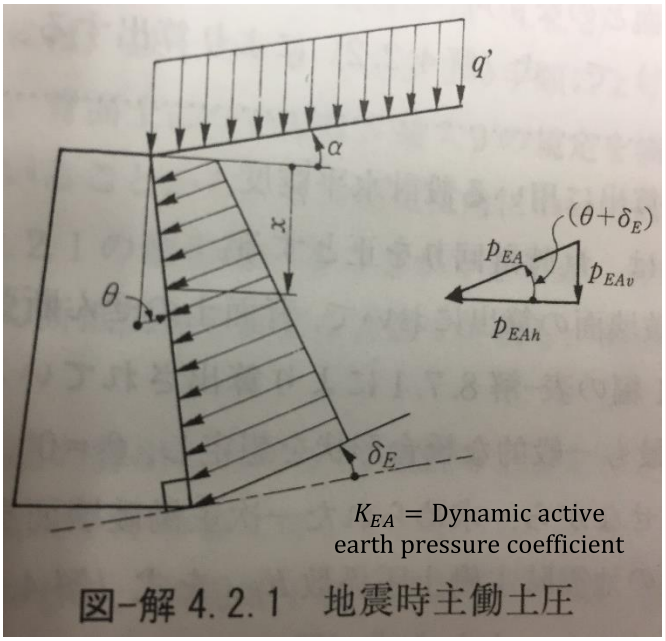

$P_{EA} = \gamma \mathcal{X} K_{EA} + q' K_{EA}$ $K_{EA} = 0.21 + 0.9 k_h$

k_h = Input acceleration γ = Dry unit weight

Specifications for highway bridges (Japan)
Part:5 Seismic design (Chapter-4)

Figure 6.5 JRB approach for the estimation of dynamic active earth pressure

JRB standard approach for the estimation of dynamic active earth pressures on a retaining wall experiencing certain amount of surcharge load is described in **Figure 6.5**.Where the variation of dynamic earth pressure from the wall top to a point of interest at a depth χ is given as described in Equation 6.5.

$$P_{EA} = \gamma \mathcal{X} K_{EA} + q' K_{EA} \quad \text{..... Equation 6.5}$$

Where K_{EA} is the dynamic active earth pressure coefficient as described in Equation 6.6 and Equation 6.7 for a soil- concrete interface.

$$K_{EA} = 0.21 + 0.9 k_h \quad \text{..... Equation 6.6 (for pure sand backfill)}$$

$$K_{EA} = 0.24 + 1.08 k_h \quad \text{..... Equation 6.7 (Sand with fine particles (clay))}$$

It is important to emphasize that the k_h in Equation 6.6 and 6.7 is not the back fill soil acceleration but the peak input acceleration. Based on Equation 6.6, Equation 6.7 it can be observed that, the JRB method consider the full active or closer to the active condition behind the wall, however at relatively small wall movements and the case of densification of backfill by seismic excitations it might underestimate the dynamic earth pressures acting on a retaining wall. In this method the point of action of the earth pressures is similar to that of static conditions at H/3.

6.2.4 Westergaard Solution for hydrodynamic pressure

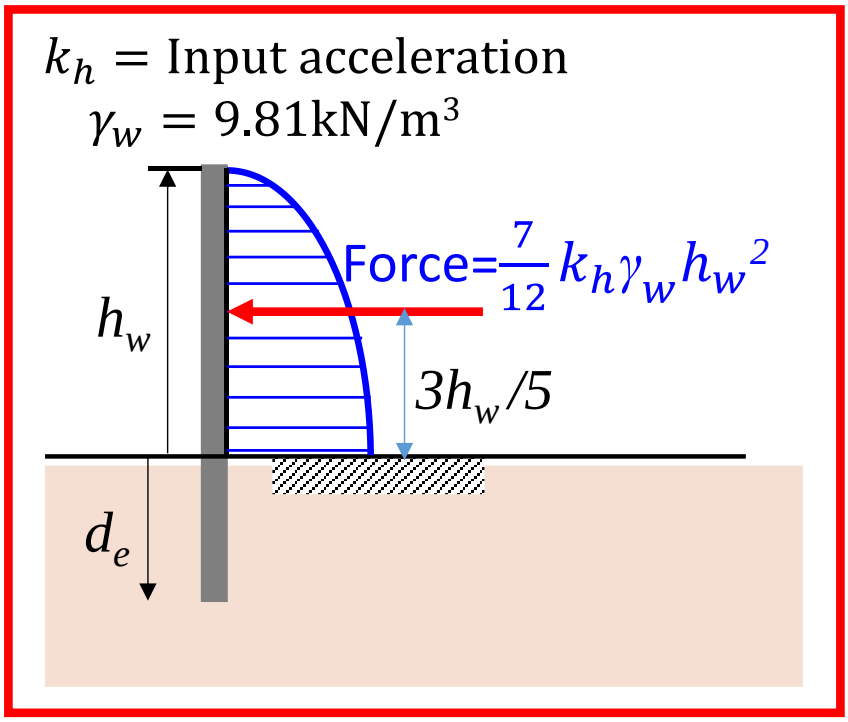

Figure 6.6 Westergaard method for the hydrodynamic pressure

Hydro dynamic pressures entirely governed by the dynamic response of the water column in the backfill. As described in Kramer, (1996), it is often estimate based on Westergaard method in which the hydrodynamic pressure amplitude increases with the square root of water depth as described in Equation6.8, when the frequency of a harmonic input motion at the rigid base of a dam is smaller than the fundamental frequency of the reservoir.

Fundamental frequency (f_0) of the reservoir is given by $f_0=v_p/4H$ where v_p is the P-wave velocity of water, which is typically about1400m/sec. H is the water height in the reservoir. For a 12 m water height computed natural frequency of the reservoir is about 29Hz which is much larger than the frequency of seismic excitations.

Amplitude of hydro dynamic pressure is:

$$p_w = \frac{7}{8}\frac{a_h}{g}\gamma_w\sqrt{Hz_w} \quad \text{..... Equation 6.8}$$

Resultant hydrodynamic thrust force can be computed as:

$$P_w = \frac{7}{12}\frac{a_h}{g}\gamma_w H^2 \quad \text{..... Equation 6.9}$$

a_h is peak input acceleration at the rigid base of the reservoir.

Point of action of resultant force is given by **3H/5** from the rigid base of the reservoir.

6.2.5 Combined method in this thesis

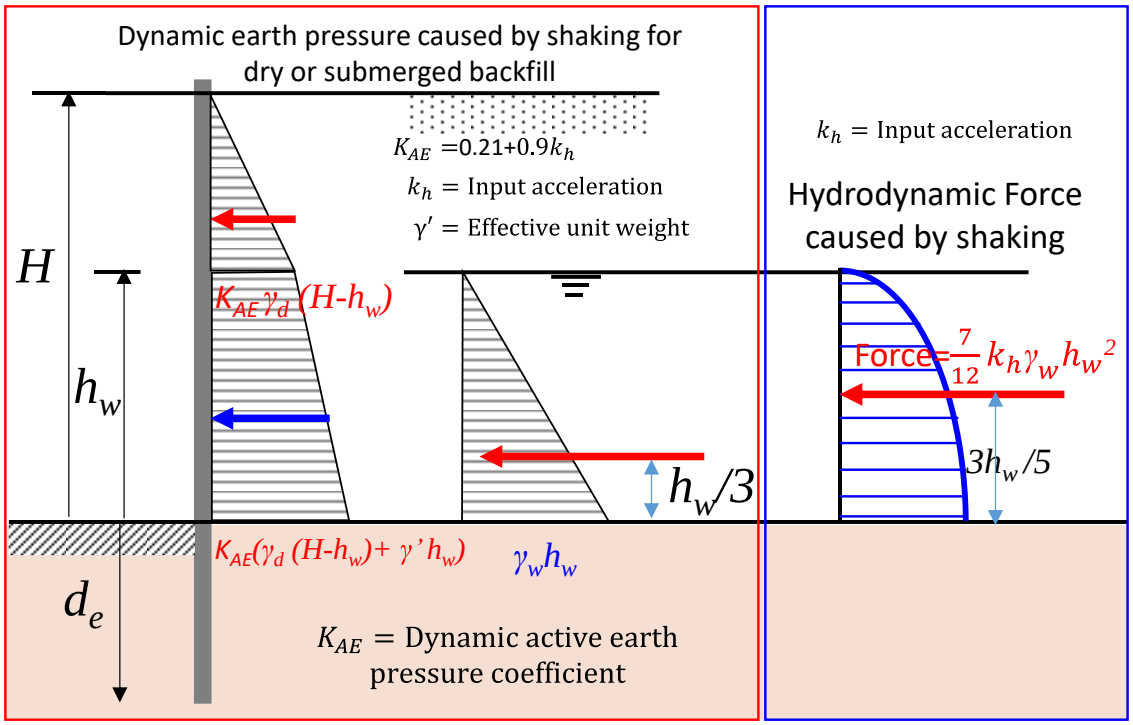

Figure 6.7 Combined JRB and Westergaard method

A combined method of JRB method with the theory of Westergaard used in this thesis to estimate the dynamic earth pressures caused by a partially submerge backfill as describe in **Figure 6.7**. The pressure distributions and forces cause by the dry backfill also can be computed simply replacing the water height as zero. Or else the descriptions given chapter 6.2.3.In this method also the point of action was considered as acting at the centre of gravity of dry and submerged stress polygons as shown in **Figure 6.7**.

6.3 Modelling concept and target structure

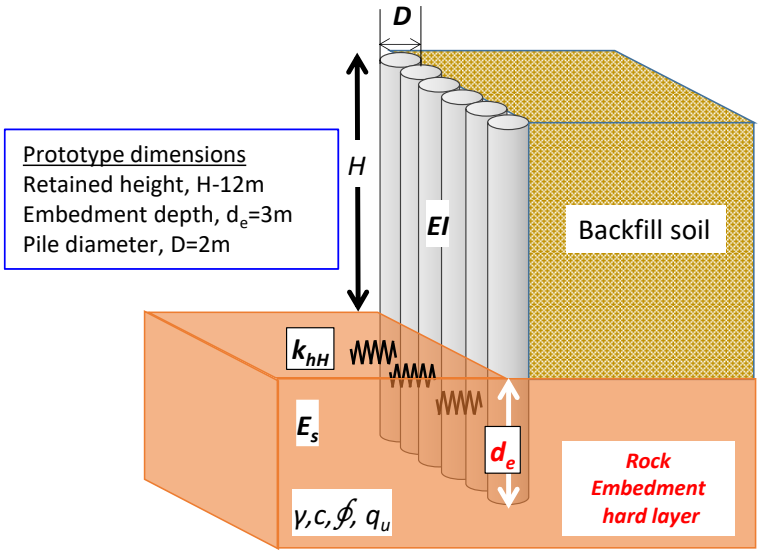

Figure 6.8 Specific prototype or Target structure

Main intention of this model study is to investigate the dynamic stability of a steel tubular pile wall embedded in soft rock with relatively small embedment depth than the current design method and observe the deformation and failure behaviors. The model tubular pile wall represent a specific prototype of 12 m retained height and 3m embedment depth in to a soft rock ground as described in **Figure 6.8**. The prototype pile diameter is 2 m as the experiment planned at 50g centrifugal acceleration.

In this modelling also two different loading conditions were considered as implemented in the chapter-3. That is the dry backfill condition and submerged backfill with the help of rubber membrane bag. The reason for the use of rubber bags are clearly mentioned in the chapter 3.3.2, by which the applied lateral loads on the wall can be increased up to 2.5 times that of dry backfill condition by means of water feeding technique. Thanks to the rubber membrane bags used in this study which helps to make a closed water boundary in the model and also create large lateral thrust.

6.3.1 Challenges in the modelling

Although several challenges had to be untangled in the modelling process of this experiment the major problem which we encounter between chapter-3 and this chapter is the transmission of shear stresses in the interface between the rock surface and backside rubber bag, which function as a closed boundary to prevent the water leakage and the contact between rock surface and water.

The use of same latex rubber bag could absorb the input energy and behave as a kind of base isolator between the backfill and the rock surface therefore input accelerations could not be effectively transmitted throughout the back fill soil and which could yield more or less a non-realistic simulation compare to the real filed. Therefore in order to effectively transmit the input accelerations we designed the rubber membrane bag using a carbon fibre base (PZ-564 real carbon: **Figure 6.9**) at the interface between soil and rock which is also a water tight membrane but quite stiffer compare to the latex rubber.

Figure 6.9 Utilized carbon fibre base for the rubber bag

6.3.2 Used materials and methods

In the centrifuge model a cantilever steel tubular pile wall was embedded in artificially made soft rock. The wall was placed throughout the reduced breadth of the container. The model container had the original internal dimensions of 600 mm in length 250 mm in breadth and 400 mm in depth as shown in **Figure 6.10**. The container was made up of a removable rear-side aluminium wall and a front-side transparent thick acrylic wall and an aluminium hollow frame to stiffen the acrylic. Both wall plates were bolted with the main container body to form a rigid box. In order to secure the plane strain conditions and to model maximum possible width of the wall (max of 5 piles) as shown in **Figure 6.12** , the breadth of the container was shorten using a lateral acrylic spacer given in **Figure 6.11**, on the inner face of back face panel. The acrylic spacer was formed using three acrylic plates having the thicknesses of 20mm, 10mm and 3mm. A 33mm thick acrylic spacer was made with the help of these plates and acrylic sand adhesive to have a face to face connection of plates. Up on forming the 33mm acrylic spacer, eight access holes (**Figure 6.11**) were made on the spacer to fix the spacer and the back face of the container by means of bolts, so that the spacer would work as a rigid back face of the container during seismic excitations. The model container had the bottom porous stones to facilitate the drainage conditions therefore, prior to the casting of unsolidified rock mix the porous stones were covered by two layers of adhesive tapes to ensure a clear isolation from the contact of rock mix.

The soft rock model was prepared in a model container, which had the internal dimensions of 600 mm in length 217 mm in breadth and 400 mm in depth. Unsolidified soft rock material was casted in the container. Prior to the casting, 0.5 mm thick Teflon sheets were pasted in the front and rear internal container wall faces and lubricated by silicon grease for easy detachment of wall from the hardened soft rock ground. The soft rock ground was then constructed by compacting the sand-clay-cement mixture layer by layer every 30 mm thickness, up to the final height of the planned rock layer. The density of compacted mixture was carefully controlled by the volume of each compacted layer and the required mass of the mixture for the layer.

6.3.2.1 Model container

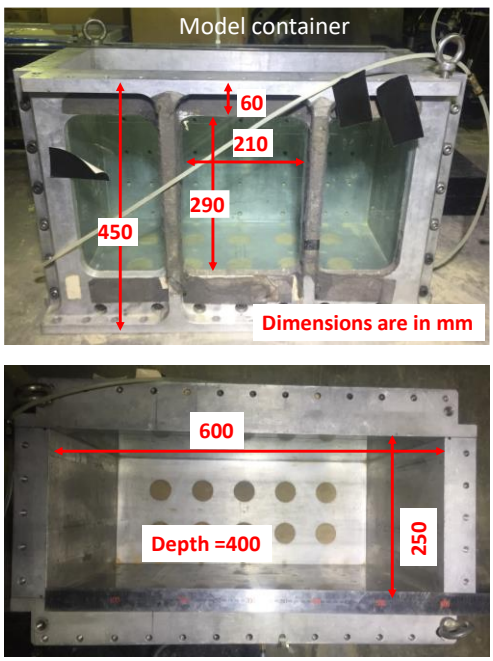

Figure 6.10 Utilized model container

6.3.2.2 Acrylic spacer with connecting bolts

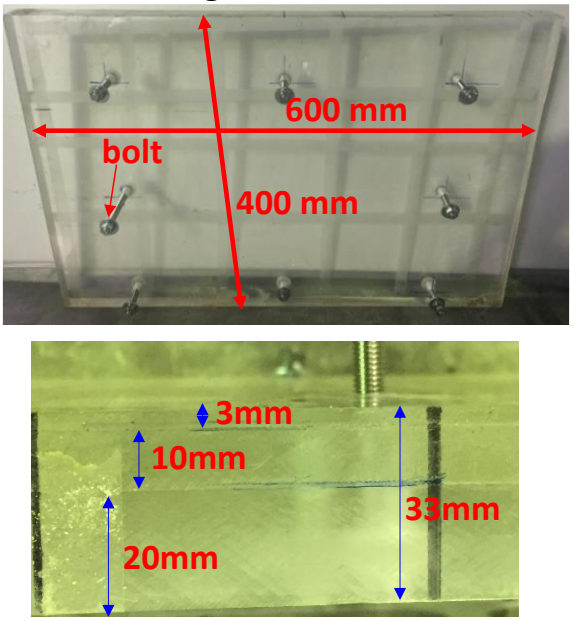

Figure 6.11 Merged acrylic plates to form 33mm thickness acrylic spacer

After that, the model steel tubular pile wall was installed upright at the centre of container up to the desired embedment depth with the help of two water levels and 1mm thick spaces in the front and rear side of the pile cap to ensure the spacing between the pile and container faces. Meanwhile the exact location of the wall and verticality was confirmed by means of previously installed lateral guide. It is important to emphasize that, with the installation of tubular pile wall the compacted rock was plugged inside the tubular piles up to the embedment level. Upon model wall installation, the unsolidified soft rock material surface was covered by wet towels and conserved under room temperature for curing. The locations of tubular pile wall and the acrylic spacer in the container are shown in **Figure 6.13**.

6.3.2.3 Model pile wall

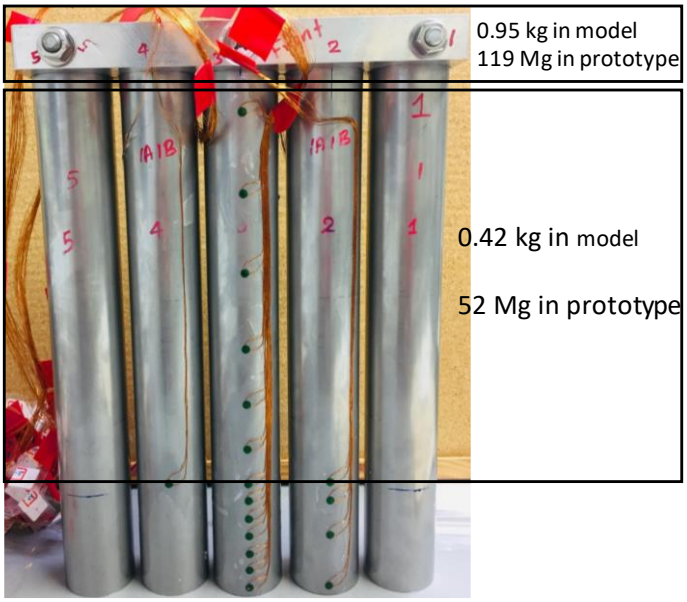

Figure 6.12 Strain gauge instrumented model tubular pile wall

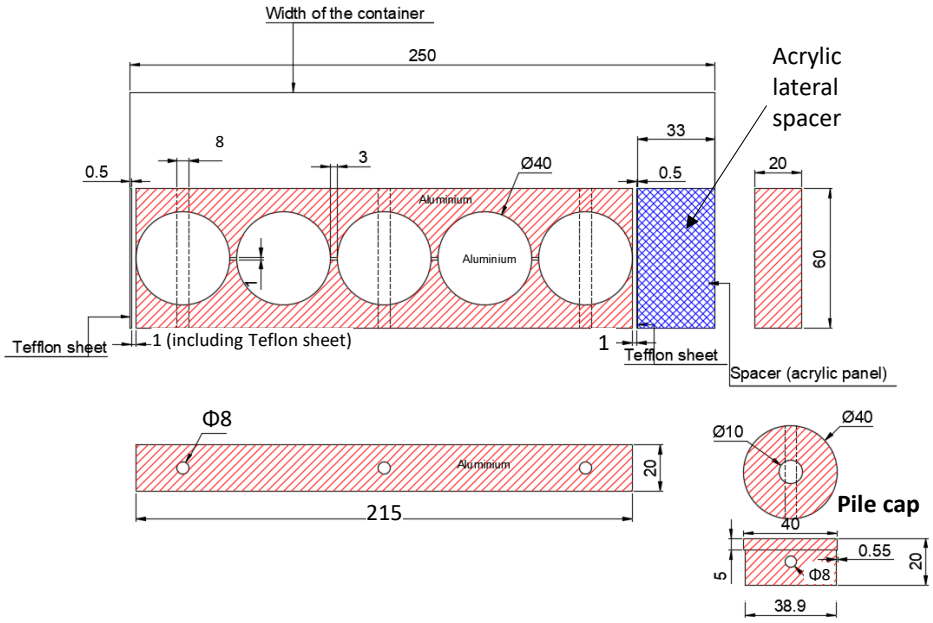

Figure 6.13 Location of wall in the container and the cap arrangements

6.3.2.4 Strain gauge arrangement and the list of sensors

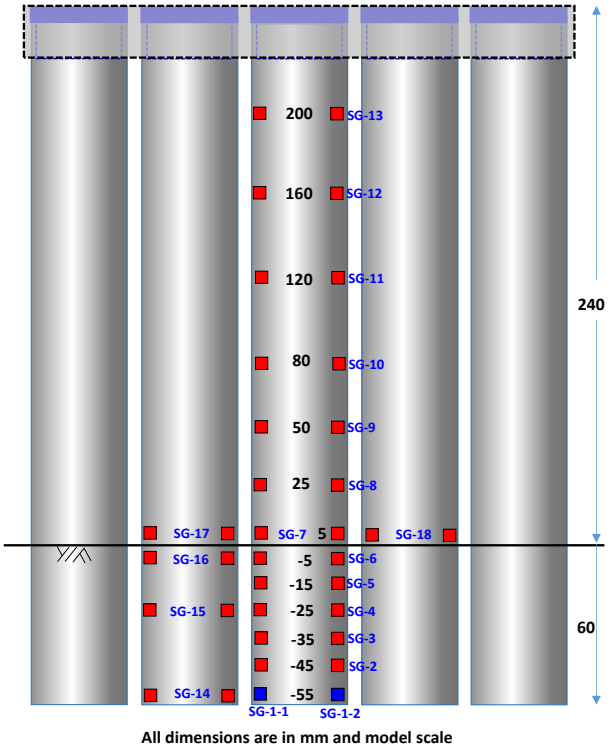

Figure 6.14 Location of wall in the container and the cap arrangements

Table 6-1 Locations of accelerometers in the model

Sensor (accelerometer)	Notation	Location
Acc-1	2980	Outside of container centre to measure the input acceleration for first channel box
Acc-2	2722	Outside of container bag side to measure the input acceleration for second channel box
Acc-3	2982	At rock surface below the bag
Acc-4 (Soil bottom)	2984	Inside bag 15mm from ground level and 50mm from wall
Acc-5 (Soil mid)	2983	Inside bag 115mm from ground level and 50mm from wall
Acc-6 (Soil top)	2987	Inside bag 215mm from ground level and 50mm from wall
Acc-7 (Wall bottom)	2985	On the wall 15mm from rock surface
Acc-8 (Wall mid)	2953	On the wall 115mm from ground
Acc-9 (Wall top)	2957	On top of the wall
Acc-10	2981	At rock surface in front of wall

Table 6-2 Location of earth pressure cells in the backfill sand

Sensor (Earth pressure)	Notation	Location
EP-1	PS2-1	Inside bag at 35mm from wall and 15mm from ground level (Capacity=200kPa)
EP-2	PS2-2	Inside bag at 35mm from wall and65mm from ground level (Capacity=200kPa)
EP-3	PS1-7	Inside bag at 35mm from wall and115mm from ground level (Capacity=100kPa)
EP-4	PS1-1	Inside bag at 35mm from wall and165mm from ground level (Capacity=100kPa)
EP-5	PS1-8	Inside bag at 35mm from wall and215mm from ground level (Capacity=100kPa)

Table 6-3 Location of PPT in the backfill

Sensor (PPT)	Notation	Location
PPT-1	P1	Inside bag at 80mm from wall and ground level
PPT-2	P4	Inside bag at170mm from wall and ground level
PPT-3	N60	Inside bag at 80mm from wall and 115mm from ground level
PPT-4	N61	Inside bag at 80mm from wall and 215mm from ground level

6.3.2.5 Model condition and sensor arrangement

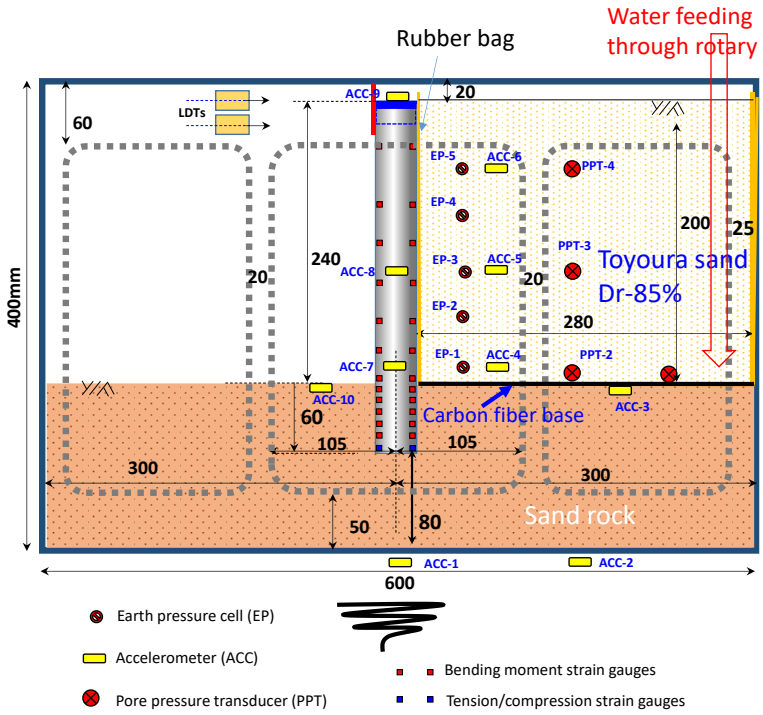

Figure 6.15 Model arrangement and location of sensors

6.3.3 Model preparation process

After 14 days curing time the front wall was detached as shown in **Figure 6.16**(a), and the rear wall also detached. The Teflon sheet on the rear wall was replaced by a new one and lubricated with grease to minimize the friction. At the front side of the model soft rock, 5 mm square grids were drawn to visualize the ground deformation and then transparent silicon grease was smeared before attaching the front wall. The backfill sand was modelled inside an open latex rubber box having the height of 260mm as shown in **Figure 6.16**(e, f) and **Figure 6.17**. The rubber bag consists of two different materials, the bottom face was a carbon fibre and vertical faces were a single piece of latex rubber membrane. The connection between latex-latex and latex-carbon fibre interfaces were made using white silicone rubber given in **Figure 6.18**(b) which function as an adhesive and prevent the water leakage. Prior to the installation of rubber bag in the centrifuge model the inner and outer faces of the bottom carbon fibre base was coated with

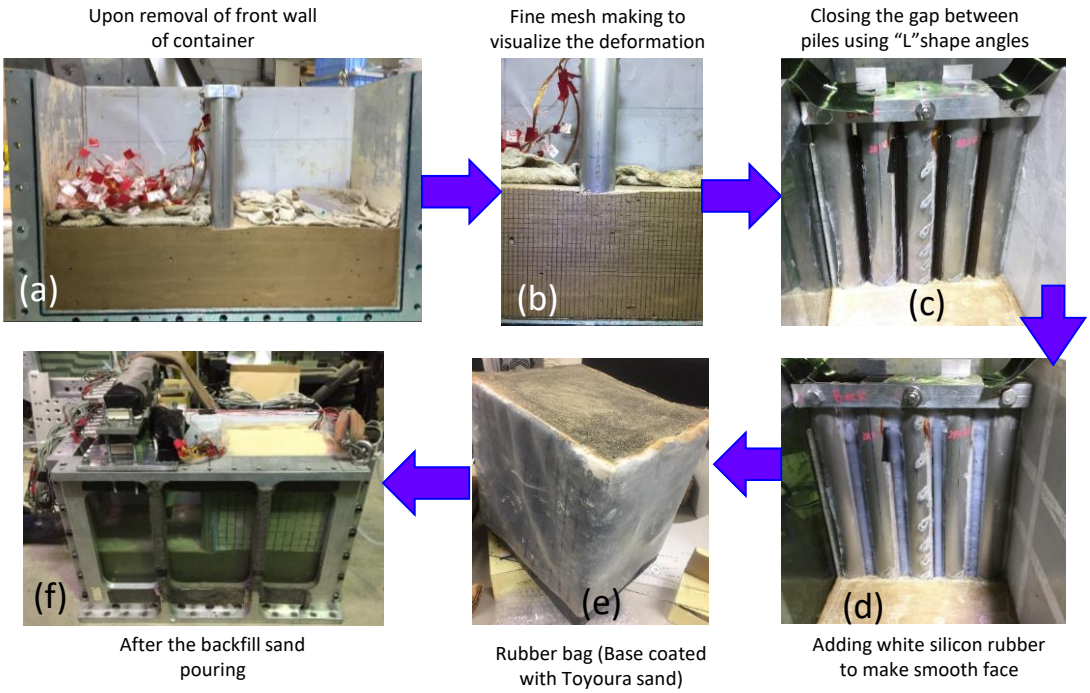

Figure 6.16 Model preparation (Only major steps)

Toyoura sand using an adhesive shown in **Figure 6.18**(a).The purpose of coating the base of rubber bag is to transmit the accelerations throughout this fibre from underlain rock layer. In order to prevent the damage of latex membrane during the g-up process and dynamic excitations, the curved space and 3mm gap between the tubular piles were closed using aluminium "L-Shape" angle having the dimensions of 10mm x 10mm and thickness of 0.5mm as described in **Figure 6.16**(c). The sharp edges as well as the Inner space of "L-angle" was coated with a transparent silicone adhesive, which helps to make more or less a uniform face in the wall back face as shown in **Figure 6.18**(d). Up on curing of the transparent silicone coating, the accelerometer on the rock surface was installed. After that the rubber bag was placed behind the wall and with lubricated outer faces of latex membrane and the inner face of the container. Thereon all four upper edges of the rubber bag was covered using adhesive tapes to prevent the intrusion of sand between bag-wall as well as the bag-container interfaces. Thereon the PPTs to measure the pore water pressure at the bottom soil layer and the water feeding pipe were installed inside the bag and 240mm thick dry Toyoura sand with 80% relative density was made in the box using a sand hopper as shown in **Figure 6.18**(f). Meanwhile the other sensors to measure the acceleration, earth pressure and pore water pressure also were installed at predefined locations as indicated in the model arrangement given in **Figure 6.15**.The exact locations of strain gauges on the wall and other sensors are described in **Figure 6.14**, **Table 6-1**, **Table 6-2** and **Table 6-3** respectively.

Detail mechanical properties of Toyoura sand are described in (Fukushima and Tatsuoka,1984; Tatsuoka et al., 1986). The friction angle ϕ =40° is assumed to calculate as-rest and active earth pressure coefficient in this study. The rubber box was made from latex rubber thin sheets (t=0.5mm) with higher flexibility and tear resistance, which creates friction less condition on the contact to the wall and rock surface. Although the situation of the loading process by feeding the water into the sand contained in the box is not a realistic case, it can create a clear

loading condition on the wall and rock surface without causing complexity or difficulty, such as the excess pore water pressure in the rock and water leakage from the side of the wall.

Accelerometers on the wall and the rock surface was installed with the help of "Scotch adhesive". Up on completion of the centrifuge model arrangement, the model was transferred to the shaking table mounted on centrifuge platform and water feeding path through the rotary joints was made with the help of solenoid valve as shown in **Figure 6.19**. Two pairs of "short range (3-5cm)" laser displacement transducers (LDTs) and a series of potentiometers (three) were also equipped to track the lateral movement, rotation of the wall top and to monitor the surface settlements of the retained sand respectively.

6.3.3.1 Sand bag

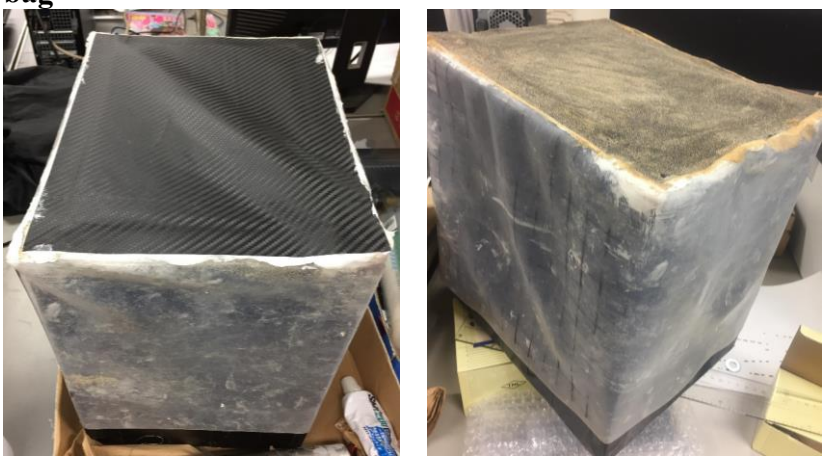

(a) (b)

Figure 6.17 Utilized rubber bag (a) before and (b) after the sand coating at the outer face of carbon fibre base

6.3.3.2 Used adhesives

Figure 6.18 Utilized adhesives for (a) sand coating on the carbon fibre base and (b) to connect the carbon fibre and latex rubber at the base of the bag

6.3.3.3 Completed model for testing and water feeding system

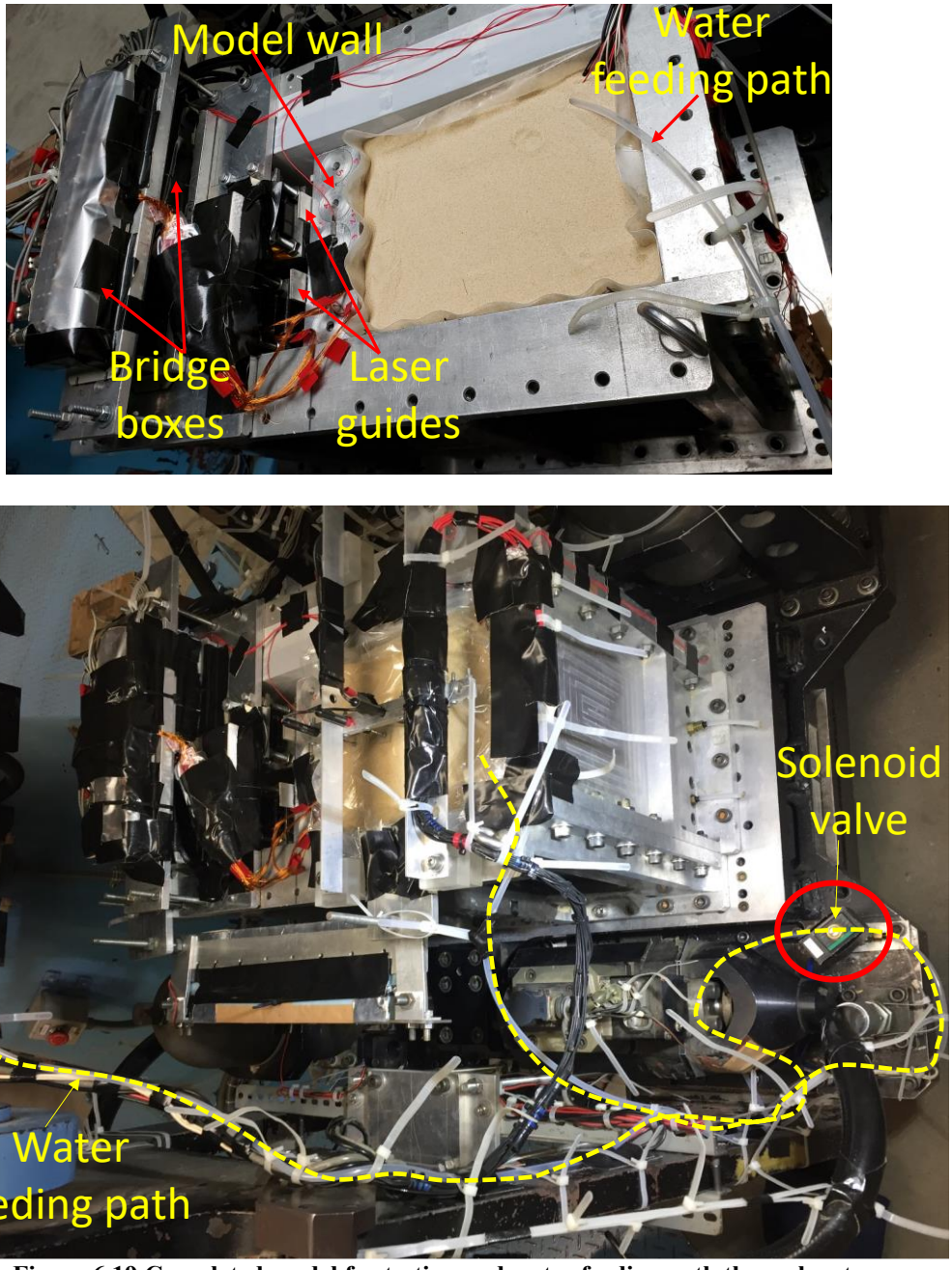

Figure 6.19 Completed model for testing and water feeding path through rotary

6.3.4 Target loading conditions

In this study two different loading conditions on a stable wall was considered as shown in the **Figure 6.20**. Similar loading in the **Figure 6.20** (a) could be expected in real filed if the back fill is a granular material and the drainage behind the wall function very well. However, in cases where the backfill material contains certain % of fines, accumulation of water table behind the wall has higher possibility due to the low permeability or the clogging of fine particle s in the drainage layer. In such situations relatively large lateral and moment loads could be act on the wall. Considering these two scenarios during an earthquake event the dynamic stability of a steel tubular pile wall was studied and reported in this chapter.

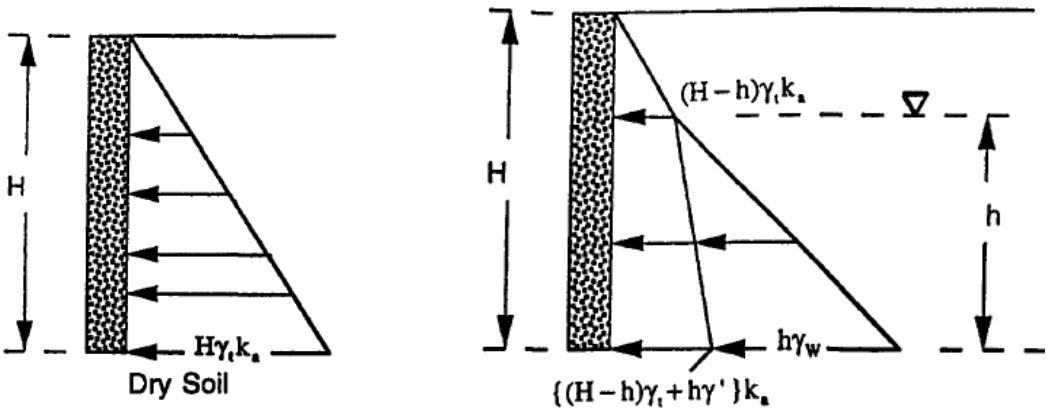

Figure 6.20 Target loading conditions (a) Dry backfill (b) Submerged backfill

6.3.5 Applied ground motion and loading sequence

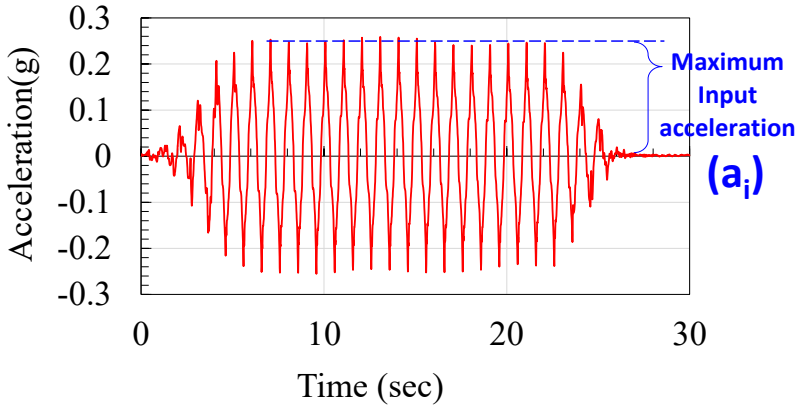

Figure 6.21 Typical input motion applied in centrifuge

The behavior of Steel tubular pile walls embedded in soft rock was investigated under a sinusoidal harmonic excitation. A typical input motion is illustrate in **Figure 6.21** where the maximum input acceleration is defined as a_i. Sequence of applied ground motions and corresponding a_i values under dry and submerged backfill conditions are shown in **Figure 6.22**. In the loading sequence of this experiment initially the behavior of rock wall system was studied under white noise-1 (WN-1).White noise characteristics are describe in 0. From the preliminary analysis of the wall top response it was found that the wall exhibited about 5Hz as its natural frequency. With this confirmation about the natural frequency, the behavior of wall was studied under a sinusoidal harmonic motion having the frequency of 1Hz in prototype scale, which is much smaller than the natural frequency of the wall. It is important to emphasize that, main objective of this study is to understand the dynamic characteristics of the wall and evaluate the performance with the increasing dynamic loads. Studying the wall under a large ground motion is out of the scope of this study. In the dynamic loading process, upon recording the characteristics of wall in WN-1, the wall behavior was studied under 5 subsequent sinusoidal motions with increasing input accelerations as described in **Figure 6.22**(a). After that WN-2 was introduced to study the changes in the dynamic characteristics of wall during first 5 input motions under dry backfill condition. With certain induced residual displacements in the first series of shaking, consequently to study the deformation characteristics of the wall under submerged backfill condition, water was fed up to 9 m behind the wall and the wall

behavior was recorded. Thereon the third WN was introduced to ensure the influence of water feeding process on the dynamic behavior of wall. Thereafter the second series of input motions under submerged back fill was introduced as described in **Figure 6.22**(b).Upon completion of second series the final white noise motion (WN-4) was applied and the water level behind the wall was further increase up to 10m and final input motion with the peak input acceleration of 0.6g was applied.

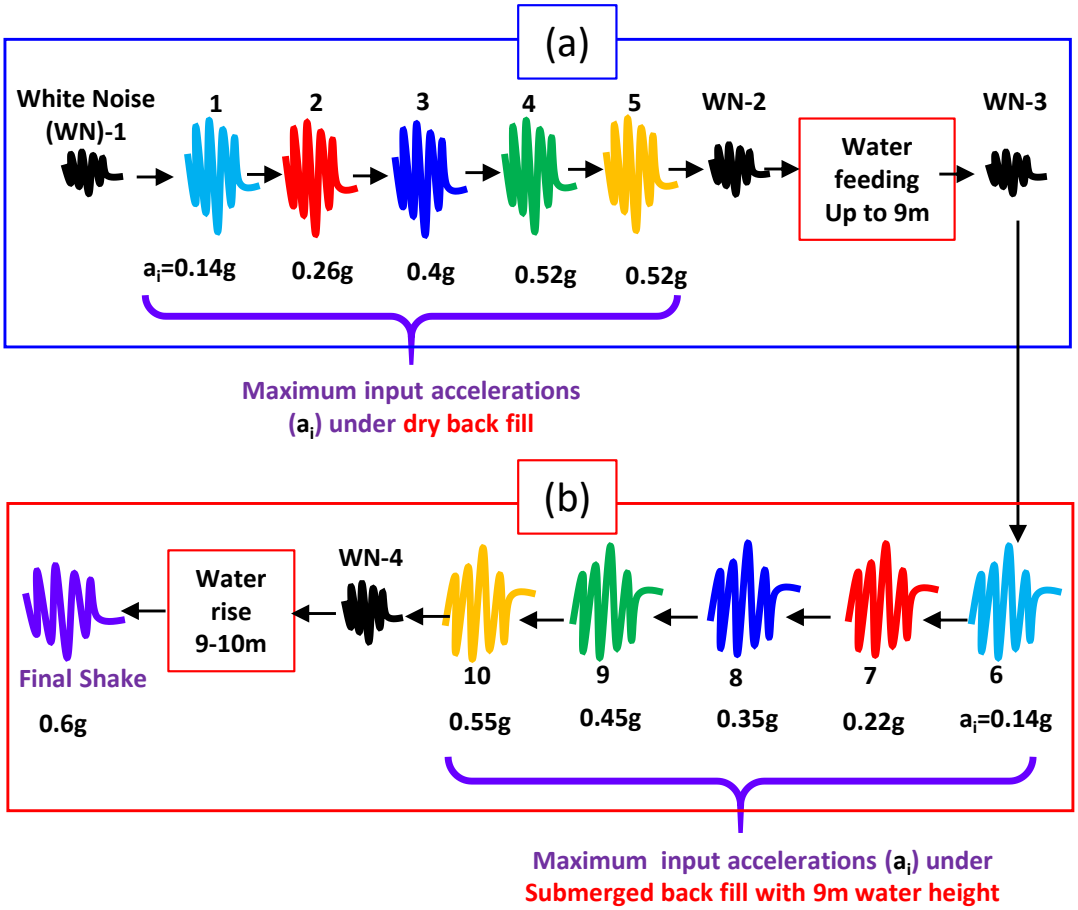

Figure 6.22 Loading sequence under (a) dry backfill and (b) submerged backfill

6.3.6 Initial conditions for dry and submerged backfill

6.3.6.1 G-up process from 1g to 50g

Wall behavior during g-up process from 1g to 50g is described in terms of measured bending profiles at each 10g gravity increments in **Figure 6.23**. Corresponding mobilized earth pressure behind the wall and the wall top displacement and rotation against centrifugal accelerations are illustrated **Figure 6.24** and **Figure 6.25** respectively. From the observed bending moments and the earth pressures behind the wall, initial state of the backfill is more or less in the K_o condition even with 20mm wall top displacement as described in **Figure 6.25**.

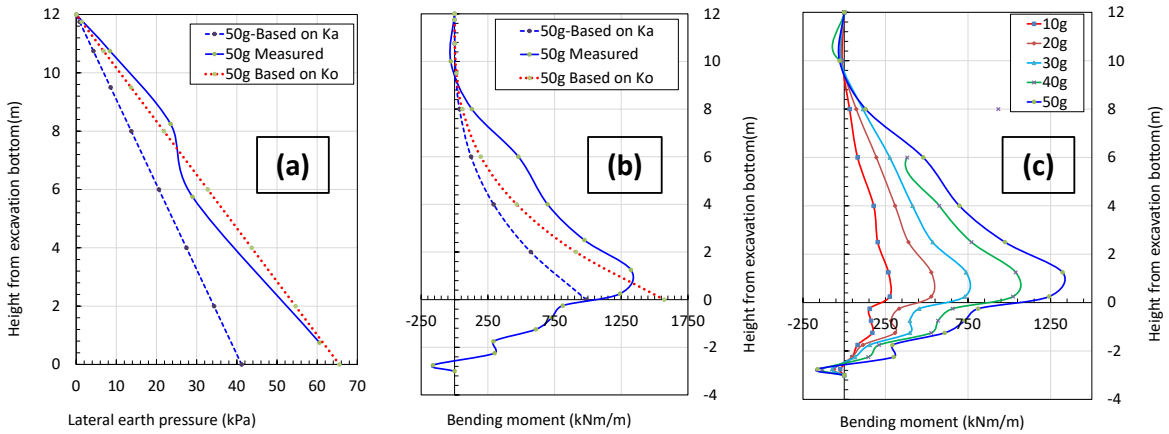

Figure 6.23 Measured and theoretical bending moments during g-up process

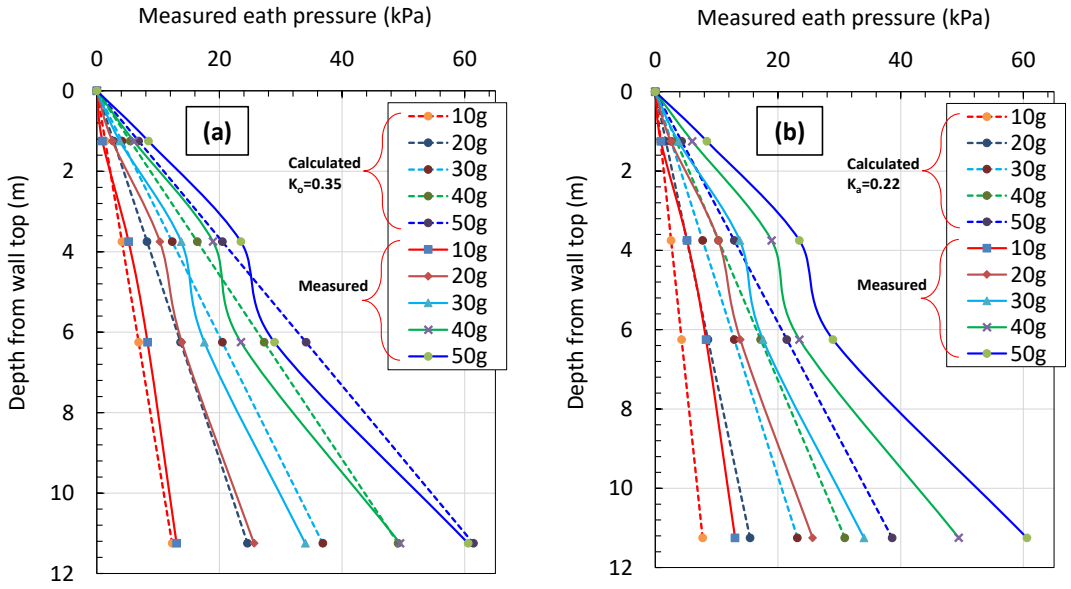

Figure 6.24 Measured and theoretical earth pressures during g-up process

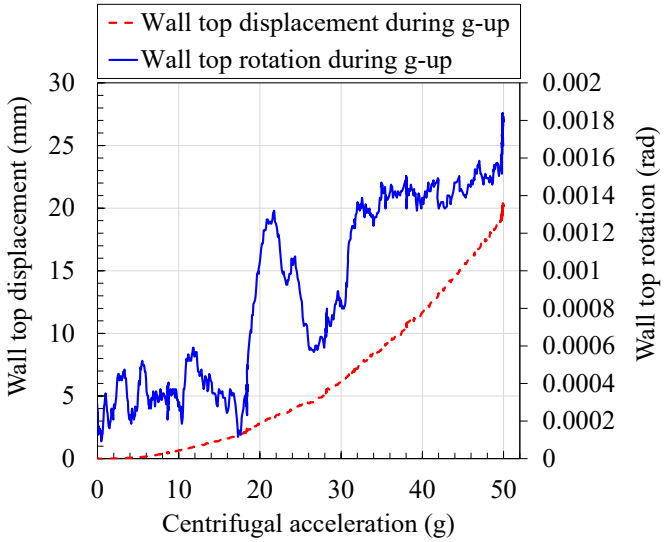

Figure 6.25 Observed wall top displacement and rotation during g-up process

6.3.6.2 Water feeding inflight

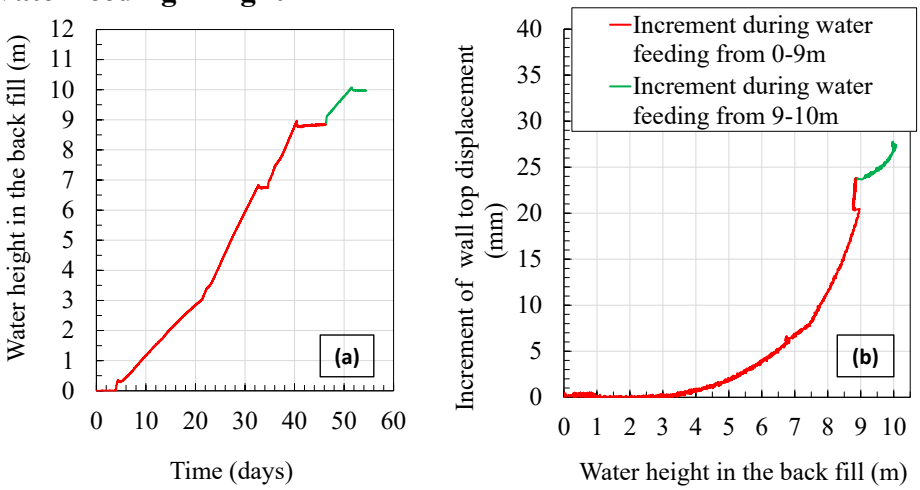

Figure 6.26 Water feeding and corresponding increment of wall top displacement

Figure 6.26(a) describes the increment rate of water height behind the wall during water feeding process, corresponding increment of wall top displacement against the water height is described in **Figure 6.26**(b).As observed in the case of simplified model in chapter-3, the increasing trend of displacement simply follow the increment trend of horizontal load by water, which is proportional to the square of water height behind the wall.

Initial conditions of each shake under dry and submerged backfill conditions are described in sub chapters 6.3.6.3 and 6.3.6.4 in terms of earth pressure and measured bending moment. From **Figure 6.27** and **Figure 6.28** increment of earth pressures and the bending moments up on completion of each shaking or the initial condition of subsequent shake can be observed. The observation clearly indicates the densification of backfill soil in each shake regardless of the backfill condition either dry or submerged. Detail discussions regarding the change of earth pressures and pore water pressures during each shake are described in sub chapter 6.4.2.

6.3.6.3 Initial conditions of measured and theoretical earth pressure under dry and saturated backfill condition at 50g prior to seismic excitations

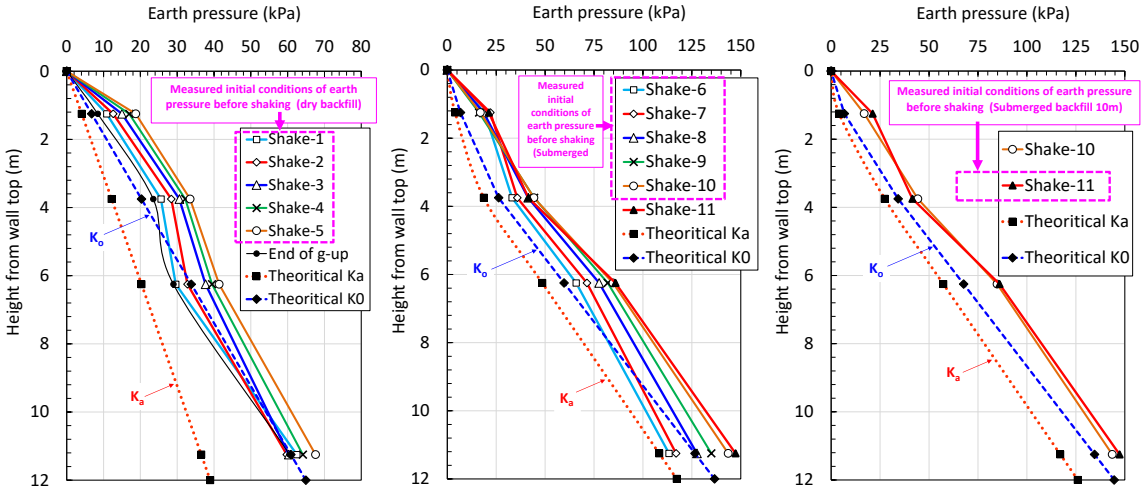

Figure 6.27 Initial conditions of measured and theoretical earth pressures under dry and saturated backfill condition

6.3.6.4 Initial conditions of measured bending moments under dry and saturated backfill condition at 50g prior to seismic excitations

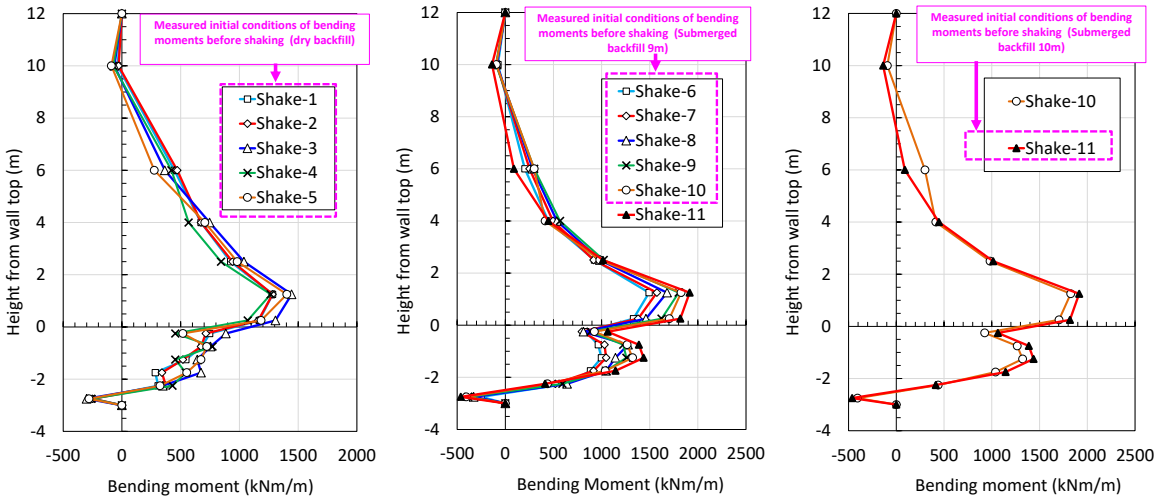

Figure 6.28 Initial conditions of measured bending moments under dry and saturated backfill condition

6.3.7 Observed behaviors

Time line of the observed wall top displacement and rotation are illustrated in **Figure 6.29**,where **Figure 6.29**(a) illustrates the measured total displacement at the wall top from shake-1 to shake-5 under the dry backfill condition. Corresponding measured total rotations at the wall top in each shake is illustrated against time in **Figure 6.29**(f). Subsequently **Figure 6.29**(b) and **Figure 6.29**(g) are describing the measured wall top displacement and rotation against the time respectively. After the water feeding, as applied in the dry backfill condition, similar input motions applied under the wet back fill condition. Corresponding measured wall top displacements and rotations from shake 6 to shake 10 are illustrated in **Figure 6.29**(c) and **Figure 6.29**(h) respectively. **Figure 6.29**(d) and **Figure 6.29**(i) indicate the wall top displacement and rotations during an additional 1m increment of water level behind the wall after the completion of shake-10. Finally Shake-11 was introduced and the corresponding measured wall top displacement and rotations are illustrated in **Figure 6.29**(e) and **Figure 6.29**(j) respectively. In order to discuss the accumulation of residual deformations and the change in the dynamic displacement of each cycle, the displacement and rotations given in **Figure 6.29** was separated as a dynamic component and residual component and illustrated in **Figure 6.30**. In **Figure 6.30** (a,d), the typical dynamic displacement, residual displacement and the dynamic component of rotation and the residual rotation are indicated by arrows. Where **Figure 6.30** (a,d) describes the separated displacement and rotational components in the dry shake from shake-1 to shake-5. Similarly the separated components of displacement and rotations are shown in **Figure 6.30** (b,e). The **Figure 6.30** (c,f) describes the components in the final shake.

Referring to the residual displacement and rotations in **Figure 6.30** from initial shake (shake-1) to the final shake (shake-11) an increasing trend in the initiation of each shaking and gradually decreasing trend towards the end of each shaking in the response of residual displacement and residual rotations can be observed. The observation could be attributed to the mobilization of horizontal subgrade reaction with the increase of residual displacement and rotation at embedded zone. Furthermore from **Figure 6.30**,dynamic component of displacement showing an increasing trend with the increase of peak input acceleration under dry and wet backfill conditions, however the response of and the dynamic rotational components are much

6.3.7.1 Wall top displacement and rotation

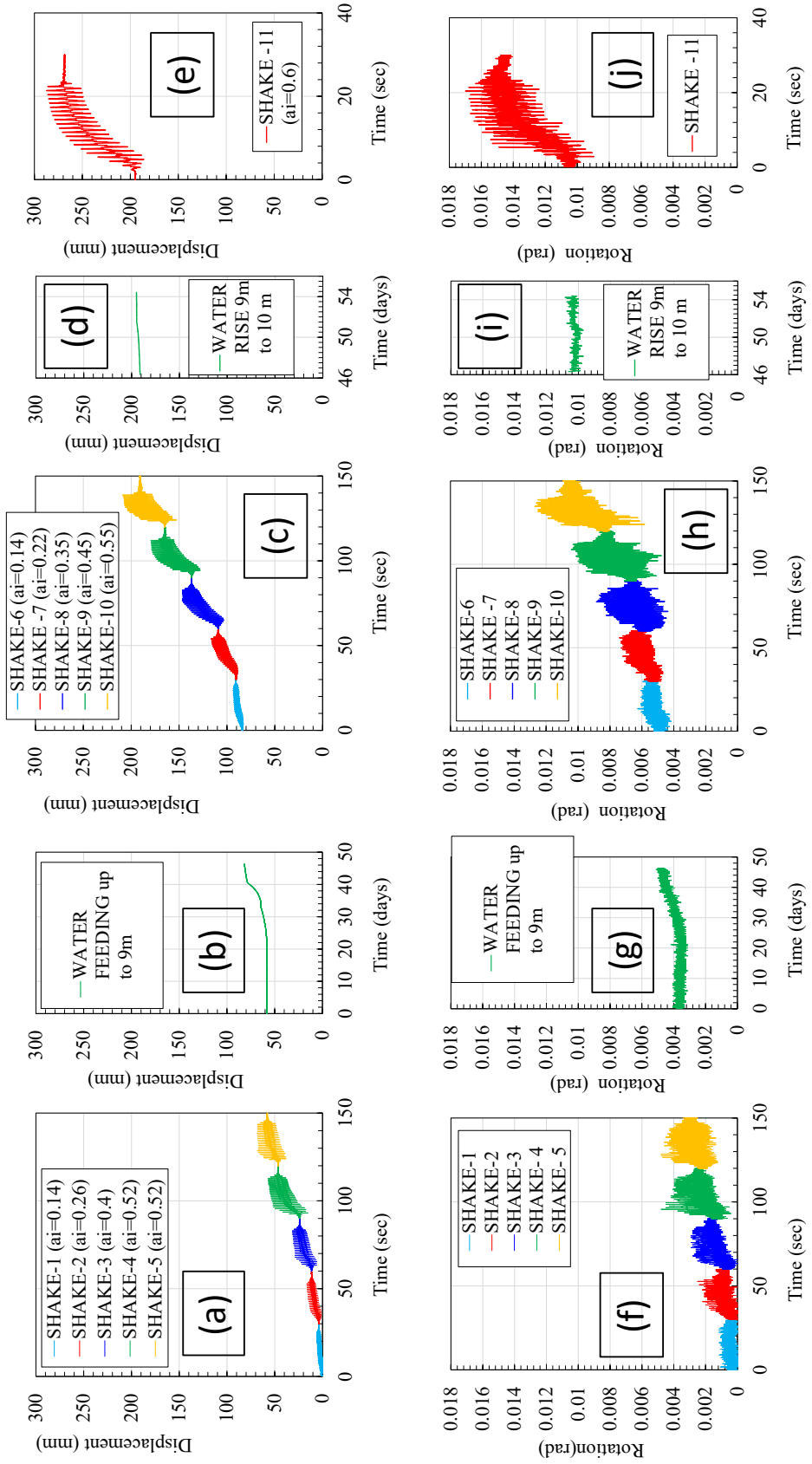

Figure 6.29 Measured wall top displacement and rotation during entire loading process

6.3.7.2 Dynamic and residual displacements

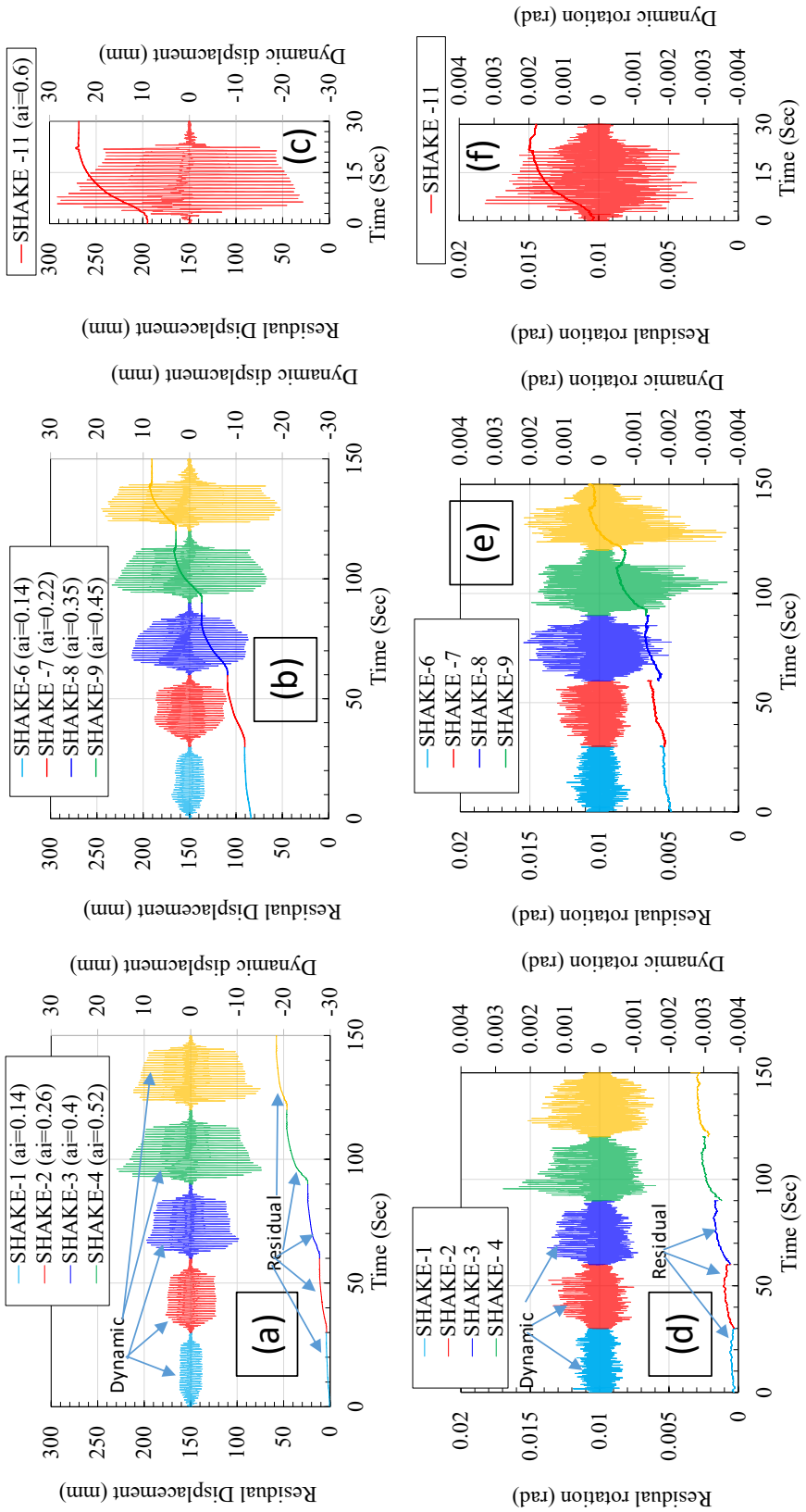

Figure 6.30 Dynamic and residual displacement, rotation during entire loading process

significant at large input accelerations compare to the smaller ones under same backfill condition.

Referring to **Figure 6.30**(d,e), relatively large dynamic rotations could be seen after the shake-3, the reflection can be observed from the residual rotations as well. Perhaps the observation could be attributed to certain level of deterioration in the embedded zone. Referring to **Figure 6.30**(c,f), even after the application of an input acceleration of 0.6g, the observed linearly increasing and gradually decreasing trend of residual rotation and displacement clearly indicates the sound lateral confinement of the wall and the translational and rotational resistances against the large lateral and moment loads respectively.

6.3.8 Characteristics of white noise and system response

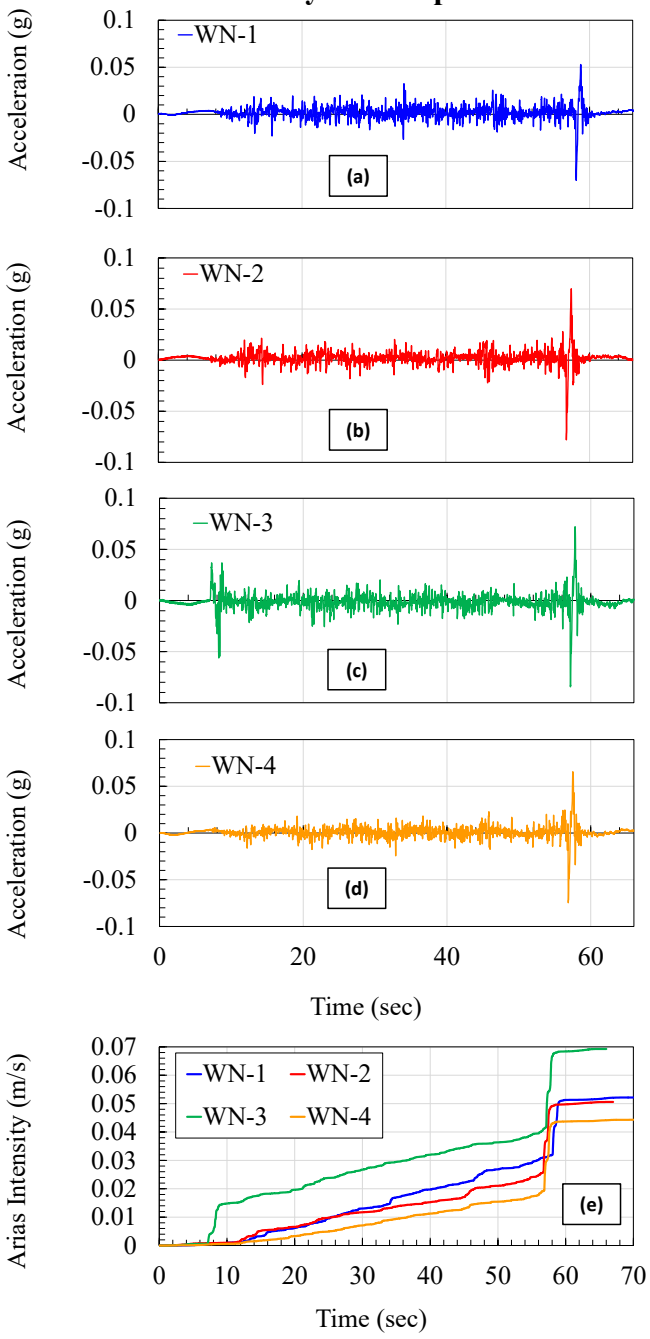

Figure 6.31 White noises and Arias intensity

Comparison between all four white noises applied in the loading process are made in the **Figure 6.31**(e) in terms of Arias intensity. From this figure the trend of variation is similar for all white noises except the peak portion below 10sec for the WN-3. Beyond 10sec it can be assume that, all the white noises are similar and the wall responses are comparable.

6.3.9 Amplification and dynamic characteristics of rock-wall system

Figure 6.32 describes the Fourier spectrum of two ground motions which were recorded during 1989 Loma Prieta earthquake at a distance of about 22km from epicentre in a rock and soil profile. **Figure 6.32**(a) shows the measured recode in rock and **Figure 6.32**(b) is in a soil profile. From this, one can distinguish the dynamic characteristic of rock type materials from that of soil. Rock exhibits relatively smaller natural period thereby a large natural frequency compare to the soil. Which could be even larger than the frequencies of most of the earthquakes. In order to investigate the changes in dynamic characteristics of the wall and the backfill soil, measured acceleration-time histories during at different locations for all four white noises are transformed in to frequency domain and the results are illustrated in **Figure 6.33**. From **Figure 6.33**, a large amplification in the response of accelerometers located at the wall top and soil top locations can be observed. Also the amplification tends reduce as move from wall top level to the embedment level. Furthermore, from the wall top response, peak amplification took place in the band of 5Hz to 7Hz indicating the range of natural frequency of the model wall. To identify the dominant or natural frequency of the wall and its alteration with residual displacements and deterioration of the fixity in the embedded zone, the spectral ratios between the Fourier amplitudes of measured acceleration responses and the input motions (WN) are illustrated in **Figure 6.34**. From **Figure 6.34**, observed spectral ratios at specific locations for all white noises are compared in **Figure 6.35**. From **Figure 6.35**(a,b) comparing the responses of WN-1 and WN-2 no significant difference can be observed in the dominant frequency at the wall top as well as soil top locations. Which clearly indicates the resilience of system stiffness even with certain residual deformations. Or in other words fixity of the embedded zone did not have significant deterioration during the input motions applied between WN-1 and WN-2.

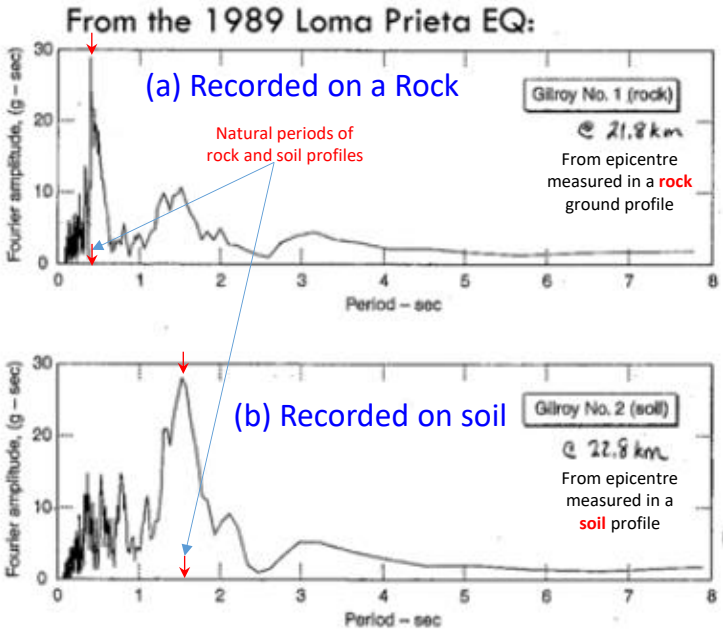

Source: CEEN 545 Lec-6 (https://www.youtube.com/watch?v=sCic4wnH1Lk&t=1570s)

Figure 6.32 Amplification characteristics of rock and soil profiles at same distance from epicentre during 1989 Loma Prieta earthquake

However, significance of water table behind the wall can confirmed while comparing the responses between WN-2 and WN-3. Where the dominate frequency of the wall changed from 6Hz to 5.2Hz. Similar alteration can be seen in the soil top behavior as well. Indicating that the increasing lateral loads acting on the wall could reduce its natural frequency. Again the comparison between WN-3 and WN-4 indicates no significant difference in the characteristics, meaning that the input motions applied with submerged backfill in between WN-3 and WN-4 also could not deteriorate the system stiffness significantly. Which could also physically confirmed up on completion of the test as described in sub chapter 6.4.5.

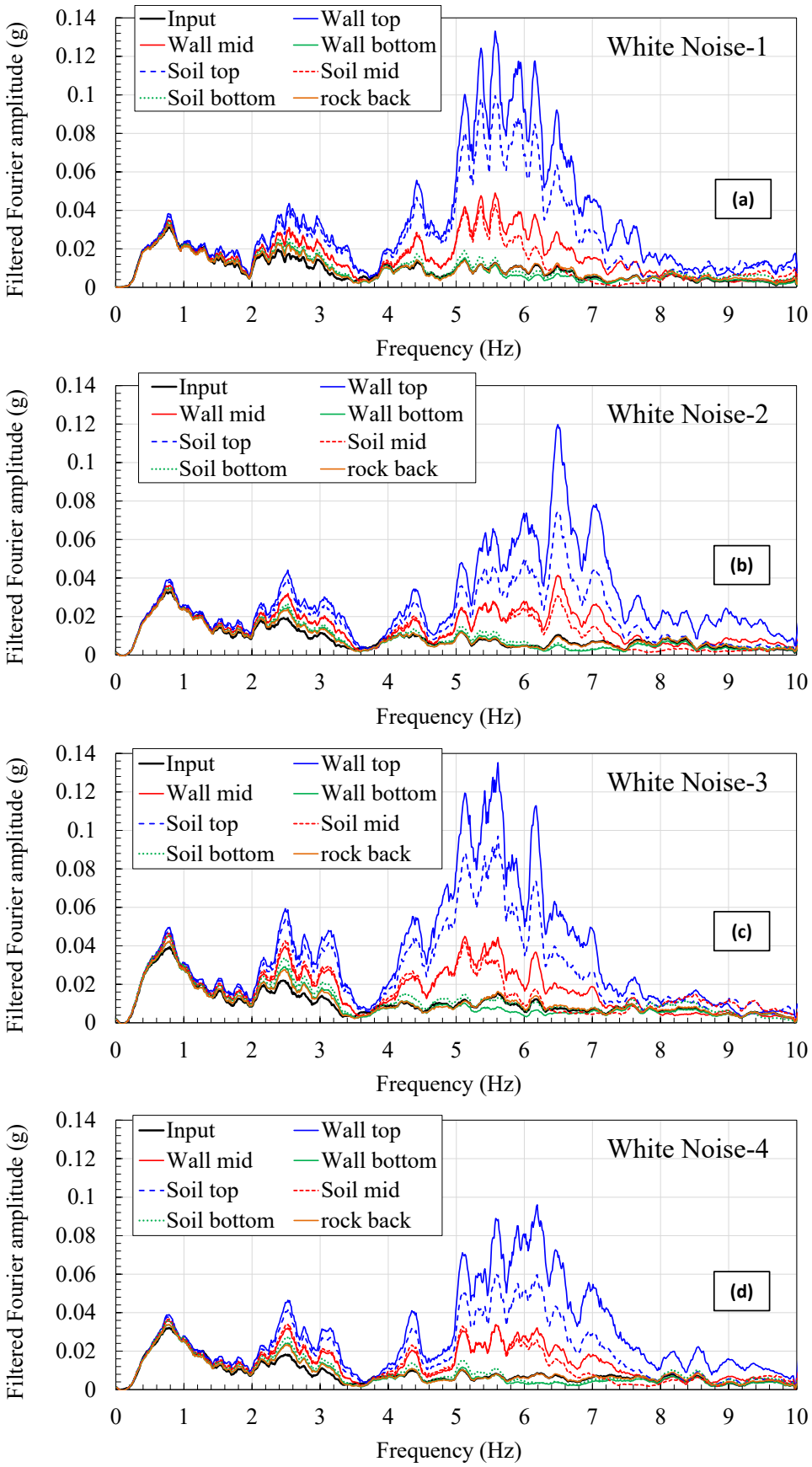

Figure 6.33 Accelerometer responses in frequency domain for white noises

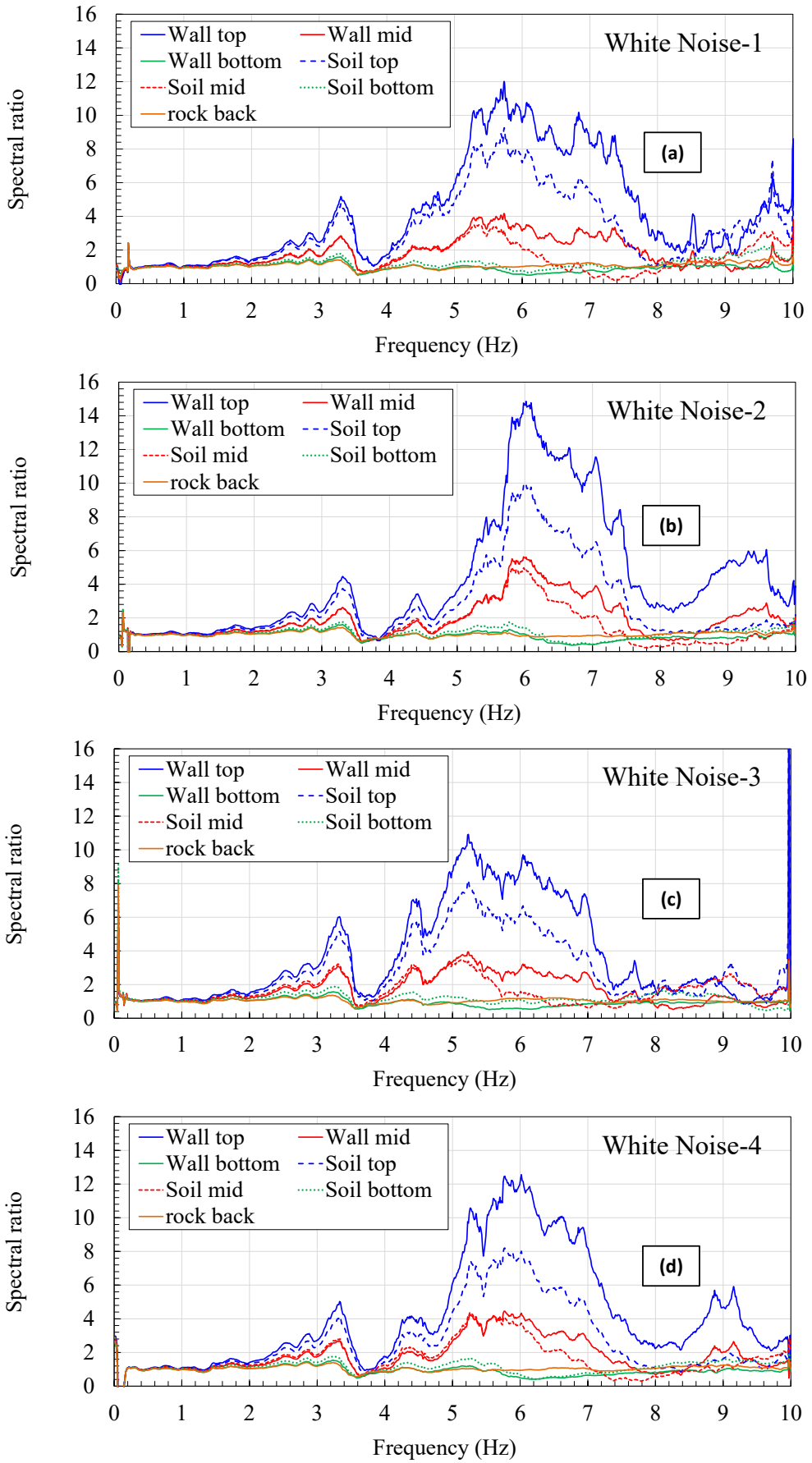

Figure 6.34 Spectral ratios at different sensor locations for white noises

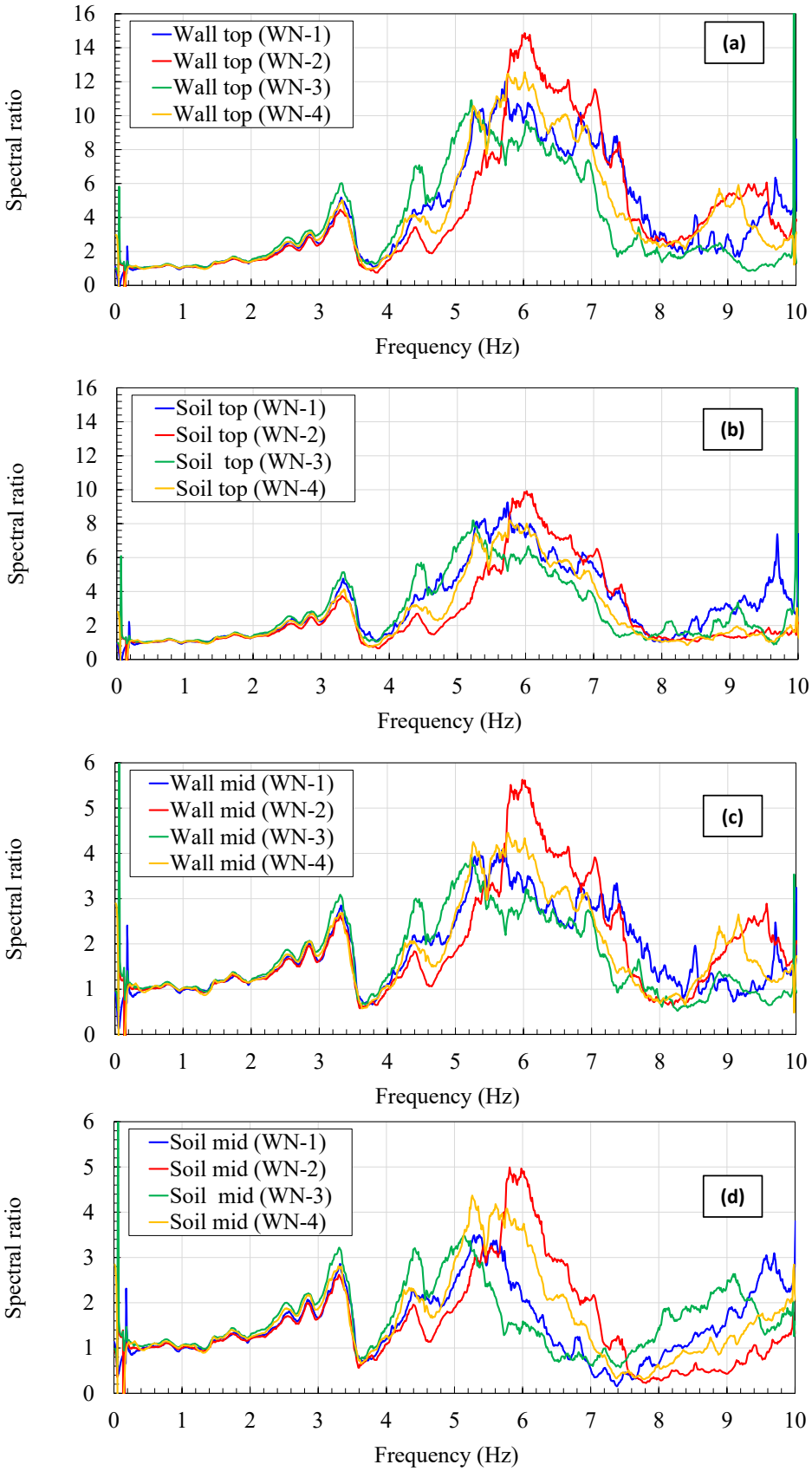

Figure 6.35 Observed dynamic characteristics of wall and backfill soil under different white noises

6.3.9.1 Typical input motion and measure acceleration time history in soil and wall

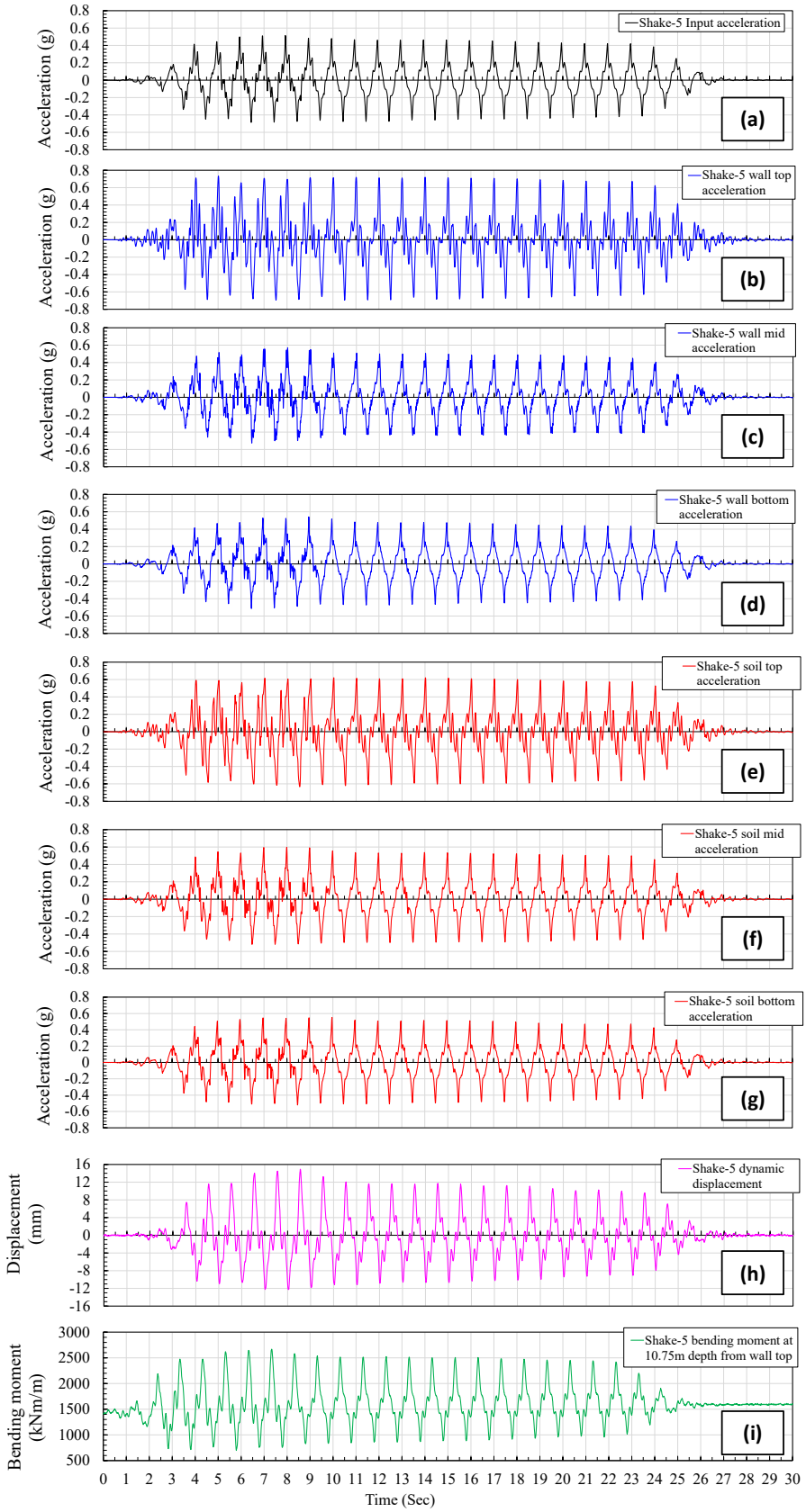

Figure 6.36 Typical acceleration time history, dynamic displacement and bending moment

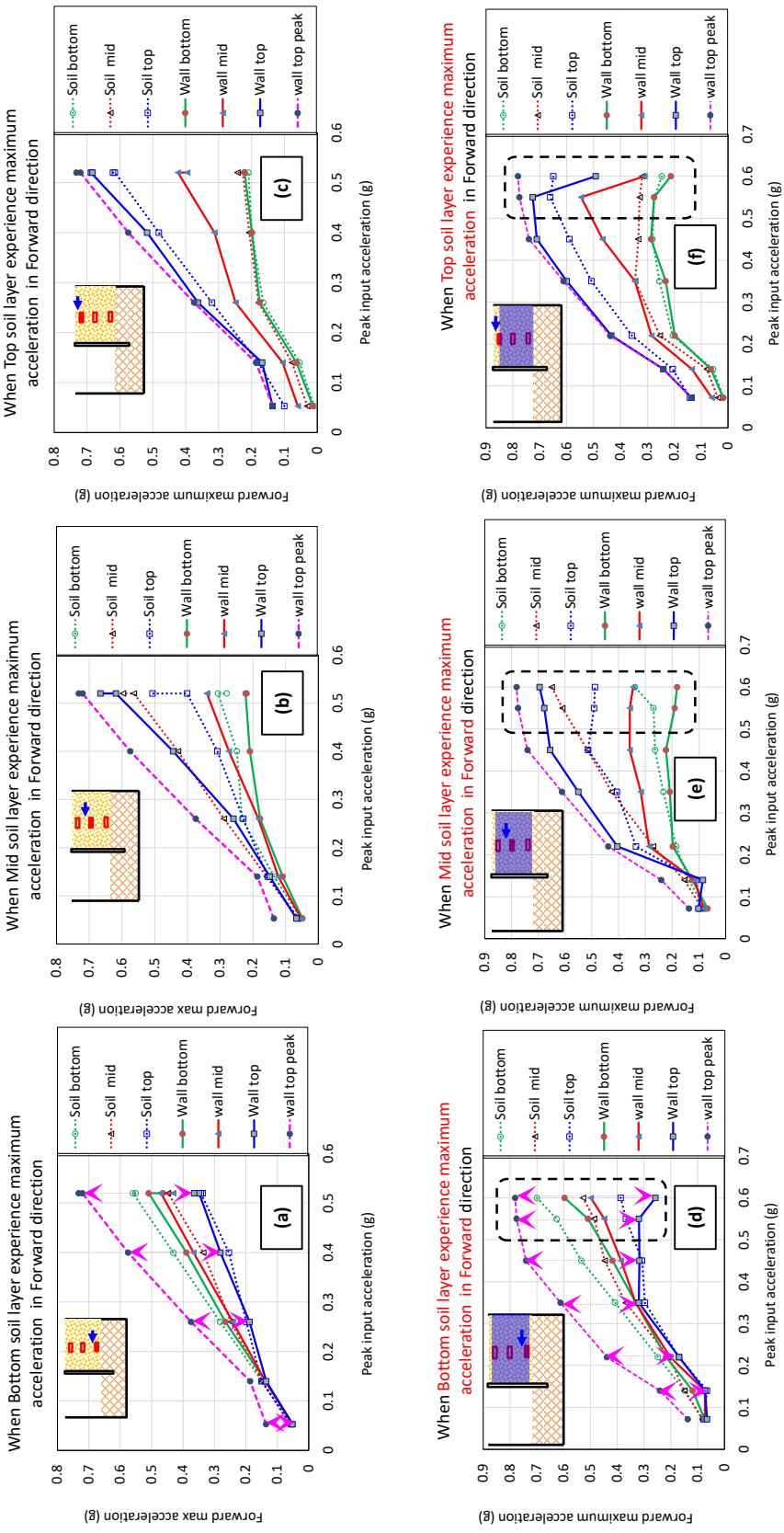

Figure 6.37 Initial conditions of measured bending moments under dry and saturated backfill condition

6.3.9.2 Typical input motion - measured earth pressures-dynamic displacement and bending moment

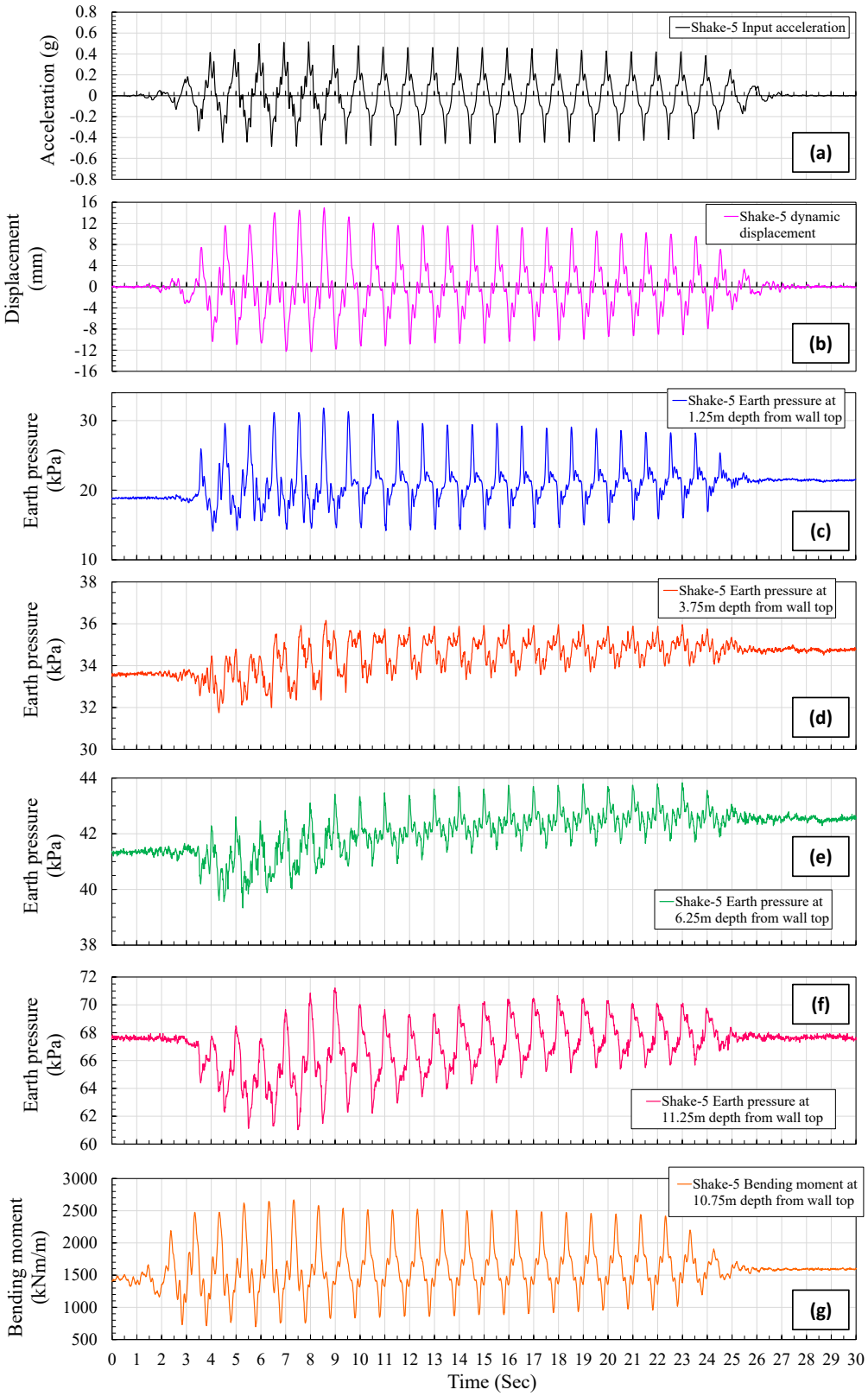

Figure 6.38 Typical Earth pressure and bending moment variation at specific locations against time

6.3.9.3 Typical input motion – dynamic displacement-measured pore water pressure and earth pressure variations in submerged back fill

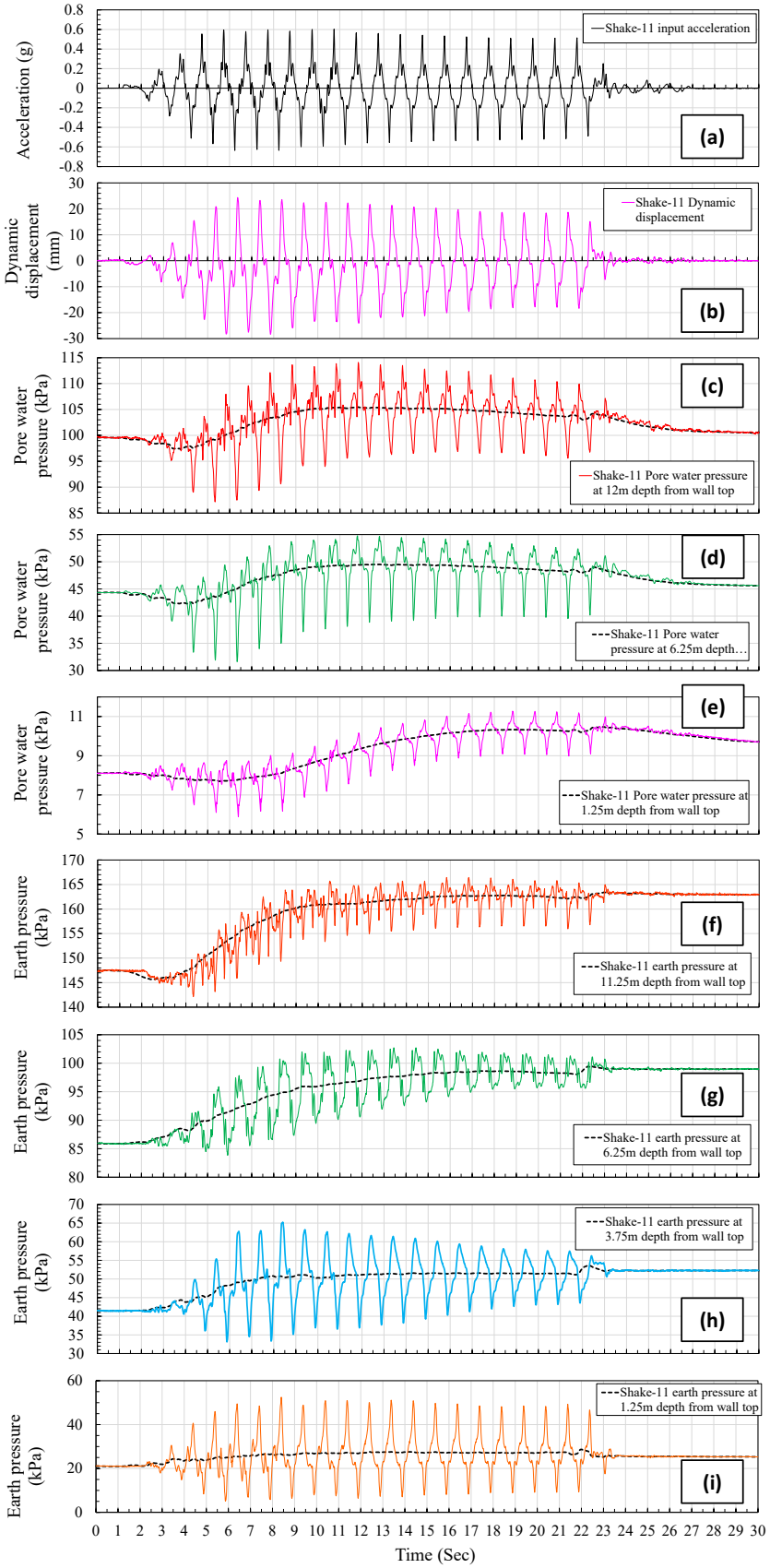

Figure 6.39 Typical acceleration time history ad measured bending moment

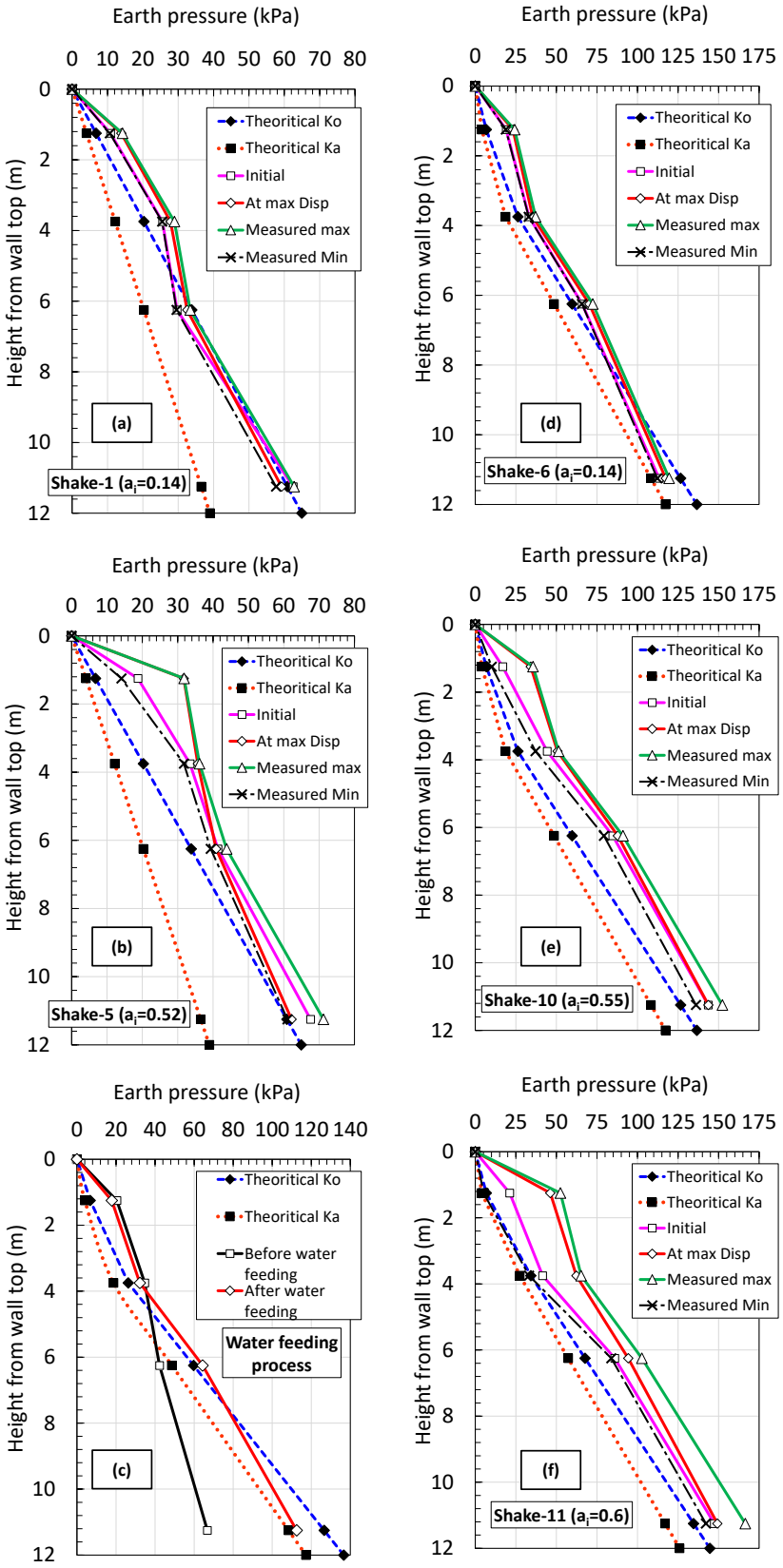

Figure 6.40 Measured earth pressure profiles at different amplitudes of harmonic motion under dry and submerged backfill condition

6.4 Results and discussion

Typical input motion (Shake-5), measured acceleration-time history on the wall and backfill soil at three different locations are illustrated in **Figure 6.36**. The detailed description of accelerometer locations are given in **Table 6-1**. As an overall observation form **Figure 6.36**, certain amplification of input motion can be seen as the wave transmitted from rock surface level to the soil top and wall top elevations. Where the amplification increases with the increasing height (Bottom to top) from the rock surface level as a common behavior in wall as well as the backfill soil. Observed amplification of the input acceleration in the backfill is a clear evidence for the well-functioning of the base of backside rubber bag, thanks to the carbon fibre membrane coated with Toyoura sand, which transmits the shear waves from the rock surface to the overlain sand.

Estimated increment of dynamic displacement component also merged with the acceleration profiles in **Figure 6.36**(h), comparing the accelerations given in **Figure 6.36**(a-g) and displacement response against time, a clear opposite phase can be observed. The observation clearly indicates the influence of inertia forces acting on the wall and soil mass, which always make an attempt to keep the body mass at its neutral position. Which is a well-known behavior in dynamics.

Considering the mechanical behavior of steel tubular pile wall in this centrifuge model, main driving forces on the measured wall displacements would be dynamic earth pressures from the backfill soil and inertia forces of wall mass. Meanwhile the resistance is given by the mobilization of subgrade reaction in the embedded zone. The wall mass is mainly concentrated in two locations as indicated in **Figure 6.12**, namely top cap mass (4.4kg/m in prototype) and the wall stem (2kg/m in prototype). Estimated inertia forces caused by wall mass is less than 5% of the net lateral forces induced by backfill during all harmonic excitations in this study. Based on this confirmation the influence of wall mass on the observed deformation behavior could be neglected.

Although it can be confirmed that the backfill behavior governs the observed deformation characteristics, in order to clarify the dominant driving mechanism causing the wall deformation, the peak soil accelerations at three locations and corresponding wall accelerations at all three measured locations of the wall at the same time frame (a specific time at which peak soil acceleration take place) for different input motions under dry and submerge backfill conditions are illustrated in **Figure 6.37**. The observed peak accelerations (irrespective to the abovementioned time frame) of the wall top also illustrated in the **Figure 6.37**.

6.4.1 Backfill behavior and acceleration response of wall embedded in stiff ground

Figure 6.37 (a-c) describes the responses of measured accelerations against the peak input accelerations at different locations of soil and wall when the bottom, mid and top soil layers experiencing their peak accelerations under dry back fill condition. Similar illustrations are given for the submerged backfill in the same **Figure 6.37** (d-f).

Comparing the acceleration responses at the wall top, the observations indicate a linearly increasing trend with the increase of input accelerations under dry backfill condition (**Figure 6.37** (a-c)). This is a clear evidence of sound lateral confinement in the embedded zone and the mobilization of subgrade reaction with the increasing residual displacements and rotations as observed in **Figure 6.30**. As the lateral loading increased by the transformation from dry to submerged condition, noticeable difference in the wall and soil acceleration response between dry and submerged can be seen. Under submerged conditions also quiet linearly increasing trend can be observed up to an input acceleration of 0.45g from **Figure 6.37** (d-f). However beyond which the response in non-linear, the observed non-liner behavior could be partly attributed to the non-linear response of backfill as we could observed from **Figure 6.37** (d-f) and

the deterioration of fixity in the embedded zone with large accumulation of permanent or residual deformations.

The influence of backfill soil accelerations on the wall response can be described by referring the difference between wall top accelerations at considered time frame given in **Figure 6.37** (a-f), and the wall top peak accelerations illustrated in the same figures. Based on the observations in **Figure 6.37** (a-f), a significant different between above mentioned accelerations can be seen from **Figure 6.37** (a & d) however the difference is relatively minor in **Figure 6.37** (b & e) and which is almost negligible in **Figure 6.37** (c & f). From this observation it can be confirmed that, the amplification of bottom soil layer has no significant influence on the acceleration response of the wall embedded in relatively stiff ground. However the response is mainly govern by the acceleration of the upper and mid soil layers or a typical Coulomb soil wedge at or above the mid height of the wall unlike the illustration given in **Figure 6.2** for a conventional retaining wall.

6.4.2 Measured earth pressures-pore water pressures and dynamic displacement

Typical time variation of measured earth pressure and pore water pressures during harmonic excitations for dry and submerged backfill conditions are illustrated in **Figure 6.38** and **Figure 6.39**.The observed dynamic displacements also merged in the abovementioned figures. Meanwhile **Figure 6.40** describes the measured earth pressure profiles behind the wall at initial condition, at maximum wall top displacement and the profiles of maximum and minimum earth pressures experienced during excitations. The profiles are compared for relatively small and large input accelerations under dry and submerged backfill conditions. The results of intermediate accelerations studied in this study are not presented here.

From **Figure 6.38**, while comparing the observed earth pressures at different locations an alternating response could be observed below and above the mid height of wall. Earth pressure cells at 1.25m and 3.75m depth from the wall top experiences their maximum values while the wall exhibiting the forward peak displacement in each harmonic cycles. However, the cells at 6.25m, 11.25m depth from wall top shows their peak almost at the time of maximum backward wall top displacement. The mechanism behind the observations could be attributed to the influence of inertia and passive earth pressures. Relatively large amplification of shallow layers and thereby induced inertia forces could be attributed to the observations at 1.25m, 3.75m. At deeper locations (6.25m, 11.25m) mobilization of passive pressures during the backward wall movement and densification of backfill under large confining pressures could be the cause of observed behavior. From **Figure 6.38**(c, d &e), certain increment in the residual pressure at the end of shaking could be observed this also a clear evidence for the densification of backfill during shaking.

Some similarities and differences could be observed from **Figure 6.39** as well, From **Figure 6.39** the earth pressures measured at 1.25m,3.75m and 6.25m from wall top are following the response of maximum wall top displacement, meanwhile the behavior of the cell at 11.25m depth from the wall top remains unchanged. **Figure 6.39** illustrates the behaviors at shake-11 where the residual wall deformations are 190 mm displacement, rotation of 0.01 rad as described in **Figure 6.30**. Mechanism behind the phase transformation of the cell at 6.25m below the wall top level could be attributed to the extension of shear wedge even below the mid height of the wall with the accumulation of wall top displacement and rotations.

The variation of measured pore water pressures at the same or closest locations of earth pressure cells also illustrated in **Figure 6.39** (c, d & e). The residual pressure rise during shaking also indicated by dotted lines in the same figures. Observing the positive and negative variations of pore pressure from this dotted lines it can be confirmed that the rise of pore

pressures are much smaller during the shearing of backfill, which occurs in the backward deformation of wall as we could see from **Figure 6.39** (b). However significant reduction of pore pressures can be seen below these dotted lines during the forward wall movement, indicating negative pore pressures from the initial condition. Abovementioned observations indicate that the volume reduction (contraction) in the backfill soil during backward movement of the wall is relatively smaller compare to the dilation in the forward wall movement. Attributing to this relatively small change in volume (undrain or partially drain) in the backward shearing, the observed rise of residual earth pressures could be caused by the increase of effective confining pressures under undrain or partially drain conditions.

Furthermore from **Figure 6.39**, the observed residual increments in measured earth pressures are much more significant compare to the dry backfill conditions shown in **Figure 6.38**. Observation clearly indicates that a higher degree of densification could be achieved during the shaking of submerged backfills compare to the dry backfill at a restrained water boundary conditions. This phenomenon could result relatively large amplifications of earth pressures from their initial condition as shown in **Figure 6.40**. Especially a large amplification of earth pressures could be observed from **Figure 6.40**(e) and **Figure 6.40**(f) compare to **Figure 6.40**(f), where the peak input accelerations are 0.55, 0.6 and 0.14 respectively.

6.4.3 Bending moment and typical increment of displacement

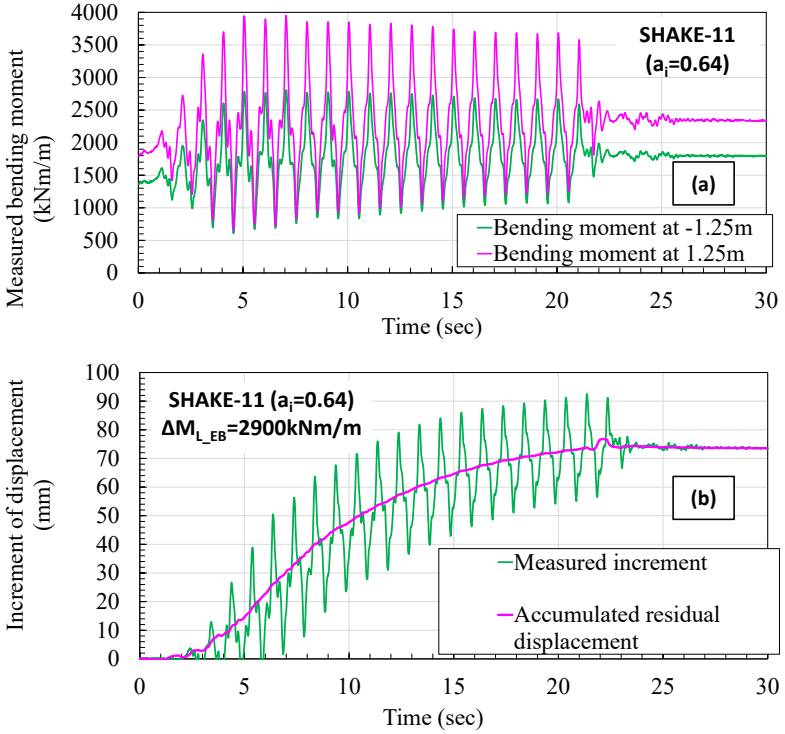

Figure 6.41 Measured wall top displacement and rotation during entire loading process

Typical variation of measured bending moment and the increment of measured displacement at wall top are illustrated against time in **Figure 6.41**.From the measured bending profiles below and above the embedment level no significant phase difference could be seen. Measured bending moments at the embedment level could be considered as a loading index representing the applied moment load at that location. Although no significant reduction can be seen in the bending response measured closer to the embedment level as shown in **Figure 6.41**(a), a decreasing trend of measured displacement given in **Figure 6.41**(b) indicates the mobilization of subgrade reaction in the embedded zone with the increment of residual deformations. As the accumulated displacement increases the subgrade reaction also increases accordingly and over

certain amount of mobilized subgrade reaction further loading could not enhance the permanent deformation. Over this limit the behavior of embedded medium tend to response as an elastic media which can be confirmed from the decreasing rate of residual deformation in **Figure 6.41**(b).

6.4.3.1 Estimation of moment load at excavation bottom

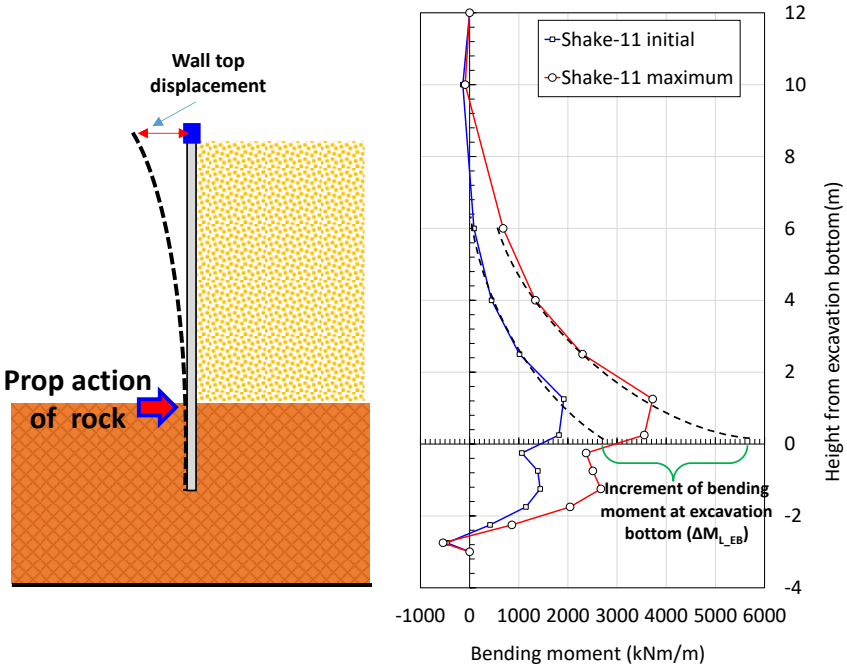

Figure 6.42 Prop action of shallow rock layers and estimation of moment loads

As described in 6.4.3 the measured bending moment at excavation bottom level could be considered as an alternative loading index for moment loads, where a sound fixity in the embedded zone is present. The validity of this assumption is examined with the estimated theoretical moment loads by two different methods in this sub chapter.

Figure 6.42 illustrates the bending moment profiles at the initial condition and at the point of maximum bending moment. From the observed bending moment profiles the influence of high stress concentration or a kind of propping action can be observed closer to the excavation bottom level. It is important to note that the observed trend is not a cause of malfunctioning of strain gauges, but the behavior is consistence in the entire loading process also the influence of this propping action tend to increase with the wall movement at excavation bottom level. This can be confirmed from the bending moment profiles given in **Figure 6.43** for all the input motions in this study.

This propping action of rock layers did not discussed by previous researchers up to the best of my knowledge and to overcome this issue related to the reliable strain measurements closer to the embedment level perhaps the individual strain measurements could at least provide reliable outcomes at one side. However, in the dynamic loading more or less tension and compression could be expected in both sides of the piles therefore it might be difficult to observe the strain measurements at embedment level. Outcome of this research provides a good lesson for those who are interested in the strain measurements in rock, especially at the level of rock surface care must be taken in to account to obtain more realistic outcomes.

Attributing to the difficulties, the bending moment at embedment level was estimated by extrapolation method using the trend of bending profile above the embedment level as described in **Figure 6.42**.

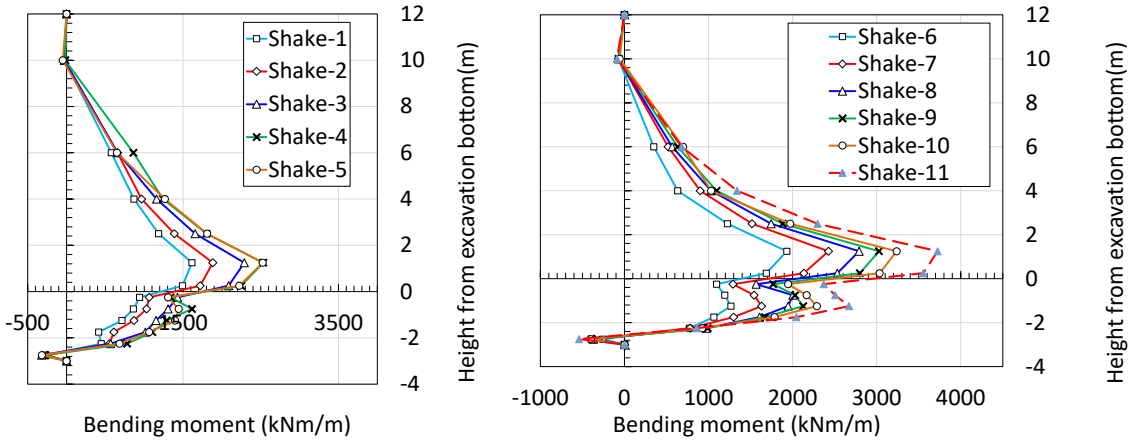

Figure 6.43 Maximum bending moment profile in each shake

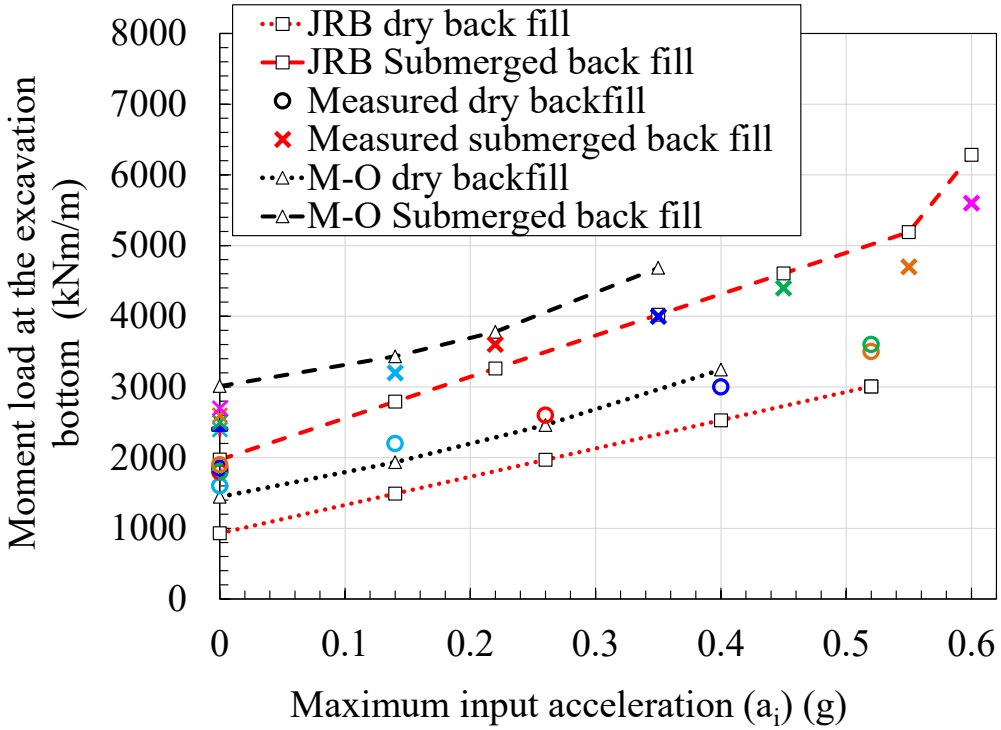

Figure 6.44 Comparison between theoretical moment loads and measured bending moments

The moment load at the embedment level was calculated using Mononobe-Okabe (M-O) method and the design method adopted in Japanese Road Bridge (JRB) slandered as described in chapter 6.2. Estimated moment loads for dry and submerged backfill conditions are compare with the measured values in **Figure 6.44**. From **Figure 6.44**, although M-O provides quiet good agreement with the measured values at certain input accelerations this might be a coincident attributing to the assumed point of action (H/2) as well as the observed over estimation under submerged backfill conditions. Also it is important to emphasize that the M-O method has several uncertainties or limitations in the calculation, the method blows up beyond the accelerations of 0.44g also it does not provide any information about the point of action of resultant force.

Estimated moment loads based on JRB method quiet closely predict the moment loads under submerged backfill conditions and which underestimate the loads under dry backfill. The

observation also true, attributing to the static earth pressure coefficient adopted in the JRB method. Where a coefficient of 0.21 is utilized, however the observed static earth pressures in the initial conditions of each shake was closer to the K_o or larger than K_o as shown in **Figure 6.27**. Furthermore, from the observations of this experiment it can be expected to have an active earth pressure closer to the K_o condition behind a stable wall even at large deformations. Most of the permanent retaining structures are constructed as a stable wall, therefore the adoption of K_o condition for static component in JRB method could yield more realistic and conservative design loads behind a stable wall either it embedded in stiff or soft ground condition.

6.4.4 Comparison between tubular pile wall and simplified model in chapter-3

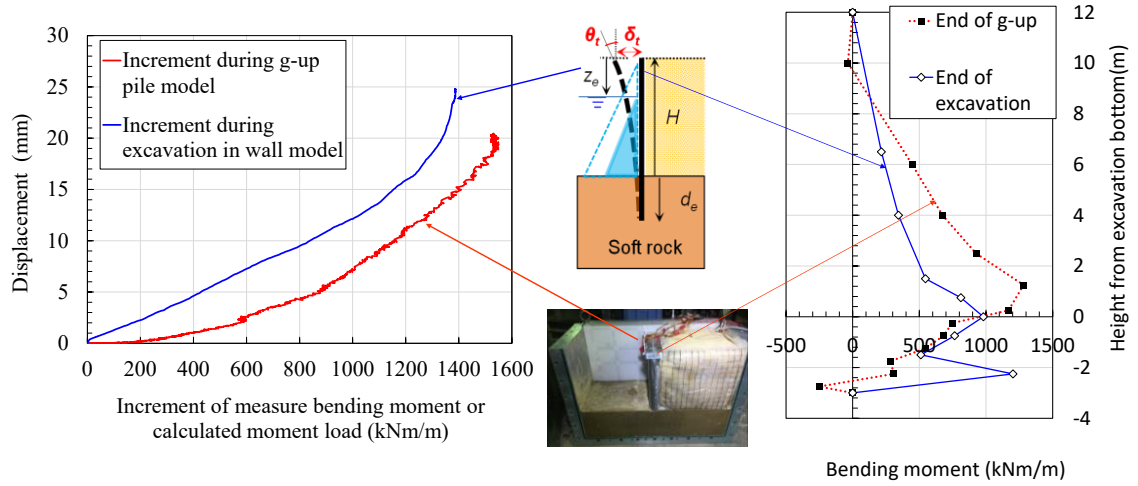

Figure 6.45 Wall top displacements caused by excavation and g-up process against the moment load

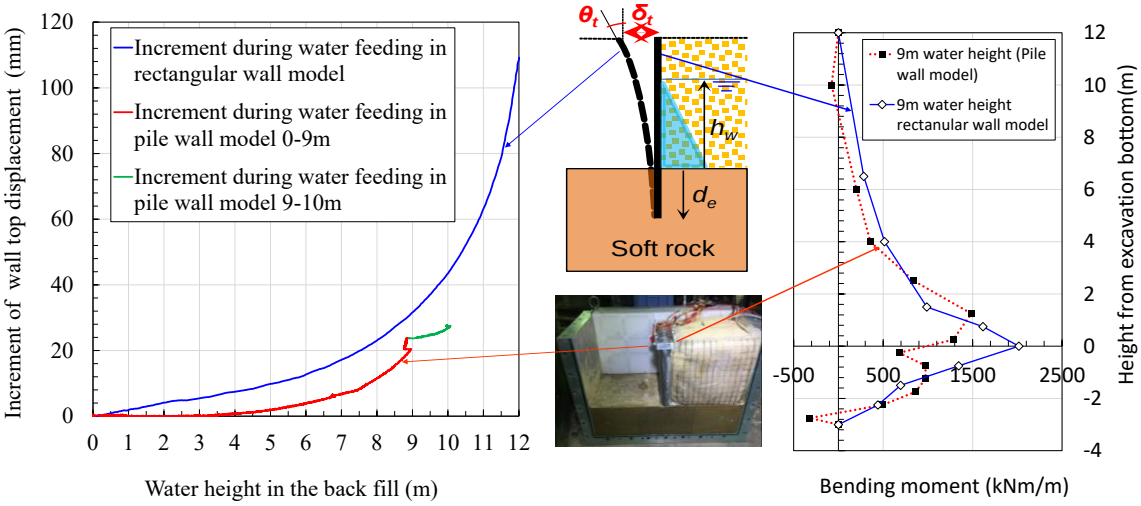

Figure 6.46 Wall top displacements caused by water feeding against the water height in the back fill

This sub chapter aims to compare the behavior between the simplified wall model in chapter-3 and the tubular pile wall model in this chapter, both are having the same embedment depth and retained height of earth. However the difference between both models is the geometry of the model piles, plugging or rock-wall interaction in the embedded zone as well as the relative stiffness. Density of the backfill also slightly different in both models 80% (γ_d=15.4kN/m^3) and 85% (γ_d=15.6kN/m^3) respectively however the influence of this 5% could be negligible.

Figure 6.45 illustrates the observed wall top displacements during the g-up process for the tubular pile wall and during the excavation process for the simplified wall model in chapter-3. Similarly the increment of wall top displacements for both models during the water feeding process from a water height of zero to nine meters behind the wall are illustrated in **Figure 6.46**. Although the embedment depth is same in both models, relatively smaller displacements under same moment load or the water height behind the wall could be observe from **Figure 6.45** and **Figure 6.46** respectively. Observed differences between actual tubular pile wall and the simplified wall model indicates the limitations of simplification and dependency of fixity on the shape or geometry, plugging conditions and effective Young's modulus of the pile as describe in Equation 2.16. Estimated equivalent E_e/G^* values for a 2.5m diameter cylindrical inclusion in the model soft rock was 44 and 24 for simplified wall model and steel tubular pile wall respectively. Furthermore, required d_{e_s}/B ratios to satisfy the flexible (Equation2.28) wall condition was 3.85 and 3.24 respectively. Based on this equivalent stiffness concept described in chapter 2.3.4.2, estimated embedment depths for simplified wall model and the tubular pile wall are 31% and 37% in terms of d_{e_s}/B. Here d_{e_s} is the required embedment depth to satisfy the flexible wall condition and the increment of embedment over which has no influence on the wall behavior for a specific wall section.

Observed large difference in the wall top displacement could not be simply attributed to 6% increment of d_{e_s}/B ratio. Which clearly indicates that the deformation mechanism of tubular pile wall model highly influence by the rock plugging and mobilization of rock-rock interface shear stresses at the bottom tip level. This mobilization of shear stresses at the tip level highly controlled by the adhesion between rock- aluminium wall interfaces in the case of simplified wall model, and the mobilized adhesion could be about 50% or less than 50% that of rock-rock interface share stresses. The observed difference in the wall top displacements for simplified and tubular pile wall models are highly influenced by this mechanism.

6.4.4.1 End of excavation in chapter-3 and end of g-up in chapter-6 as initial conditions

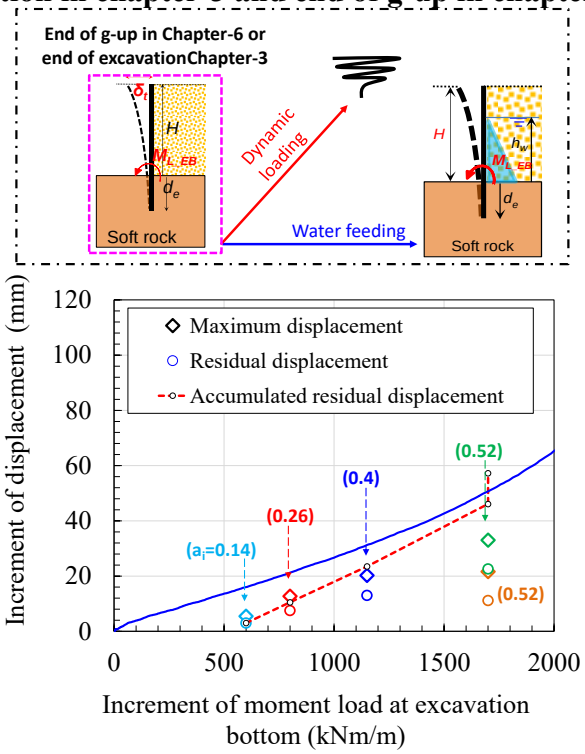

Figure 6.47 Comparison between simplified wall model and tubular pile wall based on moment load increment under dry back fill condition

6.4.4.2 Water level of 9m behind the wall as an initial condition

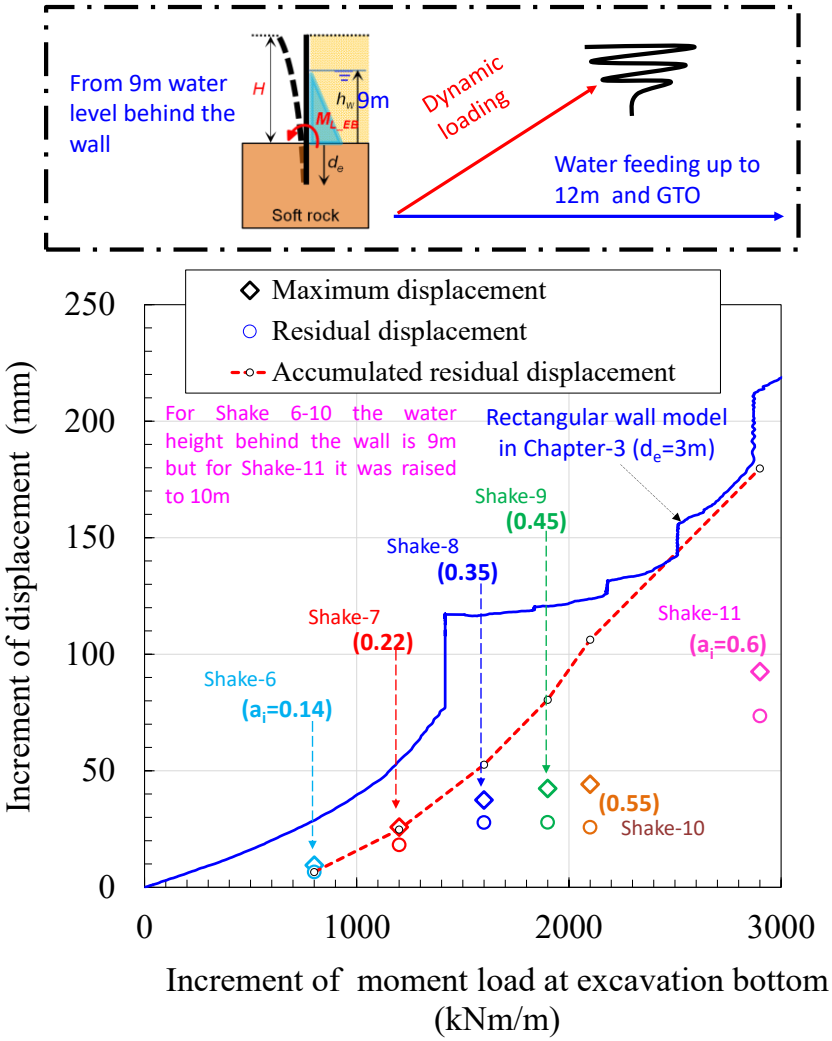

Figure 6.48 Comparison between simplified wall model and tubular pile wall based on moment load increment under submerged back fill condition

Considering two similar initial conditions of simplified wall model in chapter-3 and the tubular pile wall in this chapter are discussed in the subsequent discussion. The initial conditions are;

1. End of excavation in chapter-3 and end of g-up in chapter-6 as an initial condition
2. Water level of 9m behind the wall as an initial condition

From these considered initial states, either the behavior of both walls under the same increment of moment load or the mechanical behavior under the same increment of displacements are assessed.

Figure 6.47 illustrates the increment of wall top displacement against the increment of moment load for the initial condition-1, the similar variation of the initial condition-2 is given in **Figure 6.48**.

Based on **Figure 6.47**, while considering the maximum displacement in each shaking, the tubular pile wall exhibits as an average of 40-50% larger resistance in terms of moment load at same increment of wall top displacements, compare to the wall model in chapter-3. Observed difference could be attributed to the different loading conditions namely static and dynamic impact load. In the dynamic loading although same increment of moment load can be applied the nature of this loading is a kind of impact or instant also upon removal of the dynamic impact

the only load component is the static dry backfill. However, in the static loading of wall in Chapter-3 the static load keep increasing with the water height it also could cause large creep deformations during the loading period itself compare to the tubular pile wall. A major confirmation about the tubular pile wall model in this loading is the resistance against the large impact or dynamic loads and the stability against failure even with relatively small embedment depths. As discussed in 0, besides the loading mechanism in both models, difference in the fixity of wall model and Tubular pile walls also could be the cause of different resistances, attributing to the shape effects, stiffness ratios and the influence of rock plugging on the mobilized shear resistance as indicated in **Figure 6.49**.

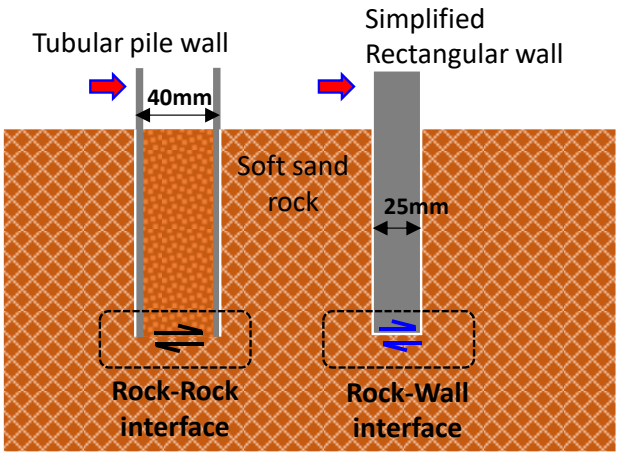

Figure 6.49 Influence of geometry and rock plugging on the mobilized shear resistance at interfaces

Figure 6.48 illustrates the behavior of both walls under the increment of large moment loads compare to **Figure 6.47**. Also at the initial stage of this evaluation, the applied lateral and moment loads are much higher compare to the initial condition-1. At this stage the accumulated residual deformation of simplified wall was about 60mm and which was 85mm for the tubular pile wall. Although tubular pile wall exhibits higher resistance against the increment of moment load as discussed above, the large residual displacement than the simplified model clearly indicates the severity of dynamic loads over the static loading.

From **Figure 6.48**, while considering the maximum displacement in each shaking, an increasing trend of resistance (No significant increment of maximum displacement in subsequent shaking) in terms of moment load can be seen at the same increment of wall top displacements, compare to the wall model in chapter-3. Increasing trend of maximum and residual displacements are linear from shake 6 to 8 against the increment of moment load, however in shake-9 and 10 almost no increment of maximum displacements and decreasing trend of residual displacement with increase moment load can be seen. The behavior could be attributed to a relatively higher rate of increment in subgrade reaction with the increasing accumulated residual displacements in the embedded zone. It also indicates the sound lateral confinement of the tubular pile wall which was physically confirmed while removing the wall up on completion of the test. Furthermore, the increasing trend of accumulated residual displacement and the displacement increment for the wall model are similar except the stable creep portion of the simplified model at the moment load increment of 1400kNm/m.

Observing the behaviors at large displacement range or the ultimate loading conditions the behavior of both wall is similar as we could see in the increment of moment load from 2000-3000kNm/m range. Perhaps, with the large residual displacements observation might be attributed to the fully mobilization of shear stresses at the bottom tip level, beyond which the

plugging portion of the tubular pile wall may not have significant influence on the wall behavior.

6.4.5 Accumulated displacements and creep deformation

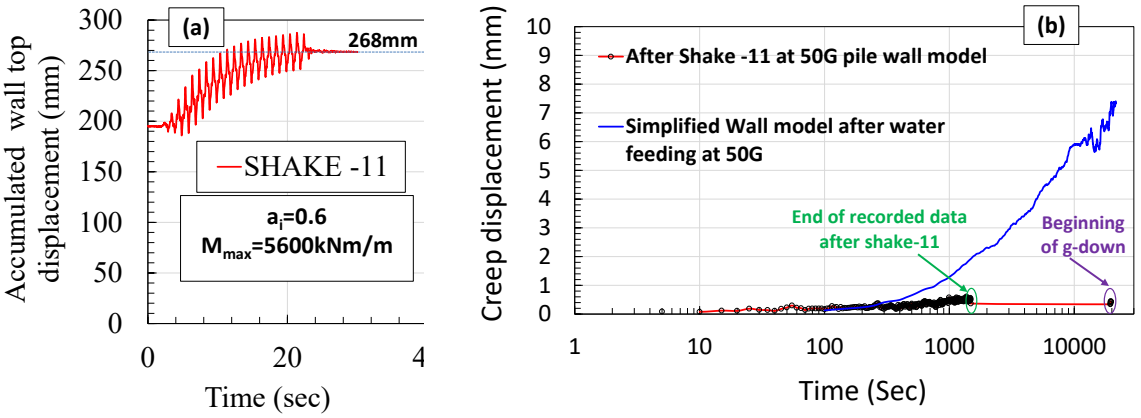

Figure 6.50 Influence of geometry on the mobilized shear resistance at interfaces

Attributing to the less redundancy of cantilever type walls, it is essential to confirm the stability under long term behavior. **Figure 6.50**(b) illustrates the creep deformation characteristics of simplified wall model at 50g up on completion of 12m water feeding and the tubular pile wall at the end of shake-11 with a 10m water level behind the wall at same g environment. Where the residual wall top displacements prior to the investigation of creep behavior was 170mm and 268mm respectively. And the experienced maximum moment load of tubular pile wall is about 1.2 times the ultimate moment load resistance (4900kNm/m) of the wall simplified wall model.

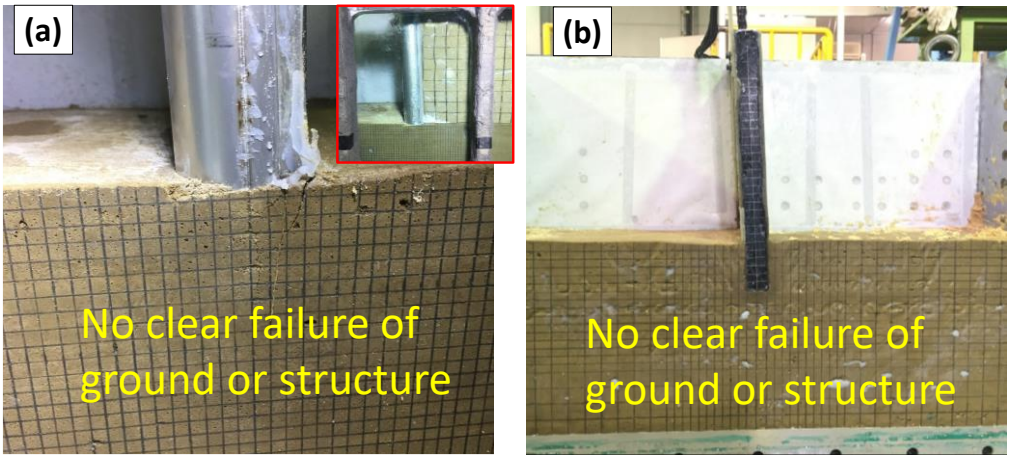

Figure 6.51 Ground deformations observed after testing for (a) Tubular pile wall and (b) Simplified wall model

Although tubular pile wall having large residual displacement and experience a large moment load compare to the simplified wall model, the creep deformation took place in a long time period is negligible compare to that of simplified wall model as described in **Figure 6.50**(b). Observation clearly indicates the sound lateral confinement in the embedded zone of the tubular pile wall and more stable conditions compare to the simplified model even after a large residual deformation. It was also confirmed physically, while removing the wall from the embedded

zone. In fact, we could not remove the wall and finally the embedded medium was crushed in to two pieces and the wall was removed. Based on the accumulated deformations, applied moment load and the creep deformation characteristics of tubular pile wall, it can be confirmed that the tubular pile wall is more stable compare to the wall model. Design proposals based on the outcomes of simplified wall model could yield more conservative design approach.

6.5 Summary

- A complicated dynamic centrifuge model was developed to study the behavior of CSTP walls under dynamic loads. From the preliminary analysis of experimental outcomes, the following conclusions were derived
- Considering different initial conditions as discussed in 6.4.4.1 and 6.4.4.2 the tubular pile wall exhibits relatively large resistance compare to the simplified wall model under same increment of displacement. No clear failure of the embedded medium or the tubular pile wall can be confirmed even at the applied maximum moment load, which is 1.2 times the ultimate resistance of the simplified wall model.
- Based on accumulated deformations described in 6.4.5, applied moment load and the creep deformation characteristics of tubular pile wall, it can be confirmed that the tubular pile wall (1.2/β) is more stable compare to the simplified wall model (1.05/β). Design proposals based on the outcomes of simplified wall model could yield more conservative design approach.

6.6 References

Ebeling, R.M. and Morrison Jr, E.E., 1993. The seismic design of waterfront retaining structures (No. WES/TR/ITL-92-11). ARMY ENGINEER WATERWAYS EXPERIMENT STATION VICKSBURG MS INFORMATION TECHNOLOGY LAB.

Kramer, S.L., 1996. Geotechnical Earthquake Engineering (Chapter 11). *1996.*, pp.466-506.

Prakash, S., and Basavanna, B. 1969. "Earth Pressure Distribution BehindRetaining Wall during Earthquake," Proceeding. 4th World Conference on Earthquake Engineering, Santiago, Chile.

D'Andrea, R. and Day, R.W., 1998. Discussion and Closure: Design and Construction of Cantilevered Retaining Walls. Practice Periodical on Structural Design and Construction, 3(2),pp.87-88.

Matsuzawa, H., Ishibashi, I. and Kawamura, M., 1985. Dynamic soil and water pressures of submerged soils. *Journal of Geotechnical Engineering*, *111*(10), pp.1161-1176.

Fukushima, S. and Tatsuoka, F., 1984. Strength and deformation characteristics of saturated sand at extremely low pressures. Soils and Foundations, 24(4), pp.30-48.

Tatsuoka, F., Goto, S. and Sakamoto, M., 1986. Effects of some factors on strength and deformation characteristics of sand at low pressures. Soils and Foundations, 26(1), pp.105-114.

7 Conclusions and recommendation

In this dissertation the mechanical behavior of simplified cantilever type larger diameter steel tubular pile walls (CSTP) embedded in artificially made soft rock have been investigated. Following to a simulation of excavation and additional lateral loading on a simplified cantilever wall, detailed investigations on the influential factors regarding to the embedment and loading conditions have been investigated through a series of lateral loading tests on large diameter steel tubular piles and steel tubular pile walls embedded in different soil profiles such as soft rock and soft rock overlain by sand. Based on the experimental outcomes the following conclusions were derived as follows:

In chapter 3, A centrifuge modelling system was developed to model the behavior of cantilever type retaining walls embedded in soft rocks from a design loading condition to the ultimate failure conditions under a constant centrifugal (50 g) acceleration. From the centrifuge model experiments done by using the developed system, the following are confirmed:

1) Stability of cantilever type retaining walls with large stiffness equivalent to 2.5 m diameter steel tubular pile wall could be secured with relatively small embedment depth (d_e=3m or 1.1/β) in soft rock against relatively high wall height of 12 m in the design condition, and could pose reasonable safety margin against ultimate failure.

2) Deflection of the cantilever retaining wall is generated by the combination of translation and rotation in the embedded part, and bending of wall under the ordinary design load. As the load from the retained soil further increases, the rigid body rotation becomes dominant displacement mode and the wall fails by the rotational failure mode with a pivot point at the location near the excavation bottom.

3) A relatively small increment of embedment depth (e.g. 0.5m (20%)) from 2.5m embedment depth could decrease the deformation under the ordinary design loading and increase the ultimate failure load significantly, and furthermore, increase the redundancy of the wall against the failure, changing the failure behavior from brittle one to ductile one.

Outcomes for the walls embedded in two different model soft rocks was analysed based on the generalized embedment depth ($d_e\beta$), and the following conclusions obtained from the analysis.

At relatively small $d_e\beta$-values (0.7 - 0.9) the influence of embedment depth become eminent at all range (small to large) of wall top displacements, i.e., moment resistance ratios between two walls having the embedment depth ($d_e\beta$) in this range of $d_e\beta$ = 0.7-0.9, could be expected to increase linearly with wall deformations from small displacement up to failure. In other words, higher dependency of wall stability on the increment of embedment could be expected in this range.

Over the value of $d_e\beta$ = 0.9, the wall deformation mechanism is governed by the influence of shallow rock layers from the initial condition to a wall top displacement of about 1% of the retained height (*H*). This *1%H* also can be considered as an alarming point prior to the catastrophic failure of a wall with $d_e\beta$ = 0.9.

The normalized embedment depth for the wall considered in this study can be categorized in to three different zones. The first zone can be considered where the $d_e\beta$< 0.9, in this zone the wall response highly controlled by the embedment depth under a load of interest, it can be regarded as an unstable zone where catastrophic failures could be expected. This zone must be avoided even for the application of temporary retaining walls.

The second zone can be defined from $d_e\beta$ = 0.9 to 1.5 or 2, here the upper limit is based on the judgement, it must be confirmed from further physical or numerical studies. In this zone the influence of shallow rock layer provides large lateral resistance prior to the significant deterioration of stiffness. Yielding of rock or significant deterioration of rock stiffness took place at about 120mm (δ_t *=1%H*) wall top displacement which is far above the allowable displacement concept (50mm) of most of the design codes.

The third zone can be considered with the $d_e\beta$ values over 2, where the ultimate failure can be expected only due to the structural deformation.

As a recommendation the boundary value of $d_e\beta$ between second and third zone must be investigated physically or numerical studies, until that this boundary value must be treated with caution. Also this study can be applicable only for a uniform mass of soft rock, where no clear planes of weakness or discontinuities are present.

In chapter 4, a series of single pile loading tests were conducted to investigate the influential factors on the behavior of laterally loaded large diameter steel tubular piles. From the outcomes the following conclusions were derived:

At small displacement (1% Ø） level no significant influence of embedment depth in rock type grounds can be observed, which indicates large lateral confinement and contribution of shallow layers of rock on the lateral resistance. In the stiff ground like the soft rock, the lateral resistance changes significantly in a small range of embedment depth. A small increment of embedment depth in soft sand rock highly controlled the displacement and failure behavior of the piles compared to the increment in the sand soil.

Over certain embedment depth, the increment of pile length becomes less significant on the increase of resistance. This depth can be considered as an optimum depth. On the other hand, due to the softening of ground materials and the change of failure mode from the ground failure to pile structural failure, the optimum embedment depth changes depending on the conditions of resistance. This Optimum embedment depth is shallower for the initial stiffness than the ultimate bearing capacity in the soft rock.

For the cases with the ground failure as the ultimate condition, the failure behaviors of sand and rock become quite different, ductile and brittle respectively.

From the laterally loaded single piles embedded in soft rock layer (Model-4), up to δ_t =1%Ø (20mm) the 3m embedment depth($(d_e/Ø)$ =1.5) could be considered as an optimum embedment with specific loading height considered in this study. This embedment depth is a kind of optimum embedment depth for relatively larger initial stiffness of soft rock more or less in the intact condition. Furthermore, from the observed buckling of the pile with 4m embedment ($(d_e/Ø)$ =2) in soft rock (Model-4), it can be considered that the optimum embedment depth covering the initial stiffness and the ultimate bearing capacity could be closer to 4m (2Ø) for this specific loading condition. However, the ultimate lateral resistance associated with the pile-rock interaction could be alternated by the loading history. Higher the imposed displacements in each cycle larger the deterioration of the rock stiffness, thereby the failure mode could be alternated from structural buckling to rock failure.

Based on the observations of single piles in two-layer profile, it can be concluded that the deterioration of underlain shallow layer rock stiffness took place at a pile top displacement of δ_t =2%Ø (40mm) for the specific loading condition in this study. Based on this study, limiting passive pressures in a 3.25Ø thick overlain layer could be expected to reach at δ_t =2%Ø. Based

on this, for the design conditions with an allowable pile top displacements δ_{all} >2%Ø at the loading height considered in this study, small strain stiffness of the underlain rock could not be expected.

From the system stiffness of single piles embedded in single rock layer, beyond an imposed displacement of 5%Ø no significant change in the system stiffness could be observed. Based on this observation and the observed structural failure of the pile SP-SR-4 as an ultimate failure condition, it can be said that, after a pile top displacement of 5%Ø the lateral resistance is mainly controlled by the structure rather than the embedded medium for the piles with a specific loading condition in this study.

In chapter 5, two centrifuge model tests were conducted to investigate the behavior of large diameter steel tubular pile walls embedded in single rock layer and a rock layer overlain by sand. From the extensive investigations the following conclusions were derived:

Similar to the single pile behavior, at small displacement (1% Ø) level no significant influence of wall embedment depth in single rock layer could be seen, which indicates large lateral confinement and contribution of shallow layers of rock on the lateral resistance.

Based on the observed structural failure of the pile and ground (shear wedge type) failure of tubular pile wall with a 4m (d_e=2Ø) embedment depth in single rock layer, the optimum embedment depth corresponding to the ultimate bearing capacity is deeper for the wall than single pile, which indicates that the rational embedment for cantilever tubular pile wall is larger than single pile with same cross section.

There is an optimum embedment depth from which the ultimate failure changes from ground failure to structural failure. From the observed ultimate failure conditions of single pile (structural failure) and tubular pile wall (shear wedge type failure) it can be concluded that the optimum embedment depth is deeper for the wall than single pile, which indicates that the rational embedment for cantilever tubular pile wall is larger than single pile with same cross section.

Based on observed system stiffness and residual deformations of tubular pile walls in single rock layer, an allowable wall top displacement of 1%Ø (20mm) and allowable maximum load of 0.3q_{ult} could be defined as the limiting values to prevent the plastic yielding or the failure of the walls embedded in single rock layer under the specific loading condition implemented in this study.

In the case of wall model (RPW-SR-3) and single pile (SP-SR-3) with the embedment depth of 1.5Φ in single rock layer showed the ground failure as an ultimate failure. However, the normalized ultimate resistance for single pile is about 1.6 times that of wall model and the wall model exhibited a clear wedge type ground failure, while the single pile showed more confined deformations.

Mechanism behind the difference in the ground failure of single pile and wall could be attributing to the 2-D and 3D boundary conditions and associated influence zones. The influence zone, which contribute to the lateral resistance for a unit width of the wall is much narrower compare to an isolated single pile. This phenomenon causes an increased stress level or strain in the shallow layer of the rock and resulting significant reduction in subgrade reaction under same loading level. This mechanism causing large deflection of the wall compare to the condition of an isolated single pile. Due to the large deflection of the wall, eventual accumulation of wall deflection in the embedded zone, causing the deterioration of subgrade reaction along the wall embedded zone and eventually causing a wedge type ground failure at the ultimate resistance of the embedded medium. However, for the case of walls in two-layer profile, large passive pressure mobilization in the shallow rock layer is prevented due to the confining effect of overlain sand and the mobilized passive pressures in the sand layer. Also it shifts the zone of mobilization to deeper locations in the wall front. This mechanism helps to prevent the shallow rock layer failure as well as prevent from wedge type failures in the toe back passive zone in underlain rock layer.

In chapter 6, A complicated dynamic centrifuge model was developed to study the behavior of CSTP walls under dynamic loads. From the preliminary analysis of experimental outcomes, the following conclusions were derived

Considering different initial conditions as discussed in 6.4.4.1 and 6.4.4.2, the tubular pile wall exhibits relatively large resistance compare to the simplified wall model under same increment of displacement. No clear failure of the embedded medium or the tubular pile wall can be confirmed even at the applied maximum moment load, which is 1.2 times the ultimate resistance of the simplified wall model.

Based on accumulated deformations described in 6.4.5, applied moment load and the creep deformation characteristics of tubular pile wall, it can be confirmed that the tubular pile wall ($1.2/\beta$) is more stable compare to the simplified wall model ($1.05/\beta$). Design proposals based on the outcomes of simplified wall model could yield more conservative design approach.